UNIVERSITAT POLITÈCNICA DE CATALUNYA
BARCELONATECH
Departament d'Enginyeria Electrònica

DETERMINATION OF THE STATE OF HEALTH OF LI-ION BATTERIES: THE IRREVERSIBLE ENTROPY PRODUCTION APPROACH.

Thesis submitted in partial fulfillment of the requirements for the PhD Degree issued by the Universitat Politècnica de Catalunya, in its Electronic Engineering Program.

Author: **Victòria Júlia Ovejas Benedicto**
Advisor: **Àngel Cuadras Tomàs**

November 2017

Abstract

In recent years, the demand of batteries has increased with the growth of portable applications. It is widely known, though, that the performance of batteries decreases with time and use. This loss of performance is measured by the State-of-Health (SoH) of the cells. However, there is no consensus in defining this parameter. Experimental, theoretical or even heuristic approaches can be found in literature and commercial systems, but usually, they only work for particular conditions and some of them are not linked to the degradation suffered by the cells themselves.

The aim of this study is to find a parameter directly related to the degradation suffered by the cells. For this purpose, we investigate the irreversible entropy production in Li-ion cells because irreversible entropy is related to energy dissipation and thus, to irreversibilities due to system or energy degradation.

In order to evaluate the degradation of the cells and its correspondence to irreversible entropy generation, we studied different Li-ion chemistries (NMC, LFP and LCO). Cells were cycled at different discharge rates (close to and far from equilibrium) and evaluated at different SoHs. Therefore, capacity fade and impedance rise (the most commonly used techniques in SoH determination) were characterized and related to irreversible entropy generation. In addition, post-mortem analysis was carried out to achieve a deeper knowledge of the causes and effects of degradation.

As a result of this study, we introduced a new parameter for system degradation characterization, the Relative-Entropy-Production (REP), defined as the irreversible entropy generation ratio between the actual state and the initial state. In particular, we found irreversible entropy production evaluated at low discharge rates was higher as more degraded were the NMC cells. In the case of LFP cells, irreversible entropy production decreased during initial cycles but then increased towards the EoL. This behavior coincided with a capacity increase during initial cycles. In addition, we found a relationship between irreversible entropy generation and the phase transformations taking place during the discharge processes in all the evaluated cells. It was associated to the fact that materials undergoing phase transformations expand and contract yielding to cracks and other structural modifications, which produce degradation and thus irreversible entropy. REP and irreversible entropy production are found to be promising magnitudes to characterize battery aging. Even though much research has still to be carried out, the idea is to define, in the future, a threshold in REP or irreversible entropy production that the cells can stand before considering their EoL is reached.

Keywords: Li-ion, SoH, irreversible entropy, degradation, damage, battery, impedance, capacity fade, post-mortem.

Acknowledgements

First, I want to acknowledge to my thesis advisor, Àngel Cuadras, the technical and emotional support that he gave me during these years. I really appreciate he was always available for helping me and that he encouraged me for doing research stays abroad. I think this part was very important in the fulfillment of this work.

During the research stays, which took place at Hawaii Natural Energy Institute (HNEI) in Hawaii (USA) and at the Institute for Power Electronics and Electrical Drives (ISEA) in Aachen (Germany), I learned many useful definitions and characterization techniques. For this reason, I am very grateful to Professors Bor Yann Liaw and Dirk Uwe Sauer for hosting me in their institutions. In addition, I would like to acknowledge everyone who helped me during these periods, especially Rita Graff who carried out some of the laboratory tests during my research stay in Aachen.

The financial support that made this possible was provided by the Institut de Recerca en Energia de Catalunya (IREC) during the first stages of the dissertation and to the financial support of FPU contract given by MCU during the last four years. In particular, I would like to mention Professor Joan Ramon Morante from IREC for the trust he placed in the project on its first stages. During the completion of this study, we also participated in various projects (TEC2015-63899-C3-1-R, TEC2011-27397 and MAT2010-21510), which also contributed to the finantial support of this work. Moreover, I also want to acknowledge Ikerlan for helping us in cycling the cells when our facilities did not allow it.

Finally, I want to highlight that it was very nice to share this experience with other PhD students, which became very good friends after that. We supported one another and we always put a touch of humor in everything we did. And last, but not least, I want to acknowledge to my loved ones the support and patience they have shown during this time, especially during the darkest episodes of this thesis.

Thank you for everything to everyone.

List of acronyms and symbols

BoC	Beginning-of-Charge
BoD	Beginning-of-Discharge
BoL	Beginning-of-Life
CT	Charge Transfer
EoC	End-of-Charge
EoD	End-of-Discharge
EoL	End-of-Life
I	Current
ICP	Inductively Coupled Plasma
NE	Negative electrode
SoC	State-of-Charge
SoH	State-of-Health
MT	Mass Transfer
OCV	Open-circuit voltage
PE	Positive electrode
RCV	Rest cell voltage
REP	Relative-Entropy-Production
V_{cell}	Cell voltage
Z	Impedance

Table of contents

Abstract i
Acknowledgements iii
List of acronyms and symbols v
Index of figures xi
Index of tables xxv
Chapter 1 General introduction 29
1.1. Introduction to batteries 29
1.1.1. Battery chemistries 30
1.1.2. Packaging styles 33
1.2. Lithium-ion cells 36
1.2.1. Redox reactions 39
1.2.2. Contributions to overpotential in Li-ion batteries 40
1.2.3. Aging mechanisms 46
1.3. SoC and SoH determination methods 50
1.3.1. SoC definition 50
1.3.2. SoH definition 52
1.4. Motivation and objectives 53
Chapter 2 Capacity fade 55
2.1. Introduction 55
2.2. Materials and methods 56
2.2.1. Battery cycling 57
2.2.2. Initial characterization 59
2.2.3. Experimental SoC definition 61
2.2.4. Capacity measurements 63
2.3. Results and discussions 63
2.3.1. Cell-to-cell variations 63
2.3.2. LGC2 cells (NMC) 65
2.3.3. LFP cells 66
2.3.4. LCO cells 70
2.4. Conclusions 70
Chapter 3 Impedance measurements 71
3.1. Introduction 71
3.1.1. Impedance Measurements 72
3.1.2. Electrochemical Impedance Spectroscopy (EIS) 73
3.1.3. Impedance from pulses 75
3.1.4. Parameters measured in Li-ion batteries by EIS 76
3.2. Materials and methods 77

3.2.1. Impedance by EIS 77
3.2.2. Impedance from current pulses 80
3.3. Results 81
3.3.1. Impedance from EIS measurements 81
3.3.2. Impedance from charging profiles and pulsed signals 93
3.4. Discussions 95
3.4.1. Impedance from EIS measurements 96
3.4.2. Impedance from charging profiles and pulsed signals 103
3.5. Conclusions 104
3.5.1. Impedance from EIS measurements 104
3.5.2. Impedance from charging profiles and pulsed signals 107
Chapter 4 Energy and Entropy 109
4.1. Introduction 109
4.1.1. Classical and modern thermodynamics 109
4.1.2. Heat transfer 114
4.1.3. Heat capacity 115
4.1.4. Entropy 116
4.1.5. Energy conversion in batteries 119
4.2. Materials and Methods 119
4.2.1. Open Circuit Voltage (OCV) measurement 119
4.2.2. Overpotential 120
4.2.3. Entropy 122
4.2.4. Incremental capacity analysis (ICA) 123
4.2.5. Heat calculations 124
4.3. Results 124
4.3.1. NMC cells 124
4.3.2. LFP cells 143
4.3.3. LCO cells 162
4.4. Discussions 167
4.4.1. OCV and hysteresis 167
4.4.2. Overpotential 169
4.4.3. Entropy 176
4.4.4. Heat generation 180
4.5. Conclusions 180
4.5.1. OCV and hysteresis 180
4.5.2. Overpotential 181
4.5.3. Entropy 182
4.5.4. Heat generation 184
Chapter 5 Post-mortem analysis 185

5.1. Introduction ... 185
5.2. Materials and methods ... 186
5.2.1. Cell opening ... 186
5.2.2. Preparation of samples ... 187
5.2.3. Visual inspection ... 188
5.2.4. Building half-cells ... 189
5.2.5. Capacity measurement of half-cells ... 191
5.2.6. Impedance measurement of half-cells ... 191
5.2.7. Inductively Coupled Plasma Optical Emission Spectrometry analysis ... 191
5.2.8. Porosimetry ... 193
5.2.9. X-Ray Diffraction (XRD) analysis ... 193
5.3. Results ... 193
5.3.1. Weighting ... 193
5.3.2. Visual inspection ... 194
5.3.3. Capacity of half-cells ... 197
5.3.4. Impedance of half-cells ... 201
5.3.5. ICP analysis ... 205
5.3.6. Porosimetry ... 210
5.3.7. XRD analysis ... 213
5.4. Discussions ... 215
5.4.1. Visual inspection ... 215
5.4.2. Metals dissolution ... 217
5.4.3. Loss of electrolyte ... 218
5.4.4. Impedance ... 219
5.4.5. Capacity fade ... 221
5.5. Conclusions ... 225
5.5.1. LGC2 cells (NMC) ... 225
Chapter 6 General discussions ... 229
6.1. Relative-Entropy-Production (REP) ... 230
6.1.1. NMC cells ... 231
6.1.2. LFP cells ... 241
6.1.3. LCO cells ... 250
6.1.4. Summary of REP evaluated in different chemistries and rates ... 251
6.1.5. Increase in $\mathrm{d}i\mathcal{S}/\mathrm{d}t$ at the end of phase transformations ... 252
Chapter 7 General conclusions ... 253
7.1. Future work ... 256
7.2. Research lines derived from this study ... 256
References ... 257

Index of figures

Fig. 1.1. Main parts and schematic behavior of an electrochemical cell [3]. 30
Fig. 1.2. Specific capacity versus specific energy for different battery chemistries [6]. 32
Fig. 1.3. Cylindrical cell on the left [9] and transversal cutting of a cylindrical cell on the right [6]. .34
Fig. 1.4. Coin cells on the left and transversal cutting of a coin cell on the right [7]. 34
Fig. 1.5. Prismatic cell on the left [10] and transversal cutting of a prismatic cell on the right [7]. ...35
Fig. 1.6. Pouch cell on the left [7] and pouch cell structure on the right [11]. 36
Fig. 1.7. Comparison of the characteristics of the most common Li-ion chemistries. Data were extracted from [13]. 38
Fig. 1.8. Schematic diagram of a Li-ion cell [15]. 40
Fig. 1.9. Dependence of the voltage profile of a Li-ion cell on the discharge rate at room temperature [19]....41
Fig. 1.10. Dependence of the voltage profile of a Li-ion cell on the temperature at a constant discharge rate [20]. 41
Fig. 1.11. Overvoltages generated in a Li-ion cell for increasing current rates [23]....43
Fig. 1.12. Polarization curve obtained from Butler-Volmer equation accounting only for activation polarization [25]. 44
Fig. 1.13. Relation between current (normalized to the limiting current i_L) and overpotential (η) in a li-ion cell [26]. Dashed lines represent the polarization curve when only activation polarization is taken into account and solid line accounts for concentration polarization effects. At the insets, relation between concentrations at the surface and the bulk are represented. 45
Fig. 1.14. Degradation mechanisms at the negative electrode of a li-ion cell [29]. 48
Fig. 1.15. Aging mechanisms at the positive electrode of a Li-ion cell [35]....49
Fig. 2.1. Charge and discharge processes always start at the same SoC independently from rate because of the remnant capacity. Remnant capacity has to be carried out at the lowest rate employed in the test in order to assure the cells are charged to the same level (C/25 in this case). Resting voltages in green and red can be directly related to SoC through the OCV curve. 60
Fig. 2.2. Example of SoC calculation at 3 different charge/discharge rates (C/25, C/5 and 1C) for a NMC cell at a particular SoH. End-of-Discharge Rest Cell Voltage (EoD RCV) and End-of-Charge Rest Cell Voltage (EoC RCV) after 4 h relaxation period was compared to the OCV-SoC curve obtained at low rates (C/25 in that case). 63
Fig. 2.3. Rate capability of a NMC cell (left) and a VIC cell (right) evaluated at C/25, C/5 and 1C at BoL and room temperature....64
Fig. 2.4. Voltage profiles of a LGC2 cell versus delivered capacity at a C/25 (left) and 3C/2 (right) discharge rates. Nominal capacity is 2.8 Ah. 65

Fig. 2.5. Capacity evolution of the NMC cells evaluated at a 3C/2 discharge rate (in Ah on the left and as a percentage of the nominal capacity on the right). Three different slopes in capacity fade were found, which were labeled and quantified. Some points have been skipped for clearer representation. 66
Fig. 2.6. Capacity evolution of the NMC cells evaluated at a C/25 discharge rate (in Ah on the left and as a percentage of the nominal capacity on the right). 66
Fig. 2.7. Voltage profiles of a VIC cell (LFP) versus delivered capacity at a C/25 discharge rate at different aging levels. Discontinuity is due to the break for the sake of clarity in the representation. 67
Fig. 2.8. Capacity evolution of the VIC cells (LFP) evaluated at a 2C discharge rate (in Ah on the left and as a percentage of the nominal capacity on the right). Some points have been skipped for clear representation. 67
Fig. 2.9. Capacity evolution of the VIC cells (LFP) evaluated at a C/25 discharge rate (in Ah on the left and as a percentage of the nominal capacity on the right). 68
Fig. 2.10. Voltage profiles of EVbat cells (LFP) versus delivered capacity at a C/25 discharge rate at different aging levels. Discontinuity is due to the break for the sake of clarity in the representation. 68
Fig. 2.11. Capacity evolution of the EVbat cells (LFP) evaluated at a 2.5C discharge rate rate (in Ah on the left and as a percentage of the nominal capacity on the right). Estimated slopes of the capacity fade at different aging levels were represented. Some points have been skipped for clear representation. $Slope_1$: 0.39 $Ah \cdot cycle^{-1}$ (0.97 $\% \cdot cycle^{-1}$), $slope_2$: - 0.066 $Ah \cdot cycle^{-1}$ (- 0.16 $\% \cdot cycle^{-1}$), $slope_3$: - 0.03 $Ah \cdot cycle^{-1}$ (- 0.08 $\% \cdot cycle^{-1}$) and $slope_4$: - 0.009 $Ah \cdot cycle^{-1}$ (- 0.02 $\% \cdot cycle^{-1}$)....69
Fig. 3.1. Schematic diagram of the transfer function of a system when it is excited by an input signal and the output is measured. 72
Fig. 3.2. Representation of pseudo-linear measurement of impedance [65]. 73
Fig. 3.3. Phase shift between applied voltage and measured current [66]. 74
Fig. 3.4. Rectangular pulse in the time domain and its corresponding Fourier transform (sinc function) [71]....75
Fig. 3.5. Interface layer between the electrode and the electrolyte [77]. 77
Fig. 3.6. Definition of different resistance contributions....79
Fig. 3.7. Typical time constants (or characteristic frequencies) of the transport effects and electrochemical processes occurring in a LFP cell [84]. 80
Fig. 3.8. Nyquist representation of impedance evolution with SoC of a LGC2078 fresh NMC cell (left) and LGC2075 degraded NMC cell (right). A zoom of this impedance at BoL and EoL is depicted in Fig. 3.9 and Fig. 3.10, respectively. 81

Fig. 3.9. Zoom of Nyquist representation of impedance evolution with the SoC of a fresh NMC (LGC2078) cell (on the left) and dependency on SoC of the total resistance ($R_\Omega + R_{CT}$), charge-transfer resistance (R_{CT}) and ohmic resistance (R_Ω) (on the right). 82

Fig. 3.10. Zoom of Nyquist representation of impedance evolution with SoC of a degraded NMC (LGC2075) cell (on the left) and dependency on SoC of the total resistance ($R_\Omega + R_{CT}$), charge-transfer resistance (R_{CT}) and ohmic resistance (R_Ω) (on the right). 82

Fig. 3.11. (left) Absolute and relative (right) increases of ohmic and charge-transfer resistances of LGC2075 cell (NMC) from BoL to EoL. 83

Fig. 3.12. Nyquist representation of LGC2074 cell's impedance at SoC = 100 % after 60, 120, 220, 285 and 335 cycles at a 1.5C discharge rate. 83

Fig. 3.13. (left) Ohmic and (right) charge-transfer resistances evolution with aging of three LGC2 (NMC) cells at SoC = 100 % obtained by impedance spectroscopy. 84

Fig. 3.14. (left) Charge-transfer resistance ($R_{V\text{-}I}$ in that case) of three LGC2 (NMC) cells at SoC = 100 % obtained from the overpotential generated at different discharge rates (C/25, C/5 and 1C) (V-I polarization curve). It has to be noted that the measurement was also affected by ohmic conduction, thus resulting as the joint contribution of both ohmic and charge-transfer resistances. In the right part, the ohmic contribution represented in Fig. 3.13 was subtracted in order to compare the charge-transfer resistance obtained by the two methods. 84

Fig. 3.15. Polarization curve of a fresh LGC2074 cell (NMC) (left) and of the same cell after 325 cycles (right) obtained at C/25, C/5 and 1C charge/discharge rates. 85

Fig. 3.16. Relative increases of ohmic and polarization resistances at SoC = 100 % during the cycle aging process of the three NMC cells. 85

Fig. 3.17. Nyquist representation of two VIC cells (LFP) impedance at SoC = 100 % after being subjected to different number of cycles. Serial resistance contribution was subtracted and only the more representative cycles were represented. At the inset, full spectra of the VIC cells at SoC = 100 %. 86

Fig. 3.18. (left) Ohmic resistance (R_Ω) evolution during the first cycles where the employed holder allowed the comparison of the data. (right) Total resistance evolution represented as the addition of charge-transfer and mass-transfer resistances. Lines were only drown as a guide to the eye. 87

Fig. 3.19. Charge-transfer resistance of VIC01 cell (LFP) at BoL obtained from the slope of the overvoltage produced at C/25, C/5 and 1C charge/discharge rates. 87

Fig. 3.20. (Left) Nyquist representation of EVbat_1 cell (LFP) impedance at different states-of-charge. The cell was cycled 50 times at a 2.5C charge/discharge rate at ambient temperature. (Right) Ohmic, charge-transfer and total resistances evolution with SoC. 88

Fig. 3.21. Ohmic resistance (top – left), charge-transfer resistance (top – right) and total resistance calculated as the addition of ohmic and charge-transfer resistances (bottom) evolution with SoC of four EVbat cells (LFP) that were set to different degradation levels. 89
Fig. 3.22. (left) Absolute and relative (right) increases of ohmic and charge-transfer resistances of the EVbat cells (LFP) from cycles 50th (EVbat_1) to 200th (EVbat_3).....90
Fig. 3.23. Impedance evolution at SoC = 100 % of four EVbat cells (LFP) which were previously cycled 50, 100, 200 and 400 times.....90
Fig. 3.24. Ohmic (top-left), charge-transfer (top-right) and total (bottom) resistances of EVbat cells (LFP) at SoC = 100 % previously set to different degradation levels.....91
Fig. 3.25. Impedance evolution of the Fresh Microbattery with SoC. On the right side, serial and polarization resistances evolution with SoC.....92
Fig. 3.26. Impedance evolution of the Old Microbattery with SoC (SoC 1 means totally charged and SoC 6 totally discharged). On the right side, serial and polarization resistances evolution with SoC.....92
Fig. 3.27. Absolute (left) and relative (right) increases of ohmic and charge-transfer resistances from BoL (Fresh Microbattery) to EoL (Old Microbattery). Old Microbattery was cycled 150 times until the capacity dropped 20 % of the initial capacity. 93
Fig. 3.28. Inferred real and imaginary parts of impedance of a supercapacitor of 1 F and 5.5V from constant current charging voltage and from pulsed current charging in comparison to measured impedance. 93
Fig. 3.29. Current response to a pulsed signal of 5 V and 1 ms (inset) averaged for 10 samples.....94
Fig. 3.30. Comparison between impedance of a supercapacitor of 1 F and 5.5 V measured using a potentiostat and injecting a pulsed signal. The SNR (bottom part) indicated that below 15 dB, no fitting was possible. 94
Fig. 3.31. Comparison between impedance of Microbattery LCO cell measured using a potentiostat and injecting a current pulse of 1 A during 1 s and doing FFT transformations of current and voltage profiles.....95
Fig. 3.32. Capacity evolution of a VIC cell measured at C/25 (top) and 2C (middle) showing the different tendencies found during the aging test. Charge-transfer and mass-transfer resistances evolution with aging measured at SoC = 100 % (bottom). Dashed lines represent the ranges in which different behaviors were appreciated..... 101
Fig. 4.1. Thermodynamic systems classified depending on how they interact with the environment. 110
Fig. 4.2. Schematic of Carnot heat engine [124]..... 112
Fig. 4.3. Pseudo-OCV evolution during cycle life of LGC2074 cell (left) and LGC2075 cell (right) calculated from charge/discharge curves at C/25..... 124

Fig. 4.4. Comparison of charge and discharge OCV curves of LGC2 cells (NMC) at BoL and EoL measured by GITT and ps-OCV. 125
Fig. 4.5. Discharge OCV curves at BoL and EoL of LGC2075 cell (NMC) obtained from GITT measurements. 125
Fig. 4.6. Hysteresis voltage at BoL and EoL calculated as the difference in OCV during charge and discharge measured by using the GITT technique. 126
Fig. 4.7. Incremental capacity curves during charge process at a C/25 rate upon cycling of LGC2074 cell (NMC). It has to be noticed that resistive contributions has been subtracted prior to the analysis 127
Fig. 4.8. Evolution of the overpotential at C/25 obtained from the ps-OCV curve of two NMC cells (LGC2074 cell to the left and LGC2075 to the right) during their cycle life. 128
Fig. 4.9. (left) OCV evolution with cycle aging and (right) overpotential evolution at C/25 with cycle aging of the Li/NMC half-cell. 129
Fig. 4.10. (left) OCV evolution with cycle aging and (right) overpotential evolution at C/25 with cycle aging of the Li/Graphite half-cell. 129
Fig. 4.11. Overpotential generated at the PE and NE electrodes measured in half-cell configurations discharged at a C/25 rate (NMC/Li and graphite/Li) at BoL (left) and EoL (right). PE and NE overpotentials were added without taking into account the matching of the electrodes in order to obtain a rough approximation of the overpotential generated at the full-cell 130
Fig. 4.12. Overpotential generated in a NMC cell at a 3C/2 discharge rate at different aging stages. 130
Fig. 4.13. Comparison of the overpotential generated at C/25 calculated from the discharge GITT OCV (line + markers) and the ps-OCV (solid line) at BoL (left) and at the EoL (right). 131
Fig. 4.14. Error in overpotential at C/25 introduced when using ps-OCV instead of GITT OCV during discharge at BoL and EoL 131
Fig. 4.15. Apparent resistance calculated from the overvoltage curves while discharging a NMC cell at C/25 (left) and at 3C/2 (right) rates. 132
Fig. 4.16. Overpotential contributions at BoL (left) and EoL (right) while discharging the NMC cell at a C/25 rate at ambient temperature. Calculations were made with discharge GITT OCV. 133
Fig. 4.17. Overpotential contributions at BoL (left) and EoL (right) while discharging the NMC cell at a 3C/2 rate at ambient temperature. 133
Fig. 4.18. Derivative of the OCV with respect to temperature of a LGC2 cell (NMC) at BoL (black filled squares) and at the EoL (red unfilled circles). 134

Fig. 4.19. Evolution of the irreversible entropy generation rate obtained from the ps-OCV curve at C/25 of two NMC cells (LGC2074 cell to the left and LGC2075 to the right) during their cycle life. 135
Fig. 4.20. Irreversible entropy production in a NMC cell at BoL and EoL when discharged at a C/25 rate at ambient temperature. It was obtained from the OCV curves obtained from the GITT measurements. 135
Fig. 4.21. d_iS/dt contributions at BoL (left) and EoL (right) while discharging the NMC cell at a C/25 rate at ambient temperature. The results were obtained from the discharge GITT OCV curves. 136
Fig. 4.22. (left) Absolute and (right) relative d_iS/dt contributions to total d_iS/dt at BoL (solid lines + filled symbols) and at the EoL (dashed lines + empty symbols) when discharging the NMC cells at a C/25 rate at ambient temperature. 136
Fig. 4.23. Irreversible entropy production in a NMC cell at a 3C/2 discharge rate at different aging stages. 137
Fig. 4.24. d_iS/dt contributions at BoL (left) and EoL (right) while discharging the NMC cell at a 3C/2 rate at ambient temperature. 137
Fig. 4.25. (left) absolute and (right) relative d_iS/dt contributions to total diS at BoL (solid lines + filled symbols) and at the EoL (dashed lines + empty symbols) when discharging the NMC at a 3C/2 rate at ambient temperature. 138
Fig. 4.26. Irreversible heat generation rate (top- left), reversible heat generation rate (top- right), and total heat generation rate (bottom) at BoL and EoL of LGC2075 cell (NMC) discharged at a rate of C/25. 139
Fig. 4.27. Evolution of irreversible heat generation rate (top-left), reversible heat generation rate (top-right) and total heat generation rate (bottom) with cycles in the particular case of LGC2074 cell (NMC) represented for every SoC during a discharge process at 3C/2 rate. 140
Fig. 4.28. Ps-OCV dependence on temperature for a LGC2 cell at BoL (left) and at the EoL (right). 141
Fig. 4.29. Overpotential evolution with temperature at C/25 of a NMC cell at BoL (solid lines) and at the EoL (dashed lines). 141
Fig. 4.30. Evolution of the irreversible entropy generation rate with temperature at C/25 of a NMC cell at BoL (solid lines) and at the EoL (dashed lines). 142
Fig. 4.31. Irreversible heat generation rate (top- left), reversible heat generation rate (top- right), and total heat generation rate (bottom) at BoL (solid lines) and EoL (dashed lines) of a LGC2 cell (NMC) discharged at a rate of C/25 at different temperatures (5 ºC, 15 ºC and 32ºC). 143

Fig. 4.32. Pseudo-OCV evolution during cycle life of VIC01 cell (left) and VIC02 cell (right) calculated from charge/discharge voltage curves at C/25. 144
Fig. 4.33. (left) Cell voltage of a VIC cell (LFP) under different charge/discharge rates. (right) ps-OCV curves of a VIC cell (LFP) obtained at different charge/discharge rates. 144
Fig. 4.34. Comparison of charge and discharge OCV curves of VIC cells (LFP) at BoL (left) and EoL (right) measured by GITT and ps-OCV. 145
Fig. 4.35. Discharge OCV curves at BoL and EoL of a VIC cell (LFP) obtained from GITT measurements at ambient temperature..... 145
Fig. 4.36. Hysteresis voltage of a VIC cell (LFP) calculated as the difference between charging and discharging GITT OCV curves at BoL and EoL. 146
Fig. 4.37. Incremental capacity analysis of a VIC cell (LFP) at different SoH at a C/25 discharge rate. On the left, IC curves. On the right: evolution of the area of peaks. 146
Fig. 4.38. Overpotential of a VIC cell (LFP) generated during a discharge at a C/25 rate and calculated from the ps-OCV at room temperature. 147
Fig. 4.39. Overpotential generated in a VIC cell (LFP) at a 2C discharge rate evaluated at BoL (solid line) and EoL (dashed line). 148
Fig. 4.40. (left) Cell voltage of a VIC cell (LFP) at a discharge rate of C/25 and discharge OCV obtained from GITT measurements at BoL and EoL. (right) Comparison of the overpotential generated at a discharge rate of C/25 calculated from the discharge GITT OCV (line + markers) and the ps-OCV (lines) at BoL and EoL..... 148
Fig. 4.41. Error in overpotential introduced when using ps-OCV instead of discharge GITT OCV at BoL and EoL. 149
Fig. 4.42. Comparison of the overpotential generated in a VIC cell (LFP) at 2C discharge rate calculated from the discharge GITT OCV and ps-OCV. 149
Fig. 4.43. Apparent resistance of a VIC cell (LFP) at a discharge rate of C/25 represented at BoL and EoL. It was calculated from OCV values coming from GITT tests. 150
Fig. 4.44. Apparent resistance of a VIC cell (LFP) at a discharge rate of 2C represented at BoL and EoL. It was calculated from OCV values coming from GITT tests. 150
Fig. 4.45. Different contributions to overpotential of a VIC cell (LFP) at BoL subjected to a discharge at a rate of C/25 (left) and 2C (right). 151
Fig. 4.46. Entropic coefficient of a VIC cell (LFP) at BoL and EoL. 152
Fig. 4.47. Irreversible entropy generation rate of a VIC cell (LFP) produced during discharge at a rate of C/25 and obtained from ps-OCV curves. 152
Fig. 4.48. Irreversible entropy generation rate of a VIC cell (LFP) produced during discharge at a rate of C/25 and obtained from GITT OCV curves. 153

Fig. 4.49. (left) Absolute and (right) relative d_iS/dt contributions at BoL while discharging the VIC cell at a C/25 rate at ambient temperature. The results were obtained from the discharge GITT OCV curves. 153
Fig. 4.50. Irreversible entropy generation rate of a VIC cell (LFP) produced during discharge at a rate of 2C and obtained from GITT OCV curves. 154
Fig. 4.51. (left) Absolute and (right) relative contributions to total d_iS/dt at BoL when discharging a VIC cell at a 2C rate. 154
Fig. 4.52. Irreversible heat generation rate (top- left), reversible heat generation rate (top- right), and total heat generation rate (bottom) at BoL and EoL of a VIC cell (LFP) discharged at a rate of C/25. 155
Fig. 4.53. Irreversible heat generation rate (top- left), reversible heat generation rate (top- right), and total heat generation rate (bottom) at BoL and EoL of a VIC cell (LFP) discharged at a rate of 2C. 156
Fig. 4.54. OCV curves of different EVbat cells (LFP) subjected to a different number of cycles (50, 100, 200, and 400). 157
Fig. 4.55. (left) IC curves at a C/25 discharge rate of different EVbat cells (LFP) subjected to a different number of cycles (50, 100, 200, and 400). (right) Evolution of the area of peaks (1) and (2). 157
Fig. 4.56. Overpotential generated at a C/8 discharge rate of different EVbat cells (LFP) previously subjected to a different number of cycles (50, 100, 200, and 400, respectively). 158
Fig. 4.57. Different contributions to overpotential generated in EVbat cells when discharged at a C/8 rate at four different SoHs (50 cycles, 100 cycles, 200 cycles and 400 cycles). 159
Fig. 4.58. Irreversible entropy generation rate during discharge at C/8 of different EVbat cells (LFP) previously subjected to a different number of cycles (50, 100, 200, and 400). 160
Fig. 4.59. Different contributions to irreversible entropy generation rate during discharge at C/8 of different EVbat cells (LFP) previously subjected to a different number of cycles (50, 100, 200, and 400). 161
Fig. 4.60. (left) Absolute and (right) relative contribution to d_iS/dt of the ohmic term, activation polarization and concentration polarization of EVbat cells (LFP) discharged at a C/8 rate and previously subjected to 50, 100, 200 and 400 cycles, respectively. 162
Fig. 4.61. OCV curves of two LCO cells at different SoH levels. 163
Fig. 4.62. Overpotential generated for two LCO cells at different SoH levels at a discharging rate of 1C. 163
Fig. 4.63. Different contributions to overpotential generated in LCO cells when discharged at a 1C rate at BoL (left) and EoL (right). 164
Fig. 4.64. Derivative of the OCV with respect to temperature (entropic coefficient) of two LCO cells at different SoH levels. 165

Fig. 4.65. Generation rate of irreversible entropy of a LCO cell at BoL (left) and EoL (right) when discharged at 1C. 165
Fig. 4.66. (left) Absolute and (right) relative contributions to the generation rate of irreversible entropy of two LCO cells at different degradation levels (BoL and EoL) when discharged at 1C. 166
Fig. 4.67. Irreversible (top-left) and reversible (top-right) heat generated in the discharge process of two LCO cells at different SoH levels at a rate of 1C. Total generation of heat corresponds to the addition of reversible and irreversible effects (bottom). 166
Fig. 4.68. Schematic representation of the energy transfers when converting chemical energy to electrical energy and the related useful work extracted from a battery. 167
Fig. 4.69. Hysteresis found in LFP (filled symbols) and NMC (empty symbols) cells at BoL and EoL at room temperature. 169
Fig. 4.70. Increase in overpotential at a C/25 discharge rate, from BoL to EoL of NMC and LFP cells at room temperature. 172
Fig. 4.71. Increase in overpotential from BoL to EoL at discharge rates between 1C and 2C of NMC, LFP and LCO cells at ambient temperature. 172
Fig. 4.72. Energy exchange in a closed system (green arrows). Output energy (work) is related to input energy through the efficiency. The arrows in red, blue and purple indicate entropy production (i.e. energy degradation). Energy losses and entropy production are divided between heat flow towards the environment and system aging. The former is divided between reversible heat and irreversible heat (friction, Joule effect, transport, charge-transfer effects…). The later can be due to the input energy or generated spontaneously in non-equilibrium systems. 177
Fig. 4.73. diS evolution with cycle aging of NMC/graphite cells discharged at C/25 calculated from ps-OCV (left) and discharge GITT OCV (right). Effects coming from PE and NE were distinguished (labeled as PE and NE) thanks to half-cell measurements. 178
Fig. 5.1. Cell-opening procedure. a) Remove the plastic cover. b) Open the can with a can-opener. c) Cut the current collector of the positive electrode and remove the top of the cell. d) Remove the can completely. e) Keep the jellyroll. f) Unroll the jellyroll and separate the electrodes and the separator. 187
Fig. 5.2. Weighting and samples preparation. a) Thickness measurement of the electrode and current collector. b) Punching the electrode for taking samples. c) Sample taken for building half-cells. d) Rinsing the samples in a solvent. e) Keeping the samples in a labeled box. f) Sample attached to a metallic support ready for XRD analysis. 188
Fig. 5.3. Unrolled electrode divided by sections. Rectangular and circular samples of different sizes were taken along the electrodes. 188

Fig. 5.4. Main steps in the process of building half-cells in a coin cell format where metallic lithium, fresh electrolyte and a new separator were added. 189
Fig. 5.5. Diagram of the different steps followed during the ICP-OES analysis [179]. 192
Fig. 5.6. Example of metal dissolution and migration of Manganese and further deposition on SEI surface [180]. 193
Fig. 5.7. Visual inspection of the negative electrode (top) and image taken with the laser microscope (bottom) of a fresh cell (LGC2079), on the left and an aged cell (LGC2074), on the right. 195
Fig. 5.8. Laser microscope image of the positive electrode of LGC2 cells (NMC) of a fresh cell (left) and an aged one (right) 195
Fig. 5.9. Visual inspection of the negative electrode (top) and image taken with the laser microscope (bottom) of a fresh cell (VIC05), on the left and an aged cell (VIC01), on the right. 196
Fig. 5.10. Laser microscope image of the positive electrode of VIC cells (LFP) of a fresh cell (left) and an aged one (right) 197
Fig. 5.11. Cell voltage versus delivered capacity of graphite/Li half-cells from samples taken at negative electrodes of fresh and aged NMC cells. 198
Fig. 5.12. (left) Incremental capacity of fresh and aged graphite/Li half-cells. Peaks (labeled from I to V) are associated to phase transitions of the electrodes. (right) Capacity associated to each one of the peaks obtained from the integration of peaks. 199
Fig. 5.13. Cell voltage versus delivered capacity of half-cells from samples taken at positive electrodes of fresh and aged NMC cells. 200
Fig. 5.14. Incremental capacity of NMC/Li half-cells from samples taken from fresh and aged positive electrodes. 200
Fig. 5.15. Impedance contribution of Negative (NE) and Positive (PE) electrodes to the total impedance of the full cell at fully charged state. As an example, inner parts of a fresh cell were represented. 201
Fig. 5.16. Impedance of half-cells at SoC = 100 % build with samples of the positive electrode of LGC2 (NMC) cells. From left to right, internal part of the jelly roll, central part and external part. Black filled squares represent the fresh cell and red empty circles the aged one. 202
Fig. 5.17. Impedance variation during lithium insertion to the positive electrode. The maximum voltage represents when the full cell is fully charged and every decrease in voltage represents a 20 % of charge extracted until the cell was fully discharged. To the left, data coming from the fresh cell and, to the right, from the aged cell. Notice the different scales. 203
Fig. 5.18. Impedance variation during lithium extraction from the negative electrode. The minimum voltage represents when the full cell is fully charged and every increase of voltage

represents a 20 % of charge extracted until the cell was fully discharged. To the left, data coming from the fresh cell and, to the right, from the aged cell. Notice the different scales. 203
Fig. 5.19. Impedance comparison of a fresh and aged negative electrodes measured in a graphite/Li coin cell configuration in a fully delithiated state. 204
Fig. 5.20. Impedance of half-cells at SoC = 100 % build with samples of the negative electrode of LGC2 (NMC) cells. From left to right, more internal part of the jelly roll, central part and more external part. Black filled squares represent the fresh cell and red empty circles the aged one. 204
Fig. 5.21. Particle size distribution of the negative electrode of LGC2077 fresh cell (NMC). Mean size of the particles was 6.0812 μm. 211
Fig. 5.22. Pore size distribution of the negative electrode of LGC2077 fresh cell (NMC). Accessible porosity was 32.27 %. 211
Fig. 5.23. Particle size distribution of the positive electrode of LGC2077 fresh cell (NMC). Mean size of the particles was 5.7213 μm. 212
Fig. 5.24. Pore size distribution of the positive electrode of LGC2077 fresh cell (NMC). Accessible porosity was 27.20 %. 212
Fig. 5.25. XRD patterns of fresh and aged negative electrodes of LGC2 cells (NMC). 213
Fig. 5.26. XRD patterns of fresh and aged positive electrodes of LGC2 cells (NMC). 213
Fig. 5.27. XRD patterns of fresh and aged negative electrodes of VIC cells (LFP). 214
Fig. 5.28. XRD patterns of fresh and aged positive electrodes of VIC cells (LFP). 214
Fig. 5.29. Metallic depositions at the negative electrode, which were stuck to the separator. 216
Fig. 5.30. Pressure patterns exerted to the negative electrode by the positive current collector tab during cycling. 217
Fig. 5.31. Sample harvested from the positive electrode of an aged NMC cell. Pressure lines were clearly observed and there was an evident detachment of the active material from the current collector, especially at those pressure lines. 220
Fig. 6.1. Impedance evolution of a NMC cell at SoC = 100 % during the aging test. Different effects are associated to the positive and negative electrodes thanks to the half-cell measurements carried out during the post-mortem analysis. 233
Fig. 6.2. Evolution of ohmic resistance (left) and charge-transfer resistance estimated from the real part of impedance that was covered by the measured semicircles (right) during the aging test. The line at the charge-transfer resistance graph indicates the cycle from which the charge-transfer resistance started increasing faster. 235
Fig. 6.3. Relative increases of R_{Ω} and R_{CT} of three NMC cells during the aging process and the associated degradation mechanisms. 235

Fig. 6.4. Capacity fade of three NMC cells cycled under the same conditions evaluated at C/25 discharge rate. 235
Fig. 6.5. Capacity fade of three NMC cells cycled under the same conditions evaluated at 3C/2 discharge rate. 236
Fig. 6.6. Absolute increase in ohmic and charge-transfer resistances of a NMC cell from BoL to EoL with respect to the SoC. 236
Fig. 6.7. Ps-OCV evolution of a NMC cell during the aging test at room temperature. The vertical lines represent the two easiest identifiable solid-solution phases to the eye. 237
Fig. 6.8. Evolution of the irreversible entropy production in a NMC cell at a C/25 discharge rate during the aging test carried out at room temperature. It was obtained from ps-OCV (left) curves and discharge GITT OCV (right). The vertical lines represent the two easiest identifiable solid-solution phases from the OCV curves. 238
Fig. 6.9. Evolution of the irreversible entropy production in a NMC cell at a 3C/2 discharge rate during the aging test carried out at room temperature. It was obtained from ps-OCV (left) curves. The vertical lines represent the two easiest identifiable solid-solution phases from the OCV curves 238
Fig. 6.10. Relative-Entropy-Production of a NMC cell at a C/25 discharge rate during the aging test carried out at room temperature (left) and REP of the various contributions to entropy production (right). It was obtained from discharge GITT OCV curves. The vertical lines represent the two easiest identifiable solid-solution phases from the OCV curves... 239
Fig. 6.11. Comparison of the Relative-Entropy-Production in a NMC cell at a 3C/2 discharge rate during the aging test carried out at room temperature calculated from ps-OCV and GITT OCV (left) and REP of the various contributions to entropy production calculated from ps-OCV (right). Vertical lines represent the two easiest identifiable solid-solution phases from the OCV curves. 240
Fig. 6.12. Relative-Entropy-Production in a NMC cell at a 3C/2 discharge rate during the aging test carried out at room temperature (left) and REP during the aging test at various SoCs (right). Vertical lines represent the two easiest identifiable solid-solution phases from the OCV curves 240
Fig. 6.13. Comparison of the Relative-Entropy-Production in a NMC cell at C/25 and 3C/2 (obtained from ps-OCV and GITT OCV curves) discharge rate during the aging test carried out at room temperature. 241
Fig. 6.14. Capacity fade of two VIC cells (LFP) evaluated at C/25 (top-left) and 2C (top-right) discharge rates and ohmic resistance (bottom-left) and joint contribution of charge-transfer and mass-transfer resistances evolution with aging (bottom-right). Vertical lines represent the cycles from which impedance and capacity changed their tendencies. 242

Fig. 6.15. Discharge GITT OCV evolution with aging. Vertical lines represent the two-phase domains (PCx) and the single-phase domains. 243
Fig. 6.16. Evolution of the irreversible entropy production in a VIC cell (LFP) evaluated at a C/25 discharge rate from ps-OCV. 243
Fig. 6.17. Evolution of the irreversible entropy production in a VIC cell (LFP) evaluated at a C/25 discharge rate from discharge GITT OCV. Vertical lines represent phase changes (PCx) at BoL (left) and at EoL (right) 243
Fig. 6.18. Evolution of the irreversible entropy production in a VIC cell (LFP) evaluated at a 2C discharge rate. Black vertical lines represent intervals corresponding to solid solutions at BoL and red ones at the EoL. The arrows represent the shifting they suffered from BoL to EoL 244
Fig. 6.19. Relative-Entropy-Production calculated from ps-OCV curves (not accounting for hysteresis) at a C/25 discharge rate (top-left) and particular values at SoC = 50 % (bottom). Increase in hysteresis during the aging test (right). Notice that in this case, REP has been calculated for the irreversible entropy production at each cycle at this particular SoC. 245
Fig. 6.20. Relative-Entropy-Production calculated from discharge GITT OCV curves at a C/25 discharge rate. Vertical lines represent the end of the plateaus and the starting point of the solid solutions at BoL (black solid line) and EoL (red dashed line). 246
Fig. 6.21. Relative-Entropy-Production at a 2C discharge rate. 246
Fig. 6.22. Comparison of the Relative-Entropy-Production in a VIC cell at C/25 and 2C discharge rate during the aging test carried out at room temperature. 246
Fig. 6.23. Capacity fade of three EVbat cells (LFP) evaluated at a 2.5 C discharge rate. 247
Fig. 6.24. Ohmic (top-left), charge-transfer (top-right), ohmic + charge-transfer (bottom-left) and ohmic + charge-transfer + mass-transfer (bottom-right) resistances of an EVbat cell. Mass-transfer resistance was only measured until the lowest measured frequency at the EIS, independently of the frequency at which the cell was working. Therefore, the absolute value of R_{MT} does not correspond with the actual one. 248
Fig. 6.25. OCV evolution with aging of three EVbat cells at room temperature. Vertical lines represent the two easiest identifiable plateaus (phase transformations). The arrow indicates the shifting of the end of the plateau at the EoL. 248
Fig. 6.26. Irreversible entropy production of three EVbat cells evaluated at a discharge rate of C/8. Vertical lines represent the end of phase transformations (in black at BoL and in red at the EoL). 249
Fig. 6.27. Relative-Entropy-Production of three EVbat cells evaluated at a discharge rate of C/8. Vertical lines represent the end of phase transformations (in black at BoL and in red at the EoL). 250

Fig. 6.28. OCV evolution with aging of a LCO cell at BoL and EoL at room temperature. Vertical lines represent the only identifiable plateau to the eye (phase transformation)..... 250
Fig. 6.29. Irreversible entropy production of the LCO cells evaluated at a discharge rate of 1C. Vertical lines represent the minimum and maximum SoC of one phase transformation..... 251
Fig. 6.30. Relative-Entropy-Production of a LCO cell evaluated at a discharge rate of 1C. Vertical lines represent the minimum and maximum SoC of one phase transformation..... 251
Fig. 6.31. REP of the different chemistries evaluated at different rates..... 252

Index of tables

Table 1.1. Characteristics of secondary batteries [1]. 32
Table 1.2. Historic and current battery sizes [8]. 33
Table 1.3. Characteristics of typical positive electrodes of li-ion cells [12]. 38
Table 1.4. Limiting cases of Butler-Volmer formulation. 46
Table 1.5. Main aging mechanisms at the negative electrode side. 47
Table 1.6. Main aging mechanisms at the positive electrode side cell [35] 49
Table 1.7. Pros and cons of various experimental methods employed in determining the SoC [46]. 52
Table 2.1. Classification of the cells investigated in this study and their nominal voltages and capacities. 56
Table 2.2. NMC cells charging/discharging parameters 57
Table 2.3. VIC LFP cells charging/discharging parameters 58
Table 2.4. EVbat LFP cells charging/discharging parameters 59
Table 2.5. LCO cells charging/discharging parameters 59
Table 2.6. Cell-to-cell variations of three LGC2 cells (NMC) at BoL. 64
Table 2.7. Cell-to-cell variations of three VIC cells (LFP) at BoL. 64
Table 2.8. Capacity evolution of EVbat cells (LFP) during discharge at 2.5C. The decrease in capacity was calculated as the difference between the maximum capacity after initial cycles and the final capacity after the aging test. 70
Table 3.1. Definition of the parameters for measuring impedance by EIS technique. 78
Table 4.1. Thermodynamic forces and flows and the corresponding laws. 117
Table 4.2. Loss of active material (LAM) and loss of lithium inventory (LLI) during the aging test of LGC2074 cell (NMC). 127
Table 4.3. Major contributors to overpotential for different chemistries discharged at different rates. 173
Table 5.1. Full-cell and half-cell areas of the electrodes and the related capacities. 190
Table 5.2. Voltage limits for cycling the manufactured half-cells. 191
Table 5.3. Weighting of the different parts of fresh and aged NMC cells. 194
Table 5.4. Weighting of the different parts of fresh and aged VIC cells (LFP). 194
Table 5.5. Capacity of graphite/li half-cells made from negative electrode samples harvested from NMC cells. Absolute and relative decreases are detailed. Capacities of the inner, central and outer parts of the jellyroll are shown separately. 199
Table 5.6. Capacity of half-cells made from positive electrode samples harvested from NMC cells. Absolute and relative decreases are represented. Capacities of the inner, central and outer parts of the jellyroll are shown separately. 200

Table 5.7. Total resistance of fresh and aged NMC/Li half-cells at SoC = 100 % evaluated at 25 ºC. 202
Table 5.8. Total resistance of fresh and aged graphite/Li half-cells at SoC = 100 % evaluated at 25 ºC. 205
Table 5.9. Stoichiometry of the evaluated LGC2 cells (NMC) by the ICP-OES technique. LGC2077 and LGC2079 were fresh cells and LGC2074 was an aged cell. 205
Table 5.10. Relation of moles of different elements comprising the positive electrodes of the evaluated LGC2 cells (NMC) by the ICP-OES technique. LGC2077 and LGC2079 were fresh cells and LGC2074 was an aged cell. The desired elements were highlighted in green and the undesired ones in red. 206
Table 5.11. Mass of the different elements comprising the positive electrodes of the evaluated LGC2 cells (NMC) by the ICP-OES technique. Mass is represented in units of mg and as a percentage of the total mass of the sample. LGC2077 and LGC2079 were fresh cells and LGC2074 was an aged cell. The desired elements were highlighted in green and the undesired ones in red. 206
Table 5.12. Relation of moles of different elements comprising the negative electrodes of the evaluated LGC2 cells (NMC) by the ICP-OES technique. LGC2077 and LGC2079 were fresh cells and LGC2074 was an aged cell. The desired elements are highlighted in green and the undesired ones in red. 207
Table 5.13. Mass of the different elements comprising the negative electrodes of the evaluated LGC2 cells (NMC) by the ICP-OES technique. Mass is represented in units of mg and as a percentage of the total mass of the sample. LGC2077 and LGC2079 were fresh cells and LGC2074 was an aged cell. The desired elements are highlighted in green and the undesired ones in red. 207
Table 5.14. Metals dissolution and migration from positive electrode to negative electrode of three LGC2 cells (NMC) at different aging states represented in mg/L and as a percentage. 208
Table 5.15. Metals dissolution of current collectors and migration to the opposite electrode of three LGC2 cells (NMC) at different aging states. 208
Table 5.16. Evaluation of the amount of Li at positive and negative electrodes of a fresh LGC2077 cell (NMC) fully discharged..... 209
Table 5.17. Evaluation of the amount of Li at positive and negative electrodes of a fresh LGC2079 cell (NMC) fully discharged..... 210
Table 5.18. Evaluation of the amount of Li at positive and negative electrodes of an aged LGC2074 cell (NMC) fully discharged..... 210

Table 5.19. Comparison of metals concentrations at the negative electrode of fresh and aged cells between the results reported in reference [87] and the results obtained in our study. 218
Table 5.20. Comparison of metals concentrations at the negative electrode of fresh and aged cells between the results reported in reference [87] and the results obtained in our study. 218
Table 5.21. Amount of lithium measured by the ICP technique in the cell and, in particular, at the NE. Total capacity fade at the full-cell associated to LLI was calculated considering the formation cycles before the BoL we defined. In addition, an estimation of the capacity fade from BoL to EoL (i.e. not considering formation cycles) was also carried out. 222
Table 5.22. Capacity fade at a C/25 discharge rate obtained at inner, central and outer parts of the jellyroll measured in half-cells and the estimated capacity fade in average obtained from the partial contributions..... 223
Table 5.23. Capacity fade at a C/25 discharge rate obtained at inner, central and outer parts of the jellyroll measured in half-cells and the estimated average obtained from the partial contributions..... 224
Table 6.1. Aging mechanisms behind the various effects measured at the impedance..... 230
Table 6.2. Estimated capacity fade of the full-cell at a C/25 discharge rate obtained from ICP and ICA analyses. 232

Chapter 1

General introduction

In this chapter, general features of batteries are first introduced. Afterwards, we focus on Li-ion cells and the main aging mechanisms they can suffer during cycle aging. Moreover, SoC and SoH are introduced and the limitations encountered in their measurement methods. Finally, the motivation and objectives of this study are detailed.

1.1. Introduction to batteries

A cell or battery is a device capable of converting chemical energy, which is stored on its active materials, into electrical energy going through a reduction-oxidation (redox) reaction [1]. The term battery is strictly related to a pack containing various cells. However, it is also commonly accepted to use the term battery even for a single cell [2]. In particular, a cell consists of three major components: the anode, the cathode and the electrolyte (Fig. 1.1). The anode is the one being oxidized by giving up electrons to the external circuit during the electrochemical reaction while the cathode is the one being reduced accepting electrons from the external circuit. The electrolyte is the ionic conductor placed between the two electrodes and it can be solid or liquid. In most cases, there is a separator placed between the electrodes, which allows the pass of the ions but protects the cell from short-circuits.

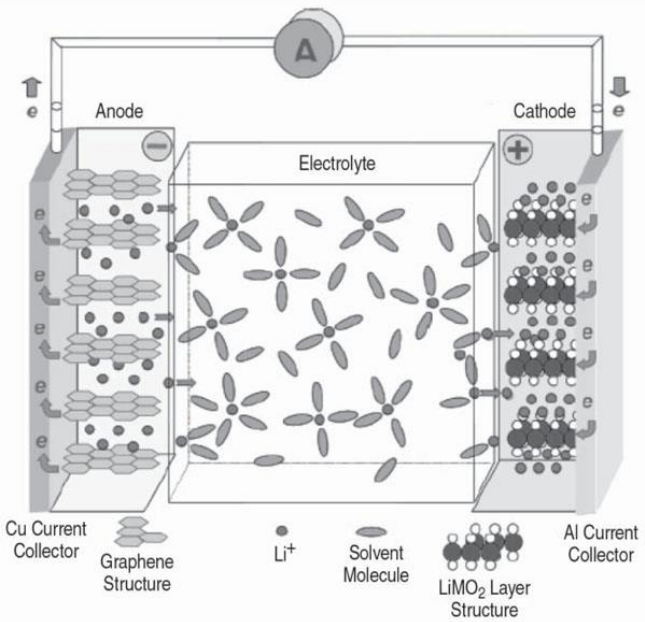

Fig. 1.1. Main parts and schematic behavior of an electrochemical cell [3].

Cells can be classified in two different groups: primary and secondary cells. Primary cells are not rechargeable since the electrochemical reaction cannot be reversed whereas secondary ones can be recharged as they are able to regenerate the chemical reactants by reversing the electrochemical reaction. The general advantages of primary cells are good shelf life, high energy density at low to moderate discharge rates, little or no maintenance, and ease of use [1]. Conversely, secondary cells have the evident advantage that can be reused once totally discharged. Moreover, they show a high power density, high discharge rate, flat discharge curves, and good performance at low-temperature. As a drawback, the energy densities of secondary cells are generally lower than those of primary cells [1].

1.1.1. Battery chemistries

Lead-acid or Pb-acid batteries were developed by Gaston Planté in 1859. They were constructed by using coiled lead strips separated by linen cloth and immersed in sulfuric acid. By initially passing a dc current between the two lead strips, an oxide grew on the one on the positive side, forming a layer of lead dioxide. This caused the development of a voltage between them, and it was soon found that charge could be passed reversibly through this configuration, so that it could act to store electrical energy [4].

Lead-acid batteries are still very popular nowadays. Despite they offer low energy and power densities, they have high capacity retention, good cycle life, they perform reliably over a wide temperature range and they are relatively cheap and easy to manufacture [1]. Currently, they are designed in many different configurations depending on the application. They are used in both mobile (as an automotive starter battery for instance) and stationary applications, ranging from very low capacities to very high. Some of the stationary applications are telecommunications systems, electric

utilities for operating power distribution controls, emergency and standby power systems, uninterruptible power systems (UPS), and in railroads, signaling and car power systems [1]. The most common application of lead-acid batteries and the one in widest use is the automotive SLI (Starting-Lighting-Ignition).

The only rechargeable battery until 1899 was lead acid. Then, NiCd broke into the market. NiCd offered several advantages over lead acid but the materials were expensive. In 1932, the active materials were placed inside a porous nickel-plated electrode giving some advances to the nickel-based batteries. In 1947, the modern sealed NiCd battery, which was able to absorb the gas generated during charge, was developed. For a long time, NiCd was the preferred chemistry for two-way radios, emergency medical equipment, professional video cameras and power tools. In the late 1980s, sixty percent more capacity was achieved by adding more active material but it increased internal resistance and reduced cycle life.

Some advantages of NiCd batteries are high cycle life if properly maintained. NiCd is the only battery that can be ultra-fast charged with little stress, has good load performance, can be stored in a discharged state if priming before use, is simple to store and transport, has a good low-temperature performance, and is the cheapest one in terms of cost per cycle. Some limitations of this chemistry are relatively low specific energy, the memory effect that causes a loss of capacity if not given a periodic full discharge cycle, toxicity of cadmium (main drawback), high self-discharge, and low cell voltage of 1.20 V. NiCd batteries are still a standard in the airline industry, but they need proper care to attain longevity.

Although NiCd batteries were used for portable devices for more than fifty years, NiMH mostly replaced them in the 1900s because of the cadmium toxicity. Nowadays, NiMH cells have thirty to forty percent higher specific energy than the standard NiCd. Compared to NiCd, NiMH is more delicate and trickier to charge. Nickel-cadmium cells show one of the highest self-discharges with twenty percent in the first 24 hours after charge and ten percent per month thereafter. In detriment of the specific energy, self-discharge and corrosion of the alloy are lowered by modifying the hydride materials.

Thereafter, the community continued seeking for lighter options, capable of giving higher energy densities. Then, lithium was found to be a good candidate because it is the lightest of all metals, has the greatest electrochemical potential and offers the largest energy density per kg [5]. Therefore, lithium metal negative electrodes were of high interest. However, during the 1980s, it was discovered that changes produced on them during cycling resulted in potential fire danger. Due to the underlying instability of lithium metal, the scientific community moved to non-metallic lithium battery employing lithium ions instead [5]. However, although Li-ions are intrinsically safe, they are slightly lower in energy density. Due to the need of shifting towards non-metallic lithium electrodes, in 1991, Sony started producing and commercializing the first Li-ion battery.

Li-ion cells offered many advantages over their predecessors. As previously mentioned, lithium is the lightest of metals what makes Li-ion cells superior in the specific energy they can deliver (Table 1.1). In addition, they release 2 or 3 times more energy density than Nickel-based cells. Moreover, there is no memory effect in Li-ion cells, so they do not require a scheduled cycling to prolong their lifetime and the self-discharge is less than half compared to NiCd or NiMH (Table 1.1). In fact, the evolution of battery chemistries yielded every time to cells capable of providing at the same time, higher specific powers and higher specific energies (Fig. 1.2).

Table 1.1. Characteristics of secondary batteries [1].

Parameter	Lead-acid	NiCd	NiMH	Li-ion
Nominal cell voltage, V	2.0	1.2	1.2	4.1
Specific energy, Wh/Kg	35	35	75	150
Energy density, Wh/L	70	100	240	400
Charge retention at 20ºC (shelf life), months	6-9	3-6	3-6	9-12
Calendar life, years	3-8	4-6	4-6	5+
Operating temperature, ºC	-40 to 60	-20 to 45	-20 to 45	-20 to 60
Relative cost per watthour (initial unit cost to consumer)	10	15	25	45

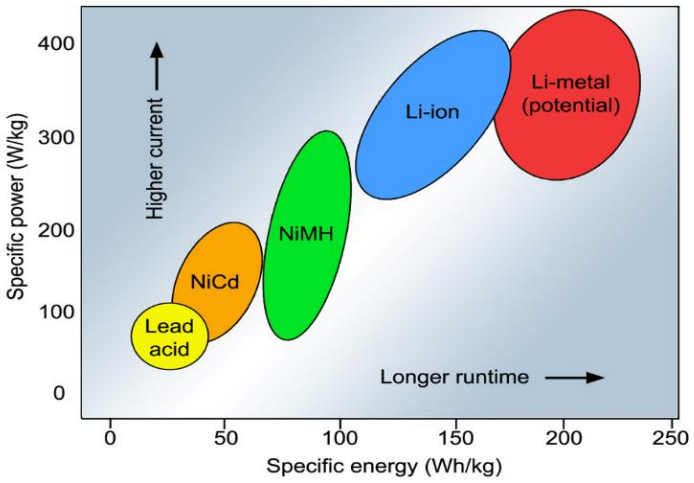

Fig. 1.2. Specific capacity versus specific energy for different battery chemistries [6].

1.1.2. Packaging styles

Nowadays, cells are manufactured in different configuration types. They are classified into cylindrical, prismatic, coin cells or pouch cells. In the 1700s and 1800s, batteries were developed for first time in Europe and they were mostly encased in glass jars [7]. Because of size limitations, they shifted to sealed wooden containers and composite materials. In the 1890s, battery manufacturing shifted to the United States. The first standard commercial cell for consumer use was produced by the National Carbon Company in 1896. It was the zinc-carbon Columbia Dry Cell Battery producing 1.5 V and measuring 6 inches in length [7].

With the increase of portable devices, the growing use of sealed cylindrical cells lead to standard sizes. The alphabet nomenclature, which is still in use, was formalized in 1917 by the National Institute of Standards and Technology [8]. The standards for most rechargeable batteries were previously standardized in 1906 by the International Electrochemical Commission (Table 1.2).

Table 1.2. Historic and current battery sizes [8].

Size	Dimensions	History
F cell	33 x 91 mm	Introduced in 1896 for lanterns; later used for radios; only available in nickel-cadmium today.
E cell	N/A	Introduced ca. 1905 to power box lanterns and hobby applications. Discontinued ca. 1980.
D cell	34.2 x 61.5mm	Introduced in 1898 for flashlights and radios; still current.
C cell	25.5 x 50mm	Introduced ca. 1900 to attain smaller form factor.
Sub-C	22.2 x 42.9mm 16.1mL	Cordless tool battery. Other sizes are ½, 4/5 and 5/4 sub-C lengths. Mostly NiCd.
B cell	20.1 x 56.8mm	Introduced in 1900 for portable lighting, including bicycle lights in Europe; discontinued in in North America in 2001.
A cell	17 x 50mm	Only available as a NiCd or NiMH cell; also available in 2/3 and 4/5 size. Popular in old laptops and hobby batteries.
AA cell	14.5 x 50mm	Introduced in 1907 as penlight battery for pocket lights and spy tool in WWI; added to ANSI standard in 1947.
AAA cell	10.5 x 44.5mm	Developed in 1954 to reduce size for Kodak and Polaroid cameras. Added to ANSI standard in 1959.
AAAA cell	8.3 x 42.5mm	Offshoot of 9V, since 1990s; used for laser pointers, LED penlights, computer styli, headphone amplifiers.
4.5V battery	67 x 62 x 22mm	Three cells form a flat pack; short terminal strip is positive, long strip is negative; common in Europe, Russia.
9V battery	48.5 x 26.5 x 17.5mm	Introduced in 1956 for transistor radios; contains six prismatic or AAAA cells. Added to ANSI standard in 1959.
18650	18 x 65mm 16.5mL	Developed in the mid-1990s for lithium-ion; commonly used in laptops, e-bikes, including Tesla EV cars.

26650	26 x 65mm 34.5mL	Larger Li-ion. Some measure 26x70mm sold as 26700. Common chemistry is $LiFeO_4$ for UPS, hobby, automotive.
14500	14 x 50mm	Li-ion similar in size to AA.

Cylindrical cells consist on many long layers including both electrodes and separator layers rolled up forming the jellyroll, which is placed, inside a metallic tubular can (Fig. 1.3). Current is passed to the external circuit through conductive tabs. Usually, negative tab is connected to the metallic can while the positive tab is connected to one of the ends of the cell. They continue being one of the most widely used packaging styles for primary and secondary batteries. Their advantages are ease of manufacture and good mechanical stability. The tubular cylinder can withstand high internal pressures without deforming [7]. As drawbacks, one has to consider the inefficient use of space and the contribution of the metallic can to the total weight. In terms of safety, most cylindrical cells feature a pressure relief mechanism, and the simplest one consists on a membrane seal that ruptures under high pressure.

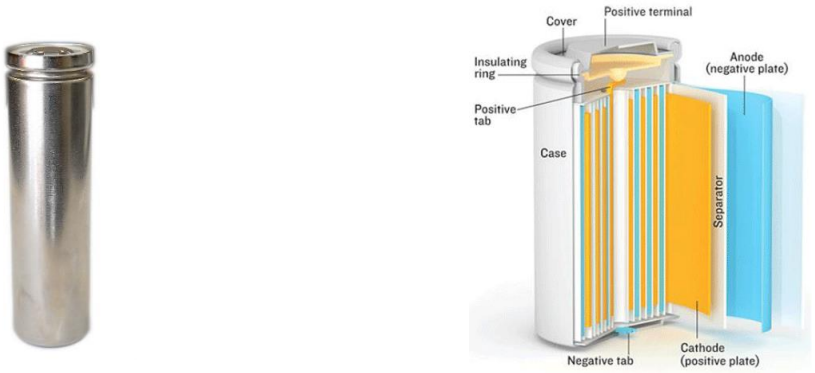

Fig. 1.3. Cylindrical cell on the left [9] and transversal cutting of a cylindrical cell on the right [6].

Coin cells or button cells (Fig. 1.4) appeared in the 1980s as a compact solution for portable devices. They are small, easy to stack and inexpensive to build. However, the rechargeable ones have to be recharged very slowly, being a very time-consuming process. Moreover, they can be swollen if charged too rapidly and they have no safety vent. Nowadays, coin cells are mostly used as primary batteries in medical implants, watches, hearing aids, car keys and memory backups [7].

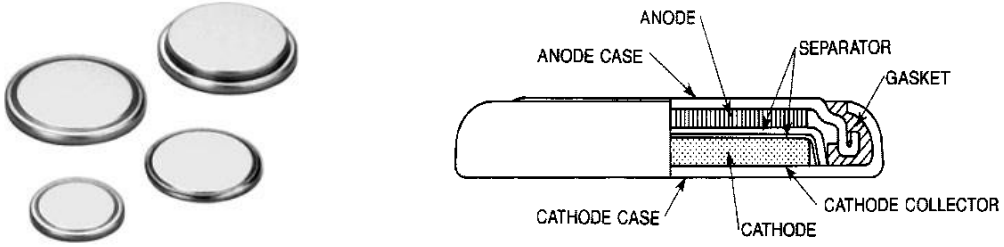

Fig. 1.4. Coin cells on the left and transversal cutting of a coin cell on the right [7].

Prismatic cells were introduced in the early 1900s due to the need of thinner cells. There are no universal sizes so each manufacturer designs its own battery depending on the needs [7]. They are made of various layers one on the top of the other or wound and flattened in a pseudo-prismatic jelly roll, making a best usage of the space (Fig. 1.5). Prismatic cells are designed to allow some swelling. They are also found in large capacity formats packaged into welded aluminum housings. As main drawbacks, prismatic cells are more expensive to manufacture, they have a less efficient thermal management and their cycle life is usually shorter than that of cylindrical cells [7].

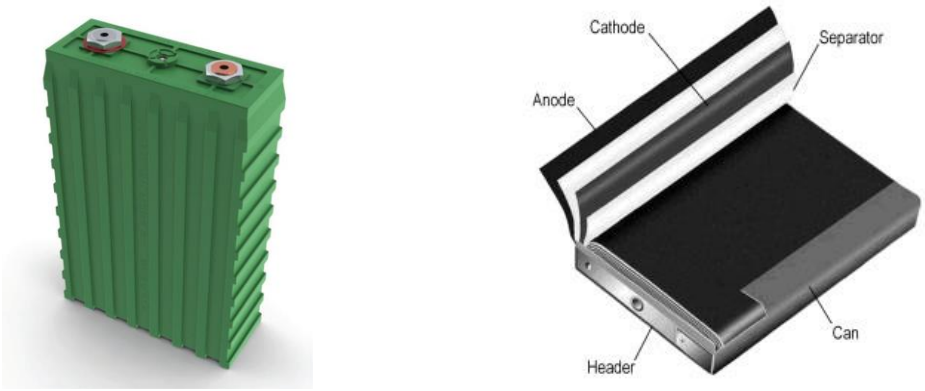

Fig. 1.5. Prismatic cell on the left [10] and transversal cutting of a prismatic cell on the right [7].

In 1995, pouch cells were the most revolutionary cells with a packaging efficiency around 90 – 95 %. Instead of using a metallic or rigid housing, they offered a completely new design where conductive foil-tabs were welded to the electrodes and brought to the outside in a fully sealed way (Fig. 1.6) [7]. Because of the particular design, they are light and cost-effective to manufacture. As they do not have hard cases, they are allowed to swell. Small batteries are swollen easily than larger ones and, in some cases, they increase in volume around 8 - 10 % in approximately 500 cycles. Consequently, stacking cells one on the top of the other is not recommended for these type of cells. It is safer when laying them flat and leaving some space between each other taking into account the possible change in volume. Cycle life of pouch cells can be fast shortened when exposed to humidity and high temperatures [7]. In addition, pouch cells are usually manufactured by adding an extra gasbag that is filled by gassing in the first cycles and then is removed from the final product. Thus, gassing is not expected to occur in following cycles.

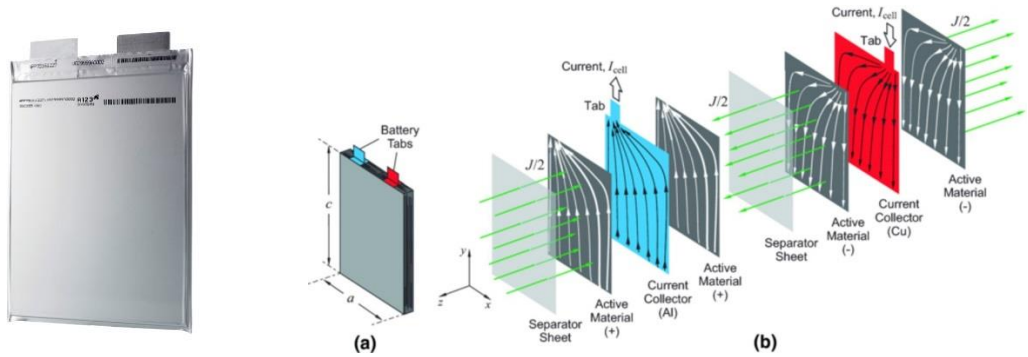

Fig. 1.6. Pouch cell on the left [7] and pouch cell structure on the right [11].

1.2. Lithium-ion cells

Li-ion cells have a negative electrode whose active material is carbon, in which lithium ions can be intercalated/deintercalated during charge/discharge processes. The positive active material of li-ion cells is a lithiated metallic oxide intercalation compound in which lithium ions can also be inserted and extracted. Common positive electrodes are made of $LiCoO_2$ (LCO), $LiNiO_2$ and $LiMn_2O_4$ (LMO) (Table 1.3). These materials are stable in air, have a high nominal voltage and the lithium insertion reaction has good reversibility [1]. $LiCoO_2$ was used by the first system commercialized based in lithium-ion technology. This material is the easiest to prepare, holds its structure during cycling, and offers good electrical performance. $LiNiO_2$ is less expensive than $LiCoO_2$, is more stable at higher temperatures, and has a lower self-discharge rate. However, commercial interest in $LiNiO_2$ has waned as its instability has been shown to contribute to safety issues. Conversely, $LiMn_2O_4$ materials are more abundant, inexpensive, and nontoxic [1].

Regarding to the structure, $LiCoO_2$ and $LiNiO_2$ have a layered structure where the cobalt or nickel would reside within oxygen octahedral, and the lithium atoms would reside in the space between the oxygen layers [1]. However, $LiMn_2O_4$ spinel materials have a three-dimensional lattice or tunneled structure where octahedral and tetrahedral structures share their faces. The insertion and extraction reactions of these three lithiated metal oxides are:

$$LiCoO_2 \rightleftharpoons Li_{1-x}CoO_2 + xLi^+ + xe$$
$$LiNiO_2 \rightleftharpoons Li_{1-x}NiO_2 + xLi^+ + xe$$
$$LiMn_2O_4 \rightleftharpoons Li_{1-x}Mn_2O_4 + xLi^+ + xe$$

In some cases, the full capacity density of some particular materials cannot be achieved as it is the case of $LiCoO_2$ and $LiNiO_2$ cathodes. Their reversible value of x is equal or lower than 0.5 while for $LiMn_2O_4$ it is equal or greater than 0.85. Therefore, theoretical capacity of $LiCoO_2$ and $LiNiO_2$ (274 mAh/g) can never be achieved if reversibility wants to be preserved. Therefore, practically, all three cathodes have approximately the same capacity density of 135 mAh/g (Table 1.3).

The search for improved layered oxide materials containing low-cost transition metals lead to other positive electrode, which combine the abovementioned metals, such as $Li(NiMnCo)O_2$ (or NMC) cells [12]. It is made of a nickel-manganese-cobalt combination and its negative electrode is made of graphite. NMC positive electrodes bring together the high energy density of $LiCoO_2$ and the rate capability of $LiMn_2O_4$ and they can be tailored to serve as energy cells or power cells. Moreover, they require less cobalt than $LiCoO_2$ making them cheaper and safer. They also have improved electrochemical properties and better structural, chemical, and thermal stability than $LiCoO_2$ cells [12]. As it is typical of many layered compounds, the voltage profile of NMC versus Li/Li^+ is gradually sloping. Below 4.3 V versus Li/Li^+, NMC cells, provide higher capacity densities, typically around 160 mAh/g than LCO (capacities around 140 mAh/g).

In 1997, Goodenough and coworkers reported on the electrochemical properties of a new class of cathode materials known as the phospho-olivines, which adopt the orthorhombic or olivine structure. $LiFePO_4$ (LFP) is an example of these cathode materials [12]. In a LFP cell with a theoretical specific capacity of 170 mAh/g, the insertion and extraction of lithium from the positive electrode proceeds at about 3.45 V [12] (Table 1.3). The voltage profile of these cells is flat so the potential is independent of the composition of x in Li_xFePO_4, what indicates that a two-phase reaction occurs. The two relevant phases are $LiFePO_4$ (triphylite) and $FePO_4$, also known as heterosite [12].

$$LiFePO_4(triphylite) \leftrightarrow FePO_4(heterosite) + e^- + Li^+$$

The active material particles are commonly coated by carbon because it ameliorates the low electronic conductivity of both the triphylite and heterosite phases and results in better rate performance [12]. Even though LFP cells offer lower energy density than LCO and NMC cells, they are inherently safer due to their better thermal and chemical stability, offer longer cycle life, and deliver higher power densities [12].

Table 1.3. Characteristics of typical positive electrodes of li-ion cells [12].

Cathode material	Structure	Potential versus Li/Li^+, V	Specific capacity, mAh/g
$LiCoO_2$ (LCO)	Layered	3.9	140
$LiNi_{1/3}Co_{1/3}Mn_{1/3}O_2$ (NMC)	Layered	3.8	160-170
$LiMn_2O_4$ and variants (LMO)	Spinel	4.1	100-120
$LiFePO_4$ (LFP)	Olivine	3.45	150-170

Summarizing, for the same price, LFP cells are superior in specific power, safety and life span (Fig. 1.7). Nevertheless, LMO and NMC cells exhibit similar characteristics except in terms of specific energy, performance and life span, in which NMC perform better. In addition, concerning to LCO, their characteristics are below the other represented chemistries except in their specific energy (better than LFP and equal to NMC) and performance.

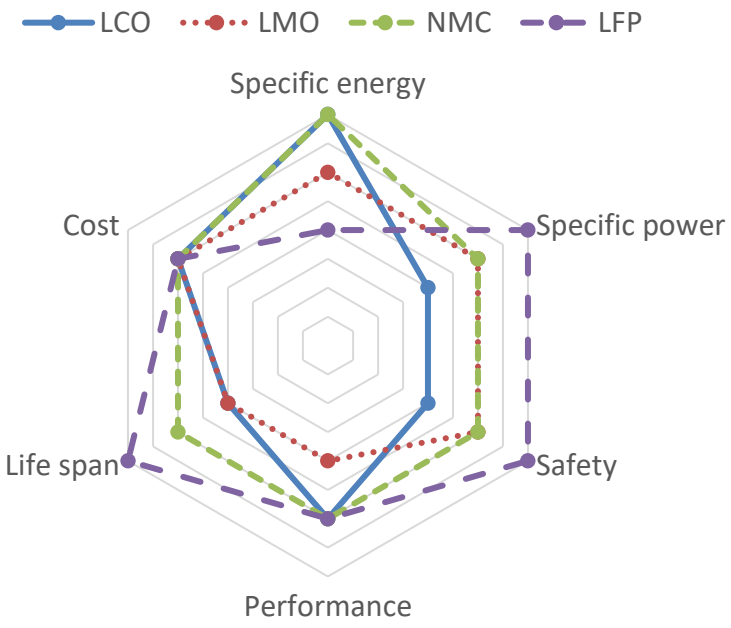

Fig. 1.7. Comparison of the characteristics of the most common Li-ion chemistries. Data were extracted from [13].

1.2.1. Redox reactions

During charge and discharge, lithium ions move back and forward between positive and negative electrodes (Fig. 1.8). The process consists on an electrochemical redox (reduction-oxidation) reaction where half-cell reactions occur at each electrode at the same time. A redox reaction is a chemical reaction in which the oxidation states of the atoms are changed due to the transport of electrons between the chemical species. In particular, lithium salts that compose the electrolyte are the responsible of the transport of lithium-ion through the liquid electrolyte [14]. Those lithium-salts (i.e. $LiPF_6$) dissolve and they separate into a lithium cation (Li^+), which is surrounded by solvent molecules, and the corresponding anion (PF_6). The ionic conductivity in the electrolyte is provided by these anions and cations. Two forces drive the lithium-ion transport: migration (transport induced by electric field) and diffusion (induced by concentration gradients) [14].

The reactions at the electrodes and the overall reaction are

Positive electrode	$LiMO_2 \rightleftharpoons Li_{1-x}MO_2 + xLi^+ + xe$
Negative electrode	$C + xLi^+ + xe \rightleftharpoons Li_xC$
Overall reaction	$LiMO_2 + C \rightleftharpoons Li_xC + Li_{1-x}MO_2$

Where $LiMO_2$ represents the lithiated metal oxide intercalation compound. From left to right, the reactions are taking place during charge and from right to left during discharge process [1].

When the cell is at chemical equilibrium, the rates of the forward reaction and the backward reaction are the same. In that case, no net flow of current is present and there is no change in products concentration. When one of those reactions is faster, there is a net flow of current through the external circuit. This process can be defined in various steps:

1. Transport of the ions from one electrode to the other through the electrolyte.
2. Conduction of the electrons through the electrode in order to reach the reacting particle.
3. Chemical reaction at the particle surface.
4. Transfer of the electroactive species from the bulk of the solution to the particle surface.
5. Diffusion at the solid phase.

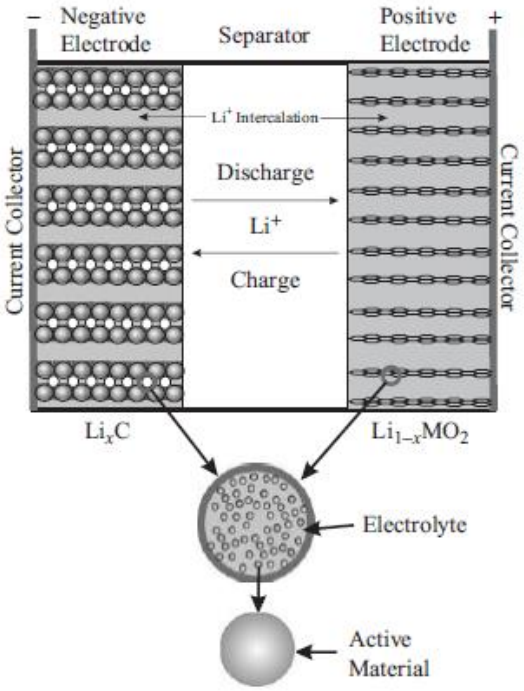

Fig. 1.8. Schematic diagram of a Li-ion cell [15].

During redox reaction, at the reducing electrode, *a* molecules of *A* take up *n* electrons to form *c* molecules of *C*. The overall reaction is the addition of the two half-cell reactions at the electrodes.

Electrode reduced in forward direction	$aA + ne \rightleftharpoons cC$
Electrode oxidized in forward direction	$bB - ne \rightleftharpoons dD$
Overall reaction in the cell	$aA + bB \rightleftharpoons cC + dD$

1.2.2. Contributions to overpotential in Li-ion batteries

The available electrical energy can be calculated from the change in Gibbs free energy of the electrochemical couple [16].

$$\Delta G = -n \cdot F \cdot OCV \tag{1.1}$$

Where *n* is the exchanged number of electrons in the reaction, *F* is the Faraday constant (96487 coulombs per mol), and *OCV* is the standard electromotive force.

Unfortunately, all the available energy when the cell is at equilibrium cannot be completely converted into useful electrical energy because some of it is lost as heat when a current is flowing through the cell; the cell potential deviates from the standard electromotive force reducing the amount of energy that can be converted. This voltage deviation is usually termed as overpotential or overvoltage (η) and is associated to cell polarization and electron and ion conductions. This decrease

in voltage during the discharge process is dependent on the employed C-rate (Fig. 1.9) and temperature (Fig. 1.10). At high C-rates the overvoltage is higher than at low rates, making the voltage to decrease faster. Thus, less charge can be extracted from the cell at the same conditions (Fig. 1.9). Concerning the temperature at which the cell is during the discharge process, higher overpotentials and thus, reduced removable capacity, occur at lower temperatures (Fig. 1.10). The characteristic voltage curves of Li-ion cells present plateaus and transitions between the plateaus. In particular, the plateaus represent phase transformations (two-phase domain) in which some of the active material particles have certain amount of lithium and the rest have a different amount [17]. Conversely, the transitions between the plateaus correspond to solid-solution phases (single-phase domain) in which all the active material particles have the same amount of lithium (i.e. they are at the same phase) [18].

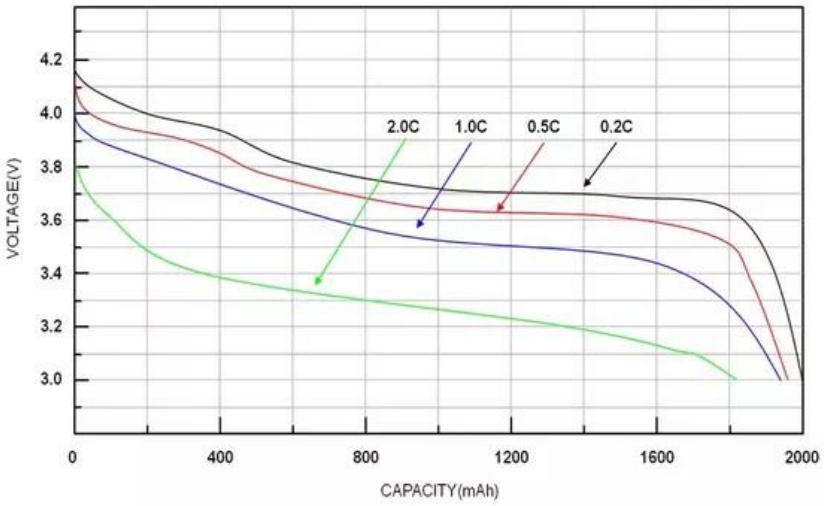

Fig. 1.9. Dependence of the voltage profile of a Li-ion cell on the discharge rate at room temperature [19].

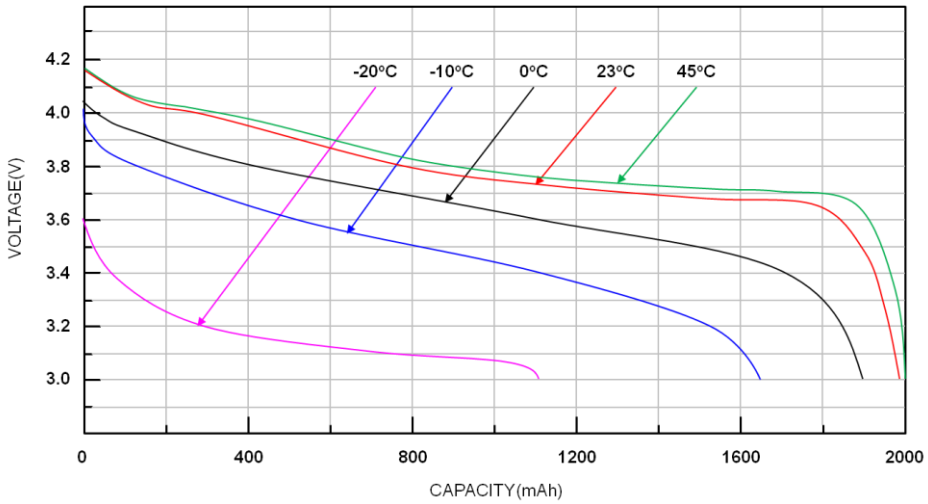

Fig. 1.10. Dependence of the voltage profile of a Li-ion cell on the temperature at a constant discharge rate [20].

The part of the overpotential associated to conduction is usually termed as ohmic drop or IR drop. It is a purely resistive effect and therefore shows a linear relationship between current and voltage, following the Ohm's law, at any current. Its physical origin comes from the contributions of the ionic resistance of the electrolyte, the electronic resistances of the active mass, the contact resistances between the electrodes and the current collectors, and the electrical tabs [21].

Polarization loses include, on the one hand, activation polarization, which drives the electrochemical reaction at the electrode surface. Activation polarization overpotential (η_{act} or η_{CT}) comes from the energy required to overcome the activation barrier for the chemical reaction to take place. The dynamics of this process is described by Butler-Volmer equation. On the other hand, they include concentration polarization, which is caused by the differences in reactants and products at the electrode surface and in the bulk of the electrolyte. Those differences are usually associated to the fast consumption of reactants during the electrochemical reaction compared to the rate at which they can diffuse into the electrode. The transport of lithium-ion driven by a concentration gradient from the surface into the center of the active material particles or vice versa, is usually termed as solid state diffusion [14]. In particular, the diffusion overpotential, termed also as concentration polarization or mass transfer overpotentials (η_{conc} or η_{MT}) is caused by the difference between lithium concentration at the surface and equilibrium concentration. It depends on the applied current, the structure of the active material, temperature and particle size [14]. Commonly, concentration polarization overvoltage is low at the beginning of discharge but grows rapidly for high current loads or towards the end of discharge [22].

Therefore, the total overpotential that a cell suffers (η) when a current I flows through it can be written as [1]:

$$\eta = OCV - V_{cell} = [(\eta_{CT})_a + (\eta_{MT})_a] + [(\eta_{CT})_c + (\eta_{MT})_c] + I \cdot R_\Omega \qquad \textbf{(1.2)}$$

Where,

The subscripts a and c stand for "anode" and "cathode" respectively,

η_{CT} is the activation polarization term or the charge-transfer effect,

η_{MT} is the concentration polarization or the mass-transfer effect,

V_{cell} is the cell voltage at the output terminals,

and R_Ω is the internal or ohmic resistance of the cell.

Moreover, overvoltage depends on the rate of current being injected or extracted from the cell. As it can be seen in the polarization curve represented in Fig. 1.11, not only the contribution of the ohmic resistance is dependent on the current as it could be expected from (1.2) but also activation and concentration polarization terms vary upon the selected current rate.

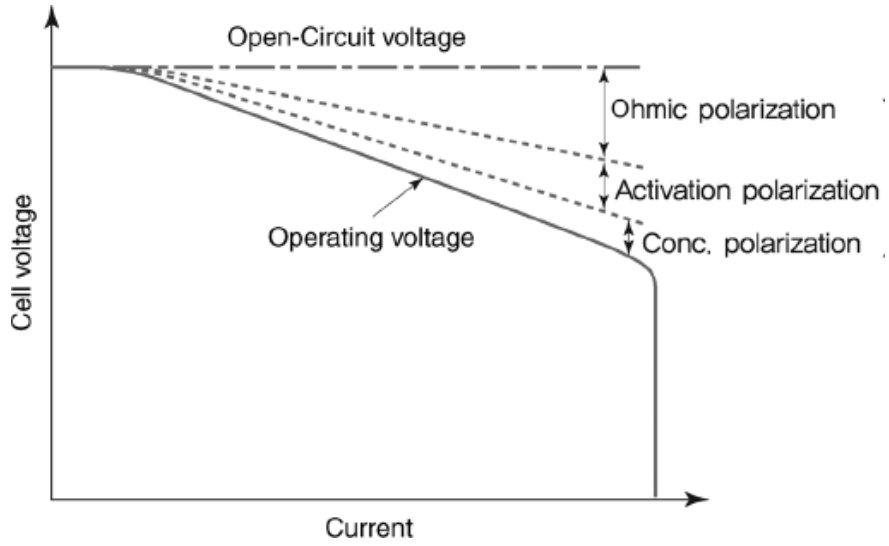

Fig. 1.11. Overvoltages generated in a Li-ion cell for increasing current rates [23].

1.2.2.1. General Butler-Volmer accounting for activation polarization

As mentioned previously, at chemical equilibrium, forward and backward reactions take place at the same rate, resulting in a net current equal to zero. Nevertheless, when one of those reactions starts being faster than the other one, a net current flows which is equal to the addition of the anodic (I_a) and cathodic (I_c) currents. It is represented in Fig. 1.12 where it can be appreciated that at zero overpotential (i.e. at chemical equilibrium), although anodic and cathodic currents are not zero, the net current is. Moreover, it can be seen that at high overpotential values (positive or negative), the current of one of the electrodes is almost zero. This figure only represents a cell limited by activation polarization and does not take into account concentration-polarization effects. This assumption is done when there are no concentration gradients in the cell. In those cases, general Butler-Volmer accounts only for activation polarization effects [24].

$$i\,(\eta_{act}) = I_a + I_c = i_0 \cdot \left\{ e^{\frac{(1-\alpha)\cdot n\cdot F}{R\cdot T}\cdot \eta_{act}} - e^{\frac{-\alpha\cdot n\cdot F}{R\cdot T}\cdot \eta_{act}} \right\} \qquad (1.3)$$

Where,

i_0 is the exchange current,

α is the electron transfer coefficient,

n is number of electrons transferred in the reaction,

F is the Faraday constant,

R is the gas constant

and T is the cell temperature.

In Fig. 1.12, it can be observed that infinite current without increasing the polarization of the cell would be obtained at high overpotentials. Therefore, if working at high rates, concentration polarization effects have to be considered for having a realistic behavior in that part (refer to subchapter 1.2.2.2).

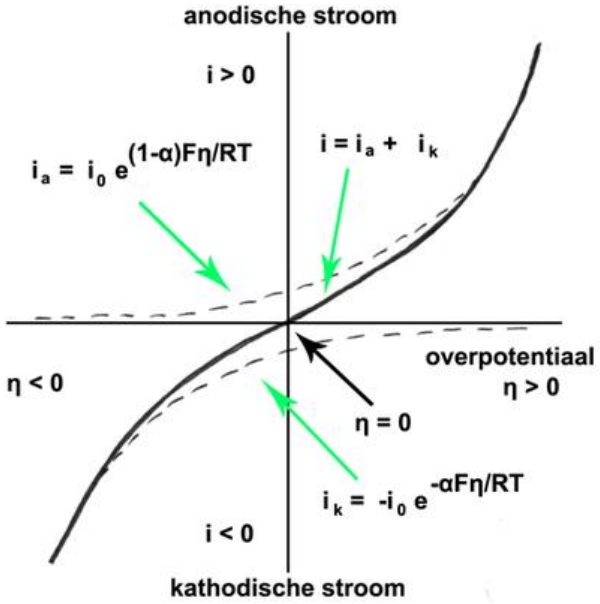

Fig. 1.12. Polarization curve obtained from Butler-Volmer equation accounting only for activation polarization [25].

1.2.2.2. Modified Butler-Volmer accounting for mass transfer effects

Butler-Volmer represented in equation (1.3) is modified to obtain equation (1.4) in the case that not only activation polarization (η_{act} or η_{CT}) is taken into account but concentration polarization (η_{conc} or η_{MT}) is also considered.

$$i(\eta) = I_a + I_c = i_0 \cdot \left\{ \frac{C_R}{C_R^*} \cdot e^{\frac{(1-\alpha)\cdot n\cdot F}{R\cdot T}\cdot\eta} - \frac{C_O}{C_O^*} \cdot e^{\frac{-\alpha\cdot n\cdot F}{R\cdot T}\cdot\eta} \right\} \qquad \textbf{(1.4)}$$

C_O and C_R are the concentrations of the oxidized and reduced species in the reaction. The quotient between C and C^* represents the ratio between the concentration at the electrode surface and the bulk of the electrolyte.

The polarization curve at high overpotentials is highly modified when the corrected Butler-Volmer equation is used (solid line in front of dashed line in Fig. 1.13). When the overpotential is increased, there is a limiting current (i_L) from which no more charge can be extracted although the overpotential continues growing. This effect is due to the concentration gradient that is formed at the electrode surface when Li ions arrive very fast due to the high currents and accumulate there because they do not have time to reach the active material and react before the following ions arrive.

Therefore, as the overpotential continues increasing, the charge or discharge process would be interrupted because the EoD or EoD voltage would be reached quickly.

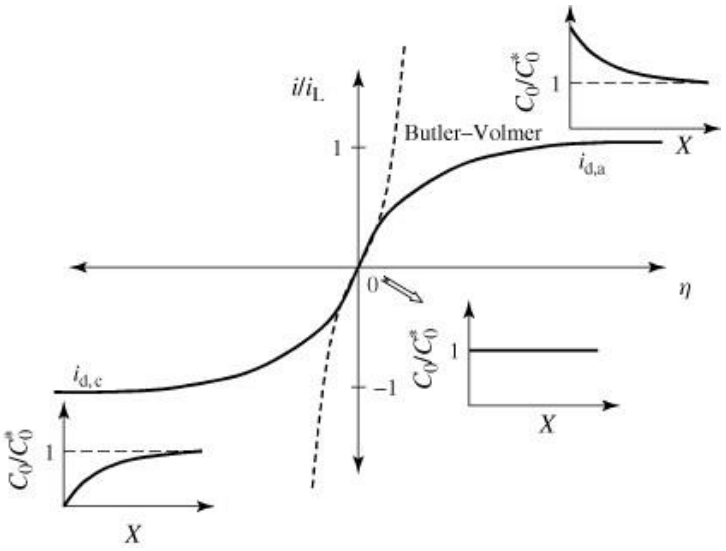

Fig. 1.13. Relation between current (normalized to the limiting current i_L) and overpotential (η) in a li-ion cell [26]. Dashed lines represent the polarization curve when only activation polarization is taken into account and solid line accounts for concentration polarization effects. At the insets, relation between concentrations at the surface and the bulk are represented.

1.2.2.3. Limiting cases of Butler-Volmer

If equation (1.3), in which the mass transfer effect is not considered, is approximated by Taylor's series and evaluated at small overvoltage values ($|\eta_{act}| \ll RT/nF$), it can be linearized (1.5). A linear relation between current and voltage is found and this is the reason why this relation is usually termed as polarization or charge-transfer resistance (R_{CT}), in analogy to the Ohm's law. When evaluating Taylor's series, the initial value for overvoltage is considered to be zero volts as we start from equilibrium, when no net current is flowing through the cell. However, if mass transfer is taken into account as it was done in (1.4), the obtained equation in that case for very small overpotentials is represented in (1.6) [26].

In the situation in which overpotential values are high ($|\eta_{act}| \gg RT/nF$), Butler-Volmer equation simplifies to Tafel equation. It can be reduced because the current of one of the electrodes vanishes at high overvoltages, as represented in Fig. 1.12. Therefore, one of the exponential factors in (1.3) and (1.4), become negligible compared to the other one. The resulting equations are (1.7) when mass transfer is not considered and (1.8) when it is taken into account [26].

Table 1.4. Limiting cases of Butler-Volmer formulation.

Limiting case	Mass transfer?	Equation	
Linear behavior (very small η)	No	$i = -i_o \cdot \frac{n \cdot F}{R \cdot T} \cdot \eta_{act}$	**(1.5)**
	Yes	$i = \left(\frac{1}{1/i_o + 1/i_{l,c} - 1/i_{l,a}} \right) \cdot \frac{n \cdot F}{R \cdot T} \cdot \eta$	**(1.6)**
Tafel behavior (large η)	No	$\ln i = \frac{\alpha \cdot n \cdot F}{R \cdot T} \cdot \eta + \ln i_0$	**(1.7)**
	Yes	$\ln i = \ln i_o + \left(1 - \frac{i}{i_{l,c}}\right) \cdot \exp\left(\frac{-\alpha \cdot n \cdot F}{R \cdot T} \cdot \eta\right)$	**(1.8)**

1.2.3. Aging mechanisms

Li-ion batteries performance degrade when cycled (cycle aging) or when stored, even if they are not in use (calendar aging) [27–31]. The degradation level depends on many factors cycling or storage conditions as temperature, State-of-Charge (which will be explained in following subsections) or charge and discharge rates (history) [29,32,33]. In literature, aging is usually expressed in terms of capacity fade or power fade [34,35]. It is well known that Li-ion batteries are complex systems to understand and the aging mechanisms are even more complicated [35]. Moreover, capacity fade and power fade originate for various causes and their interactions. Therefore, these processes usually occur at similar timescales and cannot be evaluated separately [35]. In addition, beside degradation mechanisms are complex and they are coupled between them, they are also dependent on the chemistry, design and the manufacturing process [15].

All the elements that compose a cell (electrodes, binder, electrolyte, separator, and current collectors) are affected by aging [36–38]. The most common causes of aging affecting the negative electrode are SEI (Solid-Electrolyte Interface) growth and dissolution, current collector corrosion, binder decomposition, volume changes or lithium plating [35,38]. The main causes and effects of aging at the negative electrode are summarized in Table 1.5.

Table 1.5. Main aging mechanisms at the negative electrode side.

Cause	Effect	Aging mechanism	Result in
Changes in volume*	Contact loss of active material particles	LAM	Capacity fade
	Changes in porosity	Overpotentials	Impedance rise
Solvent co-intercalation and gas evolution	Cracking of active material particles	LAM (graphite exfolitation) LLI	Capacity fade
Lithium plating	Lithium deposits and formation of dendrites	LLI	Capacity fade Impedance rise
SEI layer growth	Decrease of accessible surface		Impedance rise
	Changes in porosity		Impedance rise
	Consumption of Li	LLI	Capacity fade
SEI layer decomposition			Capacity fade Impedance rise
Binder decomposition*	Contact loss	LLI	Capacity fade Impedance rise
Current collector corrosion	Contact loss Binder dissolution	Overpotentials Inhomogeneous distribution of I and V	Impedance rise

* Discrepancies were found in [35] and [38] in which the effects were related to either capacity fade or impedance rise.

SEI is a layer that forms at the surface of the graphite because of the high reactivity of the electrolyte when they get in contact. It happens because electrolyte is unstable at the graphite electrode potential operating window. The formation and growth of SEI produces an increase of the electronic resistance what increases the potential operating window at which the electrolyte is, making it more stable and ceasing its growth progressively. SEI is basically composed by precipitates from reduced decomposition of solvents, salts, lithium ions, and other impurities within the electrolyte [39]. Part of the electrolyte and a large amount of lithium ions are consumed by SEI formation in the first cycles, which produce an irreversible capacity loss. Usually, extra lithium is added when manufacturing the cells taking into account the amount required for this initial SEI formation.

When lithium ions reach the negative electrode faster than at the rate at which they can be accommodated into the layered structure of the graphite (during charge process), they are deposited

at the surface of the electrode as metallic lithium. This implies that this lithium is not going to be available anymore for charging/discharging the cell thus producing an irreversible loss of capacity. Moreover, the lithium plating is rarely homogenous but it forms a dendritic structure that can produce internal short-circuits. Clearly, it has to be avoided for safety reasons. Low temperature operation favors lithium plating because the reaction rates slow down, thus more lithium ions stay at the surface of the electrode. The problem can be reduced by adding more graphite to the cell and therefore achieving a higher surface area of the negative electrode compared to the positive one, but there is always a trade-off between avoiding lithium plating and the extra lithium consumed in SEI formation that it produces. An illustrative representation of the main aging mechanisms acting at the negative electrode is given in Fig. 1.14.

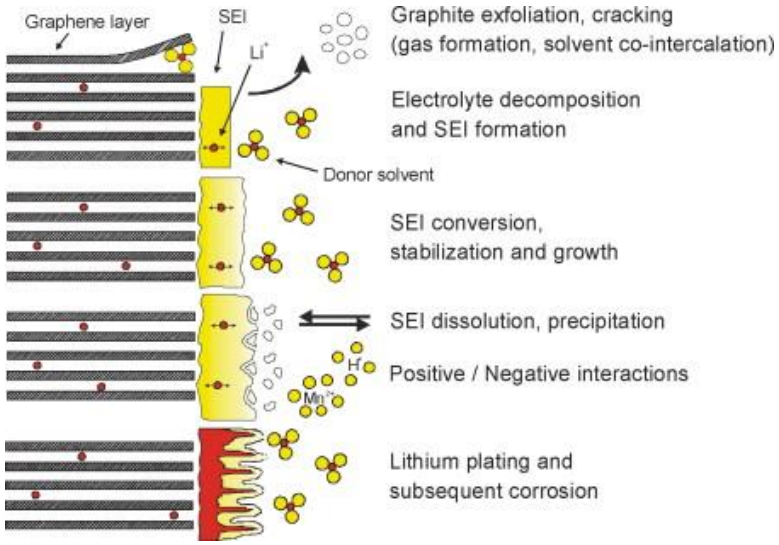

Fig. 1.14. Degradation mechanisms at the negative electrode of a li-ion cell [29].

Regarding the positive electrode, there is also the formation of a surface layer but it is less detrimental than the SEI to the battery performance. Unlike the SEI, the surface layer at the positive electrode thickness does not change significantly during aging. Its formation is attributed to the precipitation of undesired reaction products that blocks the pores of the existing layer. This makes the porosity, conductivity, and diffusion coefficient to change during aging process. Consequently, it produces an increase of impedance, a reduction of the active material that can be reached and therefore, it either reduces the cell capacity [15].

Main degradation mechanisms at the PE are due to lithium insertion/extraction and phase transitions that produce morphological changes as structural disordering or crystal distortion [35]. Aging is also attributed to metal dissolution, which produces the loss of active material and reduces the capacity of the cell and a surface layer, which makes the impedance to rise cell [35]. Moreover, binder and current collector corrosion also contribute to the degradation of the cell (Table 1.6). Unfortunately, the mechanisms of capacity fade are still not completely understood nowadays [35].

Therefore, different assumptions are made in literature [29,35,38,40]. In Table 1.6, we summarized the different contributions found in literature. In addition, a graphical representation of those effects was plotted in Fig. 1.15.

Table 1.6. Main aging mechanisms at the positive electrode side cell [35].

Cause	Aging mechanism	Result
Li+ insertion/extraction	Morphological changes: Structural disordering Change in surface porosity	Capacity fade Impedance rise
Phase transitions	Morphological changes: Mechanical stress and strain Crystal distortion	Capacity fade
Metal dissolution	Precipitation of new phases Loss of active material Surface layer formation	Capacity fade Impedance rise
Electrolyte decomposition	Gas evolution Surface layer formation	Impedance rise
Binder decomposition	Loss of contact	Impedance rise
Current collector corrossion	Loss of contact	Impedance rise

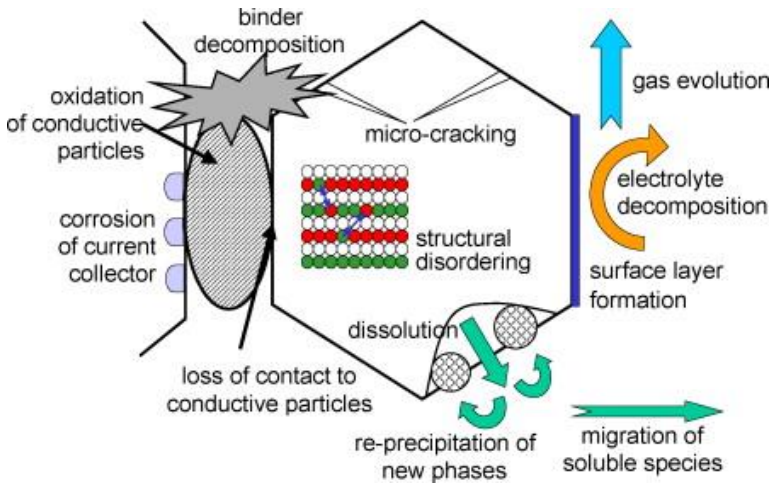

Fig. 1.15. Aging mechanisms at the positive electrode of a Li-ion cell [35].

The reactions that do not contribute to the extraction or injection of energy from or to the cell, which are undesired reactions, are usually termed as side reactions. These reactions may cause aging in both the positive and negative electrodes. Even though the SEI at the carbon-based electrode is

beneficial and essential for proper cell operation, it is considered as a side reaction because it consumes available lithium and reduces the amount of electrolyte in the cell.

Aging mechanisms not only occur when charging or discharging the cells, there are also some reactions taking place when the cell is kept under open-circuit conditions. Especially when the battery is left to open-circuit conditions at high SoCs, a local redox process occurs at the positive electrode without any external electron transfer. It is known as self-discharge process and it is caused by the decomposition of the electrolyte [1].

1.3. SoC and SoH determination methods

1.3.1. SoC definition

In thermodynamic terms, SoC is defined as a state function of the battery [41]. It implies that it has to be defined when all the species in the system are in equilibrium (at constant temperature and pressure). In these conditions, the composition of the active material of the electrode and the concentration of the active species in that composition are unique (i.e. x in $Li_xM_yO_z$ is fixed). Thus, the electrode potential at this composition and conditions will be unique versus a reference electrode [41]. In this case, SoC can be defined as a function of the lithium content in the active material [41]. Batteries comprise two electrodes each of them staying at specific potential and having different concentrations, when evaluated at equilibrium. Therefore, the OCV, which is measured at equilibrium, can be related to SoC because it expresses the difference in Li-ion concentration in the electrodes [41]. Therefore, a particular SoC can be associated to a particular OCV value for a particular cell at a certain temperature and degradation level. Moreover, SoC can also be calculated as the ratio between injected or remaining charge in the cell and the actual capacity of the cell (1.9) [41].

$$SoC\ (\%) = \frac{Q_{injected}}{Q_{actual}} \cdot 100 \qquad \textbf{(1.9)}$$

SoC measurement methods can be classified into experimental measurements, adaptive systems or hybrid methods combining both of them [42]. Experimental measurements mainly include voltage, current (Coulomb counting method), resistance or impedance measurements. Nevertheless, adaptive systems, such as Neural Networks or Kalman Filter algorithms, are designed to automatically adjust the SoC for different discharging conditions [42]. Hybrid methods are also considered in order to take advantage of the benefits of both estimation techniques. Some of the most common used experimental methods are summarized in this section.

Coulomb Counting is the most used method for determining the SoC in practical applications [41,43,44]. It consists in estimating the remaining capacity under a giving test conditions from the delivered and nominal capacities. Delivered capacity is estimated by measuring and integrating the

current $I(t)$ that goes in and out from the cell. Therefore, it is related to the nominal capacity of the cell ($Q_{nominal}$) and subsequently subtracted from the initial SoC ($SoC_{initial}$) (1.10).

$$SoC(t) = SoC_{initial} - \frac{\int_0^t I(t)}{Q_{nominal}} \cdot 100 \quad \textbf{(1.10)}$$

This is a simple method because current and time can be directly measured (Table 1.7). The accuracy of this method basically depends on the precise measurement of current and an accurate estimation of the initial SoC [43]. Moreover, when it is performed for long period discharges, the measurement errors accumulate and can be a source of high inaccuracies. Thus, regular recalibration is required when using this method [45]. The self-discharge and the coulombic efficiency also affect the capacity measurement [43,44]. In addition, nominal capacity is defined by the manufacturer for a certain working conditions. Thus, it is not a realistic value of the actual capacity of the cells. Nominal capacity does not account for the cell-to-cell variability generated during the manufacturing process, for the capacity fade due to aging [41] or the temperature and discharge current [42,45]. Therefore, in order to improve the accuracy of the method, maximum capacity of the cells under certain conditions are used in equation (1.10) instead of nominal capacity [41,45]. More precise estimations have been proposed in literature in order to reduce the effects coming from these errors [41]. Moreover, this method is commonly used in combination with other supporting methods [45].

SoC estimation from OCV was very useful for lead-acid batteries because there is a linear relationship between OCV and SoC [42,44]. However, although the OCV curves of Li-ion batteries are characteristic of their chemical composition, they do not follow a linear relationship with the SoC. Moreover, they are composed of plateaus and transition between those plateaus. At the plateaus (refer to subsection 1.2.2), the OCV is almost constant (in some cases it varies less than 5 mV) for a large range of the SoC. For example, LFP cells have a unique plateau that almost covers the full range of SoC [41]. Therefore, this method would not be suitable to these cells by only measuring one OCV point during the battery operation (Table 1.7).

SoC has also been estimated from impedance or resistance measurements [41–43]. The main drawback of using impedance to determine SoC is that additional equipment is required in order to carry out the impedance measurement (Table 1.7). Therefore, it makes it impractical and expensive. On the other hand, resistance is simple to obtain but it is inaccurate and difficult to interpret because equivalent electrical models are required. If the models are simple, they are inaccurate, and increasing the complexity of the models leads to an increase of computational effort.

Table 1.7. Pros and cons of various experimental methods employed in determining the SoC [46].

Method	Pros	Cons	Initial parameters
Coulomb Counting	• Easy to implement • Accurate if initial SoC value, current measurement and efficiency are precise.	• Initial SoC dependency • Needs accurate value of self-discharge rate and coulombic efficiency. • High accuracy in current measurement • Not suitable for cells under very dynamic conditions	• Current • Capacity • Coulombic efficiency • Self-discharge rate • Initial SoC value
OCV	• Easy to implement • Accurate (depending on the chemistry)	• Needs some rest time • Not suitable for some batteries as LFP	• Rest time • Voltage
Resistance or impedance	• Resistance: easy to implement	• Resistance: not so accurate • Impedance: hard and costly	• Resistance • Previous knowledge of impedance

1.3.2. SoH definition

SoH is generally defined as the ability of a cell in delivering a specific performance in comparison with a fresh cell [32,33,47–50]. However, this specific performance varies from study to study because there is no consensus in what SoH is and how has to be determined [46,51]. Some of the battery parameters currently employed in SoH determination are capacity, internal resistance, ac impedance, self-discharge rate or power density [46]. The unit of SoH is percent and 100 % represents a fresh cell [46,51]. There is no consensus either in defining the SoH at the EoL of the cells. In various studies it is defined as a percentage of the initial performance and in others it is defined as 0 % at the EoL [33,50]. Thus, it implies that various equations to estimate SoH can be found in literature [33,49]. The most common approximations relate the SoH to the capacity fade or resistance rise. In particular, in [49] it is defined as the ratio between the initial capacity and the capacity at time t (1.11). However, in [33] it is defined separately in terms of capacity fade (SoH_C) and resistance rise (SoH_R) at the i^{th} cycle (equations (1.12) and (1.13)). As it can be appreciated, they previously defined a threshold for

EoL as the 80 % of the initial capacity and the double of the initial resistance. Thus, EoL was defined at SoH equal to 0 %.

$$SoH(t) = \frac{discharge\ capacity\ (t)}{discharge\ capacity\ (t=0)} \quad \textbf{(1.11)}$$

$$SoH_C(i) = \left(1 - \frac{C_0 - C(i)}{C_0} \cdot \frac{1}{0.2}\right) \cdot 100 \quad \textbf{(1.12)}$$

$$SoH_R(i) = \left(1 - \frac{R(i) - R_0}{R_0} \cdot \frac{1}{0.2}\right) \cdot 100 \quad \textbf{(1.13)}$$

In particular, in electric vehicle (EV) applications, SoH is usually defined as the ratio between current capacity and initial capacity. EV cells are discarded when their SoH decreases to the 80 % [46,51,52]. SoH is usually predicted from empirical models [31]. These models can be more or less accurate, depending on the computational efforts required to simulate them. Thus, there is always a trade-off between computational complexity and accuracy in portable applications [46,47,51,52].

As it was stated in subchapter 1.2.3, it is well known that Li-ion batteries are complex systems to understand and the aging mechanisms are even more complicated. Moreover, capacity fade and power fade originate for various causes and their interactions. Therefore, it makes difficult to standardize a SoH definition valid for all the cells and applications.

1.4. Motivation and objectives

The hypothesis of this dissertation was to demonstrate that the joint contribution of impedance and entropy of a cell is a valid parameter to discriminate the contributions of SoC and SoH. However, at the beginning of this study, we focused on measuring impedance but it was difficult to separate the various contributions related to cell degradation. A deep knowledge of batteries and electrochemistry are required for interpreting impedance data. Moreover, the various effects found at the impedance spectra show similar time constants what make them even more difficult to be distinguished and interpreted. Nevertheless, during this time, we focused in getting a better understanding of entropy and we realized that irreversible entropy production could stand by itself. It means that this term is directly related to the degradation suffered by the cells. Therefore, we shifted our motivation to find a relationship between the degradation of the cells and their irreversible entropy generation.

The following chapters contain the introduction, a materials and methods section, the experimental results, the corresponding discussions and the conclusions. In Chapter 2 the results and

discussions sections were presented together. The main contents of the chapters are summarized as follows:

Chapter 1

A general introduction to bateries including some of the chemistries and packaging styles was developed. Then, a more specific description of Li-ion cells in particular was made. Their chemical and electrical behavior together with the main aging mechanisms they suffer were exposed. At the last part, State-of-Charge (SoC) and State-of-Health were defined.

Chapter 2

In this chapter, the capacity fade of the diferent evaluated cells and the evolution of their voltatge responses during the aging tests were exposed.

Chapter 3

Impedance measurements were carried out in this chapter. In particular, the evolution of impedance of the diferent cells during the cycling tests were tracked versus SoC and SoH. Moreover, impedance was estimated from digital signal processing of charging voltatge/current profiles and from pulses.

Chapter 4

In this chapter, energy and entropy relations were evaluated. In particular, OCV, hysteresis, overpotential, reversible and irreversible entropies production and heat generations were considered. Moreover, incremental capacity analysis was carried out in order to estimate the main aging mechanisms taking place.

Chapter 5

Post-mortem analysis was carried out in this chapter. The employed techniques were weighting, visual inspection, preparation of half-cells, capacity and impedance of half-cells, ICP analysis, porosimetry and XRD.

Chapter 6

In this chapter, general discussions were carried out. All the results and discussions obtained from previous chapters were discussed in a global manner.

Chapter 7

General conclusions were listed in this chapter. Moreover, future work and research lines derived from this study were also included.

Chapter 2

Capacity fade

In this chapter, the evaluated cells are subjected to prolonged cycling in order to let them at differents SoHs for further analyses in following chapters. Moreover, the main parameters of those cells are described. In the results section, voltage profiles and capacity evolution with cycling are represented.

2.1. Introduction

Cell degradation can be evaluated from either the decrease in capacity or the decrease in power capabilities. In this chapter, the evolution of capacity during cycling is investigated. Power fade in terms of impedance rise is analyzed in Chapter 3.

The available capacity of the cells is directly related to the amount of active material, the available lithium for cycling and the remaining electrolyte but, at the same time, it depends on other parameters such as the charge or discharge rate, temperature or cut-off conditions [53,54]. At high rates (those that cannot be considered as close-to-equilibrium measurements); the electrochemical reactions do not have time to be completed before reaching the cut-off conditions. This is because high overpotentials are required to drive the reactions what makes the cut-off voltage limit to be reached before all the capacity could be fully exploited (refer to Fig. 1.11). In that case, the kinetic effects would be limiting the cell performance.

The capacity threshold of a cell before being discarded depends on the intended application. For example, electric vehicles are one of the more demanding applications, whose batteries are discarded when their capacities decrease down to 80 % of the nominal capacity. In contrast, some other

applications that require less performance batteries like stationary systems allow a higher capacity fade before being discarding. Some studies revealed that second life batteries could be used for about 5 years until the capacity would decrease to 50 % of the nominal capacity [55].

State-of-Charge (SoC) is a relevant parameter that has to be well defined. When studying Li-ion cells, a poor definition of the SoC can lead to wrong results. Moreover, in actual applications, a wrong estimation of the SoC could lead to unsafe situations where the cell could be working outside the recommended voltage limits. It is not easy to estimate the SoC but it is necessary in order to have a reliable system. For that purpose, several techniques are currently employed [41,44,45,47,56]. Some examples are current integration, cell voltage related to SoC, OCV related to SoC and impedance measurements.

2.2. Materials and methods

Several Li-ion cells were evaluated in this study, with different chemistries, capacities and packaging. With respect to the chemistries for the positive electrodes, $Li(NiMnCo)O_2$ (NMC), $LiFePO_4$ (LFP) and $LiCoO_2$ (LCO) were considered while negative electrodes were made of graphite in all cases. Moreover, capacities ranged from 0.4 Ah to 40 Ah. Regarding to the packaging, prismatic and cylindrical cells were evaluated (Table 2.1).

Table 2.1. Classification of the cells investigated in this study and their nominal voltages and capacities.

Label	Model	Chemical composition	Packaging	Nominal voltage	Nominal capacity
LGC207x	ICR18650 C2	$Li(NiMnCo)O_2$	Cylindrical 18650	3.72 V	2.8 Ah
xxx Microbattery	Varta LIP 533048 AJ	$LiCoO_2$	Prismatic	3.7 V	0.74 Ah
VICxx	IFR14430	$LiFePO_4$	Cylindrical 14430	3.2 V	0.4 Ah
EVbat_x	SE40AHA	$LiFePO_4$	Prismatic	3.2 V	40 Ah

In the following sections, it will be noticeable that some cells were further analyzed than others were. We began the study with LCO and EVbat cells, whose characterization can be considered as preliminary. We gained experience on batteries and their characterization in NMC and LFP cells. This work has last six years and this is the reason why those analyses can be unbalanced in the four sets of cells.

2.2.1. Battery cycling

Cells were cycled in order to compare their performances at different degradation levels or SoH levels. Cycling was done at room temperature (between 23 ºC and 26 ºC, depending on the test) in a climatic chamber or in the laboratory with controlled temperature to avoid temperature fluctuations during day and night.

Cells were charged with Constant Current - Constant Voltage method (CC-CV) as it is the recommended method for charging li-ion batteries. CC-CV consists in applying constant current to the cell until the maximum voltage is reached. Then, maximum voltage is maintained while the current decreases progressively until it reaches the cut-off current. Charging the cells in such a way assures the fully charged state of the cells.

2.2.1.1.NMC cells

Various NMC cells of the same model were degraded in the same conditions. Thus, possible cell-to-cell variations might be identified. In particular, the cells were charged at a C/2 rate and discharged at 3C/2, as recommended by the manufacturer. The cells underwent between 300 and 400 cycles depending on the particular cell (Table 2.2). Expected cycle life by the manufacturer at which the cell maintains a capacity equal or higher than 78 % of the nominal capacity is 300 cycles when charging and discharging at C/2 at a temperature of 23 ºC ± 2 ºC.

LGC2 cells were cycled at HNEI (Hawaii Natural Energy Institute), which is a research unit of the University of Hawaii at Manoa. The cycling was done in a HVBT 5560 Arbin Tester capable of measuring current and voltage. Temperature was measured by externally attached thermocouples to the cells surface and data was recorded by a personal DAQ/50 series. Thermal paste was employed to enhance thermal contact between the cell and the sensor. Measurements were done in climatic chambers at 25 ºC. For avoiding possible heat flows that could affect the measurements, cells were placed inside a glass box only opened by one end.

Table 2.2. NMC cells charging/discharging parameters

Cell	Maximum voltage	Cut-off voltage	Cut-off current	Charge - Discharge rate	Temperature	Number of cycles
LGC2074	4.3 V	3 V	C/56	C/2 – 1.5C	25 ºC	322
LGC2075						358
LGC2076						404

2.2.1.2.LFP cells

2.2.1.2.1. VIC cells

VIC cells were charged at C/5 as it is recommended by the manufacturer and discharged at 2C. The cells were cycled around 1000 times (Table 2.3). Expected cycle life by the manufacturer at which the cell maintains a capacity equal or higher than 70 % of the nominal capacity is 1000 cycles when charging and discharging at a symmetric rate of C/5 at a temperature of 20 ºC ± 5 ºC.

The cycling of the VIC cells was done in two steps with two different equipment. The first part of the cycling (around 400 cycles) was performed in an HVBT 5560 Arbin Tester during the research stay at HNEI of the University of Hawaii at Manoa. For measuring the temperature, a thermocouple was externally attached to the cells and the output was recorded by a personal DAQ/50 series. Thermal paste was employed for better heat transfer between the cell surface and the sensor. Measurements were carried out in a climatic chamber at 25 ºC. For avoiding heat flows that could alter the results, cells were placed inside a glass box opened at one single end. The second part of the cycling was carried out once back to Barcelona with a VSP Bio-logic potentiostat/galvanostat in the same conditions. Temperature was measured by placing a thermistor to the cell surface. The output signal of the thermistor was linearized and then recorded with the potentiostat. Temperature was controlled with a laboratory cooled incubator ILW53 provided by Pol-Eko Aparatura.

Table 2.3. VIC LFP cells charging/discharging parameters

Battery	Maximum voltage	Cut-off voltage	Cut-off current	Charge - Discharge rate	Temperature	Number of cycles
VIC01	3.65 V	2 V	C/100	C/5 - 2C	25 ºC	1049
VIC02						1005

2.2.1.2.2. EVbat cells

EVbat cells were cycled at a 2.5C symmetric charge and discharge rates different times depending on the particular cell (see details in Table 2.4). Thus, individual cells of same model and capacity might be compared in terms of degradation or SoH. As we did not have devices capable of cycling those high capacity cells at 2.5C which corresponds to currents around 100 A, they were sent to Ikerlan, which is a Technology Center based in the Basque Country (Spain), in order to be cycled. They were left at different SoHs for further analysis when they would be back to our laboratory. Cycling was done at ambient temperature for cell 1, cell 2 and cell 3. In contrast, cell 4 was cycled in a climatic chamber at 25 ºC. Those prismatic cells are much larger than the other considered cells in this study (11.6 cm x 18.6 cm x 4.6 cm) and temperature was measured at different points in the cell surface with external 10 kΩ NTC thermistors.

The manufacturer estimates expected cycle life of those cells in 2000 cycles at a 0.3C charge and discharge rates.

Table 2.4. EVbat LFP cells charging/discharging parameters

Battery	Maximum voltage	Cut-off voltage	Cut-off current	Charge - Discharge rate	Temperature	Number of cycles
EVbat_1	3.6 V	2.5 V	C/8	2.5C - 2.5C	25 ºC	50
EVbat_2						100
EVbat_3						200
EVbat_4					25 ºC (controlled)	400

2.2.1.3.LCO cells

Two LCO cells of the same model were considered in this study: one of them was a fresh cell (Fresh Microbattery), and the other one (Old Microbattery) had been cycled 150 times at approximately 1C before being used in this study (Table 2.5). The cycle life of this battery is estimated by the manufacturer in 300 cycles when charged and discharged at a rate of 1C. Cycling was carried out with Cadex C7200-C battery analyzer. During charge and discharge processes, temperature and cell voltage were monitored with a Keithley 2700 data acquisition system. Temperature was measured inside the cell thanks to the internal thermistor already present in that particular battery, which is incorporated to avoid possible overheating while charging or discharging.

Table 2.5. LCO cells charging/discharging parameters

Battery	Maximum voltage	Cut-off voltage	Cut-off current	Charge - Discharge rate	Temperature	Number of cycles
Fresh Microbattery	4.2 V	3 V	C/50	0.88A/0.73A	25 ºC	10
Old Microbattery					25 ºC	150

2.2.2. Initial characterization

Initial characterization consists of a series of tests carried out to various cells of the same model prior to perform the aging tests. From the initial characterization, various relevant parameters (as differences in weight, polarization resistance or capacity ration) can be extracted at BoL and possible cell-to-cell variations can be identified. If high variability were found between the cells, it would mean that the results could not be extrapolated to other cells. Some of the tests carried out during the initial

characterization of the cells were repeated periodically during the aging tests in order to track the evolution of the measured parameters. In this study, we performed the initial characterization on the NMC cells and VIC (LFP) cells. For previous studied cells as EVbat and Microbattery, no initial characterization was done because the importance of the test was not yet well understood.

Weighting and labeling the cells are the first steps of the process. A quite consistent manufacturing process is suggested by small variations in weight among the cells. After weighting the cells and checking the OCV, few cycles were carried out in order to stabilize their capacity. These cycles are usually named formation cycles because they favor the formation and stabilization of the SEI layer at the negative electrode.

A Reference Performance Test (RPT) was carried out regularly of the cells during the aging test to evaluate their actual SoH [57]. It consisted in charging and discharging the cell at least at three different low currents (in our case C/25, C/5 and 1C) in order to have enough points for the analyses (for instance, for the calculation of the polarization resistance from its linear approximation at low rates). In this case, instead of charging by CC-CV method, constant current is preferred because, then, the injected charge is only affected by cut-off voltage limitations. Thus, the shape of the voltage curve is symmetric during charge and discharge. Remnant capacity method was applied after charging and discharging at constant current in order to always end up at the same SoC independently from the rate being used (Fig. 2.1). Remnant capacity has to be carried out at the lowest charge/discharge rate of the test (C/25 in this example). As it can be seen in Fig. 2.1, the green points represent the OCV after constant current discharging. The SoC is directly related to the OCV. Thus, it can be appreciated that the ending SoC is not the same after discharging the cells at different rates. Nevertheless, the red points represent the same OCV (i.e. the same SoC) after remnant capacity is discharged.

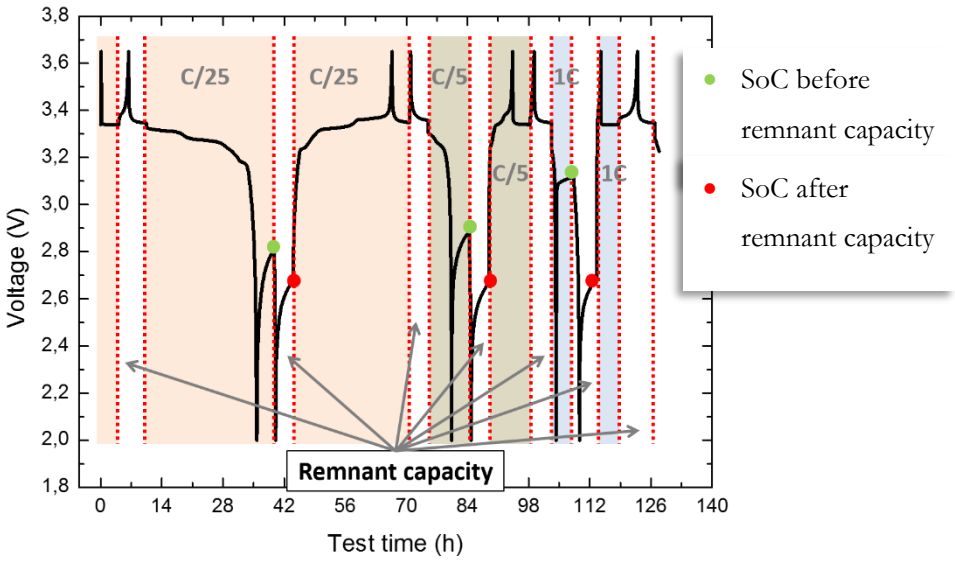

Fig. 2.1. Charge and discharge processes always start at the same SoC independently from rate because of the remnant capacity. Remnant capacity has to be carried out at the lowest rate employed in the test in order to assure the cells are charged to the same level (C/25 in this case). Resting voltages in green and red can be directly related to SoC through the OCV curve.

From the initial reference performance test (RPT), the following information was obtained:

- Charge-transfer resistance.

  Charge-transfer resistance indicates the cell voltage under polarization, thus the portion of capacity and power deliverable at low rates under a certain cut-off conditions. It has to be calculated at low rates in order to assure the cell is working at the ohmic regime of the Tafel behavior where it shows a linear voltage to current response.

- Rate dependence.

  How the cell behaves under different charge/discharge rates and which reactions are limited by the rate and consequently have no time to occur before voltage cut-off conditions.

- Ragone plot.

  It represents the specific energy versus the specific deliverable power.

- Capacity ration.

  It can be used to determine the active material in the cell what dictates the maximum capacity of the cell. Capacity ration is derived from the capacity at a given rate and the SoC range involved in delivering the said capacity. It is only useful to compare cells with the same SoH.

- Peukert coefficient.

  It indicates the capability of a cell in handling discharge rate variations dictated by kinetic factors other than polarization resistance, which are usually introduced in the manufacturing processes. Peukert coefficient does not take into account any polarization effect and assumes that all the electrode reactions are completed at a given rate.

- Rest Cell Voltage (RCV) evolution with charge/discharge rate.

  It can be related to the amount of charge injected/extracted at each of the charge/discharge rates.

2.2.3. Experimental SoC definition

The state-of-charge indicates the portion of the actual capacity that is still available for discharge or is already filled during charge. Its range is fixed between 0 % to 100 %. It is related to normalized capacity calculated at very low rates as defined in equation (2.1). Therefore, maximum available capacity was calculated at low rates where kinetic effects were minimized ($Q_{actual\_LowRates}$). Thus, the current SoC is obtained from the ratio between injected charge at any rate ($Q_{injected}$) and the $Q_{actual\_LowRates}$ [58]. It implies that, when the applied current instead of low is moderate or high, the range of the total SoC that is involved in the process of charge or discharge is diminished, resulting in discharges (or charges) that do not go to 0 % SoC but to higher values. However, the available SoC was still 100 % even though it was not fully exploited at those high or moderate rates. Moreover, it is necessary to let the battery rest to validate the present SoC. This is because, ideally, when SoC = 0 % or SoC = 100 % are reached at the EoD or EoC, all the ions are at one single electrode (positive or negative depending on the direction of the process) but when high charge/discharge currents are

applied to the cell, all the ions accumulate at the electrode surface but have no time to react. Thus, they go back to the other electrode when the current is interrupted. As the SoC is defined inside the active material particles, some relaxing time has to be left after interrupting the current in order to wait for the particles at the surface to go back to the other electrode. If the SoC at the electrode surface were evaluated instead of inside the electrode particles, it would be correct to indicate SoC = 0 % or SoC = 100 % on it.

$$SoC\ (\%) = \frac{Q_{injected}}{Q_{actual\_LowRates}} \cdot 100 \qquad \textbf{(2.1)}$$

Summarizing, SoC is independent of aging because it does not depend on capacity but on normalized capacity to the actual capacity. What changes at moderate/high rates is the deliverable portion of capacity, thus the SoC at which the cells can be charged or discharged.

2.2.3.1. Practical SoC estimation

As mentioned previously, when the cells are charged and discharged at very low rates, thermodynamic properties of the cells can be extracted because kinetics effects are minimized. Therefore, the OCV curve corresponding to the full SoC range (from 0 % to 100 %) can be obtained and stored in a look-up table for further comparisons. Then, if the measurements are carried out at higher rates, the SoC can be obtained by measuring the OCV at the EoC or EoD (after a resting period) and comparing it to the corresponding OCV-SoC look-up table obtained at thermodynamic rates. Periodically, while cycling the cells, a four hours resting period was left, in our case, in order to update the SoC at which we were charging/discharging the cells at the current SoH. Four hours were selected because it was the protocol followed in Hawaii (USA) during the research stay. We learnt from them how to estimate the SoC in that particular way. Four hours resting period offered a good trade-off between time and accuracy. Rest cell voltage after the four hours resting period was considered as the OCV, and consequently SoC was obtained from this data. An example of how SoC was determined was plotted in Fig. 2.2. In that example, a C/25 charge/discharge was carried out and it was assumed that the cell was completely charged and discharged, reaching a SoC of 100 % and 0 %, respectively. Therefore, the OCV curve was estimated as the average of charge and discharge curves at a rate of C/25. However, when charged and discharged at a constant current of C/5 rate, the 95 % of the cell was charged (from 0 % to 95 % SoC), and then remnant capacity was carried out in order to set the cell at 100 % SoC. During discharge, almost 99 % could be discharged at this constant current (from 100 % to 1 % SoC). At 1C, even less charge was injected or extracted. In particular, only the 80 % of the capacity was charged (starting from fully discharged state) and 98 % was obtained during discharge (starting from fully charged state). These values were only valid for

this particular cell at this particular SoH and they were shown here as an example of the applied method used to determine the SoC.

This particular method was employed for NMC cells and VIC cells (LFP).

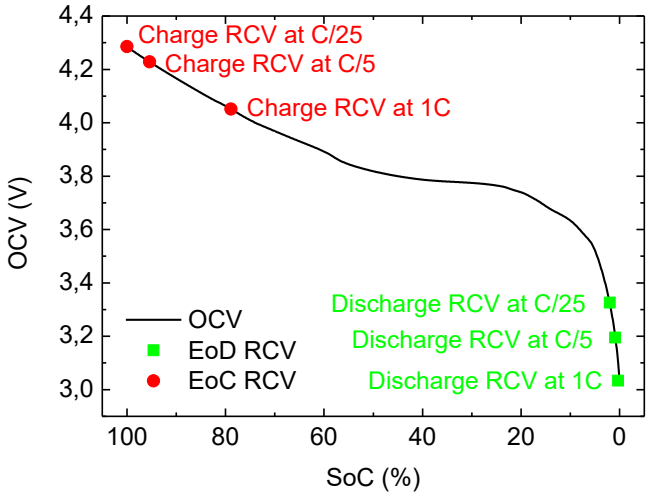

Fig. 2.2. Example of SoC calculation at 3 different charge/discharge rates (C/25, C/5 and 1C) for a NMC cell at a particular SoH. End-of-Discharge Rest Cell Voltage (EoD RCV) and End-of-Charge Rest Cell Voltage (EoC RCV) after 4 h relaxation period was compared to the OCV-SoC curve obtained at low rates (C/25 in that case).

2.2.4. Capacity measurements

We measured all capacities by Coulomb counting method. Available capacity depends on the chosen charge/discharge rate, which produces a higher or lower polarization. This polarization allows or prevents the full completion of the electrochemical reactions prior to reach the cut-off voltage. Temperature was also considered because the kinetics of reactions is temperature dependent, that is, the amount of charge stored or delivered by a cell depends on its temperature.

2.3. Results and discussions

2.3.1. Cell-to-cell variations

Initial cell-to-cell variations were estimated in order to validate the repeatability of the results among these particular cells. This initial study was carried out for LGC2 cells (Table 2.6) and VIC cells (Table 2.7). In general, a higher variability was found for VIC cells. The small deviation in weights suggested that the manufacturing process was quite consistent. Variations in charge-transfer resistance between cells contributes to disparities in the capacity of the cells. Similar values were found at BoC but variabilities in charge-transfer resistance at BoD were larger in VIC cells. Finally, capacity ration represents the amount of active material in the cells. It was also higher in the case of VIC cells but both stayed below 1 %. Thus, from these results, we assumed the analyses carried out to one VIC or LGC2 cell would be extrapolable to other cells of the same batch.

Table 2.6. Cell-to-cell variations of three LGC2 cells (NMC) at BoL.

LGC2 cells	Mean value and standard deviation	Standard deviation in %
Weight	46.2924 g ± 0.04387 g	± 0.095 %
Charge-transfer resistance BoC	74.32 mΩ ± 5.01 mΩ	± 6.74 %
Charge-transfer resistance BoD	64.37 mΩ ± 3.92 mΩ	± 6.1 %
Capacity ration	27.447 ± 0.0576 mAh.%SoC^{-1}	± 0.21 %

Table 2.7. Cell-to-cell variations of three VIC cells (LFP) at BoL.

VIC cells	Mean value and standard deviation	Standard deviation in %
Weight	14.93188 g ± 0.06557 g	± 0.44 %
Charge-transfer resistance BoC	0.219 Ω ± 0.014 Ω	± 6.5 %
Charge-transfer resistance BoD	0.116 Ω ± 0.0172 Ω	± 14.83 %
Capacity ration	4.503 ± 0.0332 mAh.%SoC^{-1}	± 0.74 %

During the initial characterization of the cells, rate capabilities of LGC2 and VIC cells were compared (Fig. 2.3). As it can be appreciated, LGC2 cells maintained the same voltage shape (including the plateaus measured at C/25) at a rate of C/5. Conversely, VIC cells maintained the plateaus during charge but at least the one at the EoD disappeared at C/5. Thus, LGC2 cells showed better rate capabilities than VIC cells.

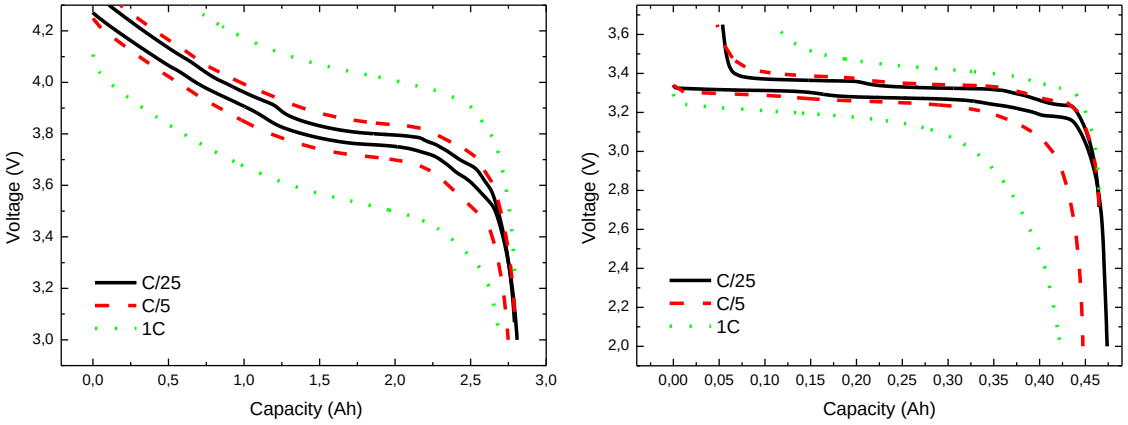

Fig. 2.3. Rate capability of a NMC cell (left) and a VIC cell (right) evaluated at C/25, C/5 and 1C at BoL and room temperature.

2.3.2. LGC2 cells (NMC)

In the voltage profiles of a LGC2 cell (NMC) at different SoHs when discharged at C/25 and 3C/2 rates, the ohmic drop at the beginning of discharge was not as pronounced at C/25 rate as it was at a 3C/2 rate (Fig. 2.4). Furthermore, the available capacity at low rates was also decreased during the aging test because the plateaus dropped faster to lower voltages in the aged cells. At high rates, the cell voltage decreased faster from the very beginning of discharge as more aged were the cells, due to the worsening of kinetics, what produced a decrease in the extracted charge with aging at the same cut-off conditions.

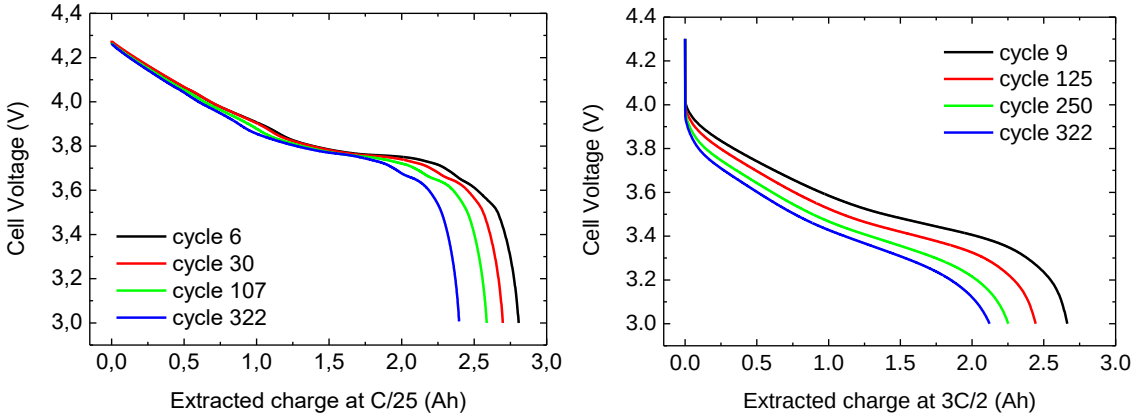

Fig. 2.4. Voltage profiles of a LGC2 cell versus delivered capacity at a C/25 (left) and 3C/2 (right) discharge rates. Nominal capacity is 2.8 Ah.

The capacity evolution of the NMC cells evaluated at 3C/2 and C/25, showed a linear decrease at both high and low discharge rates (Fig. 2.5 and Fig. 2.6). However, at 3C/2, three different tendencies in capacity fade were found during the aging test. Moreover, all three evaluated cells revealed similar trend, indicating a good repeatability among them. The expected cycle life by the manufacturer was 300 cycles when charging and discharging at a C/2 rate. Even though discharge was done at 3C/2 instead of C/2, the cells maintained the 80 % of the nominal capacity even after 275 - 325 cycles. If the application would require lower currents, as C/25, the cells would be still capable to deliver more than 85 % of the nominal capacity after 325 cycles (Fig. 2.6).

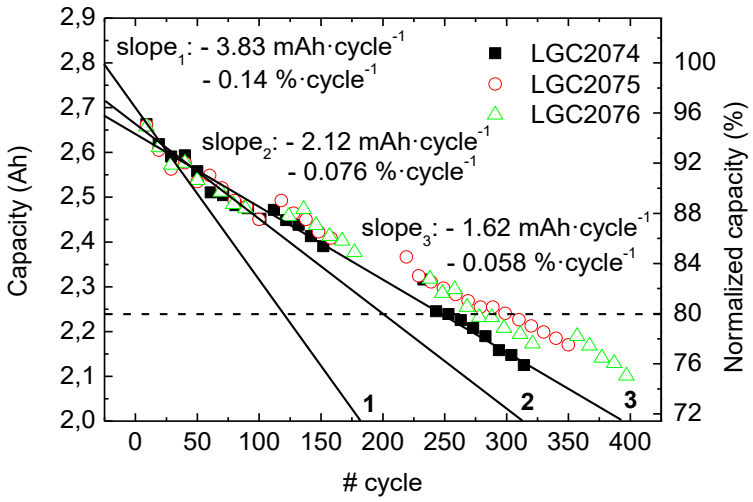

Fig. 2.5. Capacity evolution of the NMC cells evaluated at a 3C/2 discharge rate (in Ah on the left and as a percentage of the nominal capacity on the right). Three different slopes in capacity fade were found, which were labeled and quantified. Some points have been skipped for clearer representation.

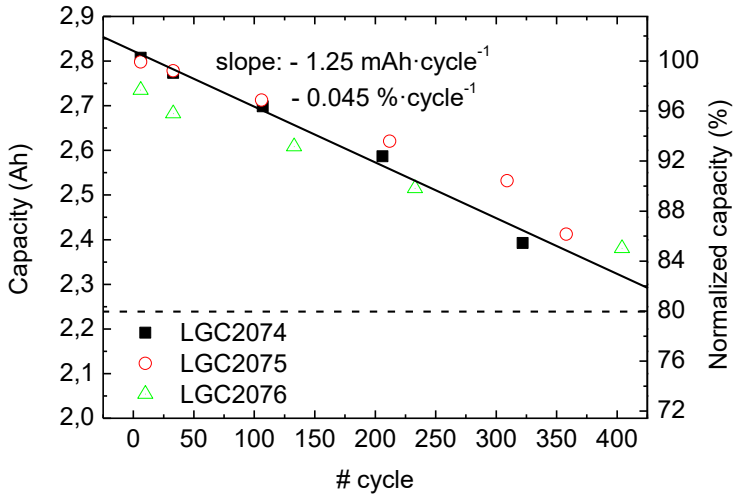

Fig. 2.6. Capacity evolution of the NMC cells evaluated at a C/25 discharge rate (in Ah on the left and as a percentage of the nominal capacity on the right).

2.3.3. LFP cells

2.3.3.1. VIC cells

Concerning the voltage profiles of a VIC cell at different SOH levels evaluated at a C/25 discharge rate, the capacity decreased as more cycles were carried out to the cells (Fig. 2.7). The drop in voltage found around 0.15 Ah at BoL, corresponding to the transition between plateaus, was shifted to near 0.08 Ah at the EoL, what produced the highesto capacity fade at this rate.

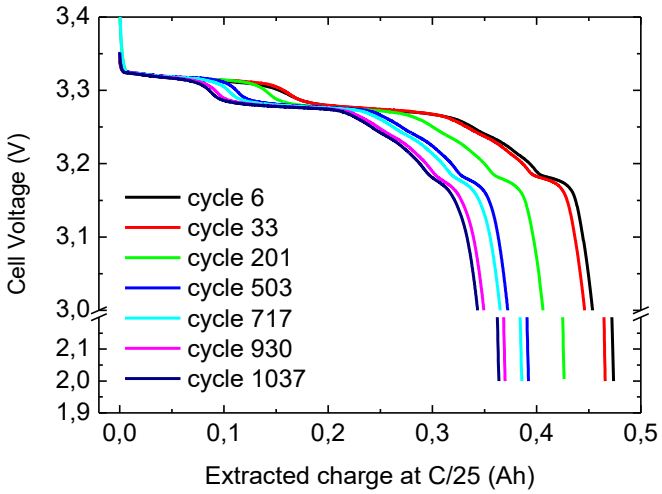

Fig. 2.7. Voltage profiles of a VIC cell (LFP) versus delivered capacity at a C/25 discharge rate at different aging levels. Discontinuity is due to the break for the sake of clarity in the representation.

The capacity evolution of VIC cells evaluated at a 2C discharge rate showed three tendencies that could be approximated as linear with different slopes: in the first 50 cycles, the capacity increased. In the following 250 cycles, capacity decreased and did it faster than from that cycle until the end of the test (Fig. 2.8). However, the capacity did not go below the 70 % of the nominal capacity after 1000 cycles even if we were discharging faster than recommended by the manufacturer (2C instead of C/5). Concerning the delivered capacity at lower rates (C/25), the cells were still capable of delived the 90 % of the nominal capacity at the end of the test (Fig. 2.9). Moreover, capacity faded following two different tendencies at cycles after and before approximately 270 cycles. From this cycle on, the capacity fading followed a linear trend until the EoD.

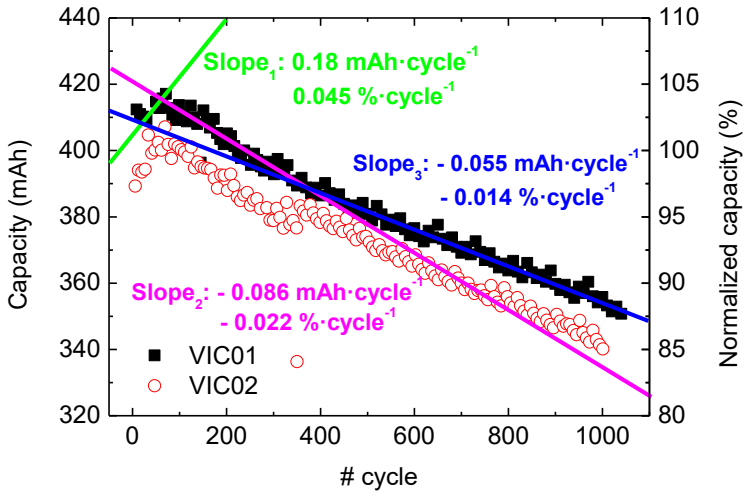

Fig. 2.8. Capacity evolution of the VIC cells (LFP) evaluated at a 2C discharge rate (in Ah on the left and as a percentage of the nominal capacity on the right). Some points have been skipped for clear representation.

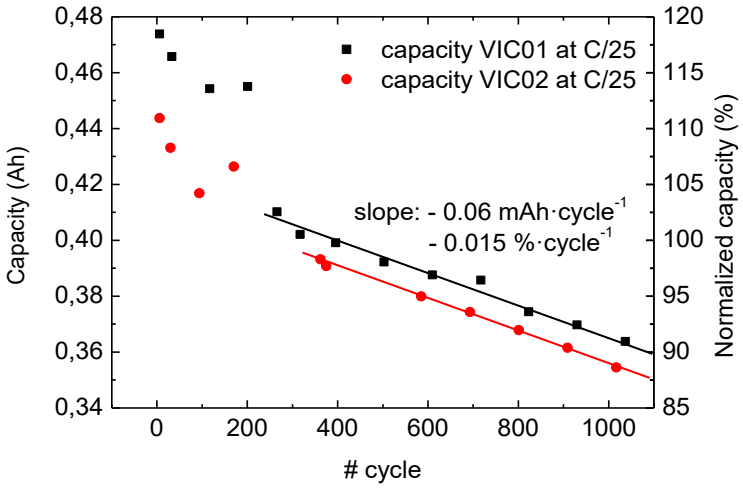

Fig. 2.9. Capacity evolution of the VIC cells (LFP) evaluated at a C/25 discharge rate (in Ah on the left and as a percentage of the nominal capacity on the right).

2.3.3.2. EVbat cells

The capacity at a C/25 discharge rate decreased as more cycles were carried out to the EVbat cells (Fig. 2.10). Moreover, a high voltage drop could be appreciated at the beginning of discharge, which indeed, seemed to not be affected by the aging level. In addition, the highest voltage plateau (around 3.32 V), was reduced at the EoL. Thus, being one of the major contributors to capacity fade at low rates.

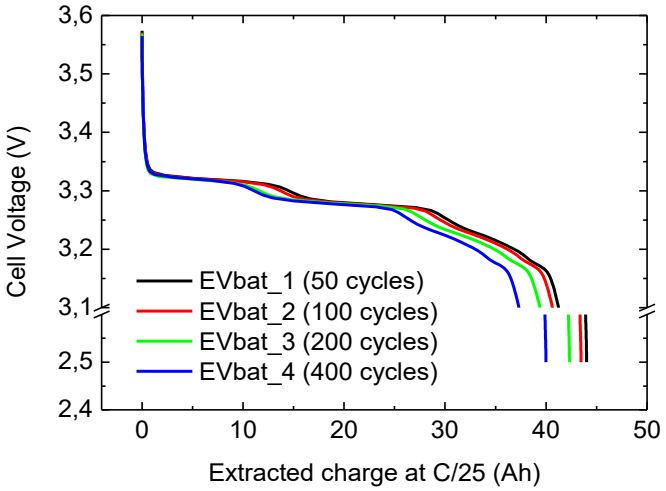

Fig. 2.10. Voltage profiles of EVbat cells (LFP) versus delivered capacity at a C/25 discharge rate at different aging levels. Discontinuity is due to the break for the sake of clarity in the representation.

The capacity evolution of EVbat cells at a 2.5C discharge rate showed an initial increase during the first 10 – 15 cycles (Fig. 2.11), as it happened in VIC cells (Fig. 2.8). Then, the capacity decreased at different rates during the aging process. In particular, three "regions" showed an approximated linear behavior with different slopes. In the first 75 cycles, the capacity decreased faster compared to

the rest of the test. From cycles 75 to 250, the decrease in capacity was slower than previously but faster than from cycles 250 to 400. Moreover, the capacity of those cells dropped below 80 % after 250 cycles although the cycle life of these cells was defined as 2000 cycles at 0.3C charge/discharge rates. Differences were expected from the specifications because discharge was done at 2.5C instead of 0.3C. From the results, it was clear that the increase in C-rate shorten battery life, in particular, ten times in our study. Although these cells are designed for operating at high discharge current pulses with a maximum amplitude of 10C (but only for ten seconds), the results suggested that continuous discharge at high rates could be severely degrading the cells. In addition, maximum allowed current by the manufacturer during charging process is 1C while we were charging the cells at 2.5C. Fast charging applied to batteries especially at high SoC levels highly reduces their cycle life [59]. Therefore, we associated the faster decrease of capacity to the fast charging process rather than to the discharge cycles.

Initial capacities of the cells and their evolution with aging were consistent for EVbat_1, EVbat_2 and EVbat_3. Conversely, EVbat_4 started the test showing up a much lower capacity. Even though EVbat_4 started the analysis with lower capacity, the normalized decrease in capacity was consistent for all the cells (Table 2.8).

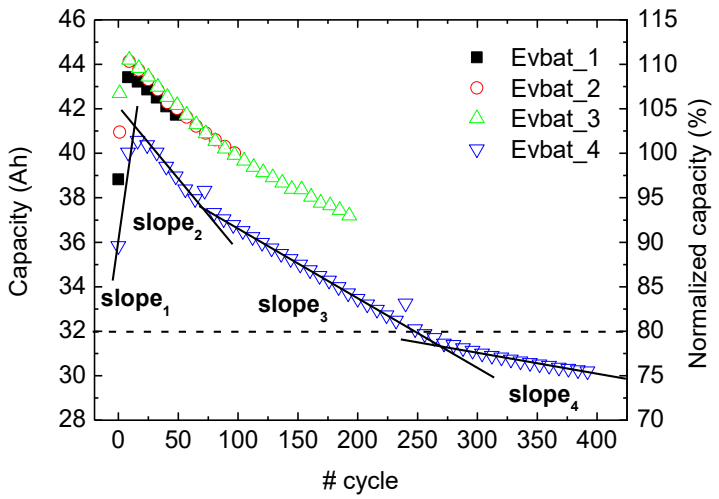

Fig. 2.11. Capacity evolution of the EVbat cells (LFP) evaluated at a 2.5C discharge rate rate (in Ah on the left and as a percentage of the nominal capacity on the right). Estimated slopes of the capacity fade at different aging levels were represented. Some points have been skipped for clear representation. Slope$_1$: 0.39 Ah·cycle^{-1} (0.97 %·cycle^{-1}), slope$_2$: - 0.066 Ah·cycle^{-1} (- 0.16 %·cycle^{-1}), slope$_3$: - 0.03 Ah·cycle^{-1} (- 0.08 %·cycle^{-1}) and slope$_4$: - 0.009 Ah·cycle^{-1} (- 0.02 %·cycle^{-1}).

Table 2.8. Capacity evolution of EVbat cells (LFP) during discharge at 2.5C. The decrease in capacity was calculated as the difference between the maximum capacity after initial cycles and the final capacity after the aging test.

Cell	Number of cycles	Initial capacity at cycle (Ah)	Maximum capacity (Ah)	Final capacity (Ah)	Decrease in capacity from maximum capacity (%)
EVbat_1	50	38.82	43.49	41.73	4.05
EVbat_2	100	40.86	44.18	39.94	9.60
EVbat_3	200	41.52	44.31	37.07	16.34
EVbat_4	400	35.84	40.58	30.18	25.63

2.3.4. LCO cells

LCO cells were cycled 150 times at 1C with a remaining capacity of the 80 % of the nominal capacity. Detailed data of the capacity evolution was not recorded during the test. Capacity was measured before the cycling process and after it.

2.4. Conclusions

- LGC2 cells showed better rate capabilities than VIC cells.
- Capacity depends on many parameters as temperature, SoH, charge/discharge rate or initial SoC. We evaluated the dependence of capacity on SoH and charge/discharge rates.
- The capacity of NMC cells at a 3C/2 discharge rate decreased at different rates during the aging test.
- VIC cells and EVbat cells (LFP) cells showed an initial increase of capacity from where capacity decreased linearly but at different rates.
- LCO were the first cells that were evaluated in this study. The importance of recording capacity evolution was not realized at that time, thus detailed data about the progress of capacity fade was not available.
- The validity of the results coming from EVbat_4 could not be assured.
- Cycle life of all the studied cells except EVbat cells, were in good agreement with the cycle life defined by the manufacturer. The faster decrease in capacity of EVbat cells was associated to the fast charging processes at which they were subjected.

Chapter 3

Impedance measurements

In this chapter we study the evolution of impedance with aging and SoC. A rough estimation of the resistive effects was carried out. The different contributors to resistance rise were analyzed and discussed. Moreover, we estimated the impedance of supercapacitors and cells by digital signal processing methods. The results were compared to impedance obtained by EIS with commercial devices.

3.1. Introduction

Resistance (R) is the opposition of a system to the flow of current (I) when a voltage drop (ΔV) is applied to it. Electrical resistance follows the Ohm's law and is defined for linear systems.

$$R = \frac{\Delta V}{I} \tag{3.1}$$

Resistance depends on the characteristics of the material and its shape. It is directly related to the material's resistivity (ρ), its length (l) and inversely proportional to the contact area (A).

$$R = \rho \cdot \frac{l}{A} \tag{3.2}$$

Impedance is a more general formulation of resistance in which not only resistive (dissipative) effects are considered, but also time-dependent effects such as electric field (capacitances) or

magnetic field (inductances) perturbations. Therefore, unlike resistance, impedance is a frequency-dependent parameter.

To measure impedance, an ac signal is applied as an excitation instead of the dc used for resistance. Impedance is defined in Linear Time-Invariant (LTI) systems. However, taking into account some particular considerations, impedance or resistance measurements can be done to non-linear systems [14] as it is the case of batteries. Impedance measurements can be performed by injecting either ac current or ac voltage signals [60]. The resulting output is equivalent to the transfer function of the system ($h(t)$) convolved with the input signal (ac current in that case) (Fig. 3.1).

$$v(t) = h(t) * i(t) \tag{3.3}$$

Impedance results inferred from Equation (3.3) are easily manipulated in the frequency domain instead of the time domain so that Fourier or Laplace transformations are usually applied.

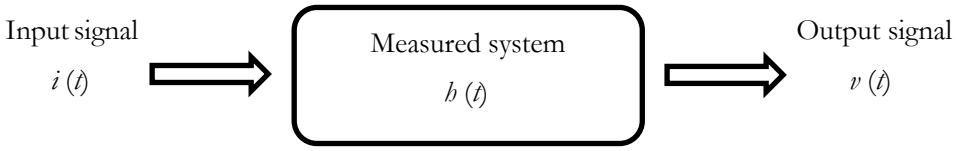

Fig. 3.1. Schematic diagram of the transfer function of a system when it is excited by an input signal and the output is measured.

When the input is a current excitation and the measured output is a voltage difference, the transfer function in the frequency domain and at steady state corresponds to the impedance $Z(jw)$, obtained from the ratio of the Fourier transformations of $v(t)$ and $i(t)$.

$$H(jw) = \frac{F\{v(t)\}}{F\{i(t)\}} = Z(jw) \tag{3.4}$$

3.1.1. Impedance Measurements

There are mainly three different types of electrical stimuli that can be applied for measuring impedance, which are commonly used. One of them is the application of a voltage step and measuring the corresponding transient current response. The ratio between voltage and current is usually referred as time-varying impedance and it is sometimes converted to the frequency domain through Laplace or Fourier transformations [60]. The second technique consists in applying a voltage signal composed of white noise to the sample and measure the current response [60]. Sometimes a sum of sinusoids with different frequencies is applied instead of white noise obtaining better signal-to-noise ratio for every single frequency. The main advantage of the aforementioned methods is that they can be performed in short periods of time but always at the expense of the quality of the signal due to

broadband non-linearities. Finally, the last one is the more time-consuming technique but gives the more accurate results. It consists in applying a small amplitude sinusoidal voltage or current signal at a single frequency and measuring the current or voltage response at this particular frequency [60]. Then, the frequency of the input signal is swept and the measurement has to be repeated until the desired frequency range is covered. This is the most commonly used impedance spectroscopy technique in the characterization of electrochemical systems. Thus, many commercial equipment ready for these measurements are available. Nevertheless, the other two techniques are commonly carried out by using methods of digital signal processing [61–63].

In our study, impedance was characterized both by electrochemical impedance spectroscopy (EIS) and by pulses through FFT transformations. Both techniques are explained in following subsections.

3.1.2. Electrochemical Impedance Spectroscopy (EIS)

Electrochemical Impedance Spectroscopy (EIS) is a non-invasive electrochemical technique used for characterizing electrochemical systems and materials. It measures the impedance of the system, which is directly related to the dielectric properties of a medium, as a function of frequency. It consists in applying an ac input signal at different frequencies and measuring the output response at each of those frequencies. Its particularity is that the applied signal has a very small amplitude, usually less than the thermal voltage, $V_T \equiv R \cdot T / F \equiv k \cdot T / e$, which is about 25 mV at 25 °C [64], in order to consider the system linear (Fig. 3.2) and, at the same time, to allow the measurement without perturbating or modifying the system itself.

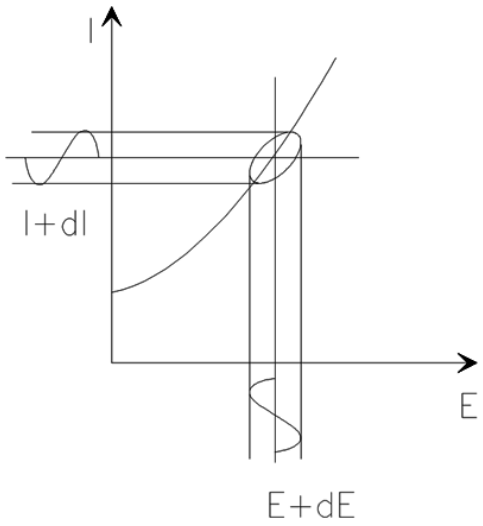

Fig. 3.2. Representation of pseudo-linear measurement of impedance [65].

A single frequency signal $v(t) = V_m \cdot \sin(wt)$ with frequency $f = w / 2\pi$ is applied to a cell and the steady state current $i(t) = I_m \cdot \sin(wt + \theta)$ is measured. θ is the phase difference between the voltage

and current and it is zero for purely resistive behavior (Fig. 3.3). The analysis of the response of the system to periodic voltage or current excitation is very complex in the time domain, usually requiring the solution of a system of differential equations. A significant simplification of the mathematical treatment of this system is achieved using Fourier transformations. Rearranging voltage to current relations in the frequency domain similar relations to dc Ohm's law are obtained (refer to equation (3.4)) [64].

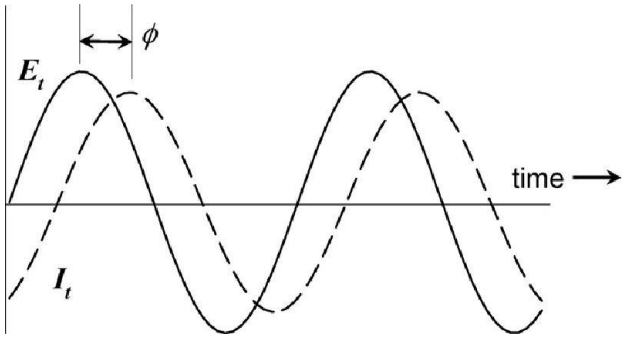

Fig. 3.3. Phase shift between applied voltage and measured current [66]**.**

As impedance $Z(w) = Z_{RE} + j\,Z_{IM}$ is a complex quantity it can be represented in either rectangular or polar coordinates. Rectangular coordinates are defined as:

$$\mathrm{Re}(Z) = Z_{RE} = |Z| \cdot \cos(\theta) \quad \textbf{(3.5)}$$

$$\mathrm{Im}(Z) = Z_{IM} = |Z| \cdot \sin(\theta) \quad \textbf{(3.6)}$$

Where the phase angle and the modulus correspond to:

$$\theta = \mathrm{atan}(Z_{IM} / Z_{RE}) \quad \textbf{(3.7)}$$

$$|Z| = \sqrt{(Z_{RE}^2 + Z_{IM}^2)} \quad \textbf{(3.8)}$$

Impedance can be represented in many different ways. In batteries-related areas the most commonly used are Bode and Nyquist plots. The main difference between them is that Bode plot gives explicit information about the frequency of the signal while Nyquist plot does it implicitly. Bode plot represents the modulus and the phase of the signal, separately while Nyquist plot is the representation in the complex plane of the signal (i.e. real and imaginary parts). Nyquist plots are widely used because they allow an easily comparison of the kinetic factors of the different signals. They show at a first sight, the values of the ohmic resistances and charge-transfer resistances. Sometimes, when working with full-cells and depending on the time constants of the different effects, these effects can be superimposed in a way they cannot be distinguished.

3.1.3. Impedance from pulses

As it was aforementioned, in order to measure the impedance of a system, other signals than sinusoidal can be considered [67]. Many other studies in which impedance spectra was obtained from other signals rather than sinusoidal can be found [61–63,68–70].

Then, whatever are the measured time domain voltages $v(t)$ and currents $i(t)$, impedance can be obtained from their Fourier transforms. For instance, if a square signal with voltage amplitude V_0 in the time range $0 < t < T_p$ and zero outside is considered, its transform bandwidth broadens according to a *sinc* function:

$$V(f) = V_0 \cdot T_p \cdot e^{-j\cdot\pi\cdot f\cdot T_p} \cdot sinc(f \cdot T_p) \quad \textbf{(3.9)}$$

where T_p (represented as τ in Fig. 3.4) determines the first zero crossing frequency: the smaller it is the broaden the main lobe is. Thus, one signal should have to be enough to determine the impedance of the whole system.

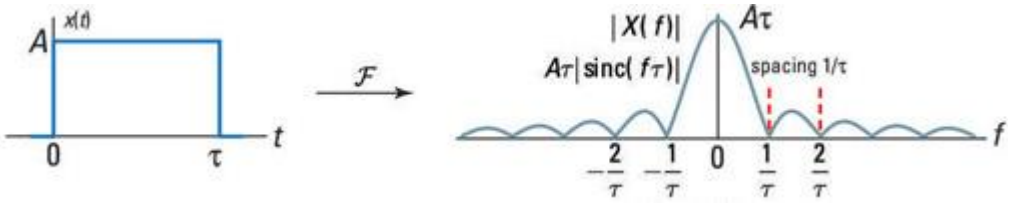

Fig. 3.4. Rectangular pulse in the time domain and its corresponding Fourier transform (sinc function) [71].

However, some considerations about the input signal are important. The frequency range in which the impedance can be obtained is determined at low frequencies by the total measurement time (T) and at high frequencies by the sampling period T_s. Thus, maximum frequency is limited by Nyquist criteria $f_{max} = 1/2T_s$ and $f_{min} = 1/T$. The spectrum of a square signal corresponds to a *sinc* function with zero amplitude values at $1/T_p$ frequencies. Therefore, T_p determines which frequencies can be measured. Moreover, it is also necessary to take into account the FFT limitations: windowing effects and low frequency leakage due to non-steady-state [72].

Signal to noise ratio (SNR) is estimated from the measurement variance σ^2 [73]:

$$SNR_V = \frac{|V|^2}{\sigma_v^2} \quad \textbf{(3.10)}$$

$$SNR_I = \frac{|I|^2}{\sigma_I^2} \quad \textbf{(3.11)}$$

$$SNR_Z = \frac{|Z|^2}{\sigma_z^2} \quad \textbf{(3.12)}$$

Where

$$\sigma_z^2 = |Z|^2 \cdot \left(\frac{1}{SNR_I} + \frac{1}{SNR_V} - 2 \cdot Re\left(\frac{\sigma_{VI}^2}{IV^*} \right) \right) \quad \textbf{(3.13)}$$

Where σ_{VI}^2 represents the covariance of V and I [73].

3.1.4. Parameters measured in Li-ion batteries by EIS

One of the advantages of using impedance spectroscopy technique is that the electrical and electrochemical processes can be modelled by electrical circuits. Thus, the following parameters can be modelled by electronic components.

Ohmic resistance (conduction)

When a current flows through a cell, there are ohmic losses associated to the electronic resistance of electrode particles and current collectors, connections between the cell and the instrument (electronic conduction) and the electrolyte (ionic conduction) [74]. The part of the resistance associated to external contacts do not truly correspond to the battery we want to measure. Therefore, appropriate connections and holders have to be selected in order to minimize those contributions. The desired resistances to be measured are those produced by ionic conduction at the electrolyte and electronic conduction at the electrodes and current collectors. In particular, the resistance of an ionic solution depends on the ionic concentration, type of ions, temperature, and the geometry of the area in which current is carried [75].

Charge-transfer resistance (electrochemical reaction)

The intercalation of ions on the surface of the electrode results in a faradaic charge-transfer reaction. In that case, electrical energy is stored electrochemically. In particular, charge transfer resistance represents the speed at which the kinetically-controlled electrochemical reaction takes place. At the same time, the speed of the reaction depends on the kind of reaction, the temperature, the concentration of the reaction products and the potential [75].

Double layer capacitance

At the interface between the electrodes and their surrounding electrolyte an electrical double layer exists. Hermann von Helmotz realized that two layers of opposite polarity form at the interface between electrode and electrolyte (Fig. 3.5) [76]. He demonstrated that this layer behaves as a molecular dielectric and stores charge electrostatically. The double layer mainly depends on the electrode potential, temperature, ionic concentrations, types of ions, oxide layers, electrode roughness, and impurity adsorption [75].

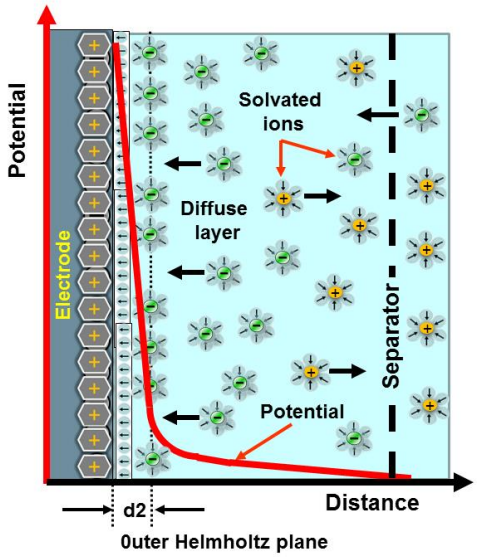

Fig. 3.5. Interface layer between the electrode and the electrolyte [77].

Mass-transfer resistance (diffusion)

Diffusion is a transport mechanisms of the ions in Li-ion (mass-transfer effect) batteries and it occurs due to the presence of gradients [78]. Those gradients can be caused by concentration differences, temperature differences or potential differences. Moreover, diffusion can occur in both liquid and solid phases. In particular, solid-state diffusion represents the diffusion of the ions inside the particles forming the active material and the diffusion at the liquid phase represents the transport of ions in the electrolyte [78]. Different Warburg elements are commonly used to describe diffusion in electrical models [79]. In particular, the real part of the diffusional branch measured in Li-ion batteries at the lower frequencies is termed as mass-transfer resistance.

3.2. Materials and methods

3.2.1. Impedance by EIS

EIS measurements can be carried out galvanostatically or potentiostatically. Each of them is appropriate for a particular situation. In the case of Li-ion cells, in which the voltage can change during the test, it is more convenient to do it in galvanostatic mode [80,81].

Impedance measurements of LGC2 and VIC cells were started during a research stay at HNEI in Hawaii (USA). The complete study of LGC2 cells was carried out during this period in which the impedance was measured with a VMP potentiostat/galvanostat from Bio-logic. Nevertheless, VIC cells were first measured with the VMP potentiostat during the research stay (around 300 cycles) and then, once back to our laboratory, with a VSP potentiostat/galvanostat from Bio-logic. LGC2 and VIC cells were measured by injecting a current signal and measuring the change in voltage. Impedance was measured approximately every 50 cycles for LGC2 cells and every 100 cycles for VIC cells.

In addition, EVbat cells were also measured with the VSP potentiostat in our laboratory. In that case, an ac voltage signal was injected to the cells and the response in current was monitored. Impedance was measured at the beginning of life and at the end of life of each of the four evaluated cells. Therefore, impedance measurements were carried out after 50, 100, 200 and 400 cycles.

Due to the fact that LCO cells were measured at the first stages of this study, before our laboratory was fully equipped, impedance measurements were carried out at IREC that is a research institute placed in Barcelona. The potentiostat employed in this period was Parstat 2273 provided by Princeton Applied Research. Impedance of LCO cells was measured at BoL and EoL (with a remaining capacity of 80 % after 150 cycles).

The main parameters that were set for EIS measurements and their periodicity were summarized in Table 3.1.

Table 3.1. Definition of the parameters for measuring impedance by EIS technique.

Cell	Excitation signal	Amplitude	Frequency range	Periodicity
LGC2 (NMC)	Current	50 mA	3 mHz to 5 kHz	Every 50 cycles
VIC (LFP)	Current	20 mA	10 mHz to 3 kHz	Every 100 cycles
EVbat (LFP)	Voltage	2 mV	3 mHz to 5 kHz	After 50, 100, 200 and 400 cycles
Microbattery (LCO)	-	-	4 mHz to 1 kHz	After 0 cycles and 150 cycles

3.2.1.1. Definition of resistance contributions

A typical impedance spectrum of Li-ion batteries is represented in Fig. 3.6. In addition, typical characteristic frequencies of the different transport effects and electrochemical processes taking place in the cells, which are represented in the impedance spectra, are summarized in Fig. 3.7. At high frequencies, there is an inductive tail mainly caused by the measurement cables and connections. Furthermore, apart from the cables and connections, it is also associated to the number of windings of the electrodes in the jellyroll in the particular case of cylindrical cells [82]. The point at which this inductive tail crosses the zero at the imaginary part, has been considered as an approximation of the ohmic resistance (R_Ω). Actually, for being precise, ohmic resistance should also include SEI-layer resistance, and the resistance associated to contacts between electrodes and current collectors (refer to subsection 3.1.4). However, in this study, they were not included in the ohmic contribution because, as they have a capacitive effect associated to them, they appear at the impedance spectra as

semicircles instead of simple resistive contributions. Therefore, as they were overlapped with charge-transfer effects and no model was fitted, it was not possible to distinguish them.

At medium frequencies, one semicircle (or more than one depending on the cell, temperature, SoC or aging level) was found. It can represent many different effects depending on its nature and origin but it is always represented by a resistive effect and a capacitive effect associated to it. The resistive effect, which is represented by the real part covered by the semicircles, represents the kinetics of the measured electrochemical process. The imaginary part represents the double-layer capacitance explained in subsection 3.1.4. In this study, only the variation with aging of the resistive part was considered. In particular, all the real part covered by the semicircles is termed as charge-transfer (CT) resistance in this study (R_{CT}). Unfortunately, there are ohmic contributions (different than CT), which not only contribute as pure resistive affects but also have a capacitive effect associated to them (they show up at the impedance spectra as a semicircle). Those ohmic contributions may arise from contact resistance, SEI-film or carbon coating [83]. Thus, their associated capacitive effect comes from the accumulation of charge at these interfaces. In this study, these contributions were not separated, thus being considered as part of the charge-transfer resistance.

At the low frequencies (until reaching the lowest measured frequency), there is a diffusional branch related to mass-transfer effects (MT), labeled as R_{MT}. The shape and the phase associated to this effect can vary depending on many factors as the SoC, the aging level, or the temperature. The capacitive effect associated to the diffusional branch tends to dominate as the frequency decreases and is related to the restricted diffusion especially at the EoD [79]. Finally, in some cases, R_{CT} and R_{MT} were grouped and labeled as $R_{CT} + R_{MT}$.

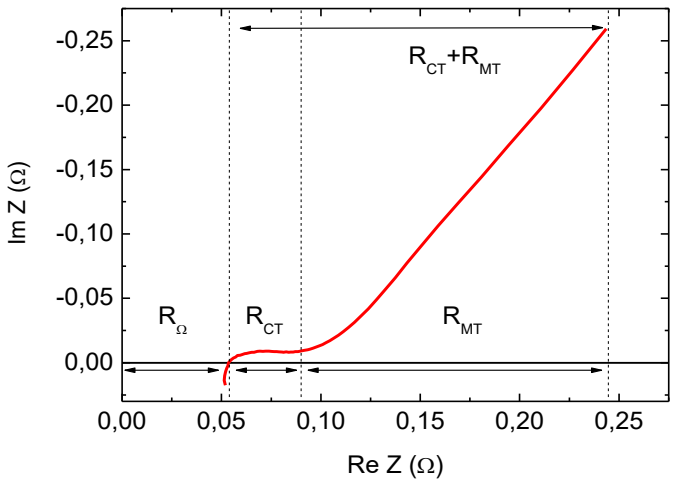

Fig. 3.6. Definition of different resistance contributions.

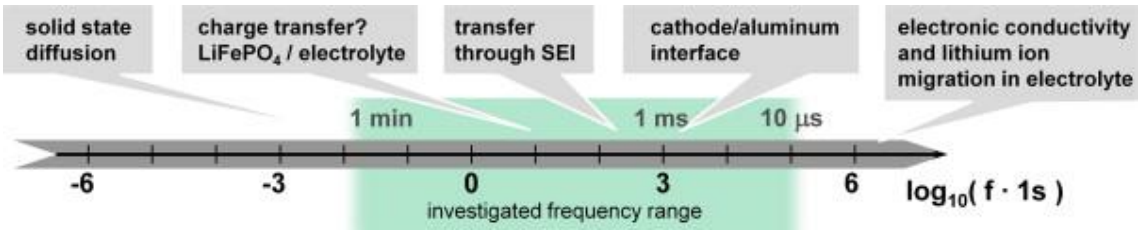

Fig. 3.7. Typical time constants (or characteristic frequencies) of the transport effects and electrochemical processes occurring in a LFP cell [84]**.**

Charge-transfer resistance was obtained by two different methods. In the first one, it was directly obtained from the radius of the resulting semicircles at the Nyquist representation of impedance. The second method was based on the reference tests carried out periodically during cycling. Charge-transfer resistance was obtained from the overvoltage obtained at least at three different low charge/discharge rates that assured to be working at the linear regime of Tafel behavior. Specifically, charge-transfer resistance corresponds to the slope of the overvoltage variation with respect to the charge/discharge current, according to equation (1.5) (for more information, refer to subsection 2.2.2). It must be taken into account that results obtained from this last method also included the ohmic drop, resulting in the joint contribution of ohmic and charge-transfer resistances.

3.2.2. Impedance from current pulses

One of the aims of the dissertation was to develop a methodology to measure SoH online during the battery operation. Because sinusoidal signals are not currently available during battery operation, we attempteded to measure impedance using squared signals, which are commonly used to charge/discharge the cells. For analysis simplicity, first essays were performed on 1 F Panasonic supercapacitors, which were composed of activated charcoal having a nominal voltage of 5.5 V. Supercapacitors were charged and discharged at constant current or by pulses (for further information refer to [72]). Data was monitored with an Agilent 34970A data acquisition system at a sampling rate of 2 s.

Charge/discharge current and voltage profiles were transformed into the frequency domain in order to get information about the impedance of the supercapacitors, according to equation (3.4). The transformations were done with FFT routines provided in either Matlab or Pspice. We carefully selected the total measurement time of voltage and current signals and the sampling period to operate in the defined impedance frequency range (refer to subchapter 3.1.3). Moreover, in order to evaluate the quality of the results, SNR was calculated for the resulting impedance according to equations (3.12) and (3.13).

The method was extended to battery impedance of a LCO cell (Microbattery). Its impedance was obtained from its response to an impulse signal. The advantage of injecting a very short pulse is that the main lobe of its Fourier transformation spreads to a wide frequency range (around 1 Hz) and it is almost flat in that range. No windowing was used in this analysis.

In order to validate the results, impedance was measured in both cases with Parstat 2273 potentiostat (Princeton Applied Research) with a frequency response analyzer unit.

3.3. Results

3.3.1. Impedance from EIS measurements

3.3.1.1.NMC cells

The evolution of impedance with the SoC, represented in Nyquist diagram in Fig. 3.8, was composed of two semicircles, a pure ohmic effect at high frequencies and a diffusional branch at low frequencies. However, the two semicircles were not clearly distinguishable in all the evaluated SoCs at BoL because their characteristic frequencies were as similar one to the other that they were overlapped in frequency. The tendency of both the fresh and the aged cells was an increase of impedance towards the EoD, especially the impedance related to the lowest frequency semicircle.

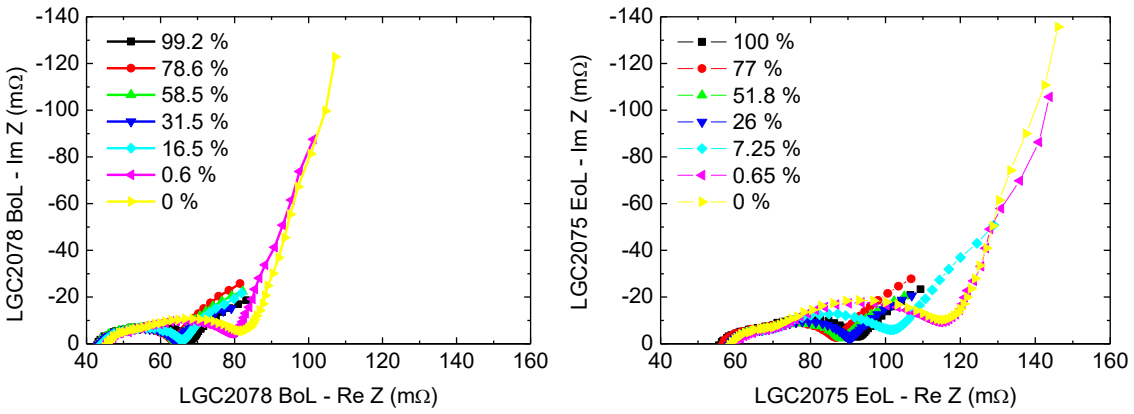

Fig. 3.8. Nyquist representation of impedance evolution with SoC of a LGC2078 fresh NMC cell (left) and LGC2075 degraded NMC cell (right). A zoom of this impedance at BoL and EoL is depicted in Fig. 3.9 and Fig. 3.10, respectively.

Impedance of the fresh cell showed one semicircle in the Nyquist representation except at very low SoCs, where two semicircles could be appreciated (Fig. 3.9). Nevertheless, in the case of the degraded cell, the two effects were clearly distinguishable even when the cell was fully charged (Fig. 3.10). Ohmic resistance (R_Ω) at BoL and EoL, which was defined as the intersection of the impedance curve with the real-axis (refer to section 3.2.1.1), was roughly constant in all the SoC range (it increased around 5 % between SoC = 100 % and SoC = 0 %), as illustrated in Fig. 3.9. Charge-transfer resistance (R_{CT}) slightly decreased at beginning of discharge, and then remained almost constant at the intermediate SoCs and finally increased towards the end of discharge. The same behavior was found at BoL and EoL. In literature, charge-transfer resistance was found to follow the same trend [85]. Moreover, although the contribution of the different charge-transfer effects were

not quantified separately, it was clear to the eye that the semicircle at higher frequencies was almost independent of SoC but, conversely, the effect at lower frequencies was strongly dependent on it.

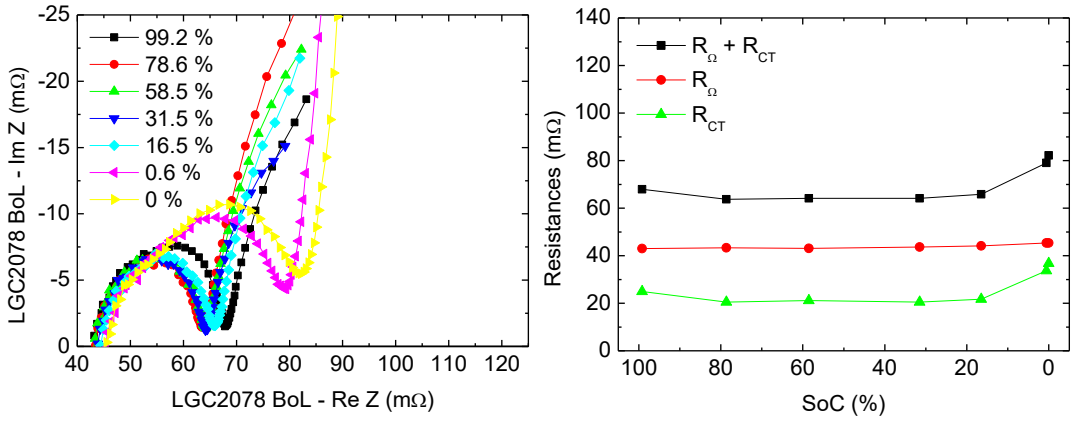

Fig. 3.9. Zoom of Nyquist representation of impedance evolution with the SoC of a fresh NMC (LGC2078) cell (on the left) and dependency on SoC of the total resistance (R_Ω + R_{CT}), charge-transfer resistance (R_{CT}) and ohmic resistance (R_Ω) (on the right).

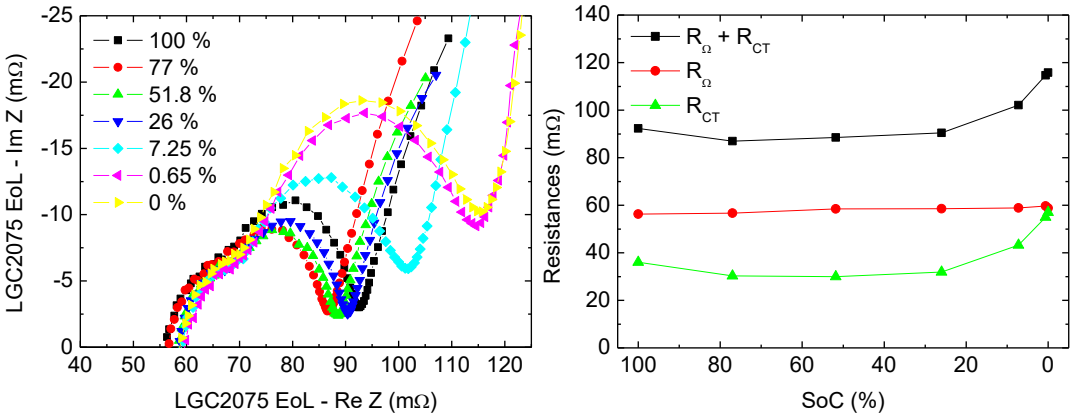

Fig. 3.10. Zoom of Nyquist representation of impedance evolution with SoC of a degraded NMC (LGC2075) cell (on the left) and dependency on SoC of the total resistance (R_Ω + R_{CT}), charge-transfer resistance (R_{CT}) and ohmic resistance (R_Ω) (on the right).

The absolute increase of ohmic and charge-transfer resistances from BoL to EoL (calculated as the difference between the resistance at the EoL and the resistance at BoL) was not constant in all SoCs (left part of Fig. 3.11). Ohmic resistance increased more at intermediate SoCs where the increase in charge-transfer resistance was lower. Moreover, the absolute increase of ohmic resistance was higher except at SoCs below 20 %, where it was higher for the charge-transfer resistance. Concerning the relative increase, it was found to be higher for the charge-transfer resistance in all SoC range (right part of Fig. 3.11).

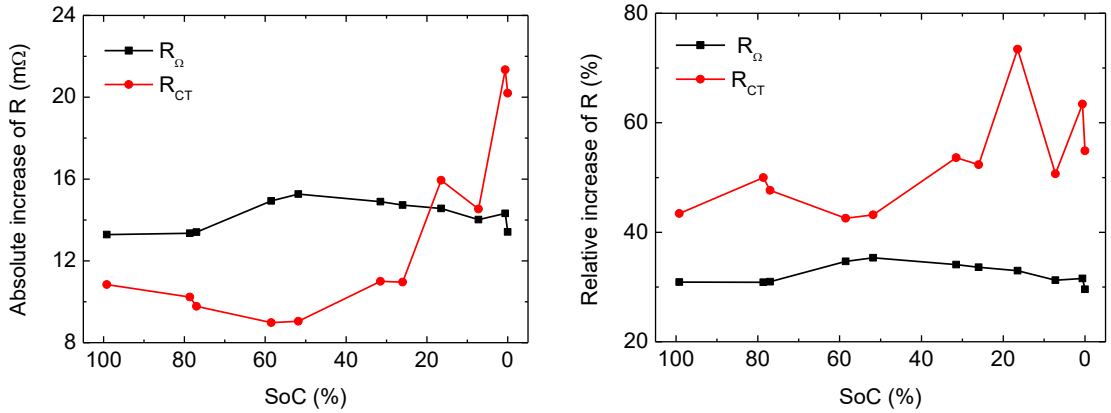

Fig. 3.11. (left) Absolute and relative (right) increases of ohmic and charge-transfer resistances of LGC2075 cell (NMC) from BoL to EoL.

Impedances of fully charged NMC cells at different degradation levels were plotted in Fig. 3.12. At the beginning of life, only one semicircle was appreciated at SoC = 100 % but it separated into two identifiable effects as long as the cell aged. Although the resistances of those effects were not estimated separately, it was clearly seen that the more affected semicircle due to cycle aging was the one at lower frequencies. The characteristic frequency of this effect after 335 cycles was around 7.75 Hz (Fig. 3.12).

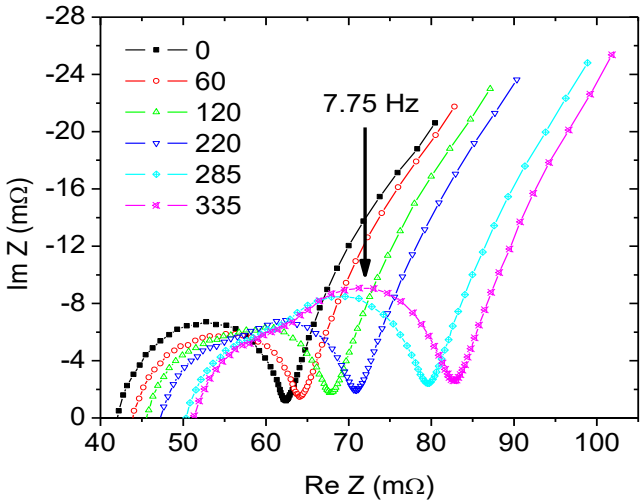

Fig. 3.12. Nyquist representation of LGC2074 cell's impedance at SoC = 100 % after 60, 120, 220, 285 and 335 cycles at a 1.5C discharge rate.

Ohmic resistance increased linearly for the three evaluated NMC cells with comparable slopes (0.028 mΩ·cycle^{-1}) (Fig. 3.13). With respect to charge-transfer resistance, it was obtained by the two considered methods: from the radius of the semicircle of the Nyquist representation of impedance (right part of Fig. 3.13) and from the slope of the overpotential produced at three different charge/discharge rates (Fig. 3.14). An example of the polarization curve from which charge-transfer resistance was calculated from the measured overvoltages was plotted in Fig. 3.15. As mentioned

previously, the resistance obtained from overvoltage measurements (represented in the left side of Fig. 3.14) also included the ohmic resistance effect. Thus, in order to be able to compare charge-transfer resistance obtained by the two methods, the ohmic contribution (estimated from impedance measurements) was subtracted from the resistance estimated from the V-I polarization curve (right side of Fig. 3.14). As it can be seen, comparable results were obtained by the two methods (right sides of Fig. 3.13 and Fig. 3.14). In particular, it could be appreciated that charge-transfer resistance increased more slowly during the first 100 – 150 cycles and then started increasing faster until the end of the cycling test. Similar values and the same trend in charge-transfer resistance with aging were found with both measurements methods.

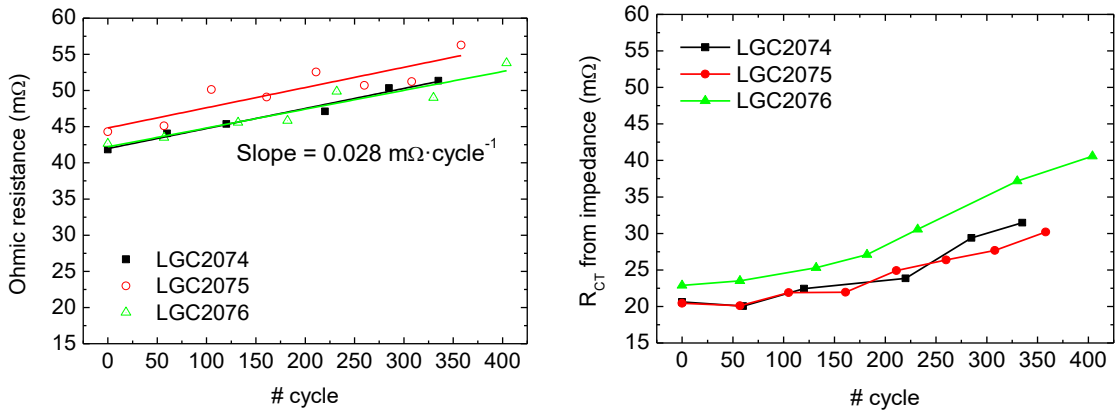

Fig. 3.13. (left) Ohmic and (right) charge-transfer resistances evolution with aging of three LGC2 (NMC) cells at SoC = 100 % obtained by impedance spectroscopy.

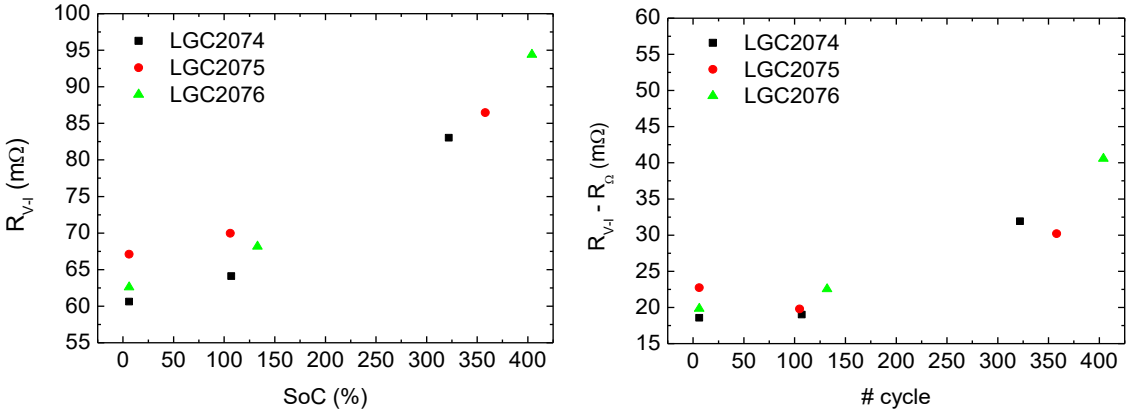

Fig. 3.14. (left) Charge-transfer resistance ($R_{V\text{-}I}$ in that case) of three LGC2 (NMC) cells at SoC = 100 % obtained from the overpotential generated at different discharge rates (C/25, C/5 and 1C) (V-I polarization curve). It has to be noted that the measurement was also affected by ohmic conduction, thus resulting as the joint contribution of both ohmic and charge-transfer resistances. In the right part, the ohmic contribution represented in Fig. 3.13 was subtracted in order to compare the charge-transfer resistance obtained by the two methods.

In the polarization curves, we noticed, on the one hand, that the overpotential at zero current did not tend to zero in any case (Fig. 3.15). On the other hand, the curves at zero current got different

values during charge and discharge. Thus, these effects might indicate hysteresis between the OCV curves obtained during charge and discharge [86]. A further analysis and explanation will be given in Chapter 4.

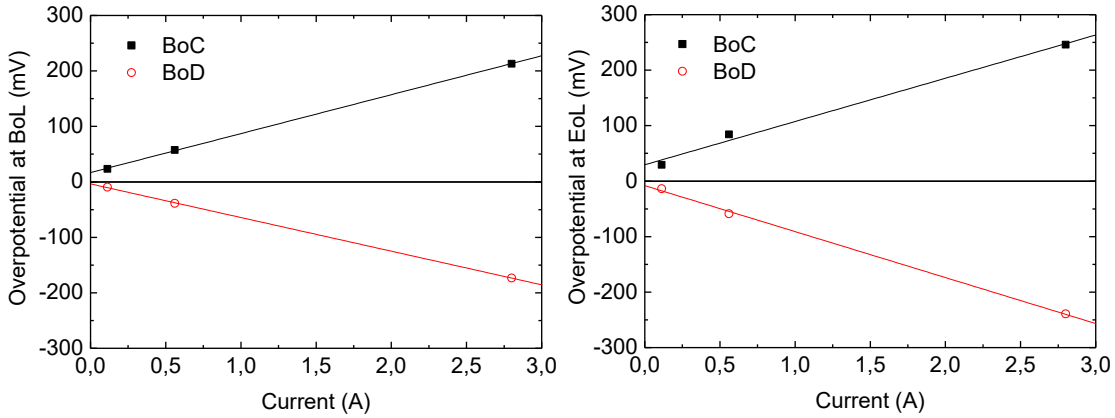

Fig. 3.15. Polarization curve of a fresh LGC2074 cell (NMC) (left) and of the same cell after 325 cycles (right) obtained at C/25, C/5 and 1C charge/discharge rates.

In the first 50 – 75 cycles, charge-transfer resistance decreased whereas the ohmic contribution increased (Fig. 3.16). From this cycle on and until cycles 150 – 200 were reached, the relative increases of ohmic and charge-transfer resistances at SoC = 100 % were comparable and followed a linear tendency. At this point, charge-transfer resistance started to increase faster than the ohmic effect did (which continued following the same linear tendency unlike charge-transfer resistance). From these results, it might be inferred that different degradation mechanisms were taking place at these various stages. Further analysis and possible causes will be discussed in subsection 3.4.

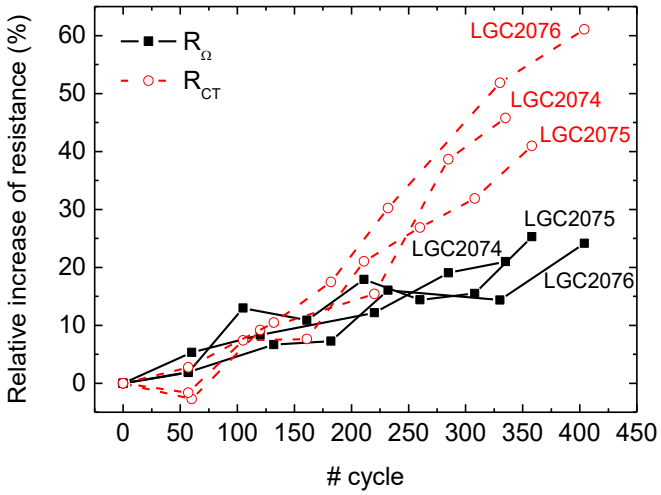

Fig. 3.16. Relative increases of ohmic and polarization resistances at SoC = 100 % during the cycle aging process of the three NMC cells.

3.3.1.2.LFP cells

3.3.1.2.1. VIC cells

Nyquist representation of impedance of VIC cells was illustrated in Fig. 3.17. In this figure, ohmic resistance was subtracted because cells were measured with different holders and setups, and thus, the comparison of ohmic resistances of VIC cells was not possible. However, during the first part of cycling the same holder was used for the impedance measurements making the results comparable at this first stage. Ohmic resistance evolution during these initial cycles was plotted in left part of Fig. 3.18. It underwent a fast increase during the initial 50 cycles and then the increase was moderated. Concerning charge-transfer resistance, it appeared as a single semicircle in the Nyquist representation at BoL, which decreased after the first initial cycles. Then, it remained almost constant until some point between cycles 300 and 400 from which a second effect was distinguishable at low frequencies.

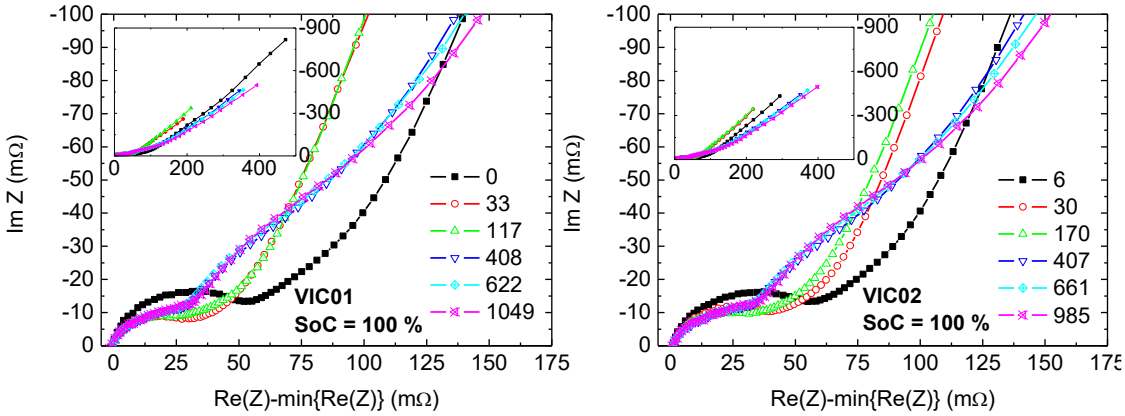

Fig. 3.17. Nyquist representation of two VIC cells (LFP) impedance at SoC = 100 % after being subjected to different number of cycles. Serial resistance contribution was subtracted and only the more representative cycles were represented. At the inset, full spectra of the VIC cells at SoC = 100 %.

A quantitative estimation of the charge-transfer resistance during the cycle aging process was not carried out because no model was fit to the impedance spectra and it was not clear to the eye where the semicircles would cross the real axis. However, in order to track the evolution of impedance, the maximum resistance in the studied frequency range was defined as the addition of R_{CT} and R_{MT} (refer to subchapter 3.2.1.1) and it was represented in the right part of Fig. 3.18. It suffered a high decrease during the first 30 cycles and then it remained almost constant until the transition between cycle 300 and 400 where a sudden increase occurred. From that point until the end of the test, the resistance increased gradually.

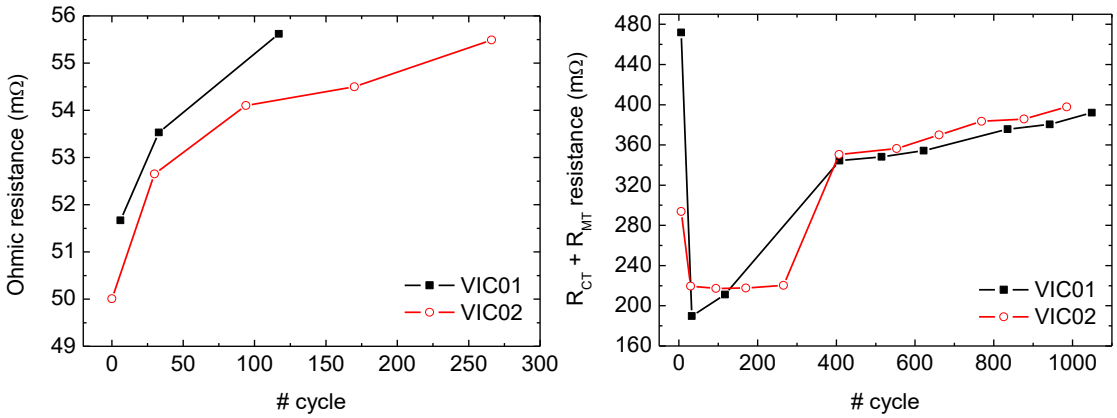

Fig. 3.18. (left) Ohmic resistance (R_Ω) evolution during the first cycles where the employed holder allowed the comparison of the data. (right) Total resistance evolution represented as the addition of charge-transfer and mass-transfer resistances. Lines were only drown as a guide to the eye.

In addition, charge-transfer resistance obtained from the overvoltage produced at three different rates obtained from the characterization cycles was not comparable for these cells because the ohmic resistive effect, which was also included in the measurement, was not consistent during the test due to the lack of an appropriate holder. Although data were not comparable, it was depicted in Fig. 3.19 an example of how the charge-transfer resistance was calculated from its polarization curve. Charge and discharge overvoltage curves were expected to cross the y-axis at the same point but measurements followed different tendencies for charge and discharge processes what could be related to hysteresis. Further analysis will be carried out in Chapter 4.

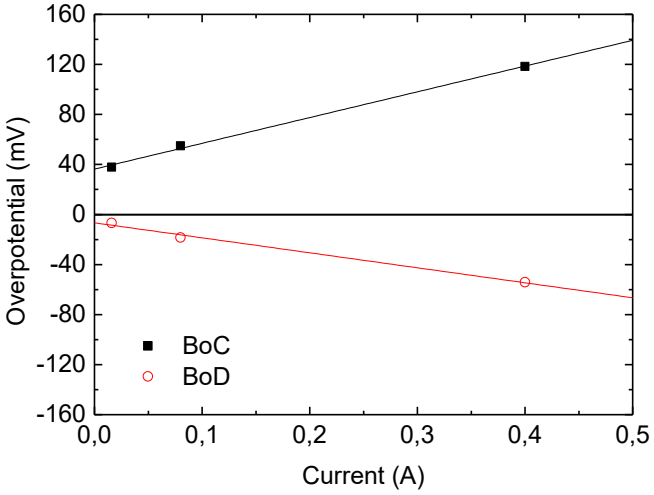

Fig. 3.19. Charge-transfer resistance of VIC01 cell (LFP) at BoL obtained from the slope of the overvoltage produced at C/25, C/5 and 1C charge/discharge rates.

3.3.1.2.2. EVbat cells

EVbat cells were the first cells evaluated in this study. In addition, we were not able to cycle them in our facilities because they were high capacity cells. Thus, they were sent to an external center in

which they were set to different SoHs. Therefore, it implied that we had no control in the cycling tests and we had to assume there were no cell-to-cell variations. The interpretation of the results was very challenging with the knowledge of batteries at that time. Moreover, these cells are composed of LFP positive electrode what even complicated more the analysis. Nowadays, we already know that the impedance of LFP cells related to charge-transfer effects sometimes decreases during the aging tests. However, during the first analysis, it was very difficult to give an explanation of the results. Nevertheless, the importance of evaluating the variations between cells and the different behavior of LFP cells compared to other positive electrodes of Li-ion cells were realized from this analysis.

In particular, the impedance of EVbat cells showed a unique semicircle and a diffusional effect at low frequencies (left part of Fig. 3.20). Resistances as a function of SoC showed a tendency to increase towards the EoD (right part of Fig. 3.20). In particular, ohmic resistance increased faster at both BoD and EoD than what it did at central SoCs, where it only suffered a slight increase. Nevertheless, charge-transfer resistance decreased from SoC = 100 % until approximately 80 %. Then, it increased until SoC = 30 % decreasing again until the last part of discharge where it drastically increased until the EoD.

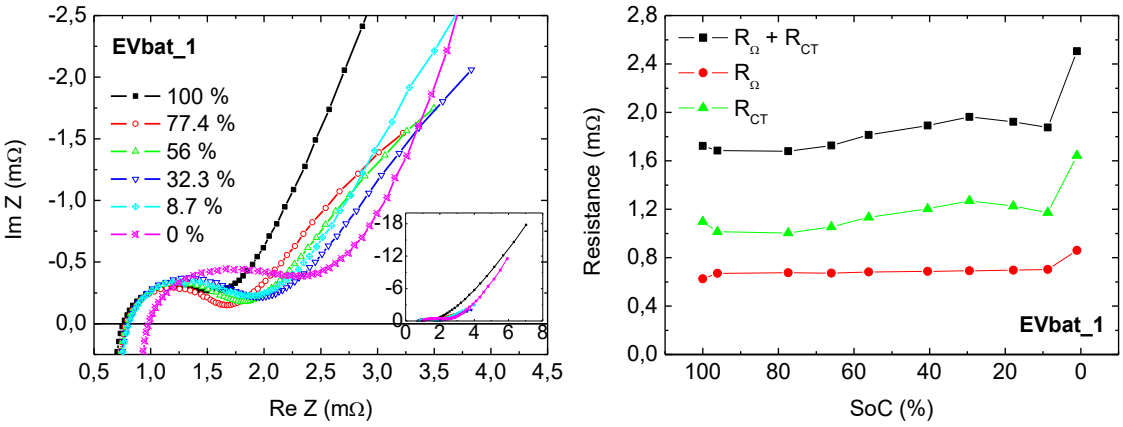

Fig. 3.20. (Left) Nyquist representation of EVbat_1 cell (LFP) impedance at different states-of-charge. The cell was cycled 50 times at a 2.5C charge/discharge rate at ambient temperature. (Right) Ohmic, charge-transfer and total resistances evolution with SoC.

The trend of ohmic and charge-transfer resistances was the same for all cells independently of their degradation level (Fig. 3.21). Regarding ohmic resistance and SoH, it followed the expected evolution for cells EVbat_1, EVbat_2 and EVbat_3 where resistance was higher for the more cycled cells. Nevertheless, ohmic resistance of EVbat_4, which was the one with more cycles, was smaller than the rest of the cells. Therefore, it did not follow the expected tendency with SoH. As for the charge-transfer resistance, the results showed a decrease in resistance from EVbat_1 to EVbat_2 but there were not many differences between EVbat_2 and EVbat_3. Furthermore, in the case of EVbat_1, EVbat_2 and EVbat_4, polarization resistance was higher than serial resistance. In

contrast, serial resistance of EVbat_3 had increased that much that had surpassed the charge-transfer resistance.

The addition of ohmic and charge-transfer resistances leaded to total resistance represented in bottom part of Fig. 3.21. Total resistance of EVbat_1 cell was slightly higher than that of EVbat_2. Moreover, EVbat_3 was the one showing the highest total resistance and EVbat_4 the lowest one. The absolute increase of ohmic resistance from cycles 50th to 200th was around 0.3 – 0.35 mΩ (representing an increase of around 50 %) whereas charge-transfer resistance decreased in approximately 0.2 mΩ (a decrease of around 20 %) (Fig. 3.22). Thus, yielding to a total resistance increase of approximately 0.125 mΩ.

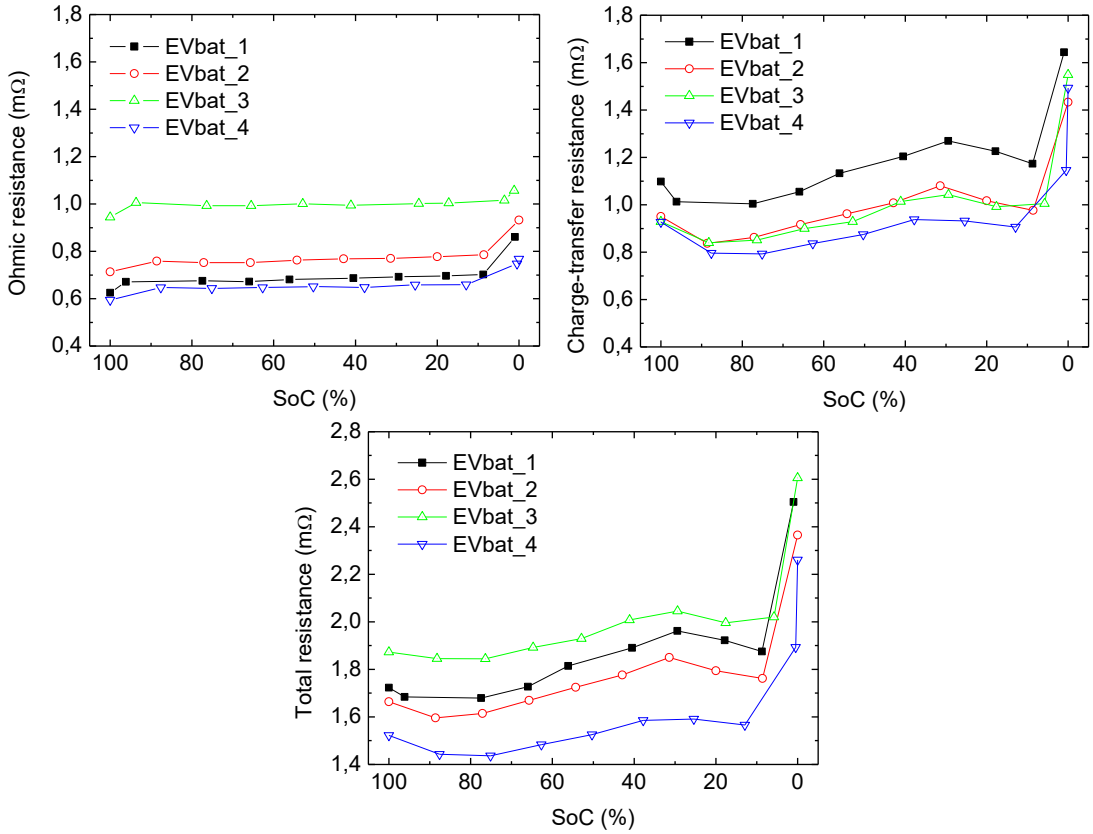

Fig. 3.21. Ohmic resistance (top – left), charge-transfer resistance (top – right) and total resistance calculated as the addition of ohmic and charge-transfer resistances (bottom) evolution with SoC of four EVbat cells (LFP) that were set to different degradation levels.

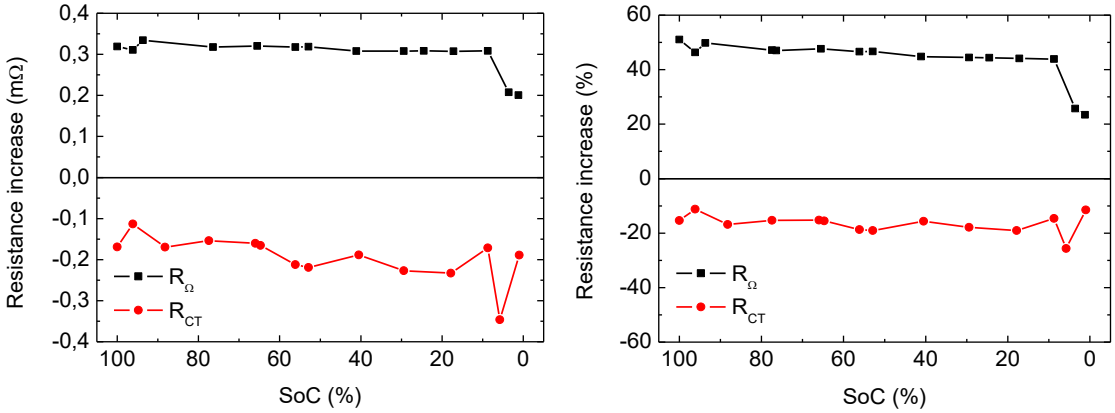

Fig. 3.22. (left) Absolute and relative (right) increases of ohmic and charge-transfer resistances of the EVbat cells (LFP) from cycles 50th (EVbat_1) to 200th (EVbat_3).

The impedance of the cells, at the particular SoC = 100 %, showed an increase of ohmic resistance except in the case of EVbat_4 and a general decrease in charge-transfer resistance (Fig. 3.23). In particular, the evolution of ohmic and charge-transfer resistances with the aging level was represented in Fig. 3.24. No data was available from the fresh cells so the results were plotted starting from cycle 50. Ohmic resistance increased between 50th and 200th cycles. In contrast, charge-transfer resistance decreased during the aging test and it did it faster between cycles 50 and 100 than during the last part of the test. Thus, producing a decrease of total resistance from cycles 50 to 100 (bottom part in Fig. 3.24).

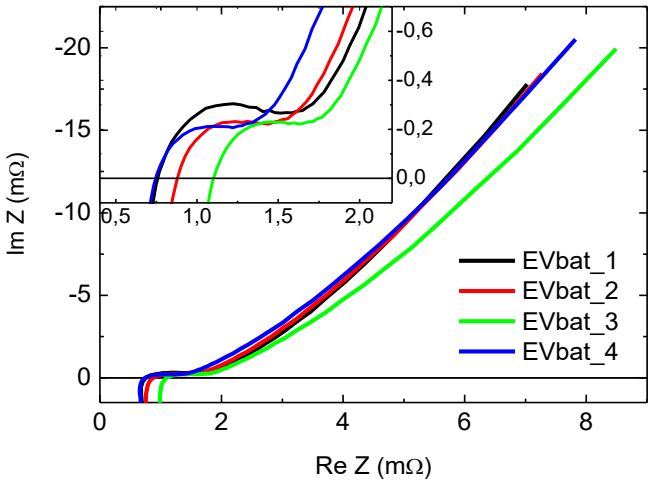

Fig. 3.23. Impedance evolution at SoC = 100 % of four EVbat cells (LFP) which were previously cycled 50, 100, 200 and 400 times.

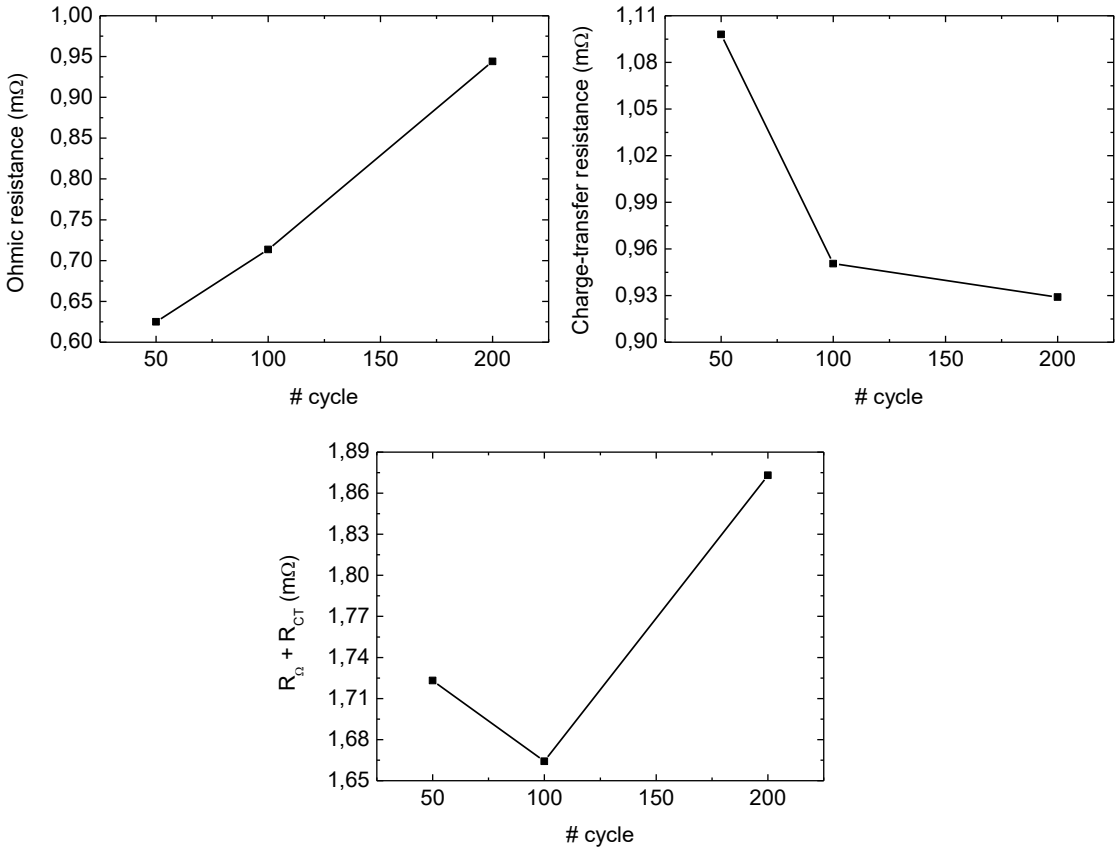

Fig. 3.24. Ohmic (top-left), charge-transfer (top-right) and total (bottom) resistances of EVbat cells (LFP) at SoC = 100 % previously set to different degradation levels.

3.3.1.3.LCO cells

At the impedance spectra of the Fresh Microbattery, one semicircle was appreciated except at SoCs below 7 % where two effects were distinguishable (Fig. 3.25). However, at the impedance spectra of the Old Microbattery, two semicircles could be easily identified in all SoCs (Fig. 3.26). Both ohmic and charge-transfer resistances followed the same tendency at BoL and EoL. Ohmic resistance slightly increased as the SoC was decreased. Nevertheless, charge-transfer resistance decreased in the first 20 % of discharge and then increased faster as the EoD was approached. In particular, concerning the charge-transfer resistance, the semicircle at lower frequencies was strongly dependent on SoC while the one at higher frequencies was found to be independent of it. In addition, the dependency on SoC of the charge-transfer resistance was more pronounced at the EoL.

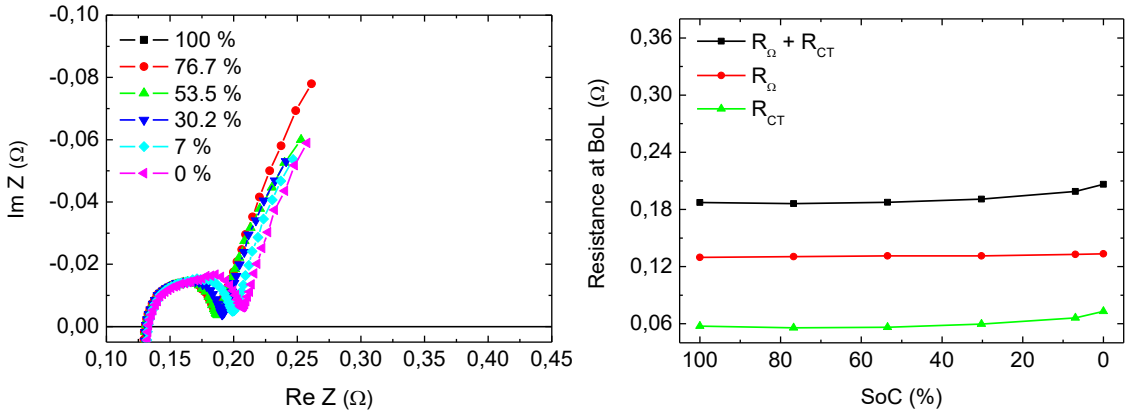

Fig. 3.25. Impedance evolution of the Fresh Microbattery with SoC. On the right side, serial and polarization resistances evolution with SoC.

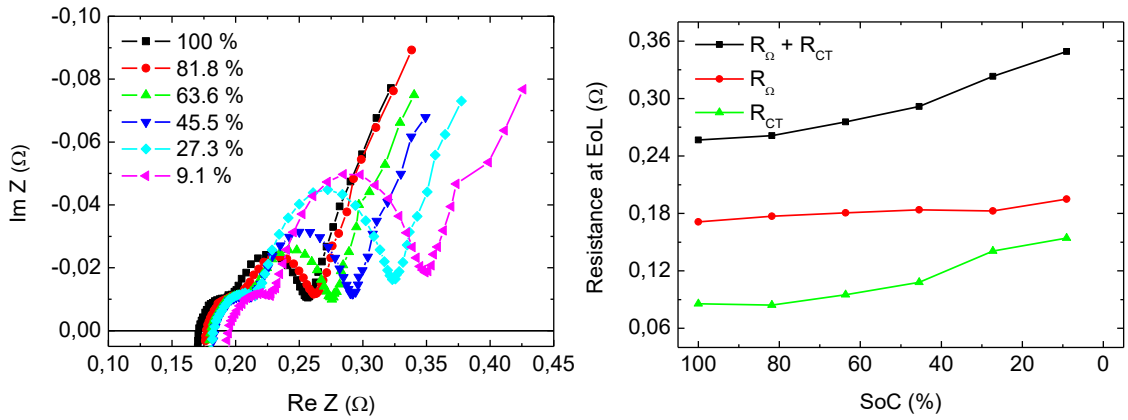

Fig. 3.26. Impedance evolution of the Old Microbattery with SoC (SoC 1 means totally charged and SoC 6 totally discharged). On the right side, serial and polarization resistances evolution with SoC.

When comparing the impedance spectra of the fresh and old microbatteries at 100 % SoC, we could extract the increase in ohmic and charge-transfer resistances during the aging test (Fig. 3.27). Charge-transfer resistance increased between 30 mΩ and 90 mΩ depending on the SoC, representing a relative increase between 50 % and 140 %. In contrast, ohmic resistance, which increased between 40 mΩ and 65 mΩ, represented a relative increase that went from 30 % to 50 %. At SoCs above 40 %, the ohmic resistance increased more than charge-transfer resistance in absolute values. However, the relative increase was higher in all SoCs in the case of charge-transfer resistance.

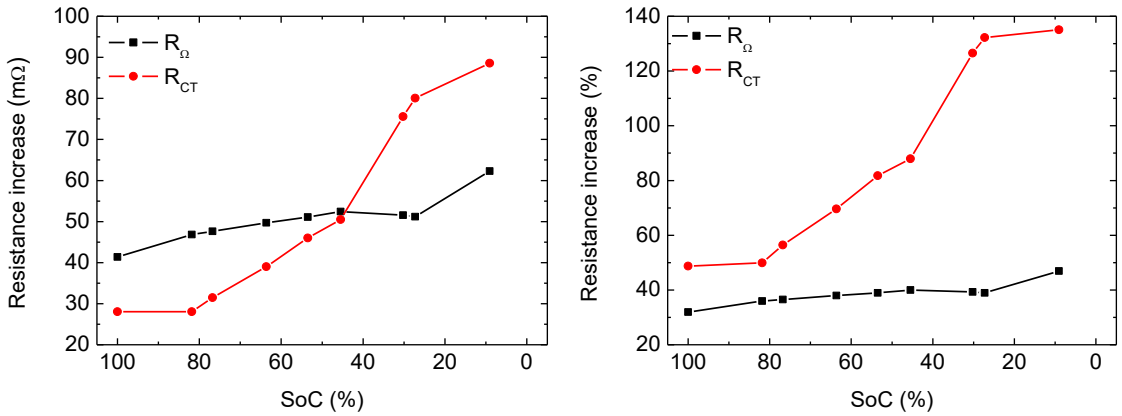

Fig. 3.27. Absolute (left) and relative (right) increases of ohmic and charge-transfer resistances from BoL (Fresh Microbattery) to EoL (Old Microbattery). Old Microbattery was cycled 150 times until the capacity dropped 20 % of the initial capacity.

3.3.2. Impedance from charging profiles and pulsed signals

3.3.2.1. Supercapacitors

We investigated a method to obtain the impedance spectra from current and voltage pulsed signals. We tested it in supercapacitors of 1 F and 5.5 V (for further details refer to [72]). Impedance was obtained from time to frequency domain transformation, using Fast Fourier Transform. The resulting impedance from the processing of temporal data was compared to EIS results (Fig. 3.28). Calculated impedance was in a good agreement with supercapacitor EIS impedance in a wide range of frequencies above 10 mHz. The real part of impedance was well adjusted from 7 mHz to approximately 200 mHz. In contrast, the imaginary part of impedance matched the measured one in a smaller frequency range going from approximately 30 mHz to 200 mHz. Similar results were obtained from constant charge (solid symbols) and pulsed charge (opened symbols).

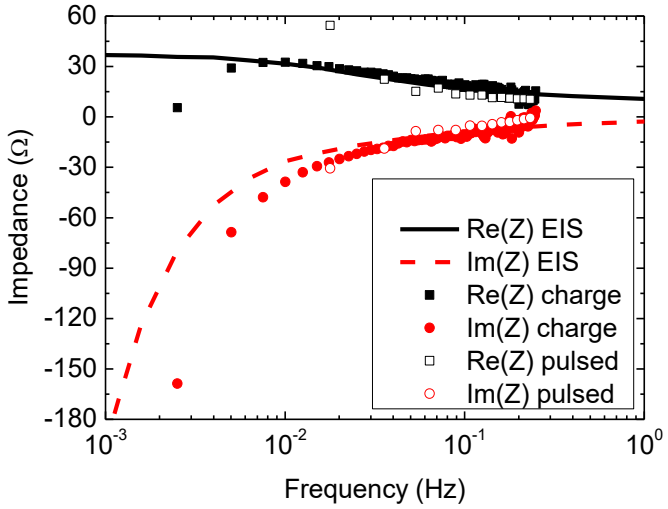

Fig. 3.28. Inferred real and imaginary parts of impedance of a supercapacitor of 1 F and 5.5V from constant current charging voltage and from pulsed current charging in comparison to measured impedance.

We also obtained the impedance profile by injecting a very short pulse. The interesting point of this methodology is that this short pulse would not change the state of charge of the cell or supercapacitor during the measurement. For supercapacitors, we injected a voltage pulse of 5 V and a duration of 1 ms; its current response was depicted in Fig. 3.29. In this case, since the signal was rather noisy, several measurements were carried out in order to average the results. Impedance was subsequently calculated with FFT transformations (see top part of Fig. 3.30). The real part showed a good agreement approximately between 8 mHz and 1 Hz and the imaginary part between 27 mHz and 1 Hz. Furthermore, the SNR was calculated in order to establish a quality threshold for the global result (bottom part in Fig. 3.30). The comparison between the EIS impedance measurement and the Fourier transform approximation showed a good agreement as long as the signal to noise ratio remained above 15 dB.

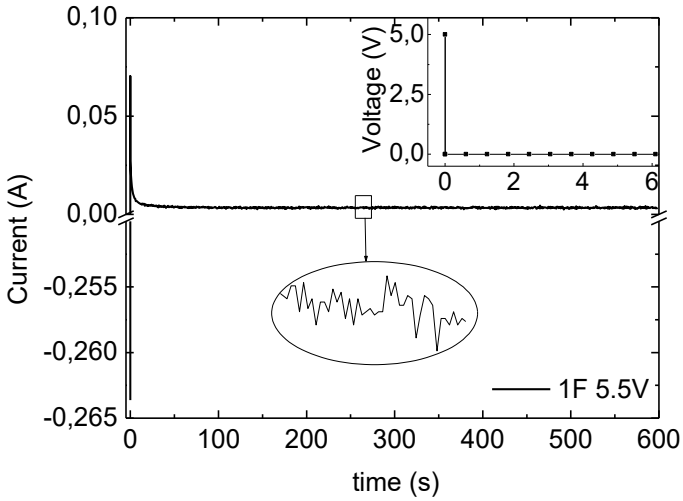

Fig. 3.29. Current response to a pulsed signal of 5 V and 1 ms (inset) averaged for 10 samples.

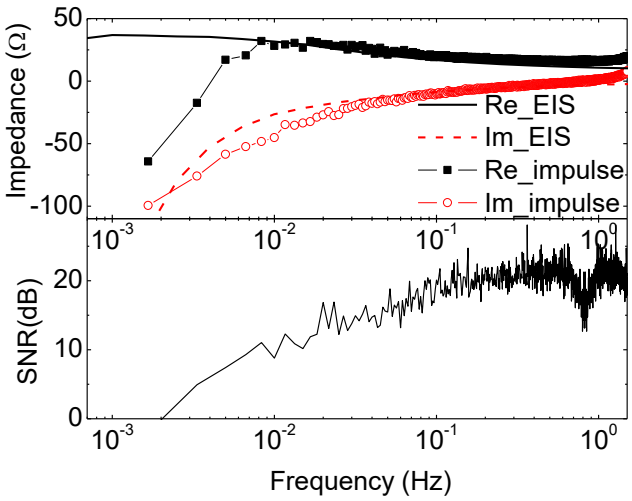

Fig. 3.30. Comparison between impedance of a supercapacitor of 1 F and 5.5 V measured using a potentiostat and injecting a pulsed signal. The SNR (bottom part) indicated that below 15 dB, no fitting was possible.

3.3.2.2.LCO cells

We evaluated impedance determination from pulsed signals in LCO cells. The injected current pulse was of 1 A (representing a rate of 1.35 C) and the time duration of the pulse was 1 s. Measured real and imaginary parts of LCO impedance were plotted together with the results of impedance obtained from our FFT transformations (Fig. 3.31). The results showed a good agreement with measured impedance in the considered frequency range.

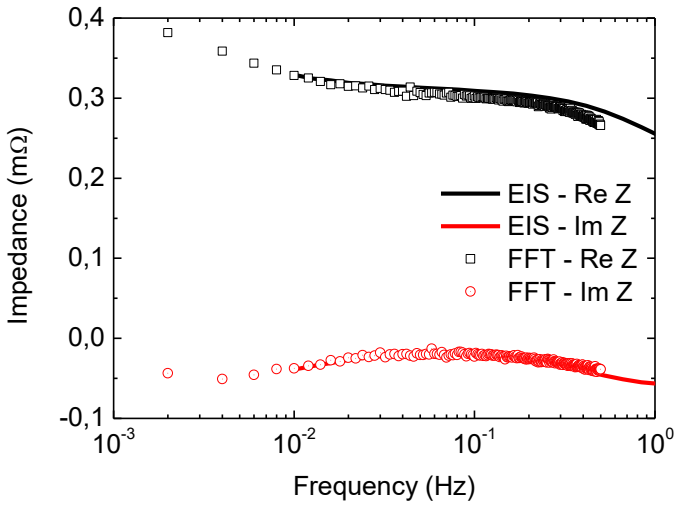

Fig. 3.31. Comparison between impedance of Microbattery LCO cell measured using a potentiostat and injecting a current pulse of 1 A during 1 s and doing FFT transformations of current and voltage profiles.

3.4. Discussions

Once we have presented the results on EIS measurements and pulses approximations, we aim to first, evaluate the different impedance effects we had measured in the cells and then, explore the obtained benefits of each measurement procedure.

In general, the identification of the physical processes occurring in a cell from impedance measurements is not an easy task. Commonly, impedance spectra show the effects occurring at both the positive and the negative electrodes. These effects overlap in frequency and thus they are indistinguishable in a regular EIS measurement. In this context, different approaches are possible: to measure half-cells, symmetric-cells or full-cells with a reference electrode, in order to identify the correspondence between the effects and the electrode producing them [87–89], or to carry out the impedance measurements at very low temperatures, so the effects occur in a slower rate and are easier to identify [87].

According to the development of the dissertation, we decided not to develop electrical models because this was not the main stream of this study, and we decided to qualitatively analyze the results. The half-cells analyses were carried out in the post-mortem, in Chapter 5.

3.4.1. Impedance from EIS measurements

3.4.1.1. LGC2 cells (NMC)

3.4.1.1.1. SoC dependency

The results showed a general increase of impedance when SoC was decreased. Similar trends were found in other studies [33,85,87,90]. Particularly, the ohmic resistance of the cell was almost SoC independent (right side of Fig. 3.9 and Fig. 3.10), as stated in [14,85,91]. Ohmic resistance R_Ω arises mainly from the contributions of the ionic and electronic conductivities coming from the electrolyte, the separator, and current collectors [36]. Specifically, electronic conductivity is SoC independent but ionic conductivity in the electrolyte depends on the concentration of ions [92]. Therefore, it would explain the variation in ohmic resistance with SoC.

In our study, we did not separate the resistance contribution of each of the processes contributing to charge-transfer polarization. However, the effect at higher frequencies (around 75 Hz) was apparently not dependent on SoC (left side of Fig. 3.9 and Fig. 3.10). Nonetheless, the one at lower frequencies was strongly dependent on it. The same trend had already been found [87]. There, the process at lower frequencies was strongly SoC-dependent but the one at higher frequencies was also dependent but not as strong as the other effect. This effect at lower frequencies was associated to the charge transfer process at the positive electrode (found between 0.1 Hz and 1 Hz) and the one at higher frequencies was associated to the charge transfer at the negative electrode (around 10 Hz). Thus, charge transfer at PE was determined to be more dependent on SoC than what charge transfer was at the NE. In contrast, the effect at higher frequencies have also been associated to SEI layer resistance [90]. The same trend of charge-transfer resistance with SoC that we found was reported in [90]. It was concluded that charge-transfer resistance and SEI-layer resistance exhibited the greatest variation with SoC, showing a monotonic relationship with it [90]. However, it was not explained why the effect associated to SEI layer was found to be SoC-dependent. Nevertheless, a possible explanation was given in [87] and [93]. Stiaszny et al. proposed that SEI-diffusion was SoC-dependent because of a possible change in SEI surface topology due to a dendritic deposition of lithium during charge/discharge cycles [87]. The lower polarization contribution at high SoCs was associated to lithium-ion deposition onto these dendrites, thus not needing to pass through the entire SEI layer. Contrarily, in [93], the SoC-dependency of the resistive effect associated to the SEI layer was related to the expansion and contraction of the NE during the lithiation and delithiation processes.

It is widely accepted that charge transfer effect is a strongly SoC-dependent process [90,93–97]. Therefore, we associated the effect at lower frequencies to a charge transfer process. However, it was not clear if the charge transfer process was occurring at either the positive or the negative electrode. In literature, it is mainly found that the negative electrode has a relatively small influence to full-cell impedance even though the SEI layer is thick [87,98]. Moreover, if we consider the results in [87], the effect at lower frequencies should have been associated to charge transfer at the PE because it

was the effect more dependent on SoC. However, post-mortem analysis is convenient for unequivocally determining the electrode causing each of the effects obtained at the impedance spectra. Half-cells or symmetrical-cells impedance measurements would clarify the results obtained from the full-cells. Post-mortem analysis of those particular cells will be developed in Chapter 5.

3.4.1.1.2. SoH tendency

In our study, we found that NMC cells showed only one semicircle at first aging states that separated into two distinct effects during the aging process (Fig. 3.12). The same trend was found in references [33,36,85]. Cells being charged at a moderate rate of 1C and discharged at 2C and 3C at a temperature of 25 ºC were investigated in [33]. This was comparable to our methodology. Fresh cells showed a unique semicircle but a change in the shape of the impedance spectra was found after 200 cycles where the two semicircles were already distinguishable. These two contributions were related to the charge transfer effect and to the resistance and capacitance associated to the SEI layer. In that case, the separation in frequency of those electrochemical effects was associated to the growth of the SEI layer. Moreover, an increase of the ohmic resistance due to aging was also found. Jalkanen et al. also reported an increase in both ohmic and charge-transfer resistances [36]. One of the cells they considered was charged/discharged at 1C/1C rate at room temperature. This cell showed only one semicircle in the beginning of cycling, which separated into two differentiable effects after 500 cycles. These two processes became even more distinguishable with cell aging. They suggested the effect at higher frequencies was mainly due to the graphite negative electrode and its SEI-layer whereas the one at lower frequencies was attributed to the charge transfer resistance at the NMC positive electrode, which was the dominant one. Regarding to the ohmic resistance, its increase was associated to the lack of electrolyte, possible blockage of the separator pores and separator resistance increase due to lithium plating on graphite electrodes and the SEI-layer formed on the top of plating. In addition, in the study of Waag et al. two semicircles could be distinguished at the impedance spectra of the aged cells [85]. They related the one at lower frequencies to interfacial charge transfer and the effect at higher frequencies to the SEI layer. Furthermore, charge-transfer semicircle increased and shifted toward lower frequencies during the aging process and the SEI growth caused the increase of the high frequency semicircle. The same trend of charge transfer resistance increase and shifting to lower frequencies was also found in [87]. Moreover, all of previously mentioned references agreed that the semicircle at higher frequencies corresponded to the SEI layer and the one at lower frequencies was associated to a charge transfer process. However, contrarily to [33], we found that the effect associated to SEI layer was not the predominant contributor to impedance rise but the one associated to charge transfer. Similar results to ours were found in [36,85,87], in which NMC/graphite cells were measured except in [87], in which the cell was composed of LMO-NMC/graphite. In particular, it was found that charge-transfer semicircle associated to PE increased and shifted towards lower frequencies being the major contributor to impedance rise of both of them.

The impedance rise is commonly associated to the SEI formation and to the degradation of the positive electrode [36,87]. In our study, we had not enough information to unequivocally determine the process or the electrode behind each measured effect. However, the ohmic and charge-transfer resistances increase at the same rate during the first 200 cycles represented in Fig. 3.16 (at SoC = 100 %) might indicate loss of lithium was the predominant aging affect. Nevertheless, charge-transfer resistance started increasing faster than ohmic resistance after 200 cycles. We associated this result to an additional aging mechanisms taking place as loss of active material. Moreover, we found that resistance rise was SoC dependent (Fig. 3.11). In all SoCs above 20 %, the increase in ohmic resistance during the aging test was higher than that of charge-transfer resistance. It suggested that the electrochemical reaction was slowed down at the last stages of discharge during the aging test. However, the relative increase was found to be larger in all SoC range in the case of charge-transfer resistance.

In addition, for a better understanding and determination of the electrode responsible of each effect measured at the full-cell impedance, post-mortem analysis will be developed in Chapter 5.

3.4.1.2.VIC cells (LFP)

The impedance of VIC cells was composed of an inductive tail at high frequencies, charge-transfer resistance represented by one or two semicircles at medium frequencies and a diffusional branch at low frequencies. The shape of the impedance spectra changed during the aging process (Fig. 3.17). The fresh cells showed only one semicircle which decreased during the first cycles until some point between 300 and 400 cycles where it separated into two distinguishable effects.

A qualitative analysis was carried out in order to compare the data at different degradation levels. Ohmic resistance was only estimated in the first stages of cycling where the holder was optimized for measuring low impedance values in a repetitive way. It suffered a sharp increase in the first 50 cycles and then continued increasing but gradually, reducing its increasing rate (Fig. 3.18). Ohmic resistance rise during cell aging is commonly found in literature [34,50,99–101], and it is usually associated to reduced ionic conductivity of the electrolyte due to electrolyte decomposition and to the increased resistance of the separator.

Regarding the charge-transfer resistance (calculated as the real part of impedance covered by the semicircles), all the effects contributing to it (charge-transfer effects at PE and NE and ohmic contributions with an associated capacitive effect) were overlapped in frequency. Thus, they showed up at the impedance spectra as one single semicircle at intermediate frequencies (Fig. 3.17). In the first part of cycling (from cycle 0 to cycle 300-400), charge-transfer resistance decreased. It was also manifested in Fig. 3.18 that R_{CT} + R_{MT} decreased sharply in the first 30-50 cycles and then stayed in those low values until the 400th cycle. Although expected to increase with aging, the same behavior was found in other publications [31,101,102]. Petzl et al. carried out accelerated aging tests at 4C rate at 50 ºC and they found that charge-transfer resistance decreased during the first cycles [101]. However, no explanation was given to it. In addition, Groot et al. found that the impedance decreased

slightly in the first few months of cycle aging [102]. It was associated to the decrease of the stoichiometric window where the maximum lithium available for insertion to the $LiFePO_4$ was diminished. It was found that transport limitations in LFP were significant, especially towards the end of discharge (i.e. large values of y in Li_yFePO_4). Thus, if y_{max} decreases due to loss of cyclable lithium, smaller impedance might be expected due to the better rate capability of LFP in that operating window. Zavalis et al. found that all cells that were cycled in a wide SoC range showed a first decrease in charge-transfer resistance followed by an increase towards the EoL [31]. It was suggested that it might be linked to rapid change in the thickness of the SEI layer. Moreover, it was observed that the cells with an initial decrease of R_{CT} resulted in an overall rapid aging pattern. Therefore, they proposed to consider the decrease in R_{CT} as an early sign of a rapid aging.

As previously mentioned, two electrochemical process were distinguishable after 300-400 cycles. Moreover, the minimum at the imaginary part situated at the beginning of the diffusion branch was no longer visible after the 400th cycle. That is the main reasons for which in Fig. 3.18 both the contributions of charge-transfer and diffusion resistances were plotted instead of charge-transfer resistance by itself. It was not clear where to separate the contribution of the semicircle and the diffusional branch. The minimum in imaginary impedance found at the beginning of the low-frequency tail was either no longer visible in [103]. They found a substantial increase of impedance during cycle aging manifested in the expansion in the imaginary and real directions of the semicircle. Zhang et al. concluded through their model that the cell cycling appeared to mostly have caused structural changes in the porous structure. Those structural changes eliminated the minimum in imaginary impedance while keeping the length of the low-frequency tail almost constant. The same behavior was found in our results.

In addition, the cells suffered a sudden and sharp increase of the joint contribution of R_{CT} and R_{MT}, which accounts for charge transfer effect and solid-state diffusion, between 300 and 400 cycles. This increase corresponds to the cycle in which the intermediate frequency effect was split into two distinguishable semicircles and the effect at lower frequencies was spread over the real and imaginary directions (Fig. 3.17). Thus, this effect pointed out that the highest contributor to impedance rise in that part of the test (not considering the ohmic resistance contribution) was the charge-transfer resistance rather than the diffusion phenomena. From cycle 400 until the end of the test (around 1000 cycles) total resistance (without R_Ω contribution) kept growing at a smaller but constant rate. It was also found in [104] a sudden increase of charge-transfer resistance between cycles 300 and 600. Yancheng et al. associated it to the increase of interfacial resistance that was induced by the catalytic growth of SEI layer due to iron impurities dissolved and deposited on the anode [104]. Nevertheless, the semicircle associated to interfacial resistance was the one at higher frequencies together with the current collector interfaces while the semicircle at lower frequencies was the one related to slower processes like charge transfer at the electrode/electrolyte interfaces [74,105–107]. This behavior was not found in our results as we found that the effect at lower frequencies was the one increasing. Thus,

the increase in resistance found in our study was associated to the charge transfer process instead of SEI or current collector interfaces. However, it was not possible to determine which electrode was causing it only from impedance measurements.

If data obtained from impedance measurements are compared to capacity evolution during the cycle aging process (refer to Chapter 2), many similarities can be found (Fig. 3.32). In fact, both impedance rise and capacity fade at low and moderate rates changed in trend when they were at the same cycling level (Fig. 3.32). Conversely, no direct relation between impedance rise and capacity fade was found in [99]. However, in [108] it was demonstrated that power fade and capacity fade were correlated. In our study, during the first 30 – 50 cycles where R_{CT} + R_{MT} impedance decreased, the total capacity of the cell at a rate of 2C increased (Fig. 3.32). This capacity rise at the first aging stages in LFP cells was found in other published studies [74,106,109,110]. However, only in [109] the effect was mentioned and a possible explanation was given. Lewerenz et al. associated it to the flow of active lithium between the inactive and the active parts of the negative electrode [109]. The inactive or passive part of the negative electrode corresponds to the geometric excess of negative electrode with respect to the positive one, which is commonly found in Li-ion batteries where the risk of lithium plating is aimed to be reduced. If lithium is shared between the passive and the active parts of the negative electrode, as suggested in [109], the effective active area for charge-transfer reaction to take place would increase. Thus, the resistance associated to it, R_{CT}, would decrease, which would confirm the obtained results.

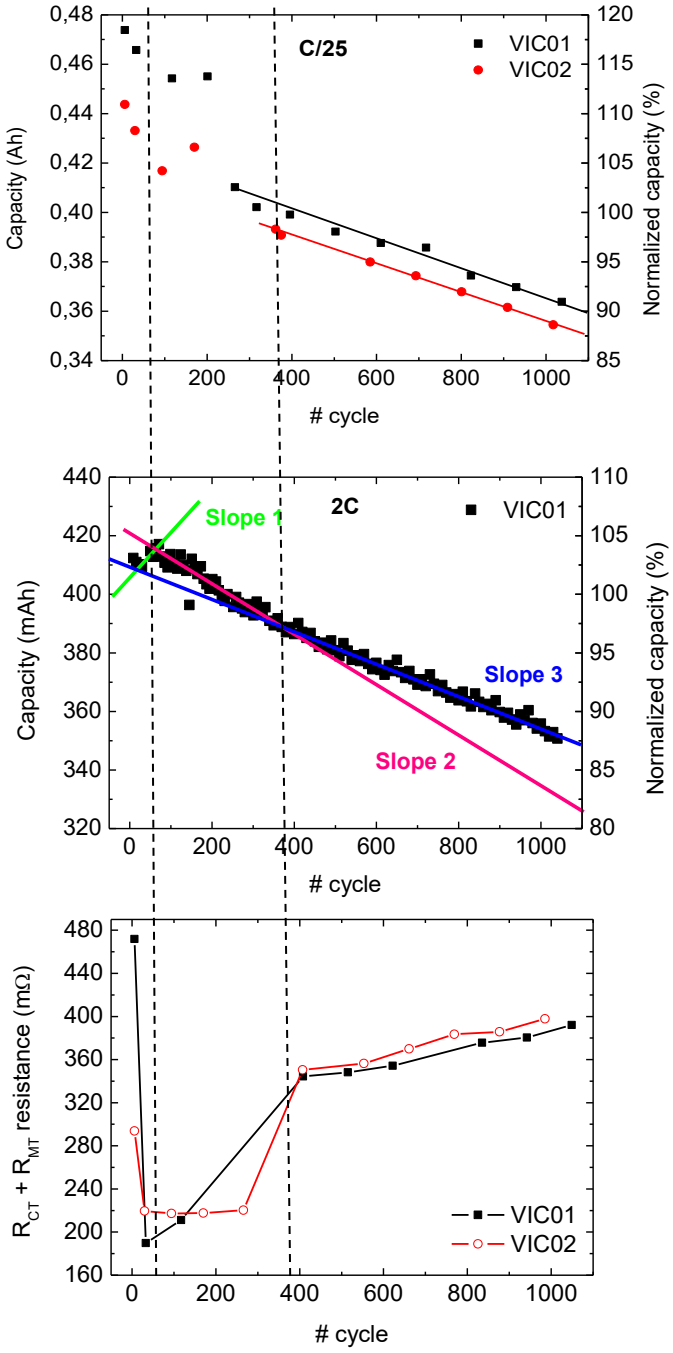

Fig. 3.32. Capacity evolution of a VIC cell measured at C/25 (top) and 2C (middle) showing the different tendencies found during the aging test. Charge-transfer and mass-transfer resistances evolution with aging measured at SoC = 100 % (bottom). Dashed lines represent the ranges in which different behaviors were appreciated.

Summarizing, we found that ohmic resistance sharply increased during the first 50 cycles, then the increasing rate was lowered but no data after cycle 300 was available. The fast increase in serial resistance during the first aging stages might be associated to the initial SEI layer formation. In the first cycling stages, SEI layer is formed at a higher rate until it stabilizes and completely covers the negative electrode. Thus, electrolyte solvents and lithium ions are consumed during this process what significantly reduces the electrolyte conductivity and consequently increases the ohmic resistance

[34,50,104]. Even though SEI formation was carried out prior to the aging test, it is possible that it was not completely formed during these formation cycles. Thus, resulting in this fast increase of ohmic resistance during the first cycles of the aging test. Regarding to charge-transfer resistance, it was found to be the main contributor to impedance rise after the 400th cycle. However, at the first stages of cycle aging, ohmic resistance was larger than charge-transfer resistance. Furthermore, the relative increase during this period was also higher for the ohmic resistance. Concerning the initial decrease in R_{CT}, we associated it to the passive electrode effect where lithium was shared between the passive and active parts of the negative electrode, what would increase the effective area for the reaction to take place.

3.4.1.3. EVbat cells (LFP)

3.4.1.3.1. SoC dependency

Only one semicircle was visible at intermediate frequencies in all SoC range (Fig. 3.20). Ohmic resistance was almost constant in the full SoC range. Nevertheless, total resistance was found to decrease between 100 % SoC and 80 % and increase towards the fully discharge state due to the SoC-dependency of the charge-transfer resistance. Same trends were found in [101] and [111] where ohmic resistance was almost SoC independent and R_{CT} increased towards the EoD. Unfortunately, the different effects overlapped in frequency could not be separated only by means of impedance measurements at room temperature.

3.4.1.3.2. SoH tendency

When impedance results were compared at different aging states, three of the four evaluated cells followed the expected tendency. EVbat_4 (400 cycles) started with a lower capacity than the rest of the cells and it was also cycled in a temperature-controlled environment what differed from the other cells. Thus, only EVbat_1 (50 cycles), EVbat_2 (100 cycles) and EVbat_3 (200 cycles) are going to be considered for the evolution of the resistances with aging represented in Fig. 3.21.

The shape and evolution of ohmic and charge-transfer resistances followed the same tendencies with SoC independently of the degradation level. No comparable data from the fresh cells was available as their impedance was measured with different connections in a different holder what affected considerably the results. Therefore, the evolution of impedance during the aging process was compared between cycles 50 and 200. EVbat cells showed only one semicircle at intermediate frequencies at the impedance spectra. This shape was maintained during all the aging process as it was found in other studies [99,112].

Ohmic resistance increased almost linearly from the 50th cycle to the 200th (Fig. 3.24). Conversely, charge-transfer resistance highly decreased between cycles 50 and 100. Although it also decreased between cycles 100 and 200, the decreasing factor was much below (Fig. 3.24). In addition, total resistance slightly decreased between cycles 50 and 100 but increased between cycles 100 and

200 due to the lower decrease in polarization resistance in that part of the aging process. Same trend was found in [99], where total resistance first decrease and then increased towards the EoL.

3.4.1.4. LCO cells

The impedance variation with SoC of the LCO cells was dependent on aging (Fig. 3.25 and Fig. 3.26). A unique semicircle was appreciated at BoL except at very low SoCs (below 7 %) whereas two semicircles were distinguishable in all SoCs at the EoL. In particular, the semicircle at lower frequencies was strongly dependent on SoC while the one at higher frequencies seemed to be independent of it. The same trend was found in [113] and [114]. In these studies, the semi-arc at higher frequencies was associated to the SEI layer and the one at lower frequencies to the charge transfer process.

Regarding to aging, the effect at lower frequencies drastically increased. The same behavior was found in literature [115,116]. Furthermore, ohmic resistance also suffered a high increase (Fig. 3.27). Schoenleber et al. found it to increase linearly during the aging test [116]. Unfortunately, we did not record the evolution of impedance at intermediate cycles so no comparison could be made. Moreover, we found that the increases in ohmic and charge-transfer resistances were SoC dependent (Fig. 3.27). The relative increase was higher in all SoC range for the charge-transfer resistance. However, in absolute values, ohmic resistance increased in a higher extent than charge-transfer resistance at SoCs above 45 %.

3.4.2. Impedance from charging profiles and pulsed signals

Impedance obtained from charging profiles or other temporal signals are of high interest to avoid time-consuming measurements of EIS impedance at very low frequencies. The time required for EIS measurements is not the only drawback but also the need of generating ac signals at different frequencies and measure them in portable systems. Thus, it would require a non-simple specific hardware that would be an inconvenient for these applications.

- Good agreement, valid methodology.

  It was possible to establish a good understanding between the behaviour in the time and frequency domains. The supercapacitor EIS spectra showed that a pure capacitive effect is only found at frequencies below 1 mHz. When charging the supercapacitor in the time domain at a constant current of 10 mA, the time to complete the charge is around 500 s, whose reciprocal frequency is 2 mHz. Under these conditions, the charging process looks like an ideal capacitor. However, in the pulsed charge, where the charging time is 60 s, and the corresponding frequency lies around 16 mHz, the resistive effects related to charge distribution and the non-ideal capacitance behaviour lead to the current flow during the resting time of the pulse signal. In this frame, it is convenient to charge the supercapacitor at low frequency (around 1 mHz) in order to have a capacitive behaviour. As long as the frequency of the pulse signal increases, the resistive effect increases.

- Noise and drawbacks.

  Concerning the results from the supercapacitor, the noise source of the signal plotted in Fig. 3.29 was attributed to the supercapacitor itself. There are not many studies dealing with supercapacitor noise [72]. However, thermal noise contribution would be negligible (of the order of 0.1 nV) which could not explain the current noise of around 0.25 mA. Thus, noise might be related to random charge movements in the double layer capacitance.

- Other studies in which impedance was obtained from FFT/Laplace transforms.

  Other studies have been found in which the impedance was calculated from digital signal processing [61,69,117]. In particular, Howey et al. obtained the impedance of a LFP cell between 1 Hz and 2 kHz by injecting a multisine and noise coming from a motor [69]. Good results were achieved in the evaluated range. Moreover, Rahmoun et al. estimated the impedance of a Li-ion cell by means of FFT transform of the voltage response to a current step [61]. The investigated frequency range in that case went between 1 mHz and 0.5 mHz. As it happened in our study, the results were not accurate at low frequencies. Finally, this method was also applied to estimate the impedance spectra of fuel cell membranes [117]. In that case, it was also done by injecting a current step and measuring the voltage response. The covered frequency range was from 5 mHz to 5 kHz.

3.5. Conclusions

3.5.1. Impedance from EIS measurements

3.5.1.1. LGC2 cells (NMC)

- A general increase of impedance was found when SoC was decreased.
- The ohmic resistance of the cell was almost SoC independent.
- In our study, we did not separate the resistance contribution of each of the processes contributing to charge-transfer polarization.
  - Two semicircles could be appreciated at the impedance spectra. These effects could not be appreciated in all SoCs at BoL.
  - The semicircle found at higher frequencies (around 75 Hz) was apparently not dependent on SoC.
  - The semicircle at lower frequencies was strongly dependent on SoC.
  - In a first approach, we associated the semicircle measured at lower frequencies to a charge transfer process. However, it was not clear if the charge transfer process was occurring at either the positive or the negative electrode.
- The resistance rise with aging was SoC dependent.
- Ohmic and charge-transfer resistances increased at the same rate during the first 200 cycles at SoC = 100 %.

  - It might indicate loss of lithium was the predominant aging affect.
- Charge-transfer resistance started increasing faster than ohmic resistance after 200 cycles at SoC = 100 %.
  - It might indicate additional aging mechanisms as loss of active material might be taking place.

3.5.1.2.VIC cells (LFP)

- The impedance of VIC cells was composed of an inductive tail at high frequencies, charge-transfer resistance represented by one or two semicircles at medium frequencies and a diffusional branch at low frequencies.
- The shape of the impedance spectra was dependent on aging.
  - The fresh cells showed only one semicircle which decreased during the first cycles until some point between 300 and 400 cycles where it separated into two distinguishable effects.
- A qualitative analysis was carried out in order to compare the data at different degradation levels.
- Ohmic resistance was only estimated in the first stages of cycling (initial 300 cycles) where the holder was optimized for measuring low impedance values in a repetitive way.
  - It suffered a sharp increase in the first 50 cycles and then continued increasing but gradually, reducing its increasing rate.
  - The fast increase in serial resistance during the first aging stages might be associated to the initial SEI layer formation.
- In the first part of cycling (from cycle 0 to cycle 300-400), charge-transfer resistance decreased.
- R_{CT} + R_{MT} also decreased sharply in the first 30-50 cycles and then stayed in those low values until the 400th cycle.
- The minimum at the imaginary part situated at the beginning of the diffusion branch was no longer visible after the 400th cycle. It was found in literature that it was caused by structural changes in the porous structure. Those structural changes eliminated the minimum in imaginary impedance while keeping the length of the low-frequency tail almost constant.
- We pointed out that the highest contributor to impedance rise between 300 and 400 cycles (not considering the ohmic resistance contribution) was charge-transfer resistance rather than diffusion phenomena.
- The increase in resistance associated to the semicircles at the impedance spectra was associated to a charge transfer process. However, it was not possible to determine which electrode was causing it only from impedance measurements.

- Impedance rise and capacity fade at low rates changed in trend when they were at the same cycling level.
- At the first stages of cycle aging, ohmic resistance was higher than charge-transfer resistance. The relative increase during this period was also higher for the ohmic resistance.

3.5.1.3.EVbat cells (LFP)

- Only one semicircle was visible at intermediate frequencies in all SoC range.
- Total resistance was found to decrease between 100 % SoC and 80 % and increase towards the fully discharge state due to the SoC-dependency of the charge-transfer resistance.
- The different effects overlapped in frequency could not be separated only by means of impedance measurements at room temperature.
- EVbat_4 (400 cycles) started with a lower capacity than the rest of the cells and it was also cycled in a temperature-controlled environment what differed from the other cells. Thus, possible cell-to-cell variations could be affecting the measurements.
- The shape and evolution of ohmic and charge-transfer resistances followed the same tendencies with SoC independently of the degradation level.
- No comparable data from the fresh cells was available as their impedance was measured with different connections in a different holder what affected considerably the results. Therefore, the evolution of impedance during the aging process was compared between cycles 50 and 200.
- Ohmic resistance increased almost linearly from the 50th cycle to the 200th.
- EVbat cells showed only one semicircle at intermediate frequencies at the impedance spectra and its shape was maintained during all the aging process.
- Charge-transfer resistance highly decreased between cycles 50 and 100. Although it also decreased between cycles 100 and 200, the decreasing factor was much below.
- Total resistance slightly decreased between cycles 50 and 100 but increased between cycles 100 and 200 due to the lower decrease in polarization resistance in that part of the aging process.

3.5.1.4.LCO cells

- The impedance variation with SoC of the LCO cells was dependent on aging.
- A unique semicircle was appreciated at BoL except at very low SoCs (below 7 %) whereas two semicircles were distinguishable in all SoCs at the EoL.

    - The semicircle at lower frequencies was strongly dependent on SoC while the one at higher frequencies seemed to be independent of it.
    - The semicircle at lower frequencies drastically increased with aging.
- The ohmic resistance also suffered a high increase with aging.
- The evolution of impedance at intermediate cycles was not recorded so the evolution could not be tracked between BoL and EoL.
- The increases in ohmic and charge-transfer resistances were SoC dependent.
    - The ohmic resistance increased in a higher extent than charge-transfer resistance at SoCs above 45 % (in absolute values).
    - The relative increase of charge-transfer resistance was higher than ohmic resistance in all SoC range.

3.5.2. Impedance from charging profiles and pulsed signals

- Impedance obtained from charging profiles or other temporal signals are of high interest to avoid time-consuming measurements of EIS impedance at very low frequencies.
- Good agreement, valid methodology.
    - A good approximation of EIS impedance was obtained from the constant/pulsed charge/discharge profiles of a supercapacitor.
    - The resulting SNR was calculated showing that the Fourier transform approximation showed a good agreement as long as the signal to noise ratio stayed above 15 dB.
    - It was possible to establish a good understanding between the behaviour of the supercapacitor in the time and frequency domains.
    - It was also successfully applied to Li-ion cells (LCO). A current pulse was injected to the cells and the FFT of input and output were calculated. Thus, obtaining a good agreement with measured impedance in the considered frequency range.
- The measured noise during the supercapacitor measurements was attributed to random charge movements in the double layer capacitance.

Chapter 4

Energy and Entropy

In this chapter, we study how the input energy is distributed along the battery in form of electrochemical storage, heat dissipation and battery degradation. For doing so, ohmic, activation and concentration polarizations contributing to heat dissipation are evaluated and quantified separately. Reversible entropy is also considered and irreversible entropy production corresponding to each of the polarizations is estimated. In addition, aging mechanisms related to capacity fade were deciphered from incremental capacity analysis.

4.1. Introduction

Energy balance is usually studied in the frame of thermodynamics. We first review the classical laws and later, we focus on irreversible and time-dependent thermodynamics. Special emphasis is placed on overpotencials and entropy generation and heat balance.

4.1.1. Classical and modern thermodynamics

Thermodynamics is the branch of science that relates heat and temperature to energy and work. It appeared in the nineteenth century and it has continuously evolved until nowadays. Classical thermodynamics was developed before the atomic theory of matter was accepted. Consequently, thermodynamics only characterize the systems macroscopically, that is, systems are always treated as continuous [118]. Moreover, classical thermodynamics is defined for systems or bodies in equilibrium with themselves and with the surroundings.

We are interested in measuring the variation of heat when it is converted to or from a different form of energy. In that case, thermodynamics introduce the quasi-equilibrium processes. A quasi-equilibrium process is defined as the transition of the system through a series of equilibrium states as it moves slowly and gradually from the initial state to the final state. Quasi-equilibrium processes are considered as reversible processes where dissipative effects are neglected [118]. Therefore, classical thermodynamics only deals with reversible processes, which are not frequent in nature, even working close to equilibrium. However, beyond classical thermodynamics, it is also possible to consider the thermodynamics of irreversible processes where *time* is considered as a variable of the system.

A key concept in thermodynamics is the definition of state. For describing the microscopic state of a system, a very detailed knowledge about the behavior of the conforming particles would be required [119]. This is investigated in statistical mechanics but it is not of interest for our battery characterization. Nevertheless, we are interested in macroscopic systems, which can be defined with few variables.

A thermodynamic system is a set of matter of fixed identity, around which a boundary can be drawn [120]. Those boundaries have to be imposed in order to differentiate the system itself from the exterior or the universe. Depending on how the systems interact with the exterior, they can be classified into isolated, closed or open systems (Fig. 4.1).

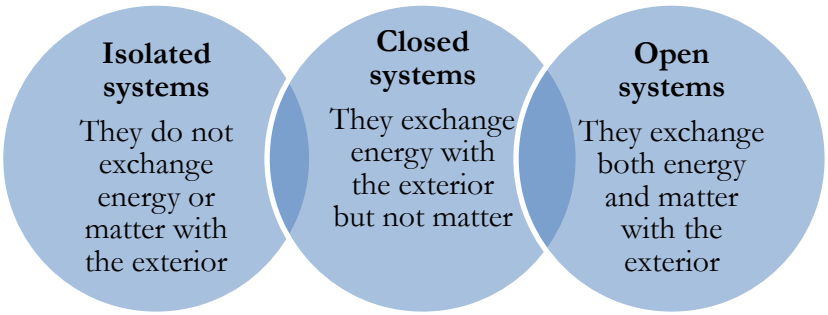

Fig. 4.1. Thermodynamic systems classified depending on how they interact with the environment.

Thermodynamic variables can be path functions or point (or state) functions. Path functions are those dependent on the path taken when going from one state to another state. As an example, work and heat are path-dependent thermodynamic variables. Conversely, a variable that is a point or state function only depends on the values of state 1 and state 2, what means that the change on it is independent from the path taken during the process. Typical macroscopic state variables are internal energy, volume, pressure, temperature, and mole numbers of the chemical constituents.

It is useful to classify thermodynamic variables into extensive or intensive. Extensive variables are the ones that are proportional to the size of the system like volume and mole number. On the contrary, temperature or pressure are intensive variables, which are independent of the size.

The fundamentals of thermodynamics are stated in four laws. Each law leads to the definition of some particular properties of a physical system that help us to understand and predict its operation.

4.1.1.1. Zeroth Law of Thermodynamics

The Zeroth Law of Thermodynamics states that when two bodies are in contact at different temperatures, heat will be transferred from the hottest body to the colder one until both of them reach the same constant temperature [121]. The final temperature of both of them will be the weighted average between their two respective initial temperatures. At this point, they are considered to be in thermal equilibrium. Moreover, the processes driving the state of a system towards the equilibrium are irreversible in nature [122]. Therefore, those irreversible processes vanish when the equilibrium is reached.

4.1.1.2. First Law of Thermodynamics

First Law of Thermodynamics describes energy conservation of a system. Energy is not created or destroyed but transformed and it can be present in form of heat or work. Internal energy variation is path independent so it only depends on the initial and final states. However, heat and work depend on the way they are obtained and therefore they are not state functions as internal energy is [122].

In a closed system, the internal energy variation $U_f - U_i$ equals the contributions of the heat transferred, Q and the work done or obtained from the system, W (4.1). Heat is considered positive when enters the system and negative when leaves it.

$$U_f - U_i = Q + W \tag{4.1}$$

In the case in which ther are only infinitesimal variations of the thermodynamic coordinates in a closed system, the differential form of the first principle becomes more convenient (4.2). In cyclic processes, the variation of the internal energy of a system can be zero as it ends up at the same initial state [123].

$$dU = dQ + dW \tag{4.2}$$

4.1.1.3.Second Law of Thermodynamics

Due to the implications of the Second Law, we develop here a brief general introduction.

4.1.1.3.1. Origin of the Second Law

Sadi Carnot analyzed the steam engines, which performed mechanical work from the flow of heat. From these studies, he identified the heat flow as the fundamental mechanism required for the generation of work. Second law of thermodynamics says that there is a limit in the maximum work that can be generated from heat engines and it is independent of the machine itself and the way it is generated; it only depends on the difference in temperature of the heat sources. Carnot published his results in 1824 but they did not attract much attention from the scientific community until ten years later, once he had already passed away, thanks to Émile Clapyron.

The heat engines defined by Carnot (Fig. 4.2) consisted of an ideal gas that generate mechanical work (W) due to its change in volume that produced the flow of heat between two heat reservoirs (Q_H and Q_C) at different temperatures (T_H and T_C).

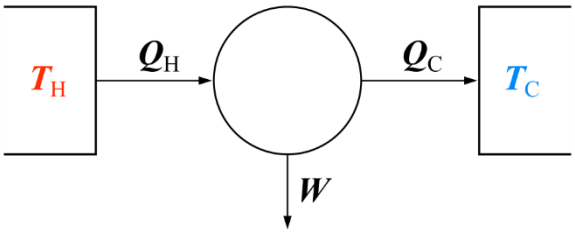

Fig. 4.2. Schematic of Carnot heat engine [124].

Carnot stated that for achieving the maximum work, all changes in volume should occur with minimum temperature gradients formation so the changes in temperature are almost all due to volume expansion and not due to flow caused by temperature gradients. It could be achieved if the transfer of heat was done very slowly so the temperature of the reservoirs remained as uniform as possible. He stated that in the limit of infinitely slow heat transfer, the operation of a heat engine is a reversible process. It means that if the heat transfer from the hotter reservoir to the colder one produces an amount of work, the same amount of work can be used to transfer the same amount of heat from the colder to the hotter reservoir. He also defined the concept of cycle, in which after a sequence of states, the engine went back to its initial state ready for starting a new cycle again.

Carnot defined that the maximum obtainable work would be the one produced by a reversible cyclic engine because producing more than that would mean that work is produced endlessly and this would not be possible. To calculate the efficiency of the process first law of thermodynamics has to be applied. In that case, we have that a part of the heat Q_H (Fig. 4.2) is going to be converted into work, $W = \eta \cdot Q_H$ and by the law of conservation of energy, we have that $W = Q_H - Q_C$. Thus, the efficiency can be expressed as stated by Carnot's Theorem (4.3) in which $f(T_1, T_2)$ is a function only

of temperatures T_H and T_C. His observations allowed to define an absolute scale of temperature that is independent of the material property used to measure it.

$$\eta = 1 - \frac{Q_C}{Q_H} = 1 - f(T_H, T_C) \tag{4.3}$$

4.1.1.3.2. Second Law of Thermodynamics

The full importance of Carnot's Theorem was realized by Rudolf Clausius, who introduced in 1865 the concept of entropy, *S*. This was a new physical quantity as fundamental and universal as energy. Clausius defined the term entropy from the closed integral (4.4) evaluated across a reversible path of arbitrary cycle by considering a cycle as an addition of an infinite number of Carnot cycles that differed by an infinitesimal amount ΔT.

$$\Delta S = \oint \frac{dQ}{T} = 0 \tag{4.4}$$

It can be inferred that in a reversible process between states A and B, the integral only depends on those states being independent of the path taken. Therefore, he defined entropy *S*, which means transformation in Greek, as a state function in a reversible process.

$$S_B - S_A = \int_A^B \frac{dQ}{T} \qquad or \qquad dS = \frac{dQ}{T} \tag{4.5}$$

Recalling Carnot cycle example (Fig. 4.2) and if an irreversible cycle is considered, only a fraction of Q_H can be converted into useful work. Therefore, the amount of heat transferred to the cold reservoir Q'_C is going to be higher than Q_C, yielding to equations (4.6) and (4.7).

Total change of entropy of the irreversible engine (system)

$$\frac{Q_H}{T_H} - \frac{Q'_C}{T_C} < 0 \tag{4.6}$$

Total change of entropy of the reservoirs (exterior)

$$\frac{(-Q_H)}{T_H} - \frac{(-Q'_C)}{T_C} > 0 \tag{4.7}$$

General expressions for an arbitrary cycle are summarized in equations (4.8) and (4.9). Total entropy of the system does not change in a complete cycle even if it is reversible or irreversible. It is because after a complete cycle, the system returns to its initial state. What usually happens is that more heat is expelled to the exterior generally converting mechanical energy to heat through irreversible processes.

For a reversible cycle: $$dS = \frac{dQ}{T} \qquad \oint dS = \oint \frac{dQ}{T} = 0 \tag{4.8}$$

For an irreversible cycle: $$dS > \frac{dQ}{T} \qquad \oint dS = 0, \qquad \oint \frac{dQ}{T} < 0 \tag{4.9}$$

A more general expression of entropy is derived in the framework of thermodynamics of irreversible processes. Entropy is obtained by separating two effects: d_eS that is the change of the system's entropy due to exchange of energy and matter, and d_iS that is the change in entropy due to irreversible processes within the system (4.10). d_eS can be positive or negative while d_iS has to be greater or equal than zero.

$$dS = d_eS + d_iS \tag{4.10}$$

There is no real system in nature that can go through a cycle and return to its initial state without increasing the entropy of the exterior. The entropy d_iS generated by the irreversible processes has to be discarded to the exterior as heat. This expression is a generalization of thermodynamics, in which both reversible and irreversible processes are represented by the Clausius inequality.

$$dS \geq \frac{dQ}{T} \tag{4.11}$$

The Second law clearly manifests the limitation that is present in all natural processes when converting heat to work. In particular, the aim of this thesis is to relate battery aging or SoH to the generation of entropy inside the cells due to irreversible processes or d_iS.

4.1.1.4. Third Law of Thermodynamics

The Second law of thermodynamics, only allows us to calculate entropy variations. However, in 1906, Walther Nernst conclude that *at the absolute zero of temperature the entropy of every chemically homogeneous solid or liquid body has a zero value* [122]. Therefore, the Third Law states that an absolute value of entropy can be obtained. The physical basis of Nernst heat theorem is explained by quantum theory, which defines the behavior of matter at low temperature.

4.1.2. Heat transfer

Heat can be transferred by conduction, convection, or radiation [118]. **Conduction** is the transmission of heat between two solids (or within one single solid) that is isolated and its parts are at different temperatures. The particles of the substance gain kinetic energy and collide between them

transmitting the heat from hotter to colder parts. Thus, a coefficient of thermal conductivity k can be defined for a particular material involved in a heat flow dQ_{cond}/dt across an area A in a temperature gradient dT/dx in the x direction.

$$\frac{dQ_{cond}}{dt} = A \cdot k \cdot \frac{dT}{dx} \tag{4.12}$$

Convection occurs when the heat source is in contact with a liquid or gas. The convective heat generation rate is given as

$$\frac{dQ_{conv}}{dt} = A \cdot h \cdot (T_a - T_b) \tag{4.13}$$

Where A is the surface area of the solid, h is the heat transfer coefficient, T_a is the solid's surface temperature, and T_b is the fluid temperature.

Radiation is the heat transmission between two bodies that do not need to be in physical contact. The heat flow due to radiation dQ_{rad}/dt is proportional to the fourth power of temperature yielding the equation

$$\frac{dQ_{rad}}{dt} = A \cdot \epsilon \cdot \sigma \cdot (T_a^4 - T_b^4) \tag{4.14}$$

Where ϵ is the emissivity of the body (it is equal to one for an ideal black body) and σ is the Stefan-Boltzmann constant ($5.6703 \cdot 10^{-8}$ W·m^{-2}·K^{-4}).

In our work, radiation is irrelevant, conduction is a key process and, even though convection is present, it is not addressed in this work.

4.1.3. Heat capacity

Heat capacity of a system is defined as the heat required to increase its temperature in ΔT increment. If it happens that the temperature goes from T_i to T_f when transferring ΔQ amounts of heat, then the average calorific capacity of the system can be defined (4.15).

$$C_{avg} = \frac{\Delta Q}{\Delta T} = \frac{\Delta Q}{T_f - T_i} \tag{4.15}$$

When the final temperature tends to the initial one meaning that Q and temperature variation are small, the average calorific capacity tends to its instantaneous value (4.16). Moreover, the calorific

capacity can be positive, negative or zero depending on the nature of the process and if it absorbs or releases heat.

$$C = \frac{dQ}{dT} \tag{4.16}$$

The heat capacity is an extensive magnitude so it depends on the amount of material involved in the process (i. e. the mass of the system, m). Therefore, it is commonly represented as the specific heat (4.17).

$$c = \frac{1}{m} \cdot \frac{dQ}{dT} \tag{4.17}$$

For example, in the simple case of a resistor in which a current I is flowing through it producing a voltage difference V on its terminals and a temperature variation of ΔT during a Δt period, the specific heat would be

$$c = \frac{1}{m} \cdot \frac{I \cdot V \cdot \Delta t}{\Delta T} \tag{4.18}$$

Where the product $I \cdot V$ represents the dissipated power by the resistor in the form of heat [122].

4.1.4. Entropy

In the field of non-equilibrium thermodynamics, entropy production is described by the contribution of thermodynamic forces F and thermodynamic flows dX [122]. Flows of heat or matter occur due to thermodynamic forces. Therefore, the irreversible entropy change within the system (d_iS) is expressed as the product of the force that is producing it and the corresponding flow.

$$d_iS = F \cdot dX \tag{4.19}$$

d_iS is always equal or greater than zero as extracted from equations (4.10) and (4.11), being zero at the ideal case of reversible processes. When a system can be divided into smaller subsystems, the total entropy is the contribution of all the entropies of the subsystems. All of them will also have the irreversible part of the generation of entropy that will be equal or greater than zero. These statements go beyond the classical thermodynamics where d_iS was only defined for isolated systems.

The entropy exchange with the exterior is expressed in terms of heat and matter. Equation (4.20) represents the entropy exchanged in an open system where a flow of matter exists. For the case in which the system is closed, there is no matter exchange so the term $(d_eS)_{matter}$ does not contribute to

the exchanged entropy. In the more restrictive case of an isolated system, d_eS is equal to zero because there is exchange of neither heat nor matter.

$$d_eS = \frac{dU + p \cdot dV}{T} + (d_eS)_{matter} \tag{4.20}$$

Some thermodynamic forces and the associated flows are summarized in Table 4.1. The thermodynamic flows are consequences of the thermodynamic forces [122].

Table 4.1. Thermodynamic forces and flows and the corresponding laws.

Law	Force	Flow
Flick	Concentration gradient	Matter
Fourier	Temperature gradient	Heat
Ohm	Voltage gradient	Electrical current

4.1.4.1. Particular cases of entropy production

4.1.4.1.1. Electrical circuit elements

The generation rate of irreversible entropy is calculated from the generic equation (4.19). In the particular case of electrical circuit elements where a current is flowing, the thermodynamic force would be the voltage gradient (V/T) and the flow would be the electrical current (I), following the Ohm's Law, what yields to equation (4.21) for the particular case of electrical circuits [122]. For a resistor, $(\phi_2 - \phi_1)$ can be identified in (4.21) as the voltage across the element and dQ/dt as the electric current I. In this particular case, irreversible entropy is produced due to heat generated by the Joule effect.

$$\frac{d_iS}{dt} = \frac{(\phi_2 - \phi_1)}{T} \cdot \frac{dQ}{dt} = \frac{V \cdot I}{T} = \frac{R \cdot I^2}{T} > 0 \tag{4.21}$$

4.1.4.1.2. Electrochemical cells

The irreversible entropy production due to the ongoing overall reaction and the current flowing through an electrochemical cell (I) is described in equation (4.22) [122].

$$\frac{d_iS}{dt} = \frac{\tilde{A}}{T} \cdot \frac{d\xi}{dt} \tag{4.22}$$

Where, $\tilde{A}$ is the electrochemical affinity of the reaction and ξ is the extent of the reaction [122].

Where,

$$I = nF \cdot \frac{d\xi}{dt} \tag{4.23}$$

$$V = \frac{\tilde{A}}{nF} = OCV - V_{cell} \tag{4.24}$$

Therefore, the resulting expression for the entropy production in an electrochemical cell would be as follows

$$\frac{d_i S}{dt} = \frac{(OCV - V_{cell}) \cdot I}{T} \tag{4.25}$$

4.1.4.1.3. Degradation and entropy

From a theoretical perspective, entropy generation rate is a parameter that "is important in engineering because its product with the temperature is a measure of the degradation or dissipation of energy in engines, and its minimization may be useful to enhance their efficiency"[125]. This approach has been applied to the study of mechanical damage and wear in solid materials [126–129]. Khonsari and Amiri have carried out a comprehensive investigation of thermodynamics of mechanical failure [130]. Also, Naderi et al. have investigated heat generation during mechanical stress in beams and proposed an entropy threshold for damage assessment [129,131]. The electrical behavior following mechanical fatigue has also been evaluated, where mechanical damage has been related to electrical damage [126]. Basaran and Yan [127] have pioneered the introduction of entropy as a damage metric in electromigration characterization, i.e., lattice degradation due to electron scattering. Thus, the combination of current and voltage as electrical variables, along with entropy from thermodynamics, could lead to an accurate description of electrical damage [127,132,133]. Entropy has also been introduced for understanding the physics leading to the failure of oxides in order to obtain accurate models of their reliability [134,135]. Reversible entropy is widely used in adiabatic computing [136], where heat dissipation must be minimized, and in electrochemical battery research, for characterizing their SoC and SoH [137,138]. Recently, Amiri and Modarres [139] have reviewed the possibilities for successfully implementing entropy as a parameter for measurement and instrumentation. While mainly theoretical, they highlighted its viability in electrical and mechanical systems. Nonetheless, entropy has not yet reached maturity for system monitoring.

.

4.1.5. Energy conversion in batteries

Energy is stored in batteries as a chemical energy, i.e., potential energy stored in the chemical bonds of the chemical reaction products. This change in energy related to the chemical bonds is termed as the enthalpy of the reaction, ΔH, which represents the total chemical available energy. Notwithstanding, when a reaction takes place, heat is absorbed, breaking bonds (endothermic) or released, forming new bonds (exothermic) [122]. The amount of heat released or absorbed (exchanged with the environment) is equal to the reversible entropy variation ΔS at a constant temperature, T. Therefore, the Gibbs free energy ΔG accounts for the available energy to perform work (4.26). In particular, for electrochemical reactions, it defines the maximum available electrical energy after the chemical-electrical conversion [122].

$$\Delta G = \Delta H - T \cdot \Delta S \tag{4.26}$$

The change in Gibbs free energy was already defined in equation (1.1) where it was directly related to the open-circuit voltage of a battery, OCV. Despite the maximum electrical energy stored in batteries is related to the OCV, the actual energy that can be extracted from the cell is below ΔG, due to the fact that the cell is not ideal. In fact, the maximum obtainable work from a battery is related to the cell voltage at its output terminals, V_{cell}. The difference between them is energy dissipated as heat (i.e. irreversible loses).

The generation of reversible entropy dS_{rev}/dt associated to the reversible entropy change ΔS is related to the variation of the OCV with temperature and the current I flowing through the cell [123] and it is expressed as (for a complete derivation of the expression of reversible heat refer to [140]):

$$\frac{dS_{rev}}{dt} = \frac{dQ_{rev}/dt}{T} = \frac{\frac{d(OCV)}{dT} \cdot T \cdot I}{T} = \frac{d(OCV)}{dT} \cdot I \tag{4.27}$$

Where, the derivative of the OCV with respect to temperature is termed as the entropic coefficient.

4.2. Materials and Methods

4.2.1. Open Circuit Voltage (OCV) measurement

In batteries, the OCV is defined as the difference in voltage between the electrodes when no current is flowing through them and when they are at chemical equilibrium. Chemical equilibrium is important because OCV is a thermodynamic parameter and consequently it has to be evaluated after the relaxation of the kinetic processes [48,141].

In this study, OCV was measured by three different methods. At the first stage of the research, OCV was measured after a resting period of 24 hours, independently of the charge/discharge rate

being used. The OCV curves of the LCO cells (Fresh and Old Microbattery) were obtained by this method after a regular pulsed discharge at a rate of 1C. Leaving such a long resting period of 24 h could lead to some self-discharge during this time, which would modify the actual SoC of the cell. The OCV of EVbat cells (LFP) was also obtained by this method but at a C/8 charge/discharge rate and resting 2 h instead of 24 h.

The second method consisted of measuring the cell voltage under very low charge/discharge rates. When charging and discharging the cells at those low rates (i.e., C/25, C/50 or lower) kinetic effects are minimized and the measured voltage response is mainly affected by thermodynamic contributions. Therefore, those voltage curves can be related to the SoC and can be used to estimate the OCV [142]. Thus, pseudo-OCV or ps-OCV was obtained at every SoC by averaging the measured charging and discharging voltages measured at those low rates. In this study, this method was applied to NMC and VIC (LFP) cells.

The third method was based on the Galvanostatic Intermittent Titration Technique (GITT). It is a common technique used to measure the OCV of batteries [48,143]. It consists in charging and discharging the cell by pulses followed by relaxation periods. At the end of each relaxation period, the OCV is measured. GITT measurements were carried out during charge and discharge so two OCV curves were obtained: one for the charge and one for discharge. The difference between them can be attributed to kinetics introduced by the measurement or hysteresis introduced by the cell itself [86,144,145]. In particular, hysteresis corresponds to the existence of several possible thermodynamic equilibrium potentials for a particular SoC [86,146]. It is also considered as a result from mechanical stress [146]. One possible explanation based on the existence of a lithium rich and lithium deficient phase within an active particle was given in [147]. In particular, in this study, GITT was set to 2 h 30 min charge/discharge pulses at C/50 followed by 16 h resting period. To assure the same starting SoC, four charge/discharge cycles at C/50 constant current followed by a remnant capacity procedure at C/50 were performed prior to the GITT analysis. OCV was measured by this method for NMC and VIC cells (LFP).

Measurements were done with a VSP potentiostat/galvanostat from Bio-logic at ambient temperature (25 ºC) placed in an incubator IL 53 provided by Pol-Eko Aparatura.

4.2.2. Overpotential

Overpotential was calculated as the difference between the OCV and the cell voltage under polarization (refer to subchapter 1.2.2). In the case of LGC2 cells (NMC) and VIC cells (LFP) where GITT data were available at BoL and EoL, the generated overpotential was calculated from ps-OCV and OCV GITT curves and compared among them.

4.2.2.1.Contributions to overpotential

Ohmic overpotential, activation polarization and concentration polarization were separated from the total overpotential when impedance data were available.

The ohmic part of the total overpotential (η_Ω) was calculated directly from the ohmic resistance estimated in Chapter 3.

$$\eta_\Omega = I \cdot R_\Omega \tag{4.28}$$

The overpotential associated to activation polarization is related to the charge transfer process during the electrochemical reaction and follows the Butler-Volmer equation described in subchapter 1.2.2. For the calculation of activation contributions, charge transfer limitations were assumed, avoiding mass transfer effects. Moreover, as it was explained, there are two possible situations, one of them in which the Butler-Volmer equation can be linearized (at low overvoltages) and the other one where current and overpotential are related through a logarithmic function (at high overpotentials). Therefore, in this study, when the measurements were carried out close-to-equilibrium, we supposed we were working at low overpotentials and the linear approximation was considered. Therefore, the employed charge-transfer resistance for the overpotential calculation coincided with the measured charge-transfer resistance at the impedance measurements that were carried out in Chapter 3. Equation (1.5) was rewritten in (4.29) for convenience for the reader.

$$\eta_{\text{act}} = \frac{-\text{R} \cdot T}{n \cdot \text{F} \cdot i_0} \cdot I = R_{CT} \cdot I \tag{4.29}$$

Contrarily, when working at high rates (far-from-equilibrium), charge-transfer resistance does not follow anymore the linear approximation. In fact, charge-transfer resistance associated to activation polarization does not represent an ohmic effect so voltage and current do not follow a linear relation (Ohm's Law). Therefore, charge transfer resistance at high rates will depend on the applied current [148–150]. In our study, we considered as high rates those above 1C. In those situations, we calculated the exchange current from the impedance data by the use of equation (4.29). The exchange current represents the current at each of the electrodes when the cell is at equilibrium, thus when the net current is zero. Therefore, it does not depend on the rate but it does on the electrode composition or the SoC [151]. Once i_0 was calculated at every SoC from the impedance data, activation polarization was calculated as follows (equation (4.30) was rewritten from (1.7) for convenience to the reader).

$$\eta_{\text{act}} = -\frac{\text{R} \cdot T}{\alpha \cdot n \cdot \text{F}} (\ln i_0 - \ln i) \tag{4.30}$$

In this study, as no experimental data was available for the electron transfer coefficient, symmetric electron transfer was assumed (α = 0.5), as it is commonly done in literature and it is referred as a good approximation to experimental data [24].

In addition, concentration polarization was also estimated. However, it was done as the difference between the total overpotential and the ohmic and activation contributions. Thus, other effects as the side reactions that could produce an overvoltage would be also included in that term.

4.2.3. Entropy

4.2.3.1.Reversible entropy

The generation rate of reversible entropy can be obtained by multiplying the entropic coefficient to the discharge current as expressed in equation (4.27). The entropic coefficient was obtained by measuring the changes in OCV when varying the temperature of the cell. In order to induce temperature variations to the cells, different devices were used depending on their availability at the time of the tests. In particular, the entropic coefficient of the LCO cells (Old and Fresh Microbattery), was measured at steps of approximately 10% SoC. First, cells were fully charged to 100% SoC from where partial discharges were carried out with Cadex C7200-C battery analyzer to lead the battery to the desired SoC. After every discharge process, a 24 hours resting period was left for the open-circuit voltage to be stable. Then, batteries were immersed in a thermal bath with a magnetic mixer (MicroMagMix provided by Ovan). Temperature ranged from room temperature (around 20ºC) to 35ºC. For every SoC, the OCV variations showed a linear relationship with respect to temperature variations. Therefore, from the slope of that curve the entropic coefficient at the specified SoC was obtained.

In the case of NMC and LFP cells, temperature variations were performed by introducing the cells in a laboratory Pol-Eko incubator and the voltage response was monitored with a VSP potentiostat/galvanostat provided by Bio-logic. Discharge was done at low rate steps (C/25) of approximately 10 % SoC followed by a 4 hours relaxation period prior to proceed with the temperature sweep. Temperature was set first to 10 ºC, then to 20 ºC, and 30 ºC at the end. For each temperature, a relaxation period was left before beginning the next temperature sweep until the cell temperature was stable, and then the open-circuit voltage was measured at that point. Linear fit was done to the corresponding measured voltage points corresponding to the three set temperatures. Therefore, the slope of that curve corresponded to the derivative of the OCV with respect to temperature, which corresponded to the entropic coefficient.

4.2.3.2. Irreversible entropy

These measurements are a novelty contribution. We briefly point out the main characteristics of the measurements but we analyze them later in the discussion section.

The irreversible entropy production in a battery was calculated from (4.22) and (4.25). Thus, it was calculated from the total measured overpotential under polarization, which represented the irreversible loses (1.2). Different contributions to overpotential were separated as explained in subchapter 4.2.2.1. The ohmic overpotential was associated to ohmic conduction as expressed in

equation (4.21) and the terms related to activation and concentration polarizations were associated to the chemical reactions. . Thus, the generation rate of irreversible entropy was obtained from voltage, current and temperature measurements. Therefore, no extra measurements other than regular cycling were required.

4.2.4. Incremental capacity analysis (ICA)

ICA was carried out at low charge/discharge rates in order to obtain the closest voltage curve to the thermodynamic voltage (OCV) by minimizing the kinetic effects. Thus, the injected or extracted charge was represented versus the measured voltage curves. At that point, incremental capacity (IC) was obtained as the portion of capacity associated to a certain voltage step ($\Delta Q/\Delta V$). Peaks in the IC curves correspond to plateaus at the thermodynamic voltage curve. A plateau represents a two-phase domain in the equilibrium phase diagram of the cell. Thus, it represents a phase transition where some particles have a certain amount of lithium (one phase) and the rest have a different one (another phase). Each peak at the IC curve has a unique shape and a particular intensity. Moreover, every chemistry has a characteristic peak pattern. Contrarily, changes in slope in the thermodynamic voltage curve (transitions between plateaus) represent a solid solution where all the particles are at the same phase (one-phase domain) [152–154].

ICA is a valuable tool to quantify capacity loss. Loss of capacity can be mainly associated to loss of lithium inventory (LLI) available for cycling, loss of active material (LAM), increase in resistance and loss of electrolyte. The loss of active material can be produced at positive or negative electrode (LAM_{PE} or LAM_{NE}, respectively) depending on whether it happens during charge or discharge processes. The isolated particles can contain lithium or not (LAM_{LiPE} or LAM_{LiNE} for lithiated particles and LAM_{dePE} or LAM_{deNE} for delithiated particles). Because of LLI and LAM, electrodes can shift, elongate or contract with respect to each other [155]. Information about loss of lithium and loss of active material can be obtained by tracking the evolution of peaks at IC analysis [155]. In addition, information about the kinetics of the reactions can be extracted from the shape of the peaks at the IC curves [155].

In the case of LGC2 cells (NMC), Alawa battery emulation toolbox in Matlab [155] was used to adjust the obtained curves to the simulated ones in order to discriminate the effects that caused the capacity fade. This software provided preloaded cycling data of the positive and negative electrodes of those particular cells. The curves were adjusted to the available curves by sweeping the loading ratio (LR) and the offset (OFS), which define the matching between the electrodes [155]. The loading ratio represents the elongation or contraction of the electrodes meaning the relation between the available active material in positive and negative electrodes. In contrast, the OFS represents the shift between the electrodes that comes from the different SoCs at which they are.

4.2.5. Heat calculations

The determination of heat generation produced inside the cell was carried out considering dissipative (dQ_P) and reversible (dQ_S) effects [156].

$$\frac{dQ_{total}}{dt} = \frac{dQ_P}{dt} + \frac{dQ_S}{dt} = (OCV - V_{cell}) \cdot I - T \cdot \frac{d(OCV)}{dT} \cdot I \qquad \textbf{(4.31)}$$

Where T is the cell temperature and the current I was defined negative during charge and positive during discharge.

4.3. Results

In this section, we present the results per battery chemistries (NMC, LFP and LCO). In particular, OCV, overpotentials, entropy production and heat evolution are investigated in detail.

4.3.1. NMC cells

4.3.1.1. OCV

The OCV of the NMC cells was estimated by two methods: ps-OCV and GITT-OCV. In particular, the evolution of ps-OCV with cycle aging showed an increase at some SoCs and a decrease at some others (Fig. 4.3). Mainly, three distinguishable SoC areas where ps-OCV followed a particular tendency were found. From 60 % to 30 % and from 15 % to 3 % the OCV was higher as more cycled was the cell. In contrast, between 30 % and 15 % the opposite happened: as more degraded was the cell, the lower the OCV. The same behavior was found in both of the represented cells in Fig. 4.3, which were cycled in the same conditions, what indicated a good repeatability of the results.

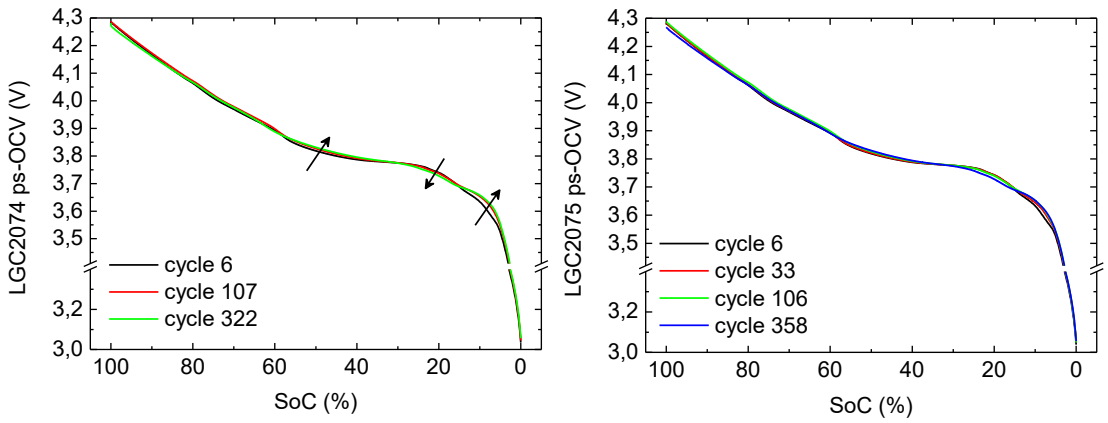

Fig. 4.3. Pseudo-OCV evolution during cycle life of LGC2074 cell (left) and LGC2075 cell (right) calculated from charge/discharge curves at C/25.

OCV curves obtained from GITT measurements were compared to ps-OCV obtained by averaging charging and discharging curves at C/25 rate. Comparison was made at BoL and EoL of the NMC cells (Fig. 4.4). The comparison of discharge OCV at BoL and EoL obtained from the GITT analysis is depicted in Fig. 4.5. Its trend was similar to the one of ps-OCV (Fig. 4.3) but the variations with aging were less pronounced.

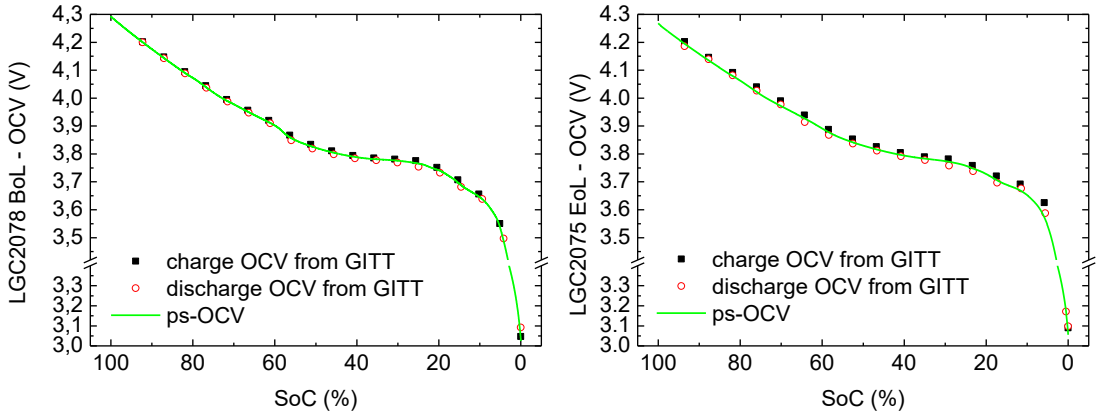

Fig. 4.4. Comparison of charge and discharge OCV curves of LGC2 cells (NMC) at BoL and EoL measured by GITT and ps-OCV.

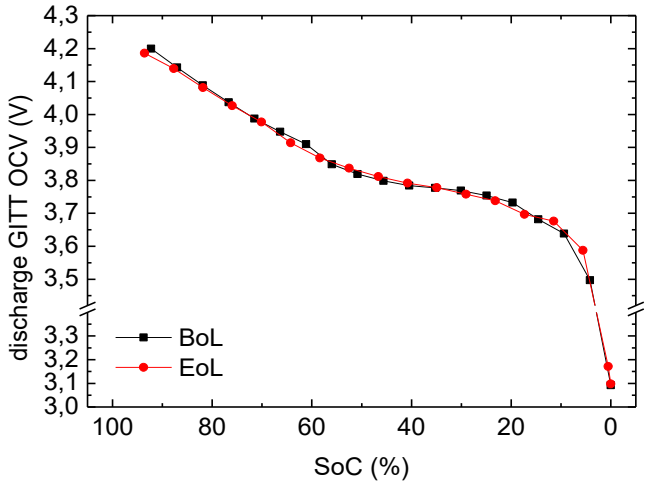

Fig. 4.5. Discharge OCV curves at BoL and EoL of LGC2075 cell (NMC) obtained from GITT measurements.

4.3.1.1.1. Hysteresis

Hysteresis voltage, calculated as the difference between OCV curves during charge and discharge processes, is represented in Fig. 4.6. At both BoL and EoL, the voltage difference was below 30 mV in all the SoC range. In addition, it was found that the hysteresis voltage was higher as more degraded was the cell. In general, hysteresis increased as the SoC was decreased.

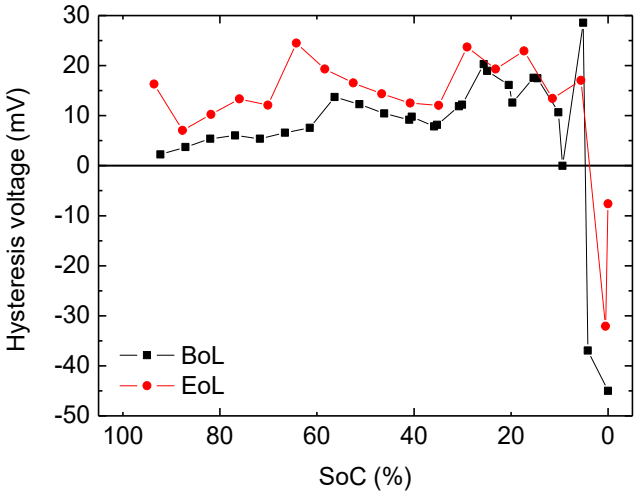

Fig. 4.6. Hysteresis voltage at BoL and EoL calculated as the difference in OCV during charge and discharge measured by using the GITT technique.

4.3.1.2. Incremental capacity analysis

Incremental capacity analysis was carried out to LGC2 cells (NMC). The results showed the evolution of the shape of peaks, their position and intensity during their cycle life at a charge rate of C/25 (Fig. 4.7). The major differences with cycles were found at peaks 2, 4 and 5. Peak 2 got higher amplitude as more cycles were carried out, peak 4 decreased in capacity and peak 5 shifted to higher voltages and decreased in intensity. From the analysis of the IC data with Alawa battery emulation toolbox [155], LLI and LAM were quantified during the cycle life of the cells (Table 4.2). The results suggested that during the first 100 cycles, the decrease in capacity was mainly due to LLI and loss of active material at the negative electrode. From cycle 107 to 322, they continued growing until the EoL and the positive electrode started losing active material. The associated capacity fades to these aging mechanisms were 4 % during the initial 100 cycles and 13 % during the full completion of the aging test.

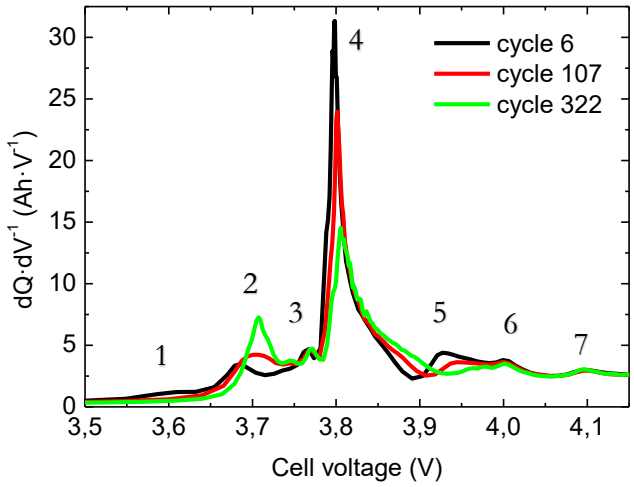

Fig. 4.7. Incremental capacity curves during charge process at a C/25 rate upon cycling of LGC2074 cell (NMC). It has to be noticed that resistive contributions has been subtracted prior to the analysis.

Table 4.2. Loss of active material (LAM) and loss of lithium inventory (LLI) during the aging test of LGC2074 cell (NMC).

	$LAM_{Li}NE$	$LAM_{de}NE$	$LAM_{Li}PE$	$LAM_{de}PE$	LLI	Capacity fade
From cycle 6 to 107	-	2.5 %	-	-	5 %	4 %
From cycle 6 to 322	0.5 %	10 %	-	1.8 %	11.8 %	13 %

4.3.1.3. Overpotential

4.3.1.3.1. Close-to-equilibrium measurements

Overpotential was calculated subtracting discharge voltage curves at C/25 from ps-OCV curves. In Fig. 4.8, overpotentials generated by two NMC cells that were aged in the same conditions were represented. In both cases, the overvoltage increased as the cell aged, showing a good repeatability of the results. However, at some SoCs the overpotential increased faster with aging than at others.

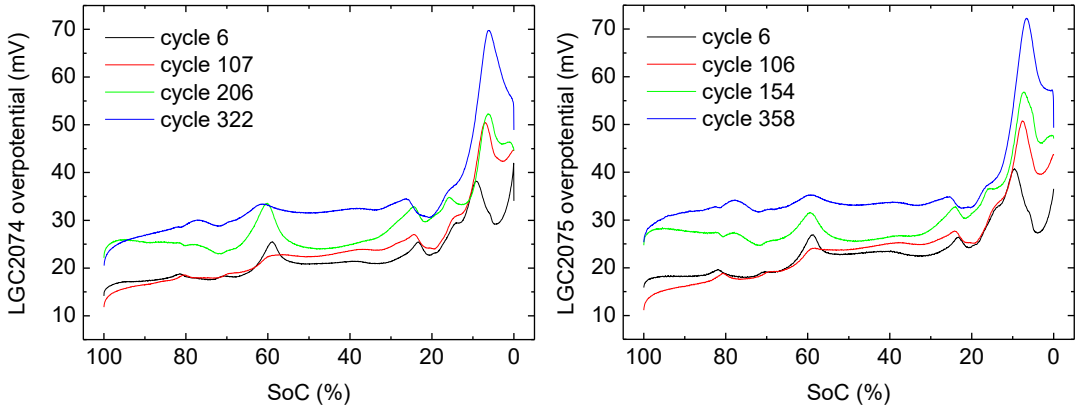

Fig. 4.8. Evolution of the overpotential at C/25 obtained from the ps-OCV curve of two NMC cells (LGC2074 cell to the left and LGC2075 to the right) during their cycle life.

Overpotential generated at NMC/Li and graphite/Li half-cells during discharge

The overpotential generated at a C/25 discharge rate at positive and negative electrodes was calculated with the data obtained from the half-cells we build during the post-mortem analysis (detailed in Chapter 5) by the use of equation (4.32) [48]. The counter electrode was lithium metal in both cases. The represented SoCs in Fig. 4.9 and Fig. 4.10 do not correspond to the full cell SoC but to the half-cells SoC. In particular, PE SoC and NE SoC were calculated between the corresponding minimum and maximum cut-off voltages selected for the tests carried out at each of the electrodes, without accounting for the electrode's matching at the full cell.

$$OCV = OCV_{PE} - OCV_{NE} \tag{4.32}$$

The OCV shifted mostly to lower voltage values in both the PE and NE electrodes, except for intermediate SoCs at the PE where it shifted to higher values (left part in Fig. 4.9 and Fig. 4.10). In addition, the overpotential increased in both electrodes (right parts in Fig. 4.9 and Fig. 4.10). The initial overvoltage of the fresh cell was higher at the negative electrode (around 20 mV in contrast to 10 mV found at the PE). However, the highest increase during the aging process was found at the positive electrode, going from those 10 mV at SoCs higher than 30 % to around 28 mV at the EoL. In contrast, the increase in overpotential between BoL and EoL at the NE was around 2 mV. Furthermore, overpotential curves showed a characteristic shape with peak pattern, which was maintained during the aging process of the cells.

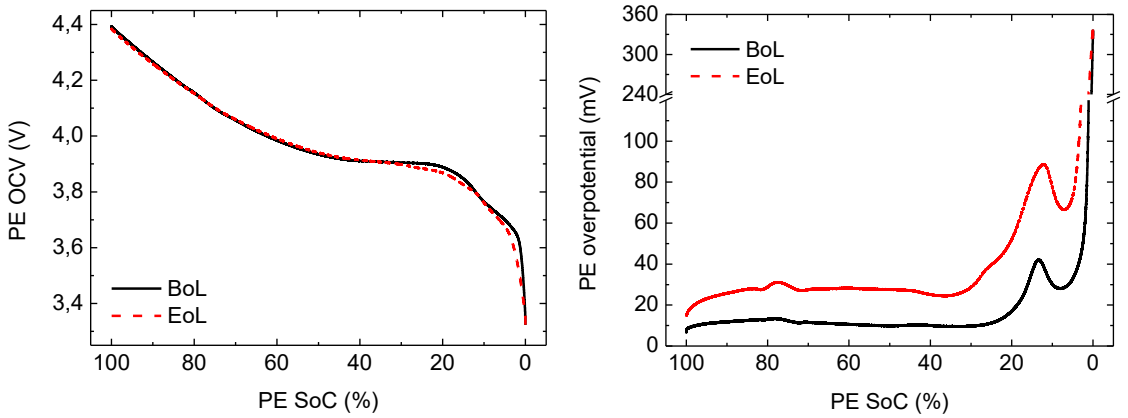

Fig. 4.9. (left) OCV evolution with cycle aging and (right) overpotential evolution at C/25 with cycle aging of the Li/NMC half-cell.

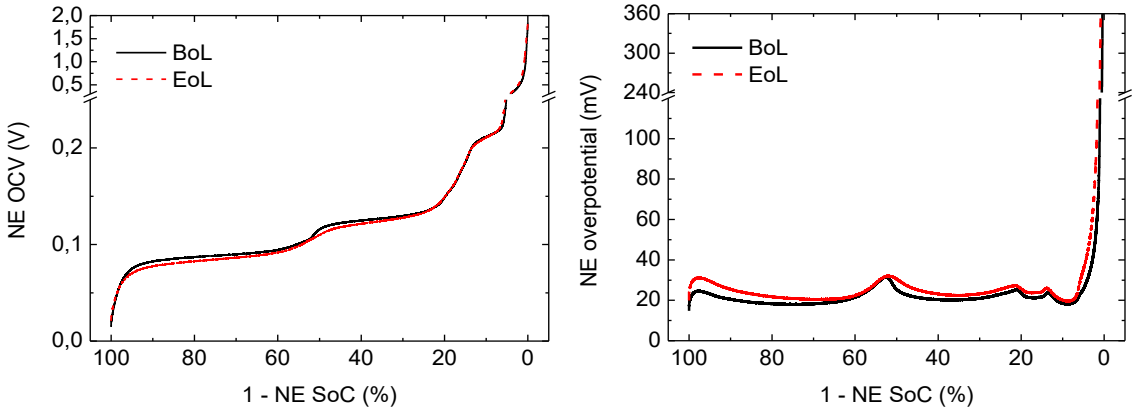

Fig. 4.10. (left) OCV evolution with cycle aging and (right) overpotential evolution at C/25 with cycle aging of the Li/Graphite half-cell.

Although it was previously mentioned that PE SoC and NE SoC did not correspond to the actual SoC of the full-cell neither they corresponded to each other, they were assumed both equal to the PE SoC in order to make a rough approximation of the total generated overpotential at the full-cell. (Fig. 4.11). The highest contributor to overpotential at BoL was the NE. However, the overpotential generated at the PE suffered a higher increase from BoL to EoL making both contributions comparable. The addition of the overpotentials generated at both electrodes, maintained a characteristic peak of the NE at intermediate PE SoCs and a characteristic peak of the PE at low PE SoCs.

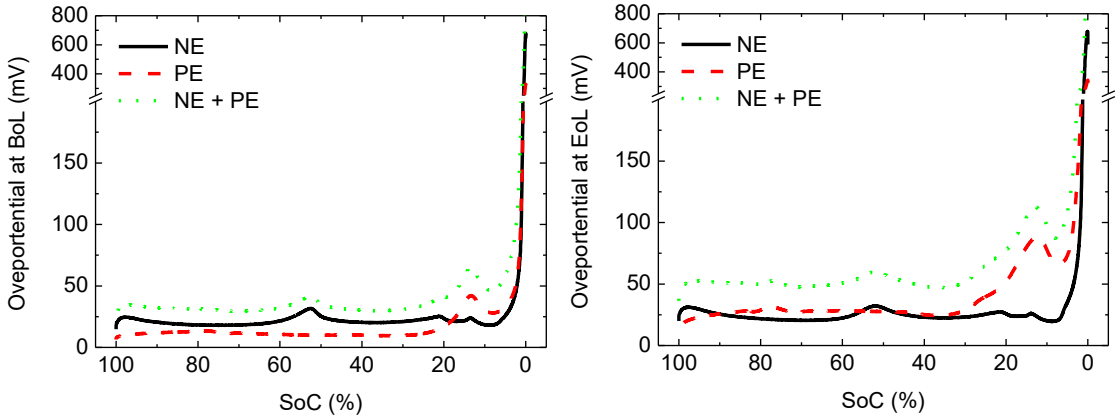

Fig. 4.11. Overpotential generated at the PE and NE electrodes measured in half-cell configurations discharged at a C/25 rate (NMC/Li and graphite/Li) at BoL (left) and EoL (right). PE and NE overpotentials were added without taking into account the matching of the electrodes in order to obtain a rough approximation of the overpotential generated at the full-cell.

4.3.1.3.2. Far-from-equilibrium measurements

Overpotential was calculated at a discharge rate of 3C/2 as the difference in voltage between the ps-OCV and the cell voltage under this current (Fig. 4.12). The evolution with cycle aging showed an increase of the overpotential in all SoCs during the aging process. In all the evaluated cycles, the shape of the curve was maintained: the overvoltage was rather constant between 100 % and 60 %, then slightly decreased from 60 % to 50 %, and finally suffered a sharp increase between 50 % and the EoD.

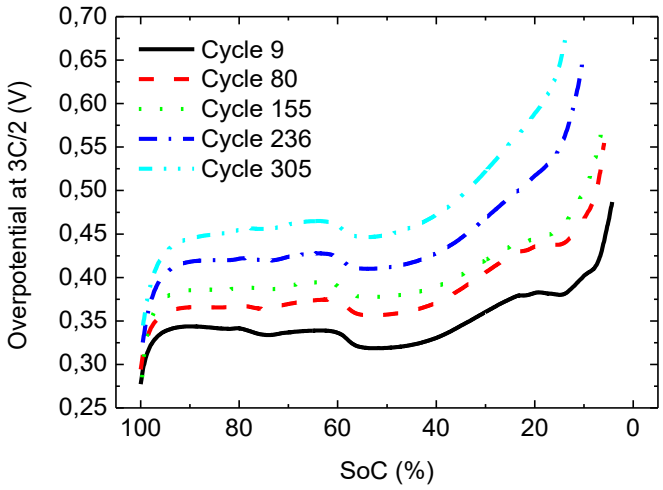

Fig. 4.12. Overpotential generated in a NMC cell at a 3C/2 discharge rate at different aging stages.

4.3.1.3.3. GITT and ps-OCV approximations

GITT-OCV and ps-OCV were compared in order to estimate the error introduced when using ps-OCV curves instead of the actual OCV of the cell. One particularity of the OCV curves obtained

from GITT measurements is that they account for hysteresis during charge and discharge, making them more accurate than ps-OCV. However, ps-OCV is a less time consuming technique and gives more resolution in the SoC range because the resolution is fixed by the V_{cell} measurement (relaxation periods before the measurements are not required). In Fig. 4.13, the overpotentials obtained by using the OCV obtained by the two methods were plotted at BoL (left) and at EoL (right). At SoC = 100 %, the difference in overvoltage obtained by the two methods (calculated as the difference between the overpotential calculated by GITT technique and the one obtained by the ps-OCV approximation) differed in less than 5 mV but then this difference went to 10 – 15 mV until 60 – 65 % SoC (Fig. 4.14). From here on, the difference decreased and stayed below 5 mV until SoC was 30 % from which both curves showed a negative error until SoC was 15 %. At that point, the difference increased sharply and positively until the EoD, where it was in between 50 mV and 60 mV.

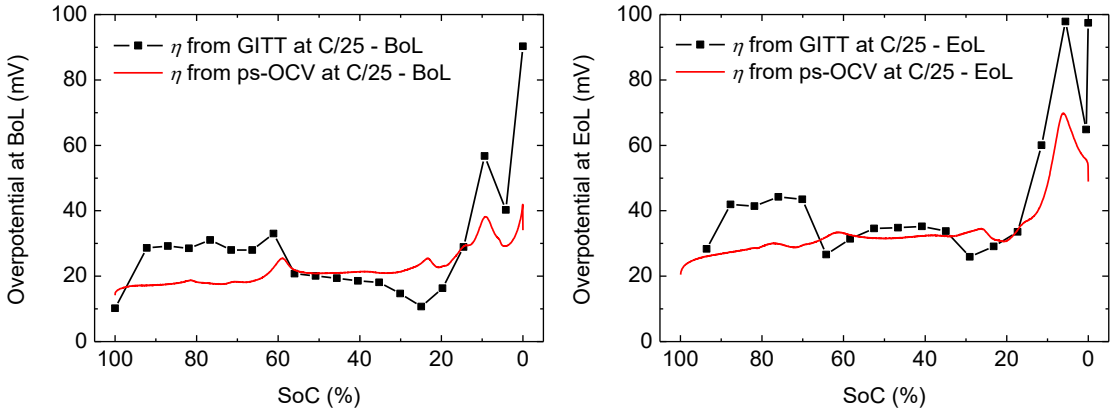

Fig. 4.13. Comparison of the overpotential generated at C/25 calculated from the discharge GITT OCV (line + markers) and the ps-OCV (solid line) at BoL (left) and at the EoL (right).

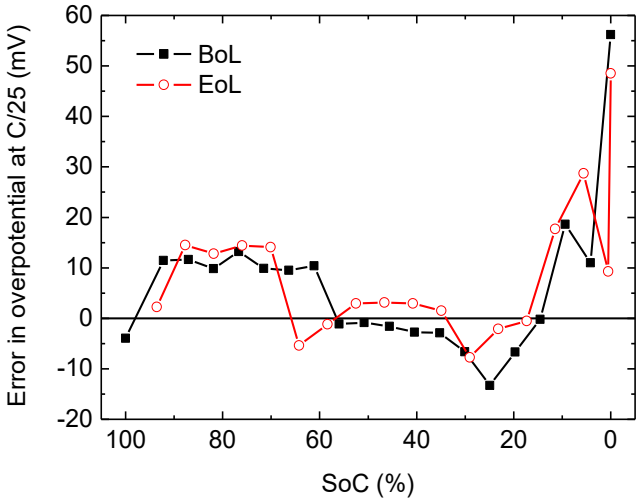

Fig. 4.14. Error in overpotential at C/25 introduced when using ps-OCV instead of GITT OCV during discharge at BoL and EoL

4.3.1.3.4. Apparent resistance

The apparent resistance was calculated as the overpotential divided by the discharge current. It was obtained at low and moderate rates at BoL and EoL (Fig. 4.15). The apparent resistance at a C/25 discharge rate was higher than that at 3C/2. Nevertheless, at both discharge rates, the associated resistance was higher at the EoL than at BoL.

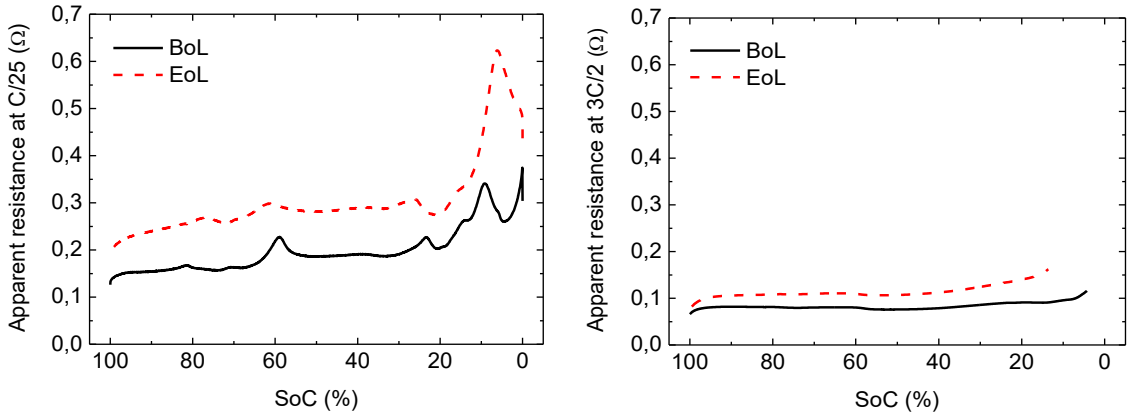

Fig. 4.15. Apparent resistance calculated from the overvoltage curves while discharging a NMC cell at C/25 (left) and at 3C/2 (right) rates.

4.3.1.3.5. Contributions to overpotential

Contributions to overpotential at a C/25 discharge rate obtained from the discharge GITT-OCV were represented in Fig. 4.16 at BoL (left) and EoL (right). As it was explained at section Chapter 4, ohmic and activation polarizations were obtained from impedance measurements carried out in Chapter 3. Thus, estimated ohmic and charge-transfer resistances from impedance measurements were employed for calculating the corresponding overpotentials. The smallest contribution was due to the activation overpotential followed by the ohmic contribution. In our impedance study, the contribution of mass transfer effects was not estimated. However, it cannot be avoided during a complete discharge cycle in which most of the cases it becomes dominant. Therefore, concentration overpotential represented in Fig. 4.16 was obtained as the difference between total overpotential and ohmic and activation overpotentials. As it can be seen, concentration overpotential became dominant at these low discharge rates (C/25) in all SoC ranges at both BoL and EoL except at SoC around 25 % at BoL.

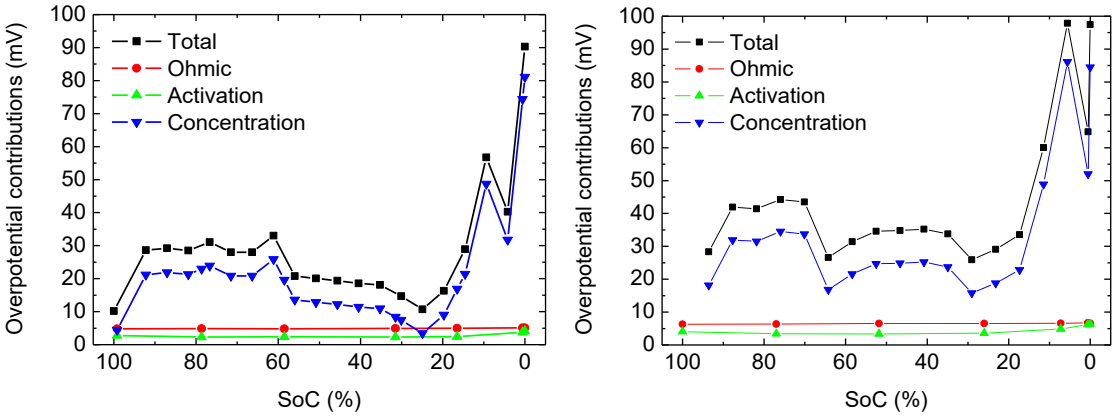

Fig. 4.16. Overpotential contributions at BoL (left) and EoL (right) while discharging the NMC cell at a C/25 rate at ambient temperature. Calculations were made with discharge GITT OCV.

The overpotential generated at a discharge rate of 3C/2 was represented in Fig. 4.17. The increasing factor of the overpotential at this rate with respect to C/25 was around 10. Moreover, the different contributions were present in a different extent when compared to lower discharge rates (Fig. 4.16). In that case, the dominant effect was the one associated to ohmic conduction. Ohmic and activation polarizations were also obtained from the impedance data analyzed in Chapter 3. However, charge transfer resistance had to be recalculated in order to account for the dependence of this resistance to high currents. In addition, concentration polarization was calculated as the difference between total overpotential and the addition of ohmic and activation polarizations. In particular, concentration polarization started the discharge process being the less dominant effect but increased during the process exceeding ohmic and activation polarizations at the EoD. The same behavior at BoD was found at a discharge rate of C/25 (Fig. 4.16).

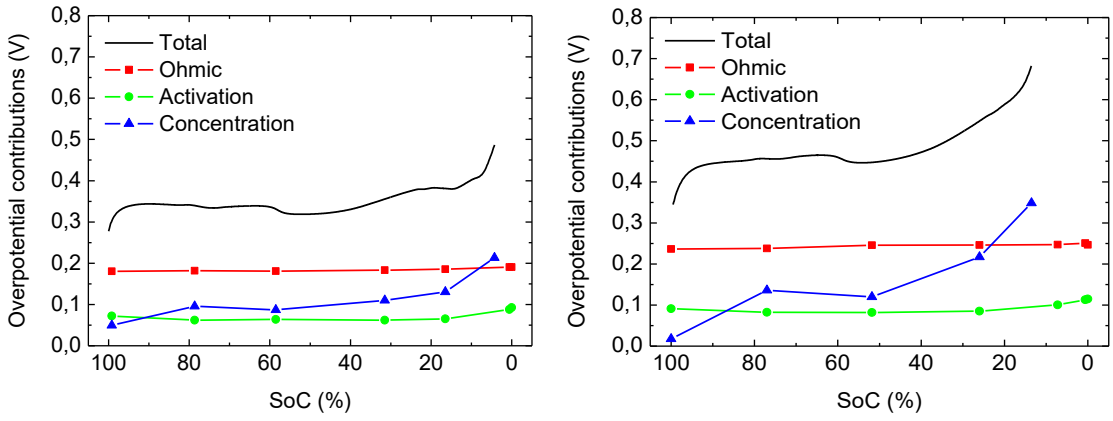

Fig. 4.17. Overpotential contributions at BoL (left) and EoL (right) while discharging the NMC cell at a 3C/2 rate at ambient temperature.

4.3.1.4. Entropy

4.3.1.4.1. Reversible entropy

The entropic coefficient measured at different SoCs was obtained from the variation of the OCV with temperature (Fig. 4.18). In all the evaluated SoCs, the entropic coefficient got negative values. Thus, contributing additional heat during discharge and subtracting heat during charge. Moreover, no significant differences between BoL and EoL were found.

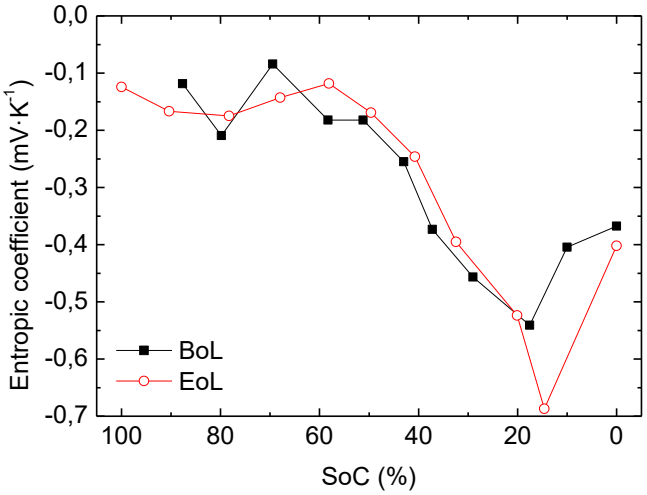

Fig. 4.18. Derivative of the OCV with respect to temperature of a LGC2 cell (NMC) at BoL (black filled squares) and at the EoL (red unfilled circles).

4.3.1.4.2. Irreversible entropy

Close-to-equilibrium measurements

The generation rate of irreversible entropy at a C/25 discharge rate was obtained during the cycle life of two LGC2 cells (NMC) at room temperature (Fig. 4.19). Right and left figures in Fig. 4.19 represent the evolution of two NMC cells cycled in the same conditions, what showed a good repeatability of the results. d$i\mathcal{S}$ showed a general increasing tendency as the cells were aged. However, in the first 100 cycles it decreased in the initial 15 - 20 % SoCs of the discharge process. Moreover, it was true for all cycles that at some particular SoCs, the increasing factor with aging of d$i\mathcal{S}$ was lower. These particular SoCs were 60 % and the range between 25 % and 10 %. Similar results were obtained from the GITT OCV curves, as illustrated in Fig. 4.20 at BoL and EoL. When comparing the entropy production obtained from ps-OCV with the one obtained with GITT, it has to be taken into account the error in overpotential calculations we introduced in the ps-OCV approximation (Fig. 4.14).

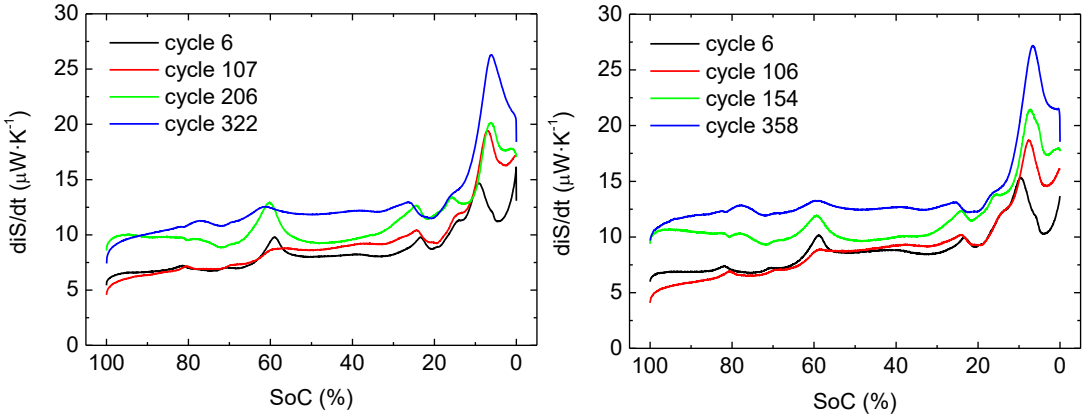

Fig. 4.19. Evolution of the irreversible entropy generation rate obtained from the ps-OCV curve at C/25 of two NMC cells (LGC2074 cell to the left and LGC2075 to the right) during their cycle life.

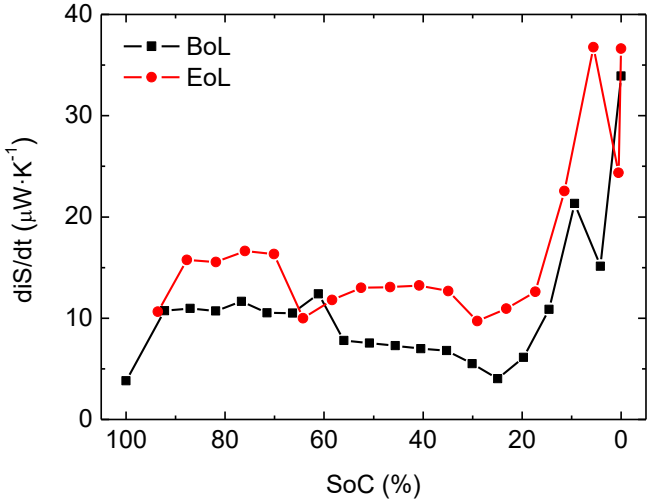

Fig. 4.20. Irreversible entropy production in a NMC cell at BoL and EoL when discharged at a C/25 rate at ambient temperature. It was obtained from the OCV curves obtained from the GITT measurements.

The different effects contributing to the generation rate of irreversible entropy at BoL and EoL were plotted in the left and right parts of Fig. 4.21. At a C/25 discharge rate, ohmic and activation effects were those that contributed least to the total generation rate. Thus, the generation rate of irreversible entropy associated to concentration polarization was the predominant effect, which increased faster towards the EoD.

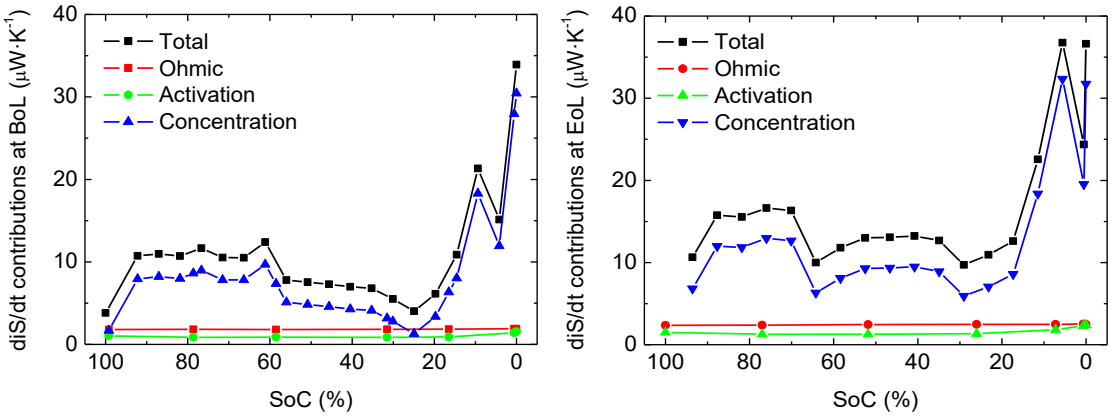

Fig. 4.21. d_iS/dt contributions at BoL (left) and EoL (right) while discharging the NMC cell at a C/25 rate at ambient temperature. The results were obtained from the discharge GITT OCV curves.

Concerning the evolution of the contributors to entropy production with the aging level, ohmic, activation and concentration polarization increased as the cell was aged, except at SoC near 60 % where the term related to concentration polarization decreased (Fig. 4.22). The relative contributions to the total entropy production coincide at some SoCs at BoL and EoL. However, at SoCs between 60 % and 20 %, the relative contribution of the concentration term at the EoL was higher than that at BoL. Consequently, the relative contributions of the other effects at EoL were reduced at these SoCs.

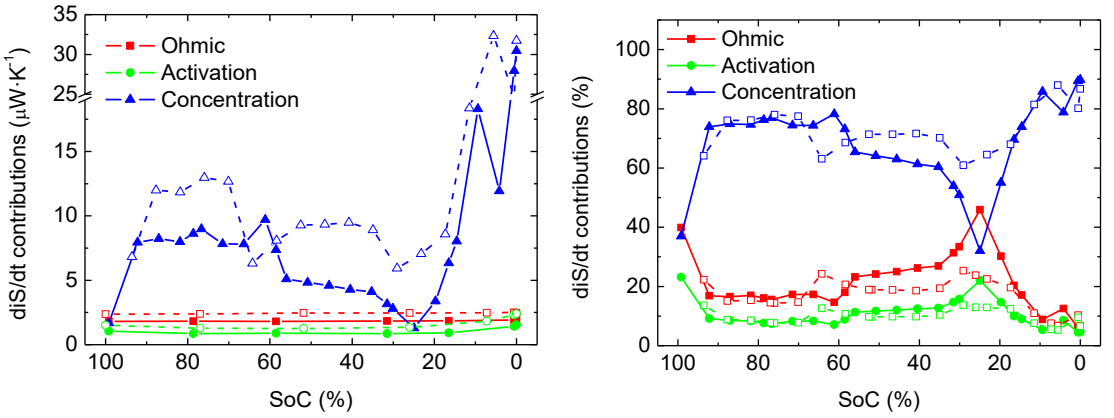

Fig. 4.22. (left) Absolute and (right) relative d_iS/dt contributions to total d_iS/dt at BoL (solid lines + filled symbols) and at the EoL (dashed lines + empty symbols) when discharging the NMC cells at a C/25 rate at ambient temperature.

Far-from-equilibrium measurements

The generation rate of irreversible entropy for the NMC cells discharged at a 3C/2 rate at different cycling levels was estimated (Fig. 4.23). It was found that d_iS/dt increased as the cells aged. It represents that irreversible entropy was generated faster as more cycles were carried out to the cells. Then, the corresponding contributions were separated at BoL and EoL (Fig. 4.24). At BoD, the less contributing effect was the concentration polarization. However, in the first 10 % SoC it got

higher than the one related to activation polarization at both BoL and EoL. Nevertheless, the major contributor was the one related to ohmic effects except at very low SoCs. The absolute and relative contributions to the total irreversible entropy production were represented in Fig. 4.25. All the effects increased their entropy generation rate as the cell aged (left side of Fig. 4.25). However, the relative increase of the irreversible entropy production due to charge-transfer effects was independent of aging (right side of Fig. 4.25). Nevertheless, the other contributions diverged at extreme SoCs but were also independent of aging at SoCs between 80 % and 50 %.

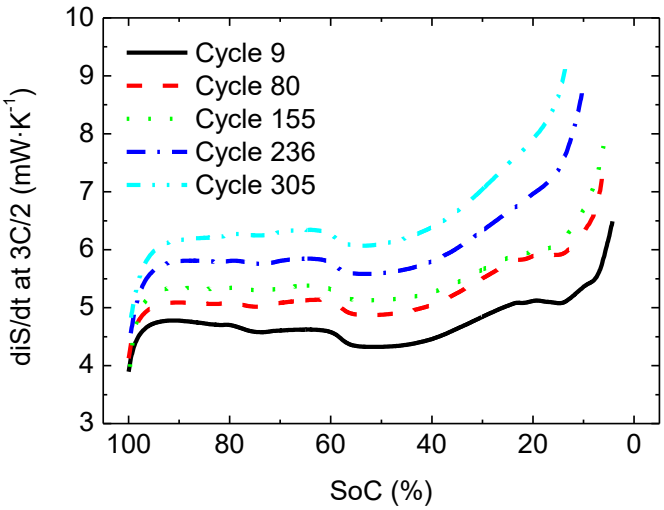

Fig. 4.23. Irreversible entropy production in a NMC cell at a 3C/2 discharge rate at different aging stages.

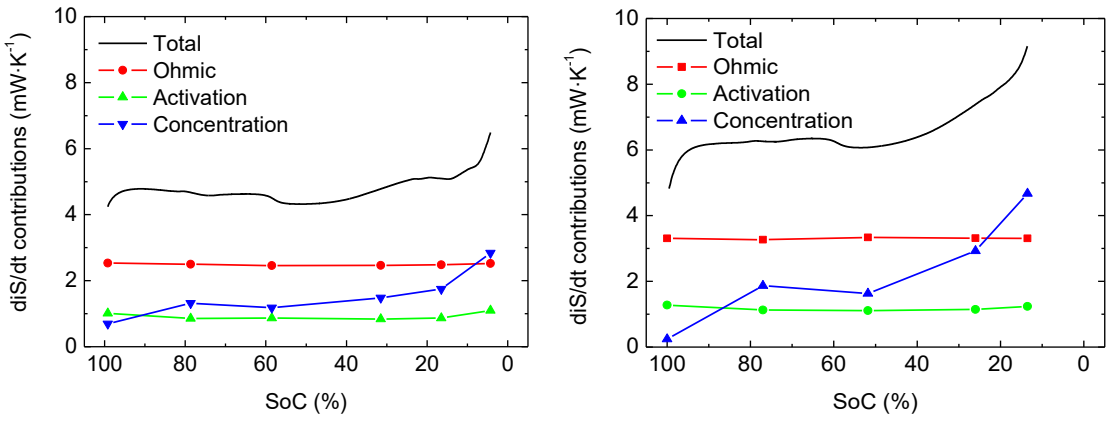

Fig. 4.24. d_iS/dt contributions at BoL (left) and EoL (right) while discharging the NMC cell at a 3C/2 rate at ambient temperature.

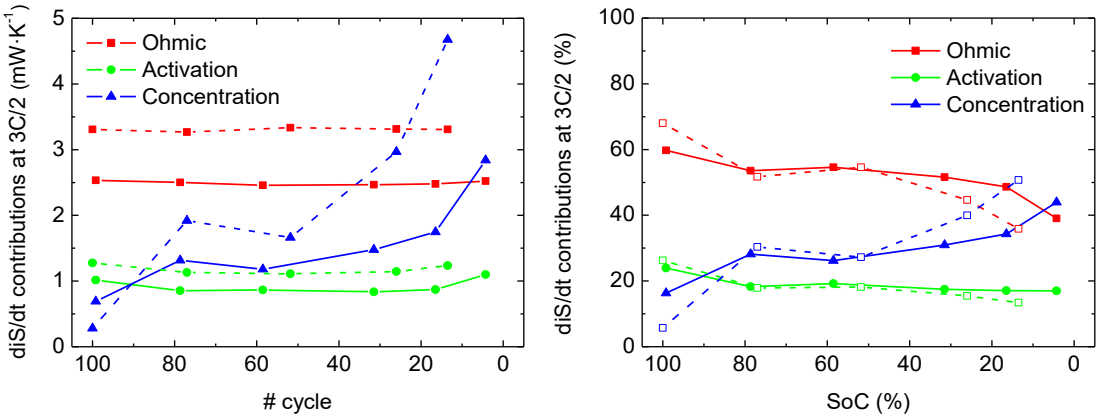

Fig. 4.25. (left) absolute and (right) relative d_iS/dt contributions to total diS at BoL (solid lines + filled symbols) and at the EoL (dashed lines + empty symbols) when discharging the NMC at a 3C/2 rate at ambient temperature.

4.3.1.5. Heat generation

4.3.1.5.1. Close-to-equilibrium measurements

From the produced overvoltage at a C/25 discharge rate, the irreversible (or dissipative) heat generation rate (dQ_P) was obtained from equation (4.31) (top-left part of Fig. 4.26). In the SoC range between 100 % and 20 %, the increase in heat generation from BoL to EoL was roughly constant of around 1.5 mW (60 % increase). In contrast, at SoCs around 10 % a larger increase of 3.5 mW (100 % increase) was found. Moreover, we also calculated the generation rate of reversible heat at a C/25 discharge rate from the entropic coefficient and the cell temperature (top-right side of Fig. 4.26). Remarkable variations were not found between the reversible heat generated at BoL and EoL during most of the evaluated SoCs but at SoCs below 20 %. The reversible heat was the dominant term in such conditions. The reversible heat is commonly neglected because at high current rates, it becomes negligible compared to the dissipative term, as we discuss in the next section. Thus, at these low rates, the shape of the total heat generation rate was dominated by the reversible term (bottom in Fig. 4.26). Between SoCs 100 % and 60 % it was almost constant and then increased until SoC = 20 % from which it decreased again. The main difference between the generation rate of heat at BoL and EoL was found at SoCs below 20 %.

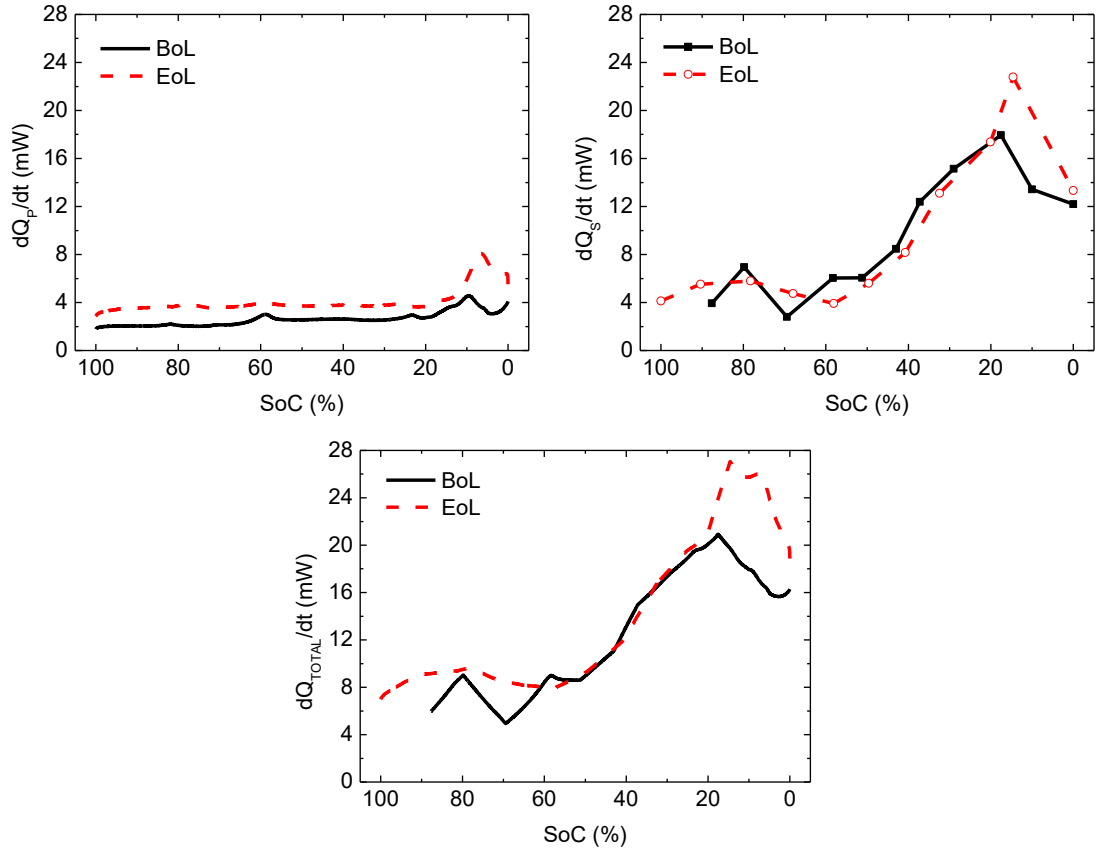

Fig. 4.26. Irreversible heat generation rate (top- left), reversible heat generation rate (top- right), and total heat generation rate (bottom) at BoL and EoL of LGC2075 cell (NMC) discharged at a rate of C/25.

4.3.1.5.2. Far-from-equilibrium measurements

Total heat generation rate was calculated as the addition of the reversible and irreversible heat productions as it was stated in equation (4.31). The three contributions were represented in Fig. 4.27. Due to the fact that the cell was working at moderate-high rates (3C/2), the irreversible contribution was much higher than the reversible one. However, the difference was not large enough to neglect the reversible term. Total generation of heat was roughly constant between 100 % and 50 % SoC. From that point and until the EoD, it increased sharply. The reversible term (dQ_S) was independent of aging. The main term increasing from BoL to EoL was the dissipative term (dQ_P). dQ_P increased around 0.5 – 0.6 W from the beginning of the aging test to the end of it, representing a relative increase of around 40 % - 50 %.

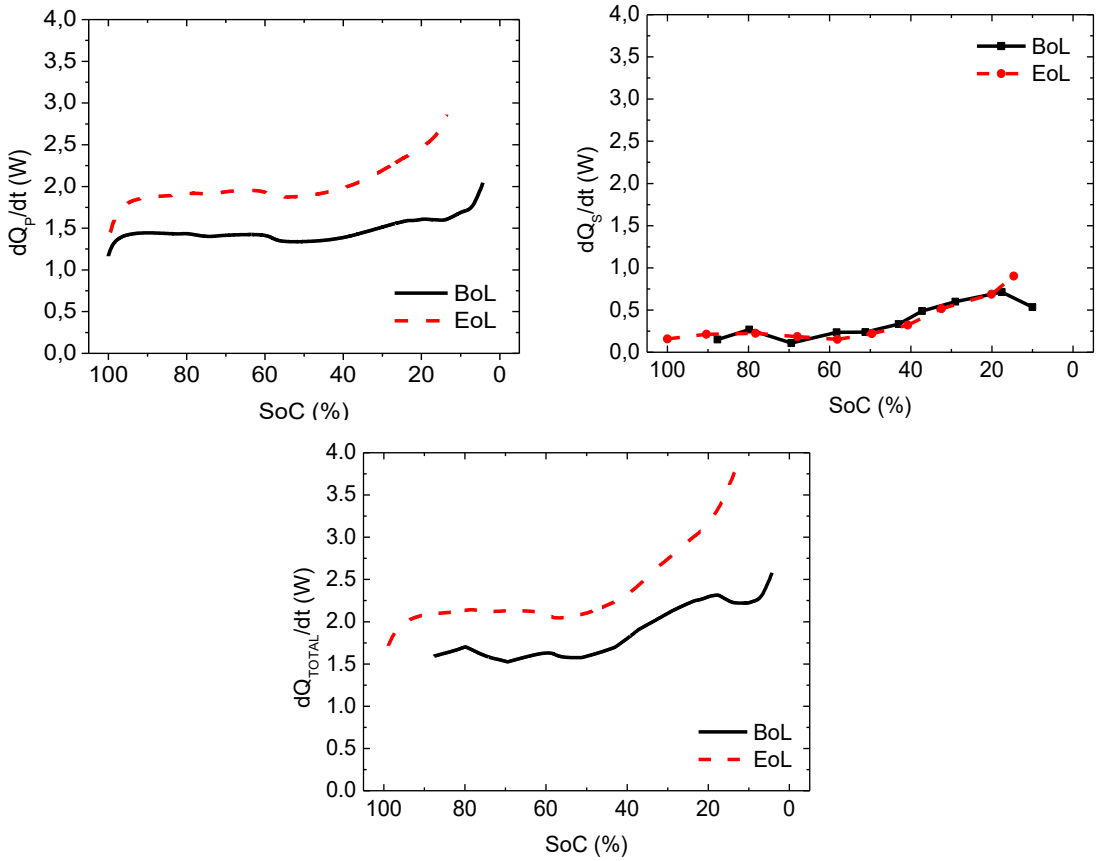

Fig. 4.27. Evolution of irreversible heat generation rate (top-left), reversible heat generation rate (top-right) and total heat generation rate (bottom) with cycles in the particular case of LGC2074 cell (NMC) represented for every SoC during a discharge process at 3C/2 rate.

4.3.1.6. Dependence on temperature

NMC cells at BoL and EoL were evaluated at different temperatures (5 ºC, 15 ºC, and 32 ºC), as illustrated in Fig. 4.28. The OCV increased with temperature for high SoCs (from 100 % to 60 %) and for low SoCs, around 10 % SoC. However, the OCV decreased for SoCs around 20 % - 30 %. In the rest of SoC values, it remained constant. Those differences in the OCV at different temperatures were more pronounced for the aged cell (right part of Fig. 4.28). Thus, the dependence of the OCV with temperature was also affected by the aging level or the SoH of the cells.

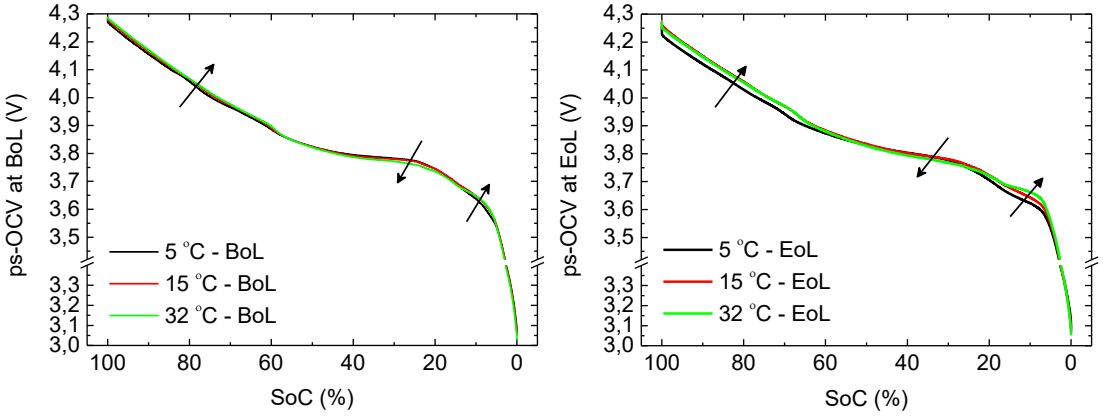

Fig. 4.28. Ps-OCV dependence on temperature for a LGC2 cell at BoL (left) and at the EoL (right).

Regarding the overpotential (Fig. 4.29) and thus, the generation rate of irreversible entropy (Fig. 4.30), we found that in general they were higher for lower temperatures at both BoL and EoL. In particular, the general tendency found at BoL was that the overpotential increased while the temperature decreased. In contrast, the overpotential at the EoL showed small differences between 15 ºC and 32 ºC at SoCs higher than 20 %. However, the irreversible entropy production followed the expected tendency at SoCs below 60 %. Therefore, even though the produced overvoltages at the same discharge current but different temperatures did not differ one from the other in some cases, $di\mathcal{S}$ that was calculated from the overvoltage, followed the expected tendency with aging (Fig. 4.30).

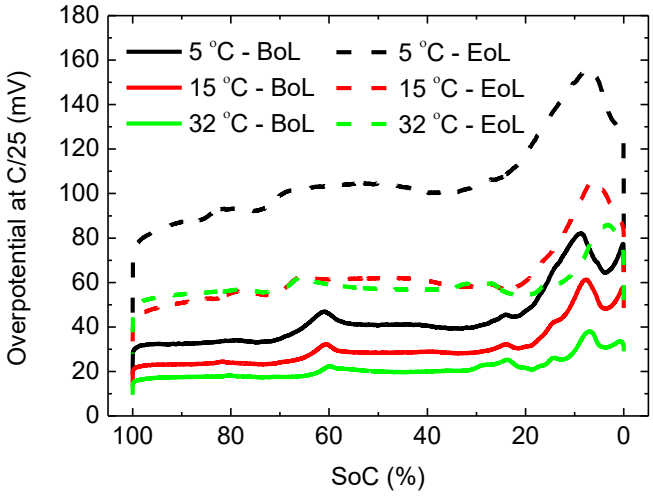

Fig. 4.29. Overpotential evolution with temperature at C/25 of a NMC cell at BoL (solid lines) and at the EoL (dashed lines).

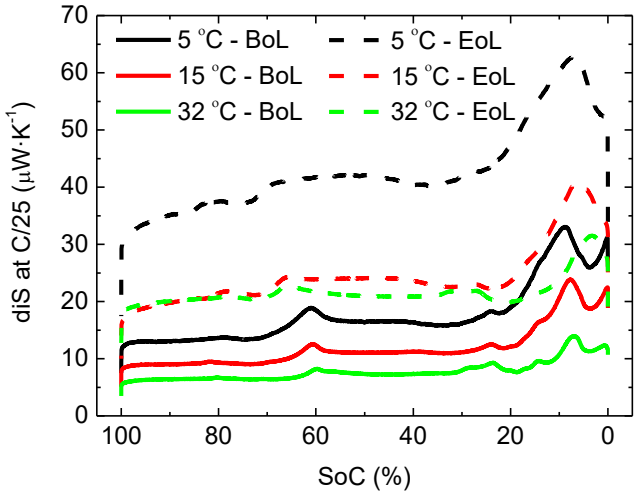

Fig. 4.30. Evolution of the irreversible entropy generation rate with temperature at C/25 of a NMC cell at BoL (solid lines) and at the EoL (dashed lines).

At the heat balance evaluated at a C/25 discharge rate at different temperatures (5 ºC, 15 ºC and 32 ºC), reversible heat was higher than the irreversible term especially at SoCs below 50 % (Fig. 4.31). Nevertheless, dQ_P suffered a high increase during the aging test (higher than dQ_S) especially at low temperatures (5 ºC) what made it comparable to dQ_S. Thus, total generation of heat (bottom in Fig. 4.31) also suffered the higher increase from BoL to EoL at 5 ºC. Moreover, relevant differences were not found between cycling the cells at 15 ºC and 32 ºC at a discharge rate of C/25.

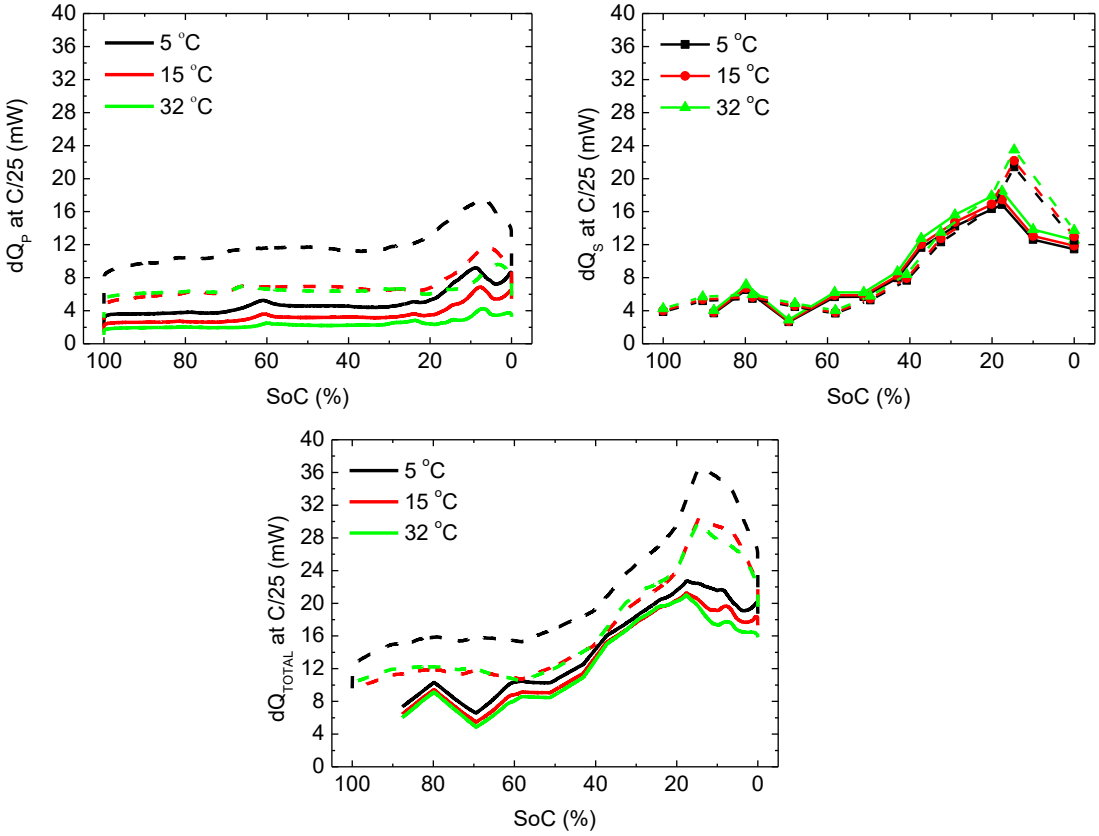

Fig. 4.31. Irreversible heat generation rate (top- left), reversible heat generation rate (top- right), and total heat generation rate (bottom) at BoL (solid lines) and EoL (dashed lines) of a LGC2 cell (NMC) discharged at a rate of C/25 at different temperatures (5 ºC, 15 ºC and 32ºC).

4.3.2. LFP cells

4.3.2.1.VIC cells

4.3.2.1.1. Open circuit voltage

Ps-OCV curves were obtained for VIC01 and VIC02 cells (LFP) at a charge/discharge rate of C/25 (Fig. 4.32). At high SoCs (between 70 % and 80 % depending on the cycle), the OCV started decreasing sooner as the cell was more aged. The first labeled plateau (1) in Fig. 4.32, maintained the same voltage value but lower percentage of SoC was employed on this plateau, as more cycled was the cell. Consequently, plateau (2) was reached sooner but it also maintained the same voltage value during cycling. Even though the SoC range covered by the plateau (2) was not decreased, the plateau was shifted to higher SoC values. In the case of plateau (3), it was also shifted to higher SoC values due to the decrease in plateau (1).

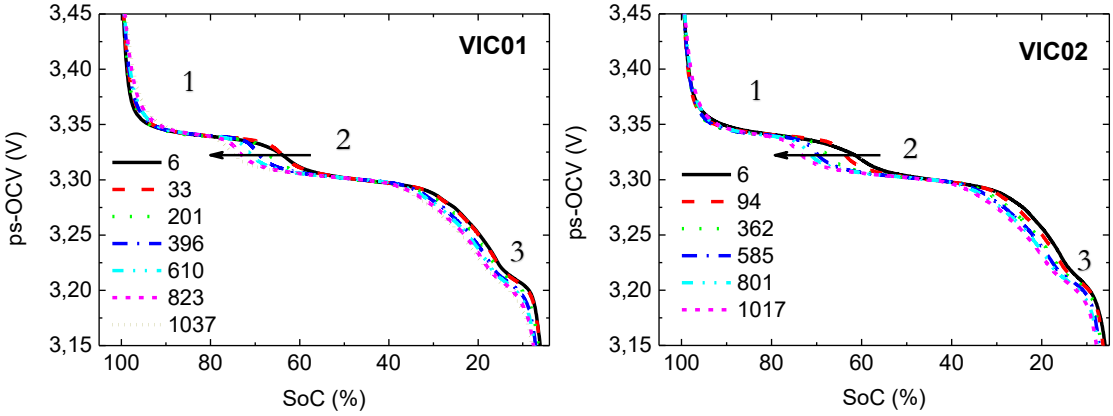

Fig. 4.32. Pseudo-OCV evolution during cycle life of VIC01 cell (left) and VIC02 cell (right) calculated from charge/discharge voltage curves at C/25.

Differences in the resulting ps-OCV curves calculated at different rates would mean that the measurements were not carried out slow enough so they were still affected by kinetics. Ps-OCV curves were obtained at C/25, C/50 and C/100 rates in order to compare the resulting OCV curves (Fig. 4.33). In the right part of Fig. 4.33, we can see the transitions between plateaus were slower at lower rates. Therefore, kinetic effects were affecting the measurements. Thus, if higher accuracies were required, ps-OCV at rates lower than C/25 (for instance, C/100) should be considered for these cells. However, discharging at lower rates means longer measurement times. Thus, working at C/25 instead of C/100 gives lower accuracies but reduces the measurement time at least in a factor 4.

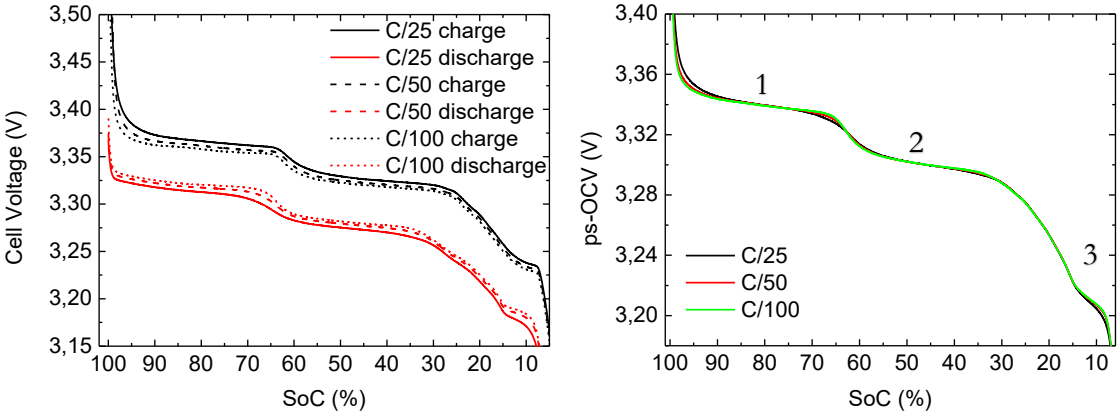

Fig. 4.33. (left) Cell voltage of a VIC cell (LFP) under different charge/discharge rates. (right) ps-OCV curves of a VIC cell (LFP) obtained at different charge/discharge rates.

The OCV obtained from averaging (ps-OCV) and that obtained during charge and discharge by the GITT technique, were plotted in Fig. 4.34. In general, the ps-OCV curves stayed between charge and discharge GITT OCV curves. However, a higher mismatch was found between them at the EoL. Furthermore, the evolution of the GITT OCV obtained during discharge from BoL to EoL was

depicted in Fig. 4.35. The curves followed the same tendency that we found with ps-OCV (Fig. 4.32) but the curves presented lower voltage values with the GITT technique.

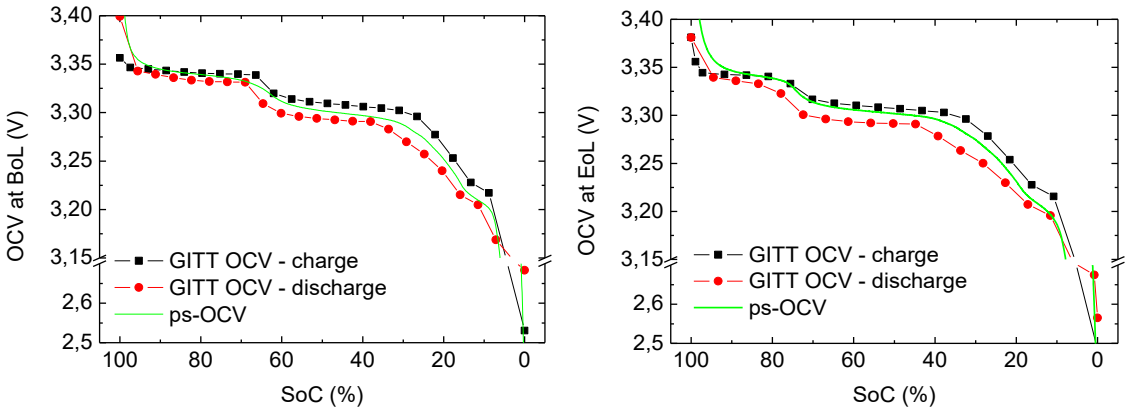

Fig. 4.34. Comparison of charge and discharge OCV curves of VIC cells (LFP) at BoL (left) and EoL (right) measured by GITT and ps-OCV.

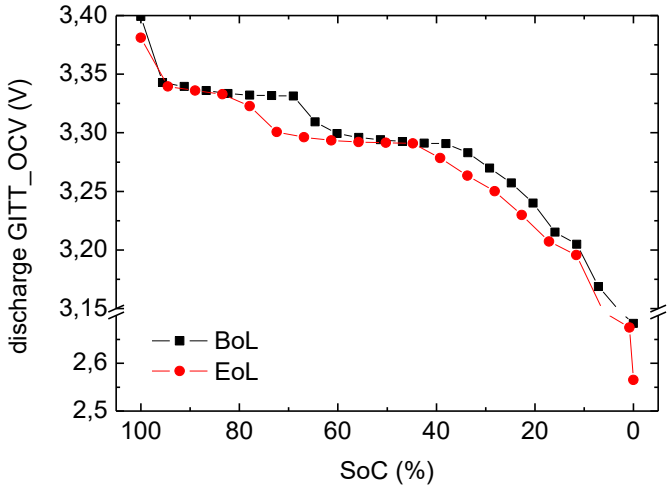

Fig. 4.35. Discharge OCV curves at BoL and EoL of a VIC cell (LFP) obtained from GITT measurements at ambient temperature.

Hysteresis

The voltage difference between OCV-GITT curves obtained during charge and discharge (hysteresis voltage) at both BoL and EoL was represented in Fig. 4.36. In general, hysteresis voltage increased as the SoC decreased. Considering the hysteresis in the SoC range between 95.5 % and 11.5%, hysteresis voltage stayed below 34 mV at BoL and 36 mV at EoL. Three different regions belonging to the three visible plateaus at the OCV curves (Fig. 4.32) were also distinguishable at the hysteresis curves. The region at highest SoCs showed the lowest hysteresis voltage, followed by the region at intermediate SoCs and then the one at lowest SoCs. Concerning to the effect of aging on

the hysteresis voltage, it increased from BoL to EoL at some particular SoC ranges (between 80 % and 65 %, between 44 % and 28 % and below 10 %). In the other SoCs, it remained unchanged.

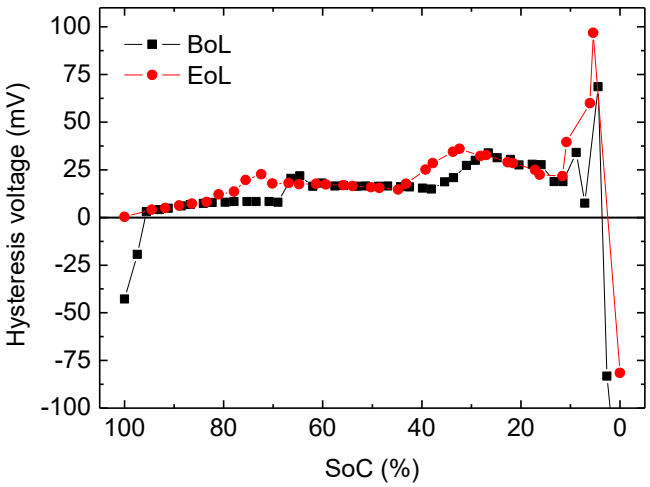

Fig. 4.36. Hysteresis voltage of a VIC cell (LFP) calculated as the difference between charging and discharging GITT OCV curves at BoL and EoL.

4.3.2.1.1. Incremental capacity analysis

Incremental capacity analysis was carried out to VIC cells. The results obtained at different aging levels were plotted in Fig. 4.37. The observed peaks correspond to the different stages of the graphite negative electrode (labeled from 1 to 5). This is because LFP electrodes exhibit a unique plateau that extends to almost all the SoC range. Thus, the peaks plotted in Fig. 4.37 correspond to lithium extraction from the graphite electrode. In particular, peaks 4 and 5 are related to the phenomena of Li^+ deintercalation at stages LiC_{12} and LiC_6, where most of the capacity is extracted [157]. As it can be appreciated, peaks 2, 3 and 4 remain almost unaffected by aging. However, peaks 1 and 5 decreased with aging. In other studies, the decrease in peaks 1 and 5 was assoaciated to LAM_{LiNE} [158]. In addition, the additional decrease measured in peak 5 was attributed to LLI [37,158].

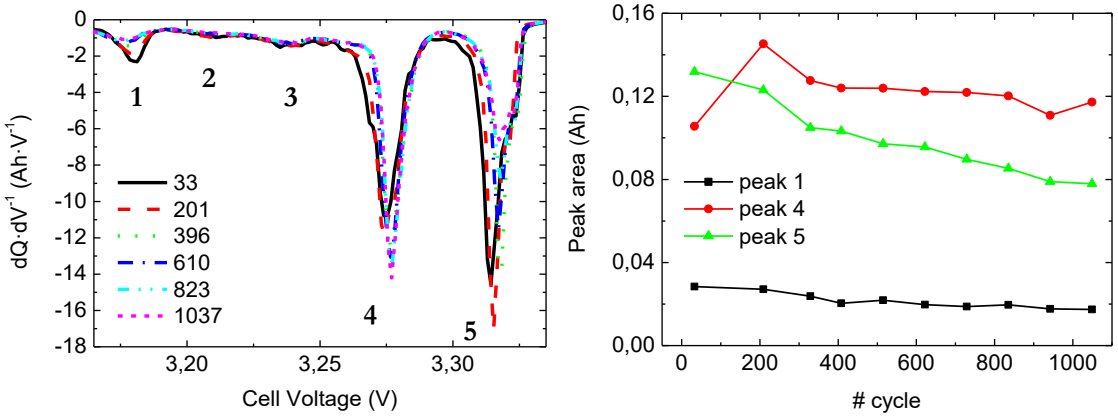

Fig. 4.37. Incremental capacity analysis of a VIC cell (LFP) at different SoH at a C/25 discharge rate. On the left, IC curves. On the right: evolution of the area of peaks.

4.3.2.1.2. Overpotential

Close-to-equilibrium measurements

The overpotential produced in a VIC cell (LFP) at a C/25 discharge rate was obtained from the difference between ps-OCV and cell voltage (Fig. 4.38). The highest overvoltages were found at very low and very high SoC values. Overpotential at central SoCs showed two main peaks that were shifted to higher SoC values as long as cycling was carried out. Furthermore, during the first 400 - 450 cycles, the overpotential decreased to its lowest value from which started increasing until the EoL of the cells (Fig. 4.38).

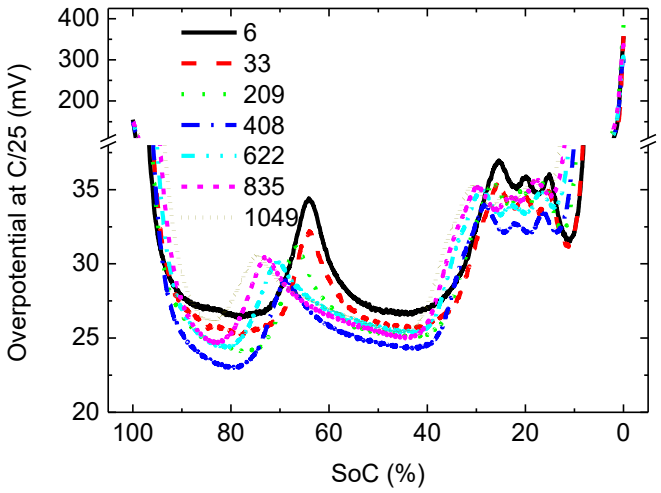

Fig. 4.38. Overpotential of a VIC cell (LFP) generated during a discharge at a C/25 rate and calculated from the ps-OCV at room temperature.

Far-from-equilibrium measurements

The overpotential generated in a VIC cell (LFP) subjected to a discharge rate of 2C was plotted in Fig. 4.39. In the SoC range between 90 % and 20 %, the overpotential generated increased between BoL and EoL. At SoCs below the 20 %, overpotentials at BoL and EoL were very similar but slightly higher at BoL.

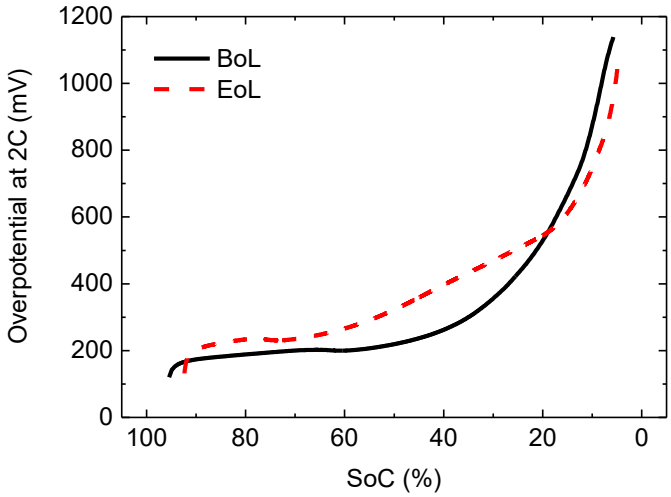

Fig. 4.39. Overpotential generated in a VIC cell (LFP) at a 2C discharge rate evaluated at BoL (solid line) and EoL (dashed line).

GITT and ps-OCV approximations

The overpotential generated at a C/25 discharge rate was calculated from the ps-OCV and compared to the one obtained from the discharge GITT OCV (right side of Fig. 4.40). The generated overpotential was larger at BoL than at the EoL. In fact, it happened because the decrease in OCV due to the aging process was higher than the decrease in cell voltage at this rate (left side of Fig. 4.40). Moreover, regarding the differences between ps-OCV and GITT-OCV methods, their absolute values differed between 5 mV and 20 mV in the SoC range between 95 % and 10 % (Fig. 4.41).

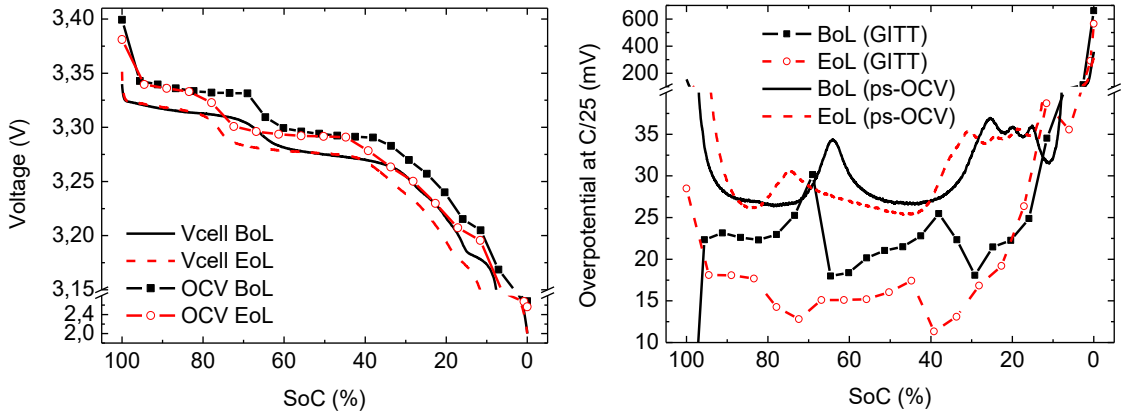

Fig. 4.40. (left) Cell voltage of a VIC cell (LFP) at a discharge rate of C/25 and discharge OCV obtained from GITT measurements at BoL and EoL. (right) Comparison of the overpotential generated at a discharge rate of C/25 calculated from the discharge GITT OCV (line + markers) and the ps-OCV (lines) at BoL and EoL.

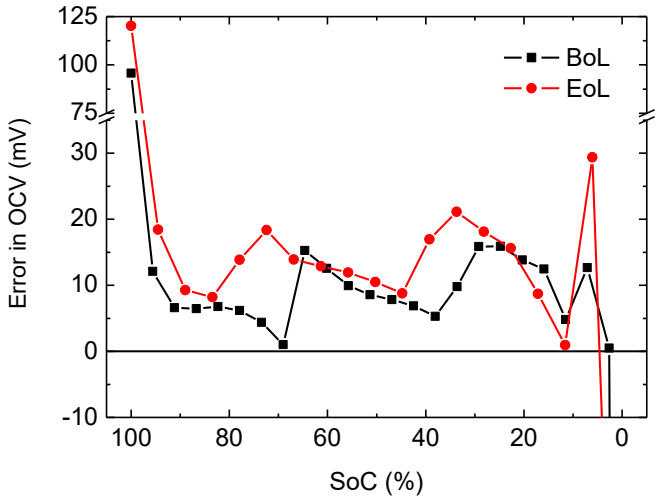

Fig. 4.41. Error in overpotential introduced when using ps-OCV instead of discharge GITT OCV at BoL and EoL.

Overpotential obtained from GITT and ps-OCV approximations was also calculated at higher discharge rates (2C). No relevant differences were found between the two methods (Fig. 4.42) because the introduced error was below 20 mV (Fig. 4.41) and the produced overpotentials at 2C were above 200 mV and raised to more than 1 V at the EoD, what made the error not relevant when compared to low rates.

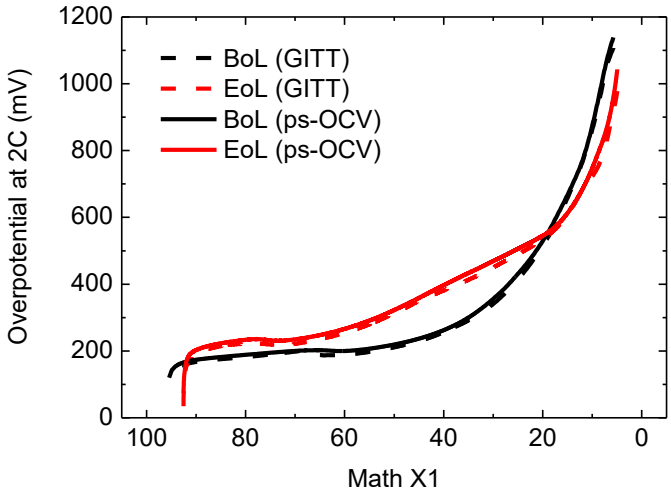

Fig. 4.42. Comparison of the overpotential generated in a VIC cell (LFP) at 2C discharge rate calculated from the discharge GITT OCV and ps-OCV.

Apparent resistance

Apparent resistance obtained from the overpotential produced at a C/25 discharge rate was represented in Fig. 4.43 at BoL and EoL. Except at SoCs between 20 % and 10 %, the apparent resistance was found to be larger at BoL.

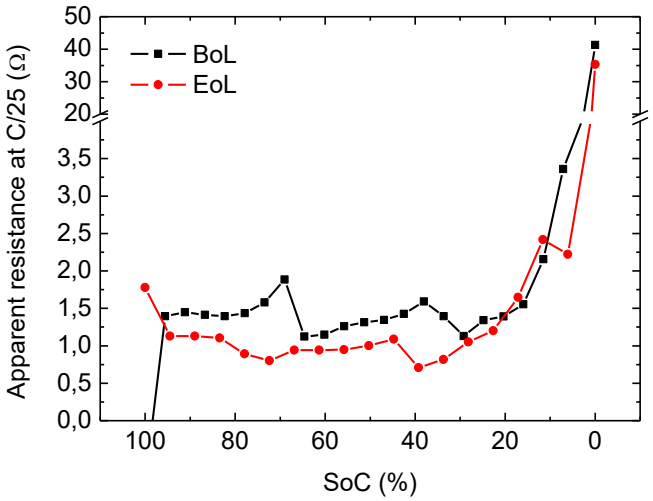

Fig. 4.43. Apparent resistance of a VIC cell (LFP) at a discharge rate of C/25 represented at BoL and EoL. It was calculated from OCV values coming from GITT tests.

The apparent resistance at high rates (2C) represented in Fig. 4.44 was much lower than that a C/25 rate, (Fig. 4.43). Concretely, the apparent resistance is calculated from the overpotential divided by the current that produced it. Thus, as the overpotential was around 8 times higher at 2C and the ratio between currents was 50, it yield to an apparent resistance around 6 times smaller at high rates. Furthermore, the apparent resistance at high rates was larger at the EoL except at SoCs below 20 %.

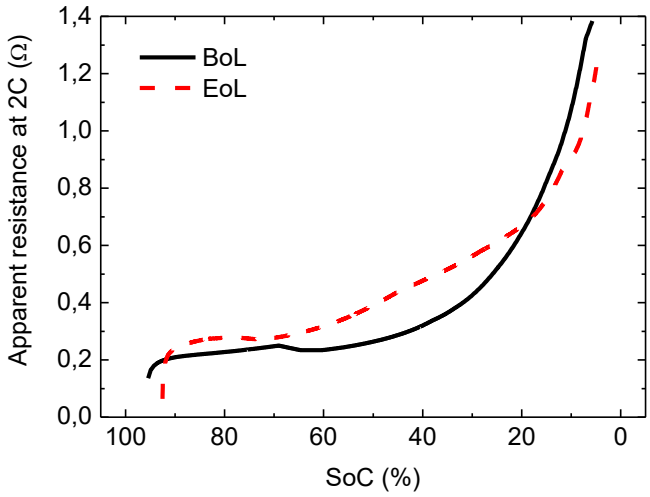

Fig. 4.44. Apparent resistance of a VIC cell (LFP) at a discharge rate of 2C represented at BoL and EoL. It was calculated from OCV values coming from GITT tests.

Contributions to overpotential

Different contributions to overpotential at BoL during a discharge at a C/25 and 2C rates were plotted in Fig. 4.45. Due to the fact that impedance of those cells was only measured at SoC equal to 100 %, the ohmic contribution was estimated from the impedance measured at this SoC and it was considered to be constant in all the SoC range. Furthermore, charge transfer resistance was also

measured at SoC = 100 %. Even though it is known that charge transfer resistance is strongly dependent on SoC, as its contribution to total polarization was small compared to concentration polarization, it was also assumed to be constant in all the SoC range. In addition, different contributions were only represented at BoL because a different holder was employed at the EoL what gave non-comparable results (for further information refer to Chapter 3). Moreover, at both discharge rates, the major contributor was the concentration polarization, which in both cases increased sharply towards the EoD.

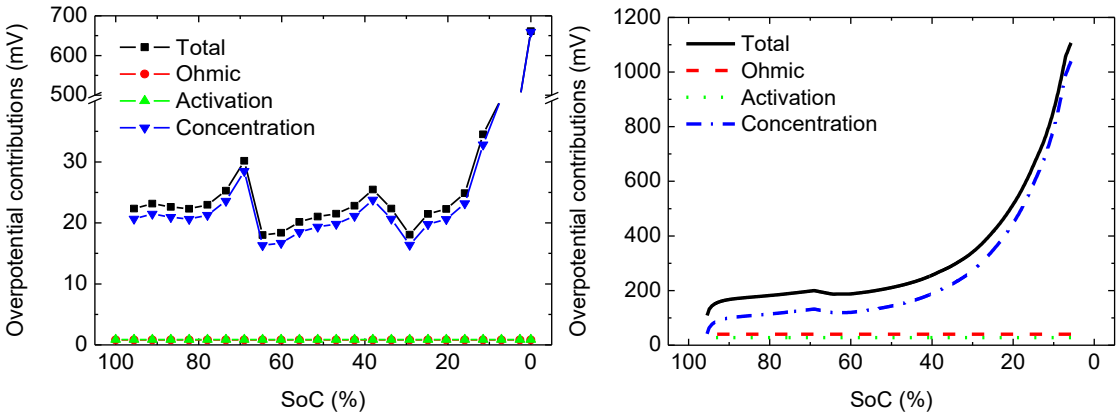

Fig. 4.45. Different contributions to overpotential of a VIC cell (LFP) at BoL subjected to a discharge at a rate of C/25 (left) and 2C (right).

4.3.2.1.3. Entropy

Reversible entropy

The entropic coefficient was calculated as the derivative of the OCV with temperature. The results at BoL and EoL were plotted in Fig. 4.46. As it can be seen, similar trends were found at BoL and EoL. The entropic coefficient showed positive values for high SoCs above 20 % - 30 % and became negative for lower SoCs. Therefore, during discharge, heat would be subtracted from the dissipative effect (refer to equation (4.31)) at SoCs above 30 % and heat will be added at the last stages of discharge.

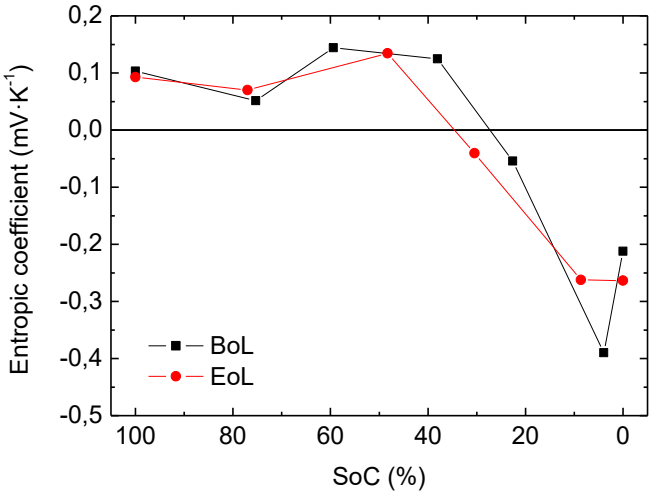

Fig. 4.46. Entropic coefficient of a VIC cell (LFP) at BoL and EoL.

Irreversible entropy

Close-to-equilibrium measurements

The generation rate of irreversible entropy calculated from the ps-OCV curves at a C/25 discharge rate was depicted in Fig. 4.47. The curves shifted to higher SoC values as the cells were aged. In general, d$i\mathcal{S}$ decreased until the 400th cycle from where it started to increase. Nevertheless, the generation rate at the EoL stayed below than that at BoL. In addition, the results were identified easily in Fig. 4.48 where GITT OCV curves were used instead of ps-OCV at BoL and EoL.

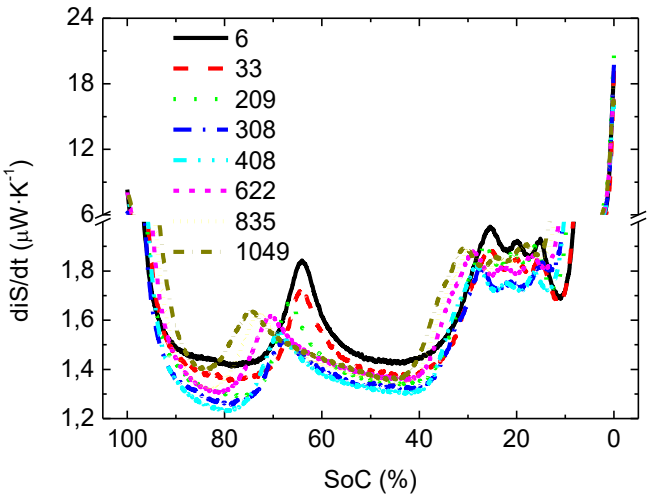

Fig. 4.47. Irreversible entropy generation rate of a VIC cell (LFP) produced during discharge at a rate of C/25 and obtained from ps-OCV curves.

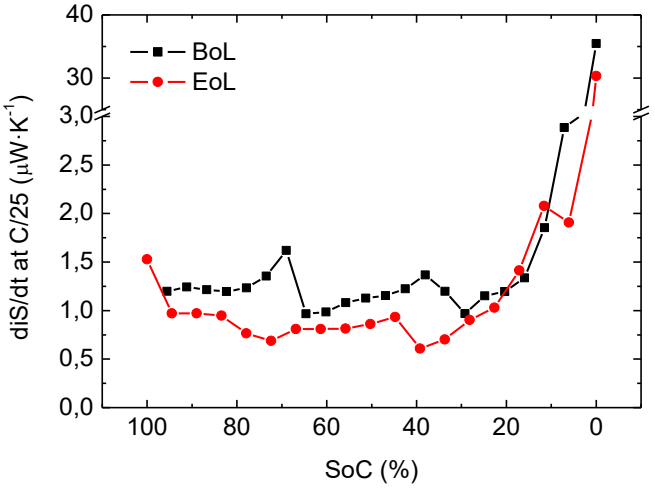

Fig. 4.48. Irreversible entropy generation rate of a VIC cell (LFP) produced during discharge at a rate of C/25 and obtained from GITT OCV curves.

The different contributions to irreversible entropy production at BoL when VIC cells were discharged at a C/25 rate were depicted in Fig. 4.49. The major contributor in all the SoC range was the term associated to concentration polarization. It represented the 90 – 95 % of the total generation while the terms associated to ohmic and activation polarizations were below the 6 %.

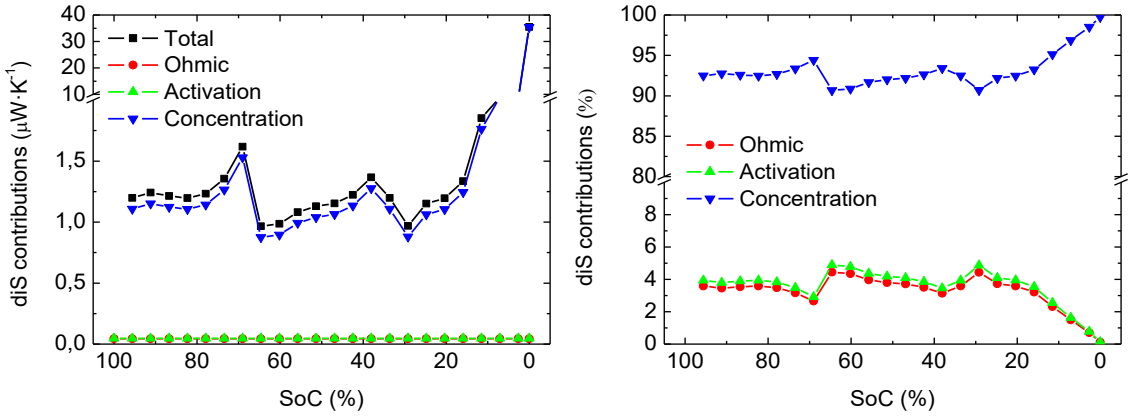

Fig. 4.49. (left) Absolute and (right) relative d_iS/dt contributions at BoL while discharging the VIC cell at a C/25 rate at ambient temperature. The results were obtained from the discharge GITT OCV curves.

Far-from-equilibrium measurements

The generation rate of irreversible entropy obtained from the GITT OCV curves at a discharge rate of 2C was represented in Fig. 4.50. At this rate, unlike at C/25 (Fig. 4.48), the generation rate at SoCs higher than 20 % was larger at the EoL (dashed line) than at BoL (solid line). The highest absolute increase of the irreversible entropy generation rate with aging was found at intermediate SoCs (between 60 % and 30 %).

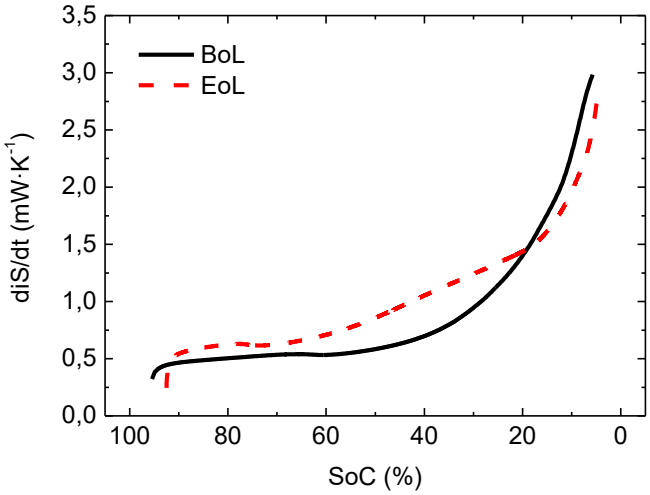

Fig. 4.50. Irreversible entropy generation rate of a VIC cell (LFP) produced during discharge at a rate of 2C and obtained from GITT OCV curves.

Absolute and relative values of irreversible entropy production at BoL when VIC cells were discharged at a 2C rate were depicted in Fig. 4.51. Except at the very BoD, the major contributor was the term related to concentration polarization, which accounted for more than the 60 % of the total entropy production. The term related to ohmic conduction was the second major contributor but much below the concentration term. However, it was very similar to the entropy production related to activation polarization. In general, ohmic and activation terms were contributing less than 30 % and decreased towards 0 % at the EoD.

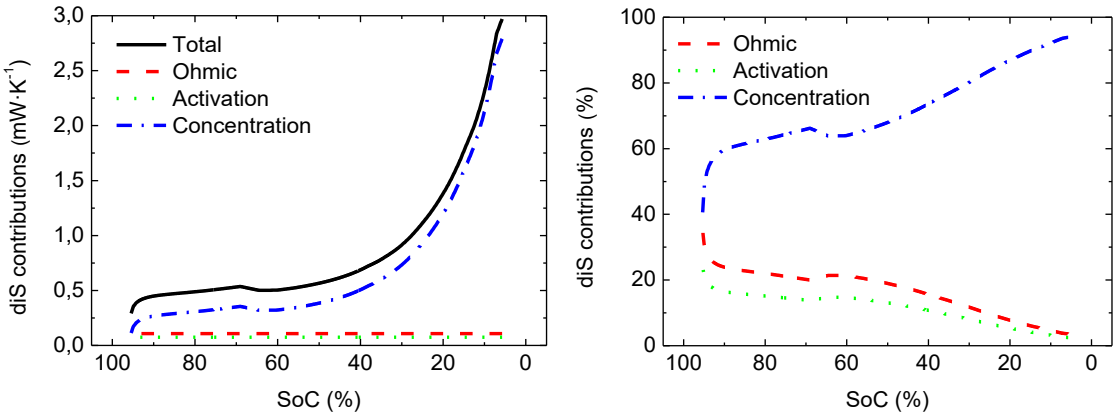

Fig. 4.51. (left) Absolute and (right) relative contributions to total d_iS/dt at BoL when discharging a VIC cell at a 2C rate.

4.3.2.1.4. Heat generation

Close-to-equilibrium measurements

Reversible and irreversible heat generation rates at a discharge rate of C/25 were plotted in Fig. 4.52. Great variations were not found at reversible generation of heat. However, at a C/25 discharge rate, the irreversible generation of heat at the EoL was below that at BoL. The smallest difference between them was found at the SoCs corresponding to the plateaus found at the OCV at the EoL. Reversible and irreversible contributions showed similar absolute values except at SoCs below 5 %, in which the irreversible term diverged towards higher values (notice the break). Thus, the resulting total heat was highly affected by both contributions. However, they had similar absolute values but one being positive and the other negative what yielded to negligible heat generation at various SoCs, in particular, at 100 %, 39 % (EoL) and 86.8 %, 68.2 %, and 34 % (BoL). This endothermic behavior was found at intermediate SoCs at both BoL and EoL. Moreover, due to the fact that the generation of irreversible heat was decreased as the cell aged, it made the total generation of heat to be exothermic between SoCs 86.8 % and 68.2 % at BoL and endothermic at the EoL. Below 40 % SoC, the total heat generation was larger at the EoL.

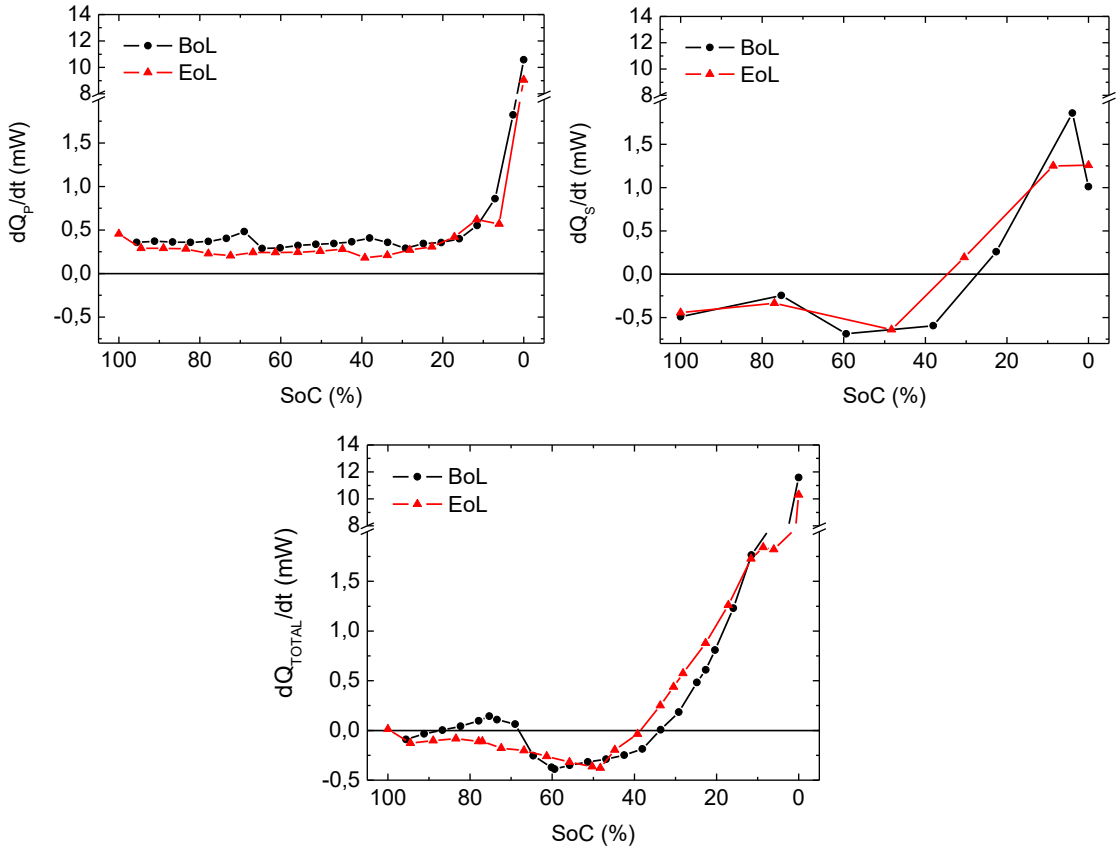

Fig. 4.52. Irreversible heat generation rate (top- left), reversible heat generation rate (top- right), and total heat generation rate (bottom) at BoL and EoL of a VIC cell (LFP) discharged at a rate of C/25.

Far-from-equilibrium measurements

The generation of heat at a high rate discharge (2C) and the corresponding reversible and irreversible contributions were represented in bottom, top-right and top-left of Fig. 4.53, respectively. At those high rates, the irreversible term became predominant being the major contributor to total heat generation. Thus, the cell exhibited an exothermic behavior in all the SoC range. In addition, the heat generated at this rate was found to be higher at the EoL except at SoCs below 20 %.

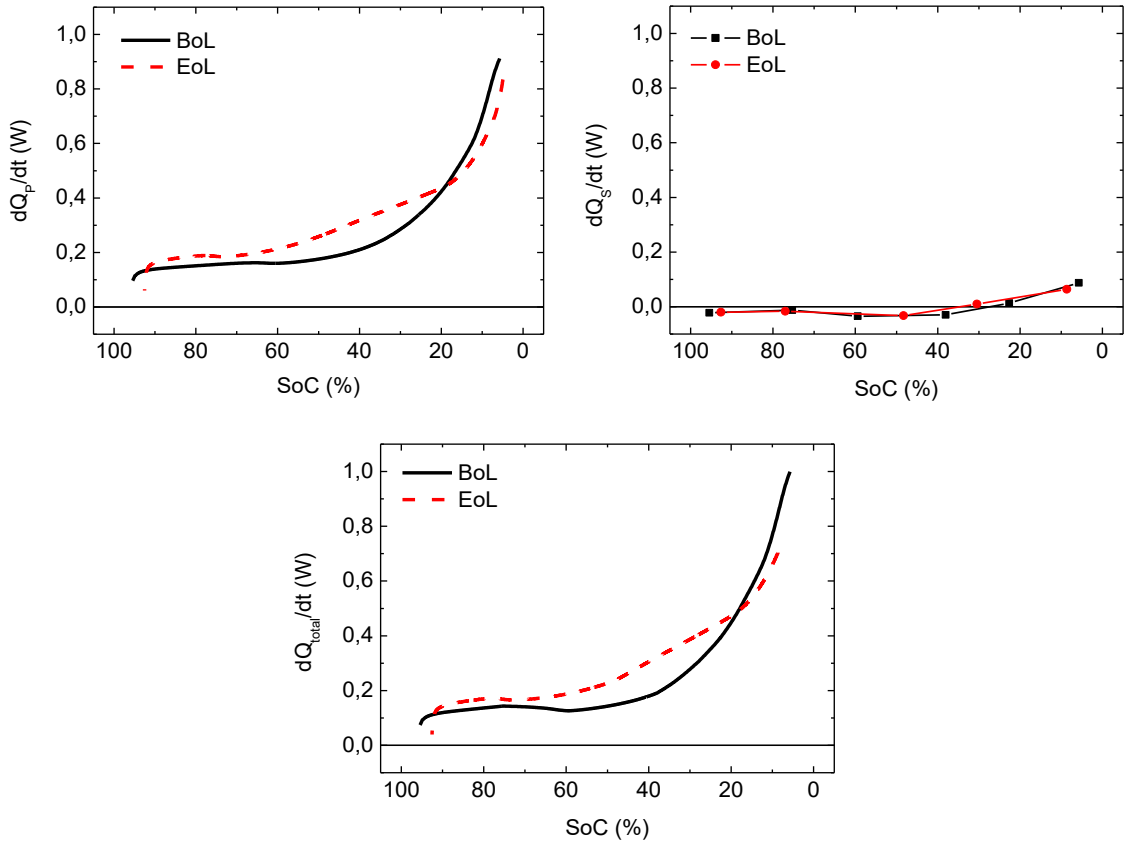

Fig. 4.53. Irreversible heat generation rate (top- left), reversible heat generation rate (top- right), and total heat generation rate (bottom) at BoL and EoL of a VIC cell (LFP) discharged at a rate of 2C.

4.3.2.2. EVbat cells

4.3.2.2.1. Open circuit voltage

The OCV curves of the four EVbat cells (LFP) at different SoH levels were represented in Fig. 4.54. The plateau at higher SoCs (1) was highly reduced in SoC range what made the OCV to decrease sooner towards the second plateau. This implied a reduction of the amount of charge injected/extracted in that chemical reaction. Plateau (2) was shifted to higher SoCs because of the reduction of plateau (1) but maintained the amount of SoC employed for the reaction to take place.

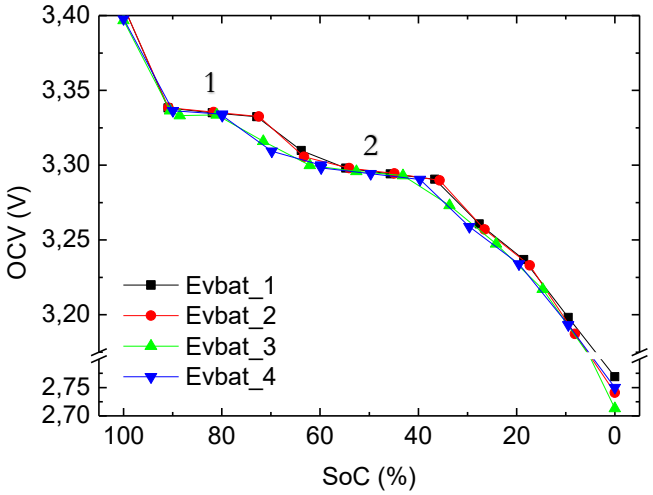

Fig. 4.54. OCV curves of different EVbat cells (LFP) subjected to a different number of cycles (50, 100, 200, and 400).

4.3.2.2.1. Incremental capacity analysis

Incremental capacity analysis while discharging the cell at a C/25 rate, which represents the extracted charge at each electrochemical reaction, is depicted in Fig. 4.55. The amount of charge extracted during the first electrochemical reaction, labeled as (1), suffered the highest decrease, as expected from the OCV curves where the first plateau was reduced (Fig. 4.54). The capacity of peak (1) at a discharge rate of C/25 was found to decrease in approximately 4 Ah after 400 cycles. In contrast, peak (2) was almost invariable during the cycle life test. Thus, the results indicated that the main loss of capacity of these cells at low rates came from the electrochemical reaction associated to peak (1), from which less charge could be extracted as the cells were aged.

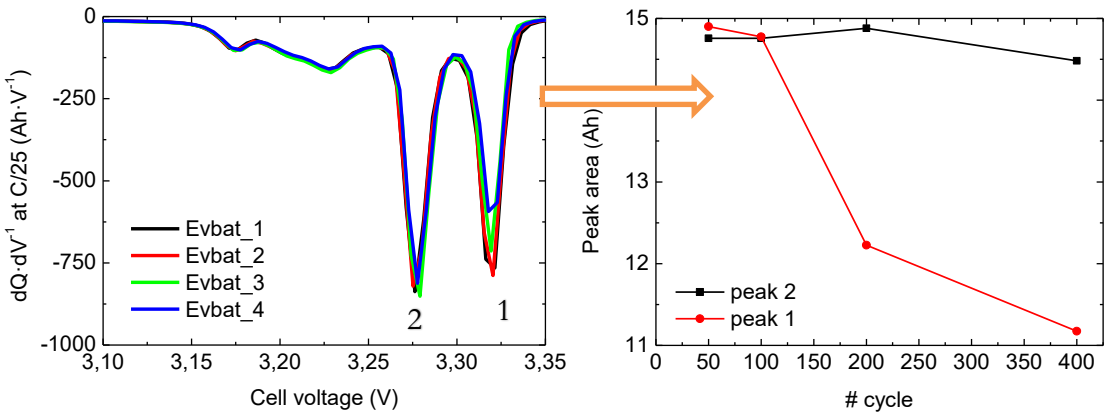

Fig. 4.55. (left) IC curves at a C/25 discharge rate of different EVbat cells (LFP) subjected to a different number of cycles (50, 100, 200, and 400). (right) Evolution of the area of peaks (1) and (2).

4.3.2.2.2. Overpotential

The overpotential of EVbat cells (LFP) at a C/8 discharge rate increased smoothly with respect to SoC until SoC = 10 % and then increased sharply until the end of discharge, in all the evaluated cells with their corresponding SoHs (Fig. 4.56). In relation to the SoH, relevant differences were not found between the cells. Nevertheless, the generated overpotentials at BoD in EVbat_3 and EVbat_4 were larger than those generated in EVbat_1 and EVbat_2. Moreover, EVbat_4 showed the lowest overpotential at SoCs between 70 % and 10 %.

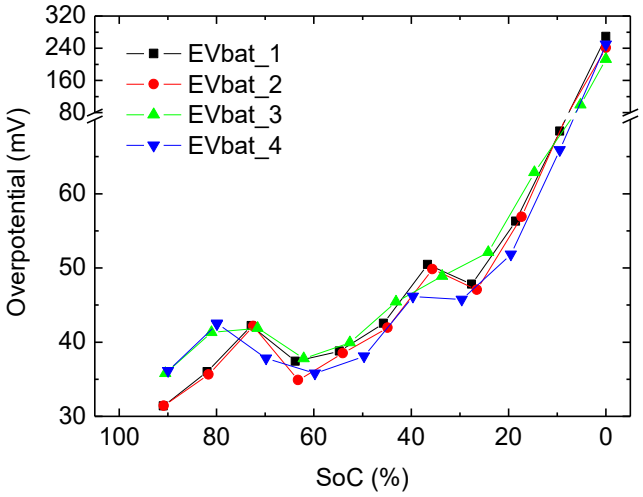

Fig. 4.56. Overpotential generated at a C/8 discharge rate of different EVbat cells (LFP) previously subjected to a different number of cycles (50, 100, 200, and 400, respectively).

Contributions to overpotential

Different contributions to overpotential at a C/8 discharge rate were plotted in Fig. 4.57. Ohmic and activation polarizations were obtained from the impedance data measured in Chapter 3. Concentration polarization was defined as the difference between the total overpotential and the ohmic and activation polarizations. At this rate (C/8), concentration polarization was the predominant contributor to overpotential independently of the degradation level of the cell. Regarding to ohmic and activation polarizations, they represented a little amount of the total overpotential and they had similar values. However, activation polarization was slightly larger than ohmic polarization in all cells except EVbat_3 (200 cycles). In this cell, only at SoCs between 40 % and 20 % and at the EoD, activation polarization was larger than what ohmic was.

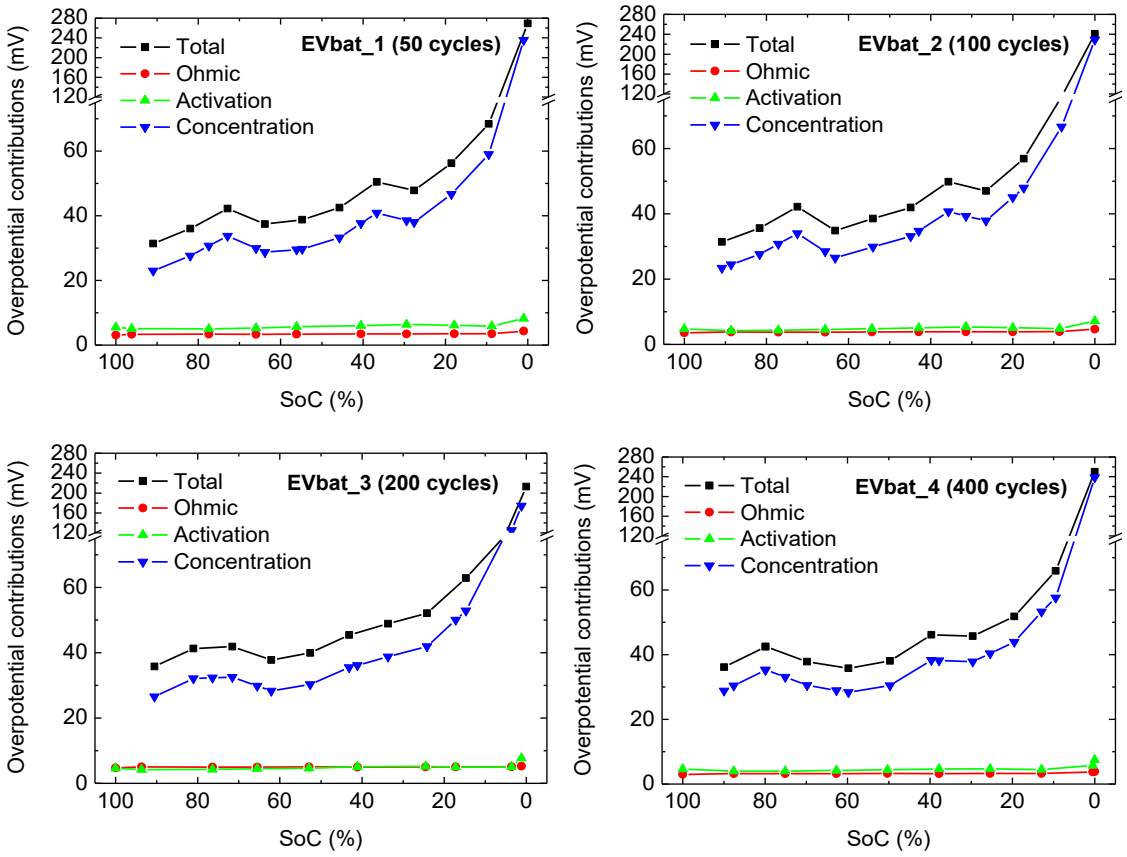

Fig. 4.57. Different contributions to overpotential generated in EVbat cells when discharged at a C/8 rate at four different SoHs (50 cycles, 100 cycles, 200 cycles and 400 cycles).

4.3.2.2.3. Irreversible entropy

In Fig. 4.58, total generation rate of irreversible entropy was represented for the four cells at different SoH levels when discharged at a C/8 rate. The more aged cell (EVbat_4) only generated irreversible entropy faster than the other ones at SoCs higher than 75 %. EVbat_3 cell generated similar amount than that of EVbat_4 in the same SoC range. However, from this SoC and until the EoD, irreversible entropy was generated at a similar rate in all the evaluated SoHs. Thus, no clear tendency with aging was found. Particularly, mostly all the time the generation rate was between 0.5 $mW \cdot K^{-1}$ and 1 $mW \cdot K^{-1}$ and, at the EoD, irreversible entropy was generated at a rate of around 4.5 $mW \cdot K^{-1}$.

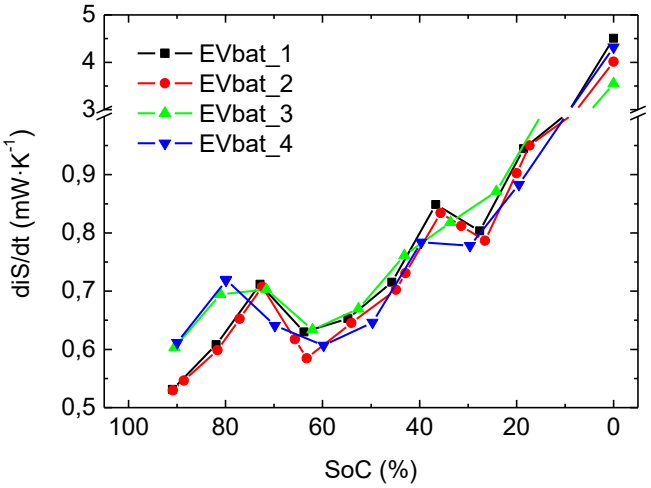

Fig. 4.58. Irreversible entropy generation rate during discharge at C/8 of different EVbat cells (LFP) previously subjected to a different number of cycles (50, 100, 200, and 400).

Contributions to irreversible entropy generation rate were related to the different overpotential sources (Fig. 4.59). At all cycling stages the term related to concentration was the highest contributor to total entropy production. The ohmic contribution at C/8 discharge rate was the lowest one unless after 200 cycles where it surpassed the activation effect. Absolute and relative contributions at different SoH levels were depicted in Fig. 4.60. The relative ohmic contribution increased with cycling except for EVbat_4, which showed similar values to EVbat_1. The tendency with SoC of the relative ohmic contribution was to decrease starting at values between 9 % and 14 % (depending on the evaluated cell) and going to near 2 % at the EoD. Contrarily, the term related to activation or charge transfer, decreased with cycling. In that case, the same trend was followed by all the evaluated cells at different SoHs. Moreover, it also decreased towards the EoD because of the sharp increase in concentration polarization. Finally, regarding to the concentration contribution, it showed similar values in all the cells but a larger relative contribution was found at the 400th cycle.

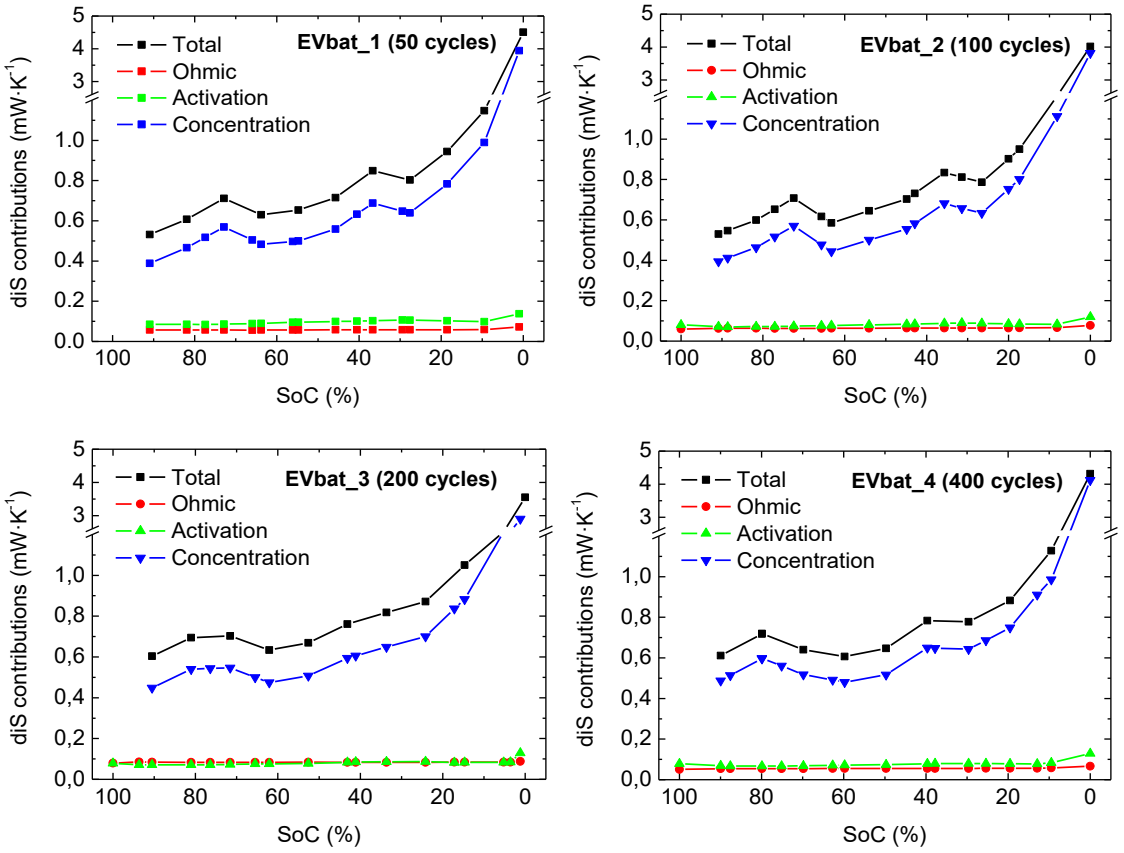

Fig. 4.59. Different contributions to irreversible entropy generation rate during discharge at C/8 of different EVbat cells (LFP) previously subjected to a different number of cycles (50, 100, 200, and 400).

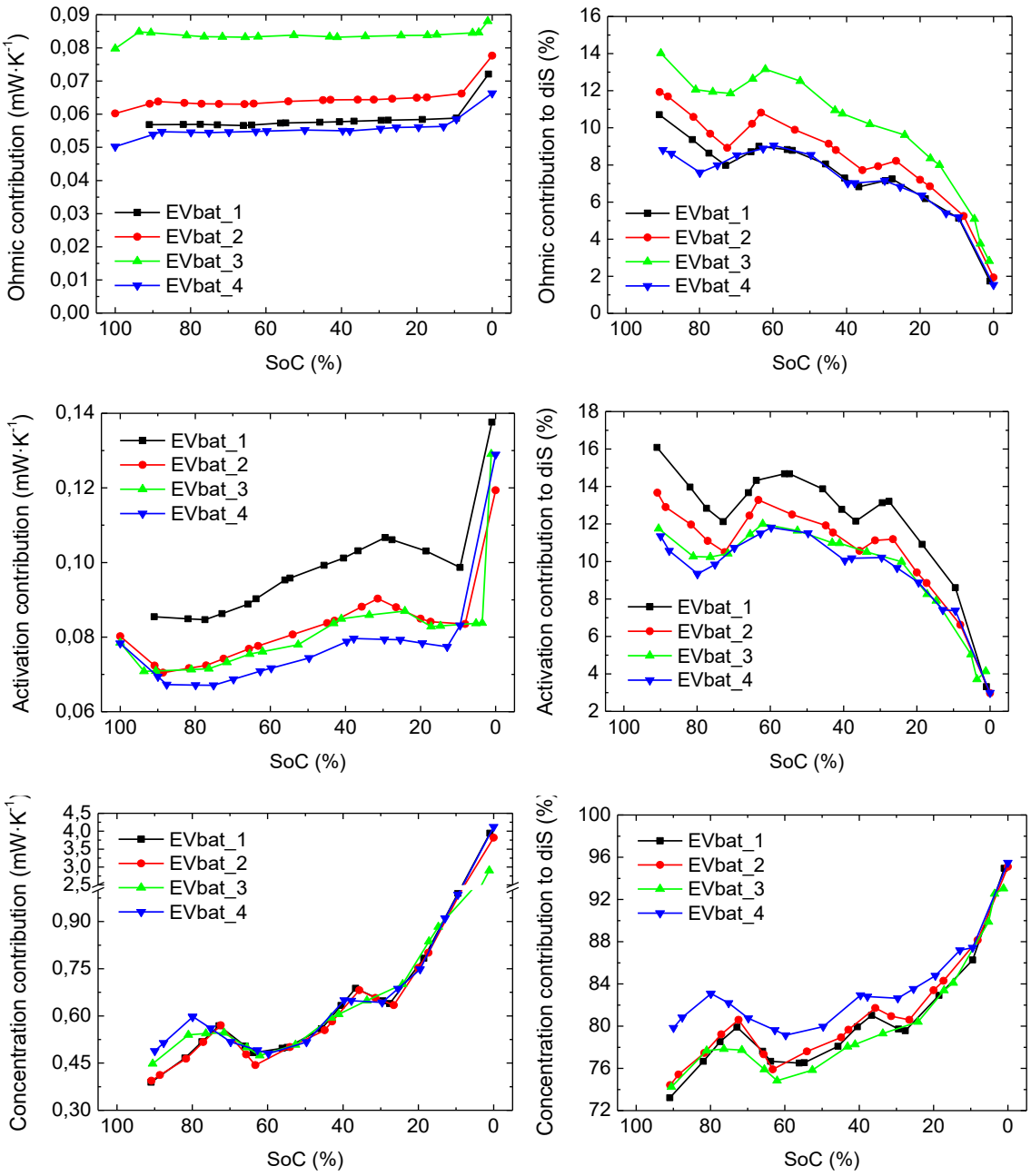

Fig. 4.60. (left) Absolute and (right) relative contribution to d_iS/dt of the ohmic term, activation polarization and concentration polarization of EVbat cells (LFP) discharged at a C/8 rate and previously subjected to 50, 100, 200 and 400 cycles, respectively.

4.3.3. LCO cells

4.3.3.1. Open circuit voltage

The OCV of the degraded LCO cell was higher than that of the fresh cell in all SoCs except at SoC = 100 % (Fig. 4.61). The smaller difference in OCV was found at the plateau located between 40 % and 20 % SoC. Moreover, the highest difference was found at the lowest SoCs.

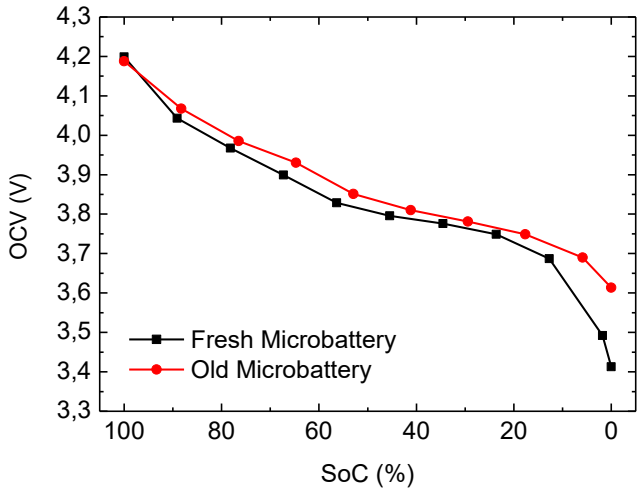

Fig. 4.61. OCV curves of two LCO cells at different SoH levels.

4.3.3.1. Overpotential

When discharging fresh and aged cells at a 1C rate, the overpotential generated at the Old Microbattery was two times larger than that generated at the Fresh Microbattery (Fig. 4.62). At both SoHs, there was a higher increase in overpotential as the EoD approximated. Nevertheless, at SoCs above 20 % the overpotential was almost constant at both BoL and EoL.

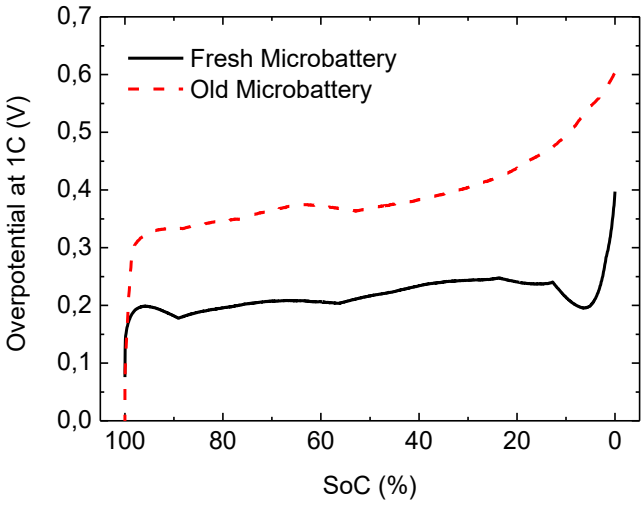

Fig. 4.62. Overpotential generated for two LCO cells at different SoH levels at a discharging rate of 1C.

4.3.3.1.1. Contributions to overpotential

The different effects contributing to total overpotential at BoL and EoL of a LCO cell being discharged at a 1C rate were represented in Fig. 4.63. The major contributor at BoL was the ohmic

term except at the last stages of discharge where concentration polarization dominated. Contrarily, the predominant effect at the EoL was the concentration polarization in all the evaluated SoCs.

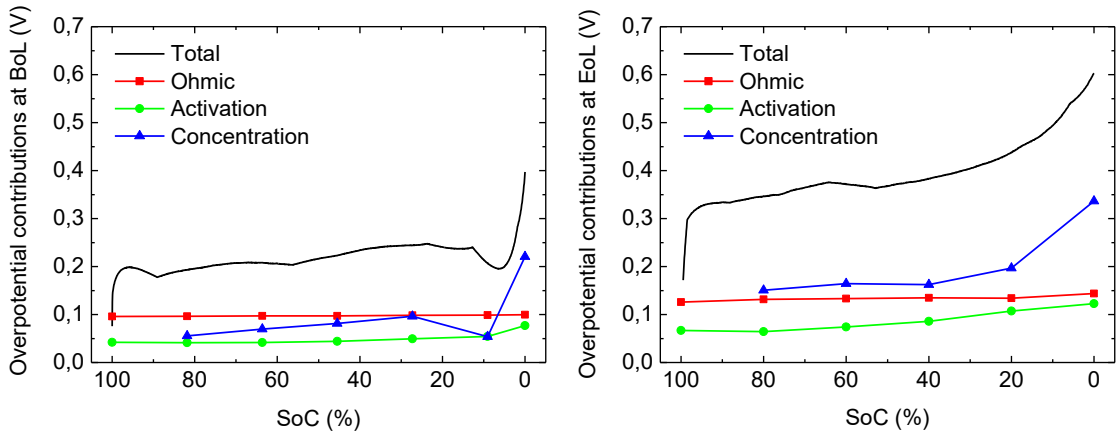

Fig. 4.63. Different contributions to overpotential generated in LCO cells when discharged at a 1C rate at BoL (left) and EoL (right).

4.3.3.2.Entropy

4.3.3.2.1. Reversible entropy

The entropic coefficients of the LCO cells at BoL and EoL were represented in Fig. 4.64. Relevant differences were not found in the shape of the curves not even in the absolute values. However, the highest divergence between BoL and EoL was found at SoCs below 20 %. In addition, a peak between SoCs 50 % and 60 % could be appreciated especially at BoL. Characteristic peaks were also found in other studies in which they were related to LCO positive electrode or to graphite negative electrode [159,160]. The characteristic peak around SoC = 80 % was associated to LCO while a smaller-amplitude peak measured between SoCs 50 % and 60 % was associated to intercalation at the graphite electrode. In particular, the peak between 50 % - 60 % was associated to the phase transition between stage 2 and stage 1 of the lithiation of graphite [159]. In our study, no peak was evidenced at SoC = 80 %, which was associated to crystal structure changes in the LCO PE [160]. Furthermore, variations in those peaks with aging were also revealed in [159].

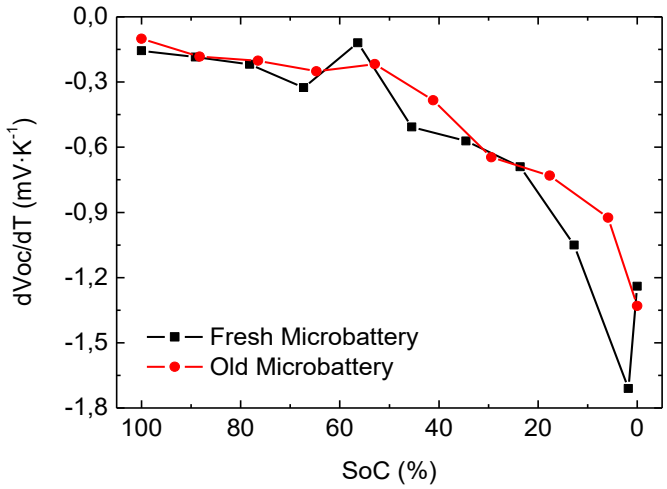

Fig. 4.64. Derivative of the OCV with respect to temperature (entropic coefficient) of two LCO cells at different SoH levels.

4.3.3.2.2. Irreversible entropy

The generation rate of irreversible entropy at BoL and EoL at a 1C discharge rate was plotted in Fig. 4.65. Different contributions coming from ohmic, activation and concentration overpotentials were also represented. All those contributions increased from BoL to EoL. Particularly, at BoL, the main contributor was the ohmic conduction, except at very low SoCs, where the term associated to concentration polarization was dominant. For all SoCs, the lowest contribution came from the term associated to activation polarization. Nonetheless, at the EoL, the main contributor was the generation rate of irreversible entropy coming from the concentration polarization and the lowest contribution came from the term associated to activation polarization. Relative values were represented in Fig. 4.66. Although the absolute values increased between BoL and EoL, the corresponding relative values showed that the term associated to activation was always contributing in the same amount to total irreversible entropy generation rate. Nevertheless, the relative contribution of the ohmic conduction was found to be smaller at the EoL. This decrease was translated into an increase of the term associated to concentration polarization.

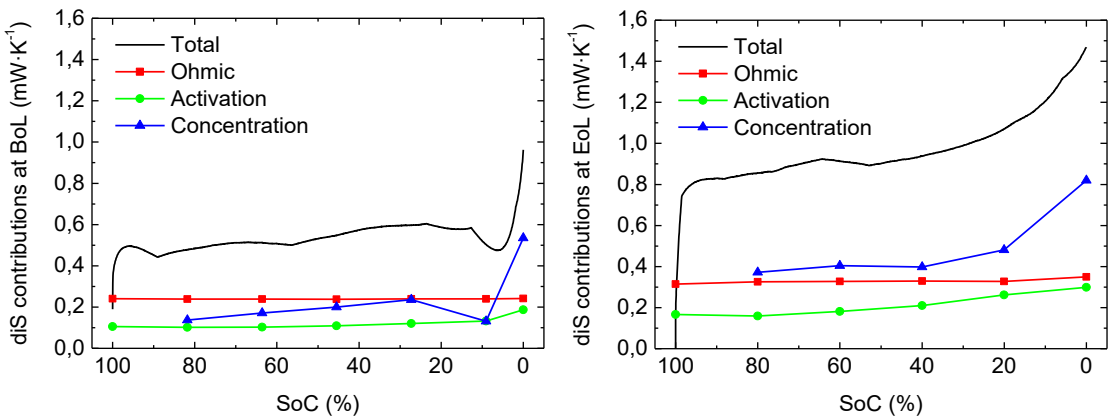

Fig. 4.65. Generation rate of irreversible entropy of a LCO cell at BoL (left) and EoL (right) when discharged at 1C.

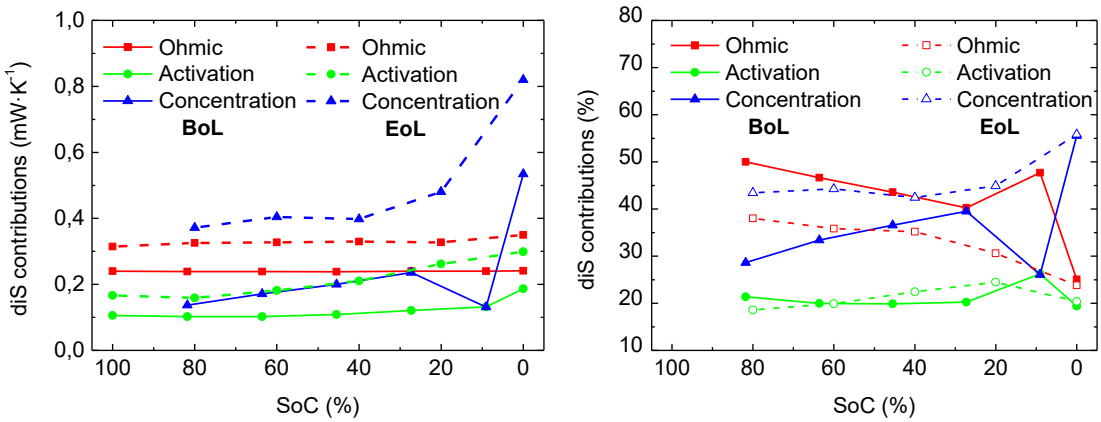

Fig. 4.66. (left) Absolute and (right) relative contributions to the generation rate of irreversible entropy of two LCO cells at different degradation levels (BoL and EoL) when discharged at 1C.

4.3.3.3. Heat generation

Reversible, irreversible and total generation of heat at a discharge rate of 1C were represented in Fig. 4.67. At this discharge rate, none of the contributions could be neglected. The reversible heat generation added extra heat to the total heat generation rate in all SoC range, especially at low SoC values. The difference between the heat generation rate at BoL and EoL was almost constant during all the discharge process and it was of about 100 mW.

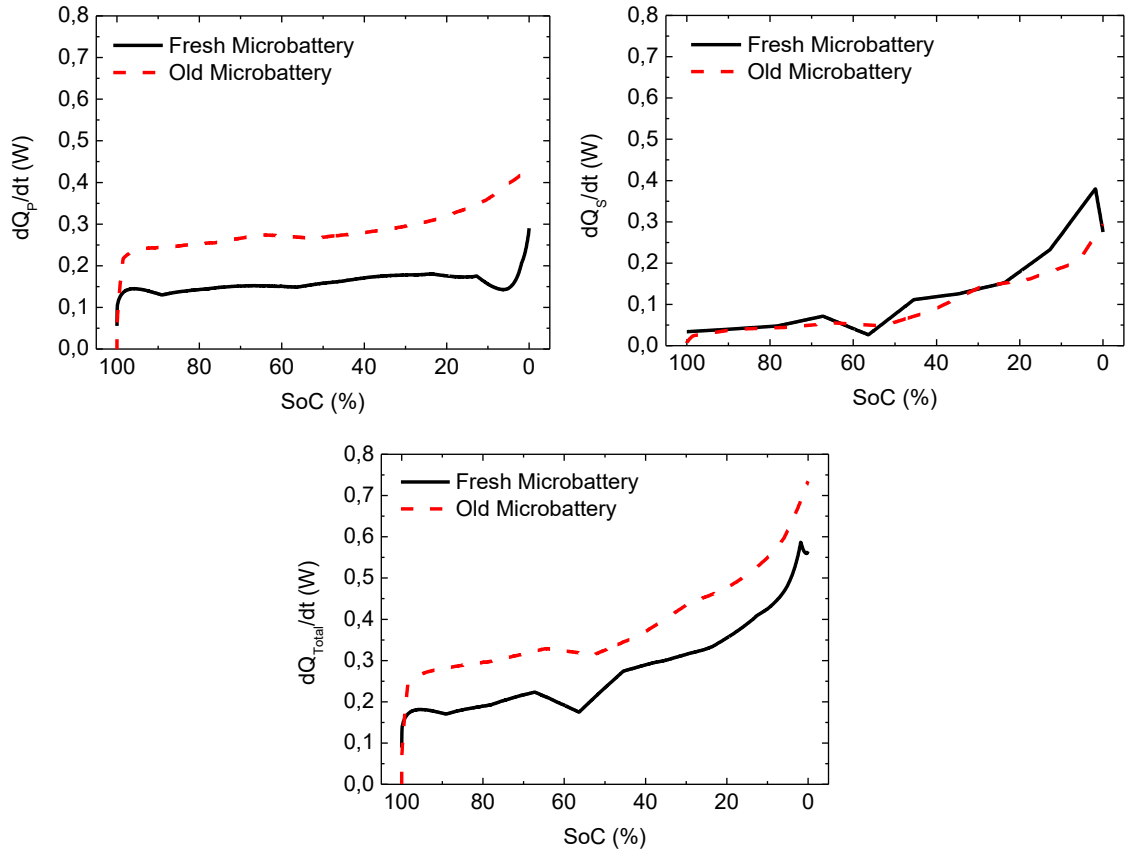

Fig. 4.67. Irreversible (top-left) and reversible (top-right) heat generated in the discharge process of two LCO cells at different SoH levels at a rate of 1C. Total generation of heat corresponds to the addition of reversible and irreversible effects (bottom).

4.4. Discussions

From equations (4.26), (1.1) and (1.2), a graphical representation of the process of energy conversion and extraction in batteries was represented in Fig. 4.68. This representation encompases the classical definition of chemical-electrical conversion (and the corresponding reversible entropy), coming from equations (4.26) and (1.1), and the energy lost orreversibly during the electrical/ionic conduction, represented in equation (1.2). In this study, we evaluated both the reversible and irreversible heat generations during a discharge process of different Li-ion cells. Moreover, we evaluated the irreversible entropy production due to the electrical/ionic conduction.

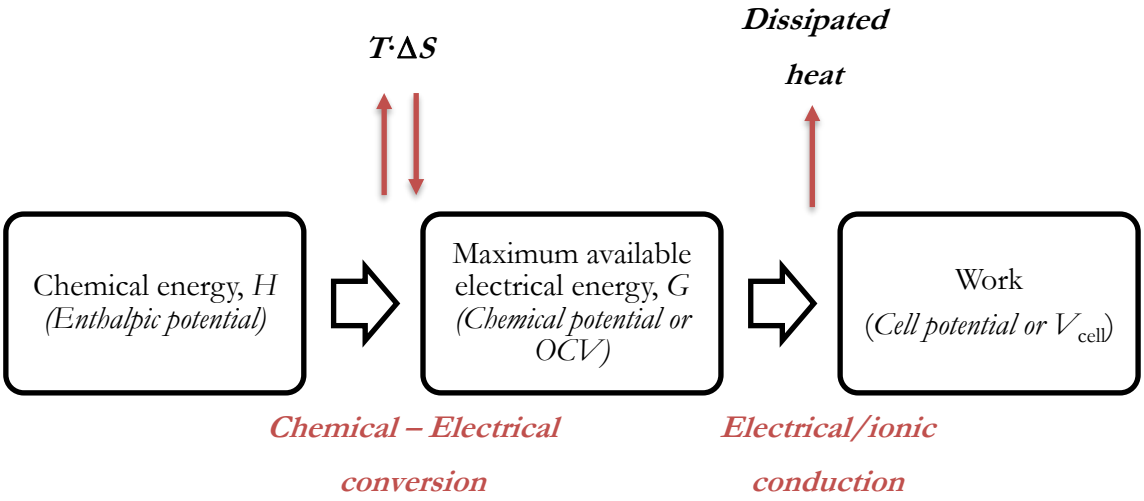

Fig. 4.68. Schematic representation of the energy transfers when converting chemical energy to electrical energy and the related useful work extracted from a battery.

4.4.1. OCV and hysteresis

The evolution of the OCV with the aging of the cells was different for the various evaluated chemistries. The OCV of the NMC cells slightly changed during the aging process (Fig. 4.3 and Fig. 4.5). Particularly, the voltage increased at some SoCs and decreased at some others. Unlike NMC, the OCV curves of LFP cells remained constant between SoCs 95.6 % and 82.3 % and between 44.7 % and 11.6 % and highly decreased otherwise (Fig. 4.32, Fig. 4.35 and Fig. 4.54). Contrarily to them, the OCV of LCO cells increased with aging in all SoC range (Fig. 4.61). These slight variations in the OCV due to aging of NMC cells are consistent with results found in reference [146], in which the OCV changed during the cells lifetime mainly at SoCs below 35 %. Regarding LFP cells, the same evolution of the OCV was found [146,161]; the plateau at higher voltages (above 3.3 V), which was labeled as (1) in Fig. 4.32, tended to disappear and the following plateau found around 3.3 V, which was labeled as (2) in Fig. 4.32, shifted to higher SoCs. In [146], the decrease of the plateau in the LFP cells, was associated to the loss of lithium inventory available for cycling. Moreover, the shifting of the second plateau to higher SoCs was related to an increase of battery impedance. Concerning the

evolution of the OCV during the cell lifetime in the case of LCO cells, relative information was not found in literature.

Hysteresis was found between OCV curves measured after charge and discharge processes in both NMC (Fig. 4.6) and LFP (Fig. 4.36) cells. We found that hysteresis of the NMC cells in general tended to increase as the SoC was decreased, unless at SoCs between 60 % – 36 % at BoL and 69 % – 35 % at the EoL were it decreased as SoC was decreased. At BoL we found a local maxima of 20.3 mV at SoC = 25.6 %. At the EoL, this peak shifted to SoC =29 % and increased from 20.3 mV to 23.7 mV. However, the local maxima at the BoL that was found at SoC = 56 % with an amplitude of 13.7 mV shifted to SoC = 64 % at the EoL with an amplitude of 24.5 mV. In reference [146], one of the evaluated cells showed a local maxima between 25 % and 35 % but of 30 mV amplitude at both BoL and EoL instead of 20.3 mV (BoL) and 23.7 mV (EoL). Barai et al. evaluated the shape of the hysteresis curve at one of the cells [86] and they found an increase of hysteresis during the initial part of the discharge process (SoC above 70 %), in which the values were below 10 mV. It was also found in [146] that hysteresis was below 10 mV at SoCs above 70 %. Then the hysteresis took values around 10 mV but slightly decreased until SoC was approximately 38 % from where it started increasing and reaching the maximum value of 27 mV at SoC = 25 %. From that point, hysteresis decreased until the EoD. In particular, Farmann et al. investigated two NMC cells and compared the generated hysteresis between fresh and aged cells. The hysteresis of one of those cells decreased with aging at SoCs below 70 % while the hysteresis of the other one was almost unchanged. In our study, we found that hysteresis voltage increased from BoL to the EoL in all SoCs except below 10 %.

Hysteresis of LFP cells with respect to SoC followed a similar tendency to NMC cells (Fig. 4.69). Moreover, it is widely mentioned in literature that LFP cells exhibit the highest hysteresis compared to the other chemistries [86,146]. However, we found that the hysteresis generated in NMC cells was comparable to that of LFP (Fig. 4.69). Indeed, the same results were found in [86]. In particular, in the variation of LFP hysteresis with SoC, there was a first stage at BoL at SoCs above 70 % in which hysteresis increased but stayed always below 10 mV. Afterwards, there was a peak at 65 % of approximately 20 mV that decreased until SoC = 38 %. Going below 38 %, there was again a local maxima at 26.6 % with an amplitude of 33.8 mV that decreased until SoC = 10 %. Below 10 % SoC, large divergences were found between the OCV curves. In reference [146], two peaks were also found at the same positions (65 % and 35 %). However, the hysteresis values corresponding to those peaks were larger (26 mV at 65 % and 40 mV at 30 %) than the ones measured in our study (22 mV at 64.6 % and 34 mV at 26.6 %). They did not track the evolution of the hysteresis of that cell with aging. In addition, they studied another LFP cell whose results did not match at all with our results. This would elucidate that hysteresis not only depends on the chemistry. In particular, they found only one peak of 20 mV at SoC = 20 %. Moreover, no variation with aging was appreciated, only a slight difference at SoCs above 70 %. Nevertheless, two local maxima were also found in references [144] and [162]. In particular , those peaks were found at SoC = 65 % and SoC = 20 %, which is very close to our

analysis [162]. Nevertheless, they found the highest hysteresis voltage was approximately 60 mV, which is far from our results. Hysteresis evolution during the battery lifetime was not considered in their study. In addition, in reference [144], the local maxims were found around SoC = 30 % and SoC = 68 % with maximum values of 33 mV and 15 mV, respectively.

As it was previously mentioned in section 4.2.1, hysteresis has been related to mechanical stress or to the existence of a lithium rich and lithium deficient phase within an active particle, which depends on the direction of current. Therefore, an increase in the measured hysteresis could indicate or either the cells suffered from mechanical stress during the cycling test or the different gradients formed inside the active material particles during charge and discharge were more differentiated with aging. In fact, it is known (and validated by post-mortem analysis in the case of NMC cells) that the cells suffer from mechanical stress during the lithium insertion and extraction at the NE. Thus, it might be an indicator of this stress.

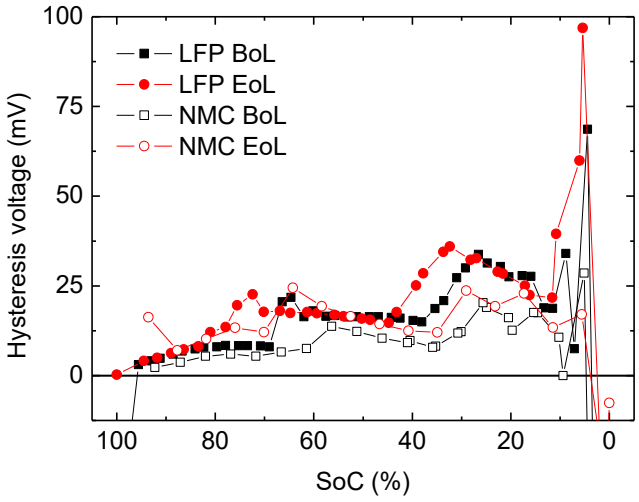

Fig. 4.69. Hysteresis found in LFP (filled symbols) and NMC (empty symbols) cells at BoL and EoL at room temperature.

4.4.2. Overpotential

It was not an easy task to find references in which the evolution of the overpotential with the SoC or the aging level of the cells would have been tracked. The dependence of the overpotential with C-rate and the corresponding polarization curves are more commonly found in literature. Moreover, we could not found other studies verifying the applicability of the linear and Tafel approximations of the Butler-Volmer equations in Li-ion batteries. We have not found either the recalculation of activation overpotential at high rates from charge-transfer resistance measured by EIS. Thus, the obtained the discussions of the results are presented below and compared to literature only when it was available.

The overpotential was defined as the difference between the OCV and the cell voltage (refer to equation (1.2)). The assumption for having the battery operating in the linear regime or in the Tafel

region of the Butler-Volmer equation, developed in subchapter 1.2.2.3, was detailed in equation (4.33).

$$\begin{cases} |\eta| \ll \dfrac{R \cdot T}{nF} \longrightarrow Linear\ regime \\ |\eta| \gg \dfrac{R \cdot T}{nF} \longrightarrow Tafel\ region \end{cases} \quad \textbf{(4.33)}$$

If calculus are carried out at ambient temperature (25 ºC) and considering $n = 1$, as we are working with Li-ion batteries, the absolute value of the overpotential has to be much below or much above 25.8 mV in order to be working at the linear regime or at Tafel region, respectively.

In our study, we have differentiated between linear regime and Tafel region. At rates equal or below 1C, we considered that the cells operated at the linear regime and above this rate, at the Tafel region. The average overpotential at a C/25 discharge rate of the NMC cells at BoL was found to be between 10 mV and 30 mV (Fig. 4.13) and at a 3C/2 rate it was around 350 mV (Fig. 4.12). VIC cells (LFP) produced an overpotential between 17 mV and 30 mV at a rate of C/25 (Fig. 4.38) and above 200 mV at a discharge rate of 2C (Fig. 4.39). The generated overpotential in EVbat cells (LFP) at a rate of C/8 was found to be between 30 mV and 50 mV (Fig. 4.56) that probably would be different if the OCV were calculated by the GITT technique, as it happened with VIC cells (Fig. 4.40). GITT data was not either available for LCO cells where the obtained overpotential at 1C at BoL was around 200 mV (Fig. 4.61). Nevertheless, the aforementioned overvoltages belonged to all the present contributions, not only to activation polarization, which is the only effect that has to be considered when using Butler-Volmer equation. Therefore, for calculating the actual contributions due to activation overpotential, it was done from the impedance data obtained in Chapter 3, which was measured at very low potentials (i.e. at the linear regime) because of the definition of impedance itself. In that case, for the NMC cells working at a C/25 discharge rate, the activation overpotential would be estimated as the product of the charge transfer resistance (around 20 mΩ) and the discharge current (2.8 Ah divided by 25 h which is equal to 0.112 A). Thus, the resulting activation overpotential of the NMC cells working at a C/25 discharge rate was around 2.24 mV, which was much lower than the proposed 25.8 mV for the validity of the linear approximation. The same calculation was made for the other cells were the overpotential of VIC cells (LFP) at a C/25 discharge rate was estimated to be around 0.8 mV at BoL, of 5.5 mV for the EVbat cells at C/8 and 44 mV for the LCO cells at 1C. The latter was the only one that deviated from the linear approximation but the other cells worked in the linear regime. Nevertheless, other effects like SEI transfer (ohmic contribution) were included in the estimation of the charge transfer resistance because they were overlapped in frequency and could not be separated with the available data. In any case, this would not be counterproductive to the applied approximation, as it would reduce even more the estimated activation polarization.

The separation of contributions to overpotential at high rates was not as straightforward as it was at low rates. This was because charge transfer resistance decreases as the discharge rate increases [83]. Therefore, charge transfer resistance obtained during the impedance measurements was not suitable for these calculations at high rates. Thus, the relation between current and activation overpotential had to be obtained from the general Butler-Volmer equation (1.3). At sufficiently high rates, where the reaction at one electrode is dominant in comparison to the other electrode, Butler-Volmer equation can be approximated by Tafel equation (for further information refer to subchapter 1.2.2.3). The activation overvoltage at high overpotentials related to each of the discharge currents was calculated through equation (4.30).

We found that the overpotential at low discharge rates of C/25 and calculated from the discharge GITT OCV curves, increased from BoL to EoL in the case of NMC cells around 15 mV in average (Fig. 4.70). Contrarily, it was reduced in the case of VIC cells (LFP) in around 5 mV and in a higher amounts at some peaks (Fig. 4.70). The evolution of overpotential with aging at different cycling levels was calculated from ps-OCV curves (Fig. 4.38). Peaks were appreciated and they were found to shift towards higher SoC during the aging process. The same tendency was found in [27] in which the peaks shifted to higher SoCs and, in some cells, it was also found that the distance between peaks was decreased. As LFP electrodes exhibit only one plateau, those peaks were associated to the graphite electrode. In particular, the shifting of the peaks was associated to LLI and the decrease in distance between them to LAM at the NE. However, Liu et al. clarified that the LAM_{NE} not necessarily decreases the capacity of the cell because there is always enough storage capacity in the active material for the remaining lithium [27]. In our results, no clear evidence of a reduction in the distance between peaks was appreciated. Thus, it might indicate LLI was the main aging mechanism and LAM was not taking place, at least, at the NE. In reference [163] an increase of the overvoltage of 28 mV after 1000 cycles in a NMC cell was specified. However, they only left a relaxation period of 15 minutes, which might not allow the complete relaxation of the OCV. Moreover, their results were not completely comparable to ours because the capacity of their cells underwent a larger decrease than ours.

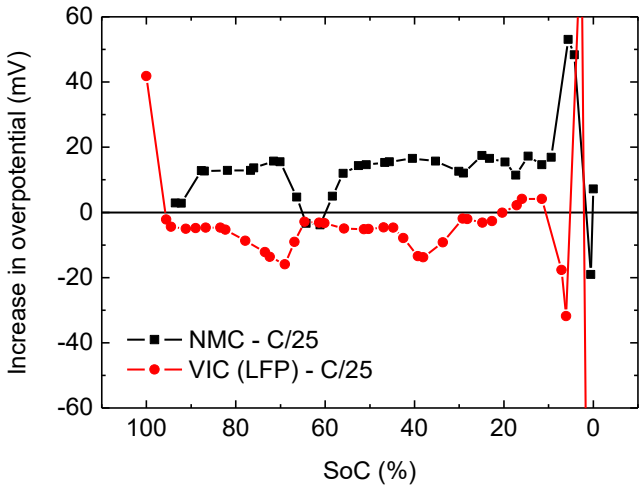

Fig. 4.70. Increase in overpotential at a C/25 discharge rate, from BoL to EoL of NMC and LFP cells at room temperature.

The increase in overpotential during the battery lifetime when discharged at rates equal or greater than 1C were represented in Fig. 4.71. The LCO cells suffered the highest increase at 1C even higher than the one suffered for LFP cells discharged at 2C and NMC at 3C/2. As in the case of NMC cells at 3C/2, the overpotential of LCO presented the highest increase at low SoCs. Contrarily, the increase in overpotential of the VIC cell (LFP) tended to increase at SoCs above 40 % but then decreased sharply and even became negative, meaning the generated overpotential was higher at BoL than at EoL.

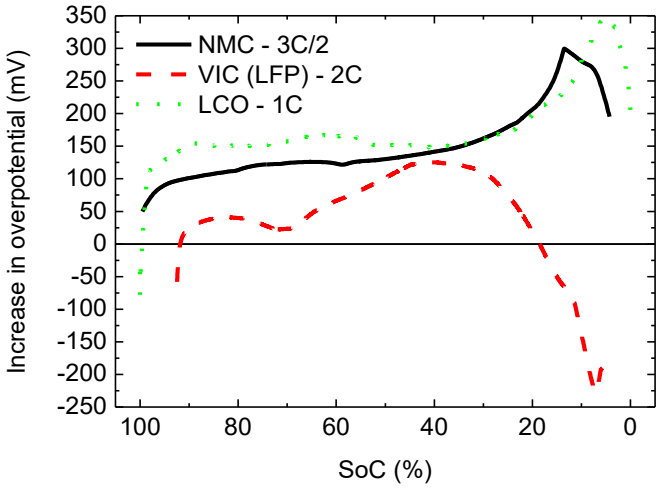

Fig. 4.71. Increase in overpotential from BoL to EoL at discharge rates between 1C and 2C of NMC, LFP and LCO cells at ambient temperature.

Regarding to the major contributors to overpotential, different results were found depending on the evaluated chemistry. Concentration polarization was the predominant effect when the cells were discharged at low rates for all cells (Table 4.3). In polarization curves, it can be appreciated that concentration polarization is the limiting factor at high discharge rates, when the current

approximates the limiting current as it was represented in Fig. 1.13. However, the dependency of the different overpotential contributions with time are not commonly found in literature. In fact, concentration polarization is not only accountable at high rates but can also become the predominant effect when the cells are discharged during long times (i.e. when discharging at low rates) [22,164,165]. Particularly, concentration polarization is associated to concentration gradients that form either at the solid or liquid phases. All of them limit the transport of ions from one electrode to the other. In particular, concentration gradients at the liquid phase (electrolyte) occurs when lithium-ions are depleted at the electrolyte because of the limited lithium transport at the porosity [14]. Furthermore, lithium-ions can be depleted at the surface of the active material if the solid-state diffusion is the limiting factor (i.e. diffusion at the solid phase or inside the active material particles). Moreover, the depletion of reactants is the responsible of the sharp decrease in voltage at the EoD [14].

Table 4.3. Major contributors to overpotential for different chemistries discharged at different rates.

Chemistry	Rate	Predominant effect
NMC	C/25	Concentration polarization
	3C/2	Ohmic polarization
LFP (VIC)*	C/25	Concentration polarization
	2C	Concentration polarization
LFP (EVbat)	C/8	Concentration polarization
LCO	1C	Ohmic at BoL and concentration at EoL

* The different contributions were only separated at BoL because of impedance data availability.

The time constant of the charge transfer effects is lower than that of mass transfer. It can be stated from the semi-arcs at the impedance spectra of the cells representing the charge transfer processes and the diffusional branch at lower frequencies representing the mass transfer effects (for further information refer to Chapter 3). Therefore, the elapsed time of discharge from which the cells started to be limited by mass-transfer effects could be approximated from the impedance measurements. Frequency at the beginning of the diffusional branch was estimated and converted to time for all the evaluated chemistries. For NMC cells, it was 1.7 s (0.6 Hz), for VIC (LFP) it was 0.14 s (7 Hz), for EVbat (LFP) it was around 0.6 s (1.5 – 2 Hz) and for LCO it corresponded to 1 s (1 Hz). Thus, it implied that from the very beginning of the discharge process, the results were affected by concentration polarization effects (difussion). Furthermore, those effects continued growing as the time went by, in the same way as the real part of impedance increased while the frequency decreased. Therefore, long-time discharges would be highly affected by diffusional effects as it could be extracted from the impedance data. In addition, the time constants for lithium diffusion in the solid phase in [164] were found to be 2016 s at the negative electrode and 35 s at the positive electrode. Although the values they found were much higher than those found in our study, even with their

data, cells discharged at C/25 would be also affected by diffusion in the solid phase in the first stages of the discharge process. The found tendency with SoC in the concentration overpotential corresponded with the expected: it started being a small contribution at BoD and became the predominant effect at the EoD [165].

When comparing the overpotentials generated at high and low discharge rates, concentration polarization was found to be the dominant effect at low discharge rates whereas the ohmic contribution was dominant at high rates, except for LFP cells, where concentration polarization was also the major contributor at high discharge rates. This could be attributed to the higher contribution to impedance of the term related to mass transport (i.e. the diffusional branch at lower frequencies) in the evaluated LFP cells compared to NMC or LCO. These differences were evidenced in Fig. 3.8, Fig. 3.17 and Fig. 3.25 in which this tail was around 15 – 20 mΩ for NMC and LCO until frequencies of 3 - 4 mHz whereas it was between 300 – 400 mΩ in the case of the LFP cells in a narrower frequency range (10 mHz). Thus, mass transfer effects were expected to be predominant in LFP cells. In addition, activation polarization contributed in a very small amount at high rates. In fact, for large enough kinetic currents, activation polarization can be neglected [26].

Concerning the overpotential produced in the LCO cells at a 1C discharge rate, the predominant effect at BoL was the ohmic contribution while, at the EoD, the concentration polarization surpassed it (Fig. 4.63). It suggested that the diffusion phenomena was the more affected part by the aging process. Thus, yielding to a larger overpotential at the EoL due to the higher increase suffered by the cells in terms of concentration polarization.

4.4.2.1. Overpotential correspondences from NMC half-cells

The overpotential produced at a C/25 discharge rate at the NMC PE and at the graphite NE were estimated separately from half-cell measurements (Fig. 4.11). Despite the fact that each of the electrodes was represented with respect to its particular SoC (not accounting for the full-cell SoC), they were added in order to obtain a curve that approximates the full cell overpotential. However, the results would not reflect the true full-cell overpotential because the matching of the electrodes was not taken into account. Moreover, the overpotential generated at the lithium metal electrode in the half-cells was not subtracted from the results. Thus, Fig. 4.11 only served as non-accurate approximation of the resulting overvoltage, which was used to identify possible tendencies coming from each of the electrodes. If the results are compared to the full-cell overpotential, especially to the overpotential obtained from the ps-OCV curves, where more resolution in SoC was achieved, some parts could be associated to the PE or to the NE (Fig. 4.9 and Fig. 4.10). At SoCs around 60 %, there was a peak associated to the NE that did not increase from BoL to EoL. However, it almost disappeared at the EoL and it was because of the high increase in the PE overpotential from BoL to EoL. The major contributor at BoL was the NE but although both of them increased towards the EoL, the increase in PE overpotential was much higher what lead to same contributions from PE

and NE at the EoL except at PE-SoCs below 20 % where the PE predominated. These results suggested that diffusion at the NE and side reactions were limiting the discharge process at BoL. Moreover, diffusion at the PE was also becoming a limiting factor as the cell was aged.

4.4.2.2.Limitations

We must point out that these overpotential analyses have some limitations:

- Activation polarization include other effects as conduction in the SEI layer and the current collector. Those effects should have belonged to the ohmic contribution [83] but they could not be separated from the charge-transfer effect at the electrode/electrolyte interface. This is because although they are ohmic effects, they have a capacitive effect associated to them, yielding to additional semi-arcs at the impedance spectra instead of simple resistive effects.
- The ohmic contribution was obtained from the estimation of resistance from the impedance spectra. It was done by measuring the real part of impedance when the imaginary part was zero. For being more accurate, it should have been previously subtracted the inductive effect at high frequencies.
- Tafel approximation was considered at rates higher than 1C. When this approximation is assumed, it is supposed that the rate of the reaction at one of the electrodes is much higher than that at the other electrode. Thus, the reaction taking place at the lowest rate was neglected for the calculations of activation polarization at high rates. However, further checks of the validity of the approximation at those medium-high rates (between 1C and 2C) should be carried out.
- Impedance of VIC cells was only measured at SoC = 100 %. Therefore, because of the low variability of the ohmic effect and activation polarization with the SoC, especially with respect to concentration polarization, they were considered as constant with SoC.
- Concentration polarization ($\eta'_{concentration}$ in equation (4.34)) was calculated as the difference between total overpotential produced at the cells and both the contributions of the ohmic effect and activation polarization. Thus, other effects that could be producing an additional overvoltage, as the side-reactions, would be included in that term. Particularly, these other effects could be generated by side reactions taking place in the cell ($\eta_{side-reactions}$). Concretely, side reactions are undesired electrochemical reactions taking place at the electrodes, which can also be defined by the Butler-Volmer relation for electrochemical reactions thus adding an extra overpotential [166,167]. Some of those side reactions could be electrolyte reduction, metals plating, current collectors dissolution or metals dissolution [166].

$$\eta = \eta_{ohmic} + \eta_{activation} + \eta_{concentration} + \eta_{side-reactions} = \eta_{ohmic} + \eta_{activation} + \eta'_{concentration} \quad (4.34)$$

- During discharge at high rates, the temperature of the cells rises as the discharge progresses. Thus, it implies that the different resistive contributions would change during the discharge process. Nevertheless, the ohmic and activation contributions to overpotential were considered as constant with respect to temperature. Therefore, an error that was not quantified would be introduced in the results at high rates especially towards the EoD.

4.4.3. Entropy

4.4.3.1.Reversible entropy

The entropic coefficients of LGC2 cells (NMC/graphite) (Fig. 4.18) and Microbattery cells (LCO/graphite) (Fig. 4.64) cells were negative in all the SoC range. It implied that the reversible heat was adding heat to the total heat flow generated during discharge (it contributed in releasing heat). Unlike for these two cells, the entropic coefficient of VIC cells (LFP/graphite) was positive at SoCs above 30 % (Fig. 4.46). Thus, the associated reversible heat would be subtracted from the total generation of heat during discharge, what will reduce it (it contributed absorbing heat). The general tendency of the three evaluated chemistries was to decrease as the SoC decreased.

Furthermore, great differences between BoL and EoL were not appreciated. However, it has to be mentioned that even though variations were small, they could be appreciated at some SoCs. Slight variations were also found in [160] and [159] (although they were referred as great differences) and they were associated to crystal structure deterioration. Reversible entropy variations with SoC are commonly related to different staging or graphitization levels [168–170]. Thus, they are rather used to determine the actual SoC of the cells than their degratadion level.

4.4.3.2. Irreversible entropy

Before the introduction of the detailed discussions, it is convenient to clarify the framework of irreversible entropy. In Fig. 4.72, we propose the energy/entropy balance in the battery. Green arrows represent the energy balance in a closed system. In addition, the heat exchange with the sorroundings in an open system are represented in the top part of the figure with their corresponding entropy productions. Heat is exchanged reversibly and irreversibly due to the chemical reaction and to the conduction and charge transfer, respectively. At the bottom, aging effects consuming part of the input energy are represented. Thus, this lost energy is consumed in side reactions and mechanical degradation. Therefore, they generate internal irreversible entropy due to the degradation of the cells, in which part of its associated energy is employed in the degradation process itself and the rest is expelled to the exterior as heat.

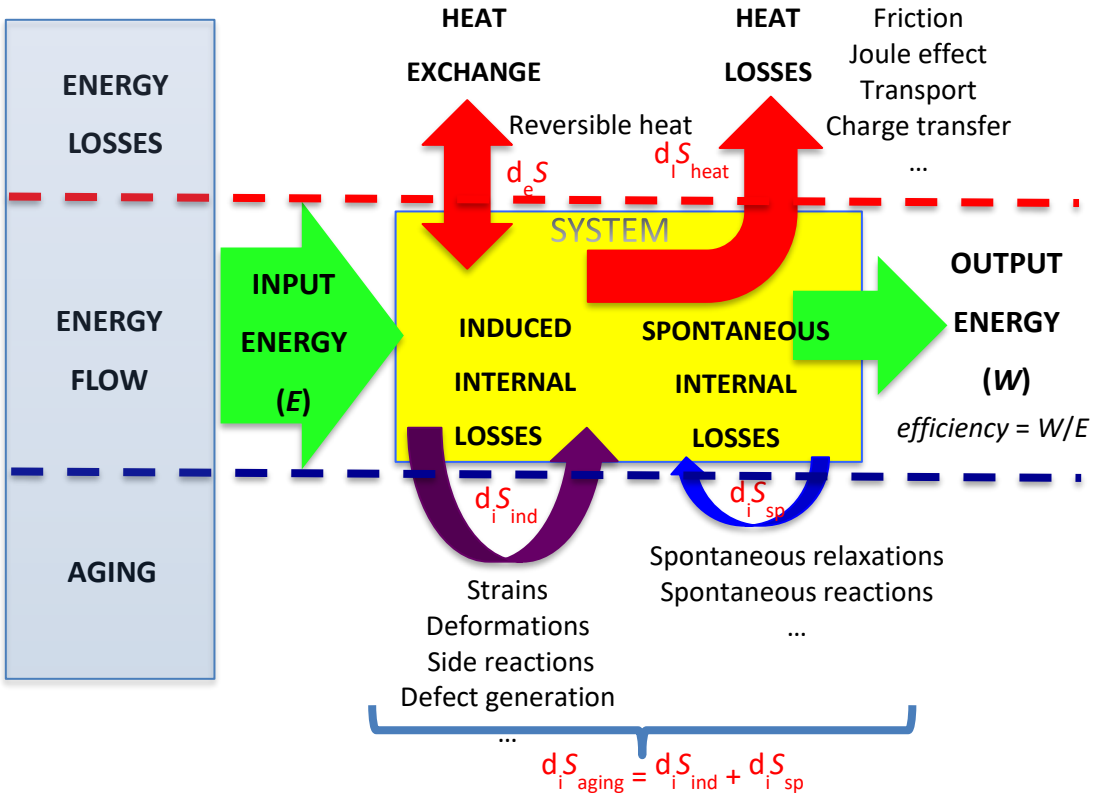

Fig. 4.72. Energy exchange in a closed system (green arrows). Output energy (work) is related to input energy through the efficiency. The arrows in red, blue and purple indicate entropy production (i.e. energy degradation). Energy losses and entropy production are divided between heat flow towards the environment and system aging. The former is divided between reversible heat and irreversible heat (friction, Joule effect, transport, charge-transfer effects…). The later can be due to the input energy or generated spontaneously in non-equilibrium systems.

4.4.3.2.1. Close-to-equilibrium measurements

The generation rate of irreversible entropy was calculated from the measured overpotential at different rates and aging levels. Therefore, all the limitations described in 4.4.2.2 for the overpotential estimations also apply to the calculations of entropy production.

The generation rate of irreversible entropy refers to the entropy that was produced inside the cells. All the evaluated chemistries exhibited different behaviors in terms of production of irreversible entropy. NMC cells produced irreversible entropy faster at the EoL than at BoL (Fig. 4.22). It was true for all SoCs except at SoCs around 60 % where it was the contrary and the production at the EoL was lower than that at BoL. Concerning LFP cells, no much information could be extracted from EVbat cells but VIC cells showed a decrease in the generation rate of irreversible entropy from BoL to EoL (Fig. 4.51). However, if the evolution of d_iS is checked in Fig. 4.47 where intermediate cycles between BoL and EoL were represented, it can be appreciated that the entropy production decreased during the first 400 cycles and then it started increasing again until the end of the cycling test. Nevertheless, a decrease was found between BoL and EoL because although it was increasing it

was not enough to surpass the initial generation rate. Moreover, LCO cells increased their generation rate from BoL to EoL in all the SoC range (Fig. 4.65).

In particular, in NMC cells, the major contributor to the generation rate of irreversible entropy at a C/25 discharge rate was the term related to concentration polarization and side reactions (labeled as *Concentration* in Fig. 4.22). This term represented in average the 60 % to 80 % of the total d_iS and went up to 90 % at the EoD. Ohmic, activation and concentration polarizations tended to increase from BoL to EoL. However, the relative values of ohmic, activation and concentration terms with respect to total generation rate were unchanged from BoL to EoL at SoCs above 75 %. Nonetheless, at SoCs around 60 %, the total contribution of the term related to concentration was decreased by increasing the ohmic and activation terms. From this SoC until 15 %, the relative contribution of the concentration polarization term was higher at the EoL and both ohmic and activation contributions were lower. Furthermore, at SoCs around 20 – 25 %, the contribution to total entropy production at BoL of the ohmic term was higher than the concentration one. However, this behavior was not found anymore at the aged cell.

From the overpotential measurements carried out at the half-cells, we inferered that, at BoL, diffusional processes and side reactions at the NE dominated the entropy production. Nevertheless, diffusional processes and side reactions taking place at the PE increased in such a way from BoL to EoL that the PE ended up producing irreversible entropy at the same rate as the NE. In addition, the entropy production at the EoD was mainly produced at the PE (Fig. 4.73) for both BoL and EoL. In particular, the high increase in overpotential at the EoD was related to the depletion of reactants produced during the discharge process [171].

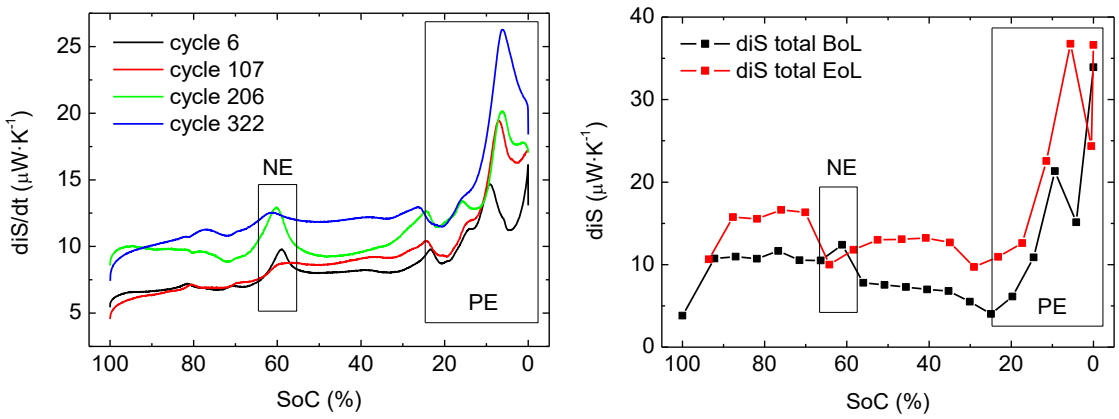

Fig. 4.73. diS evolution with cycle aging of NMC/graphite cells discharged at C/25 calculated from ps-OCV (left) and discharge GITT OCV (right). Effects coming from PE and NE were distinguished (labeled as PE and NE) thanks to half-cell measurements.

In VIC cells (LFP), the major contributor at a C/25 discharge rate was also the term related to concentration polarization and side reactions (Fig. 4.49). At BoL, it represented in average the 90 –

95 % and increased to almost the 100 % at the EoD. Unfortunately, it was not possible to separate the different contributions at the EoL due to the lack of impedance data at that aging level.

In EVbat cells (LFP) when discharged at a C/8 rate, the major contributor was also the term related to concentration polarization and side reactions (Fig. 4.60). It represented the 72 – 88 % of the total generation rate and increased to 96 % at the EoD. The entropy production related to the ohmic term increased as the cells were aged in the case of cell 1 (50 cycles), cell 2 (100 cycles) and cell 3 (200 cycles). However, the ohmic contribution of cell 4 (400 cycles) was below the one of cell 1 (50 cycles). In addition, the entropy production related to the activation term decreased as the cells were aged. From cycle 100 to 200, the variation was lower than what is was between cycles 50 and 100 or between 200 and 400. Regarding the term related to concentration polarization, it was very similar in all aging stages except at SoCs above 70 % where cell 3 and cell 4 deviated, being higher the contribution as more aged was the cell. With respect to the relative contributions to the total generation rate of irreversible entropy, the ohmic term contributed in the same way at BoL and EoL except at SoCs above 70 % where the contribution was higher at BoL. However, if the contributions at intermediate cycles are evaluated, it can be seen that the ohmic term increased from BoL to cycle 100 and 200 and then decreased until the EoL. It could not be assured that cell 4, which was considered as the EoL cell, started at the same SoH as the others did because some differences were found at the capacity evolution represented in Chapter 2. Moreover, this cell was cycled in a climatic chamber at 25 ºC what differed from the rest, which were cycled in a temperature-controlled room. Nevertheless, if data were taken as valid, the decrease in ohmic resistance could be related to the degradation of the cell. In fact, in our previous study [172], we found that when resistors are degraded they can either increase their resistance or decrease it, because resistance trend depends on the degradation mechanism. Moreover, the relative contribution of the activation term decreased as the cells were aged in all the evaluated cycles. Finally, even though the term related to concentration polarization and side reactions was rather constant from BoL to EoL, its relative contribution to irreversible entropy generation stayed rather constant from cycles 50 to 200 and then increased from cycle 200 to 400.

In LCO cells subjected to a discharge rate of 1C, the predominant effect at BoL was the term associated to the ohmic effect and at the EoL it was the term related to concentration polarization (Fig. 4.65). However, at the EoD, the major contributor was the concentration term at both BoL and EoL, probably due to the depletion of reactants at this last stage [171]. During the aging process, all three contributions were found to increase (Fig. 4.66). Nevertheless, the relative contribution of the activation term was the same at BoL and EoL. Moreover, the relative contribution of the ohmic effect decreased from BoL to EoL and the one related to concentration polarization (and possible side effects) increased.

4.4.3.2.2. Far-from-equilibrium measurements

Measurements at discharge rates higher than 1C were carried out to NMC and VIC cells. Thermodynamic measurements are useful in determining the degradation in terms of LLI and LAM. However, cells operating at high loads are also highly affected by kinetic limitations. Moreover, side reactions are favoured under high loads [29,173]. Therefore, it is also convenient to us to consider the evaluation of the behavior of the cells at higher rates. The major contributor to irreversible entropy production in NMC cells at 3C/2 discharge rate was the ohmic term at both BoL and EoL (Fig. 4.25). Ohmic, activation and concentration related terms increased from BoL to EoL, except the term associated to concentration polarization at SoC = 100 %. The relative contribution to entropy production of the activation term was independent of aging. Therefore, when concentration term contributed less, the ohmic effect contributed more and vice versa.

The generation rate of irreversible entropy at VIC cells (LFP) discharged at a 2C rate, increased from BoL to EoL except at SoCs below 20 % (Fig. 4.51). The major contributor at BoL was the term related to concentration polarization and side effects as represented in Fig. 4.51. It was the responsible of the 60 – 70 % of the irreversible entropy generation and it increased until almost the 95 % at the EoD. The entropy production due to the ohmic conduction was slightly higher than the one associated to the charge transfer process. Each of them accounted for near the 20 % of the entropy production decreasing their contribution as the discharge proceeded.

4.4.4. Heat generation

We found that the heat generation during discharge at high and low rates was exothermic in all cases except in VIC cells (LFP). They showed an endothermic behavior at SoCs above 30 – 40 % when discharged at low rates (C/25). Moreover, the irreversible generation of heat at low rates decreased at the EoL compared to BoL. It could be attributed to the decrease in charge-transfer resistance with aging encountered in Chapter 3 (it will be further analyzed in Chapter 6). However, at high rates, at which the ohmic contribution is enhanced, the irreversible generation of heat was larger at the EoL. Nevertheless, concerning the other cells (NMC and LCO), the irreversible generation of heat increased at both rates from BoL to EoL. In general, we found that the reversible term slightly changed with aging compared to the irreversible one. Differences between the heat generation LFC cells and other chemistries were also found in literature [174].

4.5. Conclusions

4.5.1. OCV and hysteresis

- OCV depended on the aging level in all the evaluated chemistries.
    - In NMC cells, the OCV slightly increased at some SoC values and slightly decreased in some others.
    - In LFP cells, the OCV stayed constant at some SoCs and highly decreased in some others. In other studies, this behavior was related to LLI.

  - In LCO cells, the OCV increased in all SoC range.
- Hysteresis between charge and discharge processes was evaluated in LGC2 cells (NMC) and VIC cells (LFP). Hysteresis was dependent on the aging level in both cases.
  - Hysteresis voltage in NMC increased from BoL to the EoL in all SoCs except below 10 %.
  - Hysteresis voltage of VIC cells (LFP) increased at some particular SoC ranges (between 80 % and 65 %, between 44 % and 28 % and below 10 %) from BoL to EoL and remained unchanged at the other SoCs.
  - The increase in hysteresis was related to mechanical stress suffered by the cells during the aging process.

4.5.2. Overpotential

- Ohmic, activation and polarization contributions were separated from the total overpotential at low and high discharge rates.
  - At low discharge rates of C/25, the overpotential increased from the BoL to EoL in the case of NMC cells and it was reduced in the case of VIC cells (LFP).
  - The shifting in peaks found at the overpotential of VIC cells was attributed to LLI. Increase in the distance btween peaks was not appreciated thus, LAM_{NE} was discarded.
  - At high rates, LCO cells suffered the highest increase at 1C even higher than the one suffered for LFP cells discharged at 2C.
- Concentration polarization was the dominant effect at low discharge rates and the ohmic contribution at high rates, except for LFP cells in which concentration polarization dominated at both rates.
  - It was attributed to the lower time constants related to mass transport effects in LFP cells.
  - Activation polarization contributed in a very small amount at high rates.
- The differences in predominant effects between BoL and EoL in LCO cells suggested that the diffusion phenomena was the more affected part by the aging process.
- The found tendency with SoC in the concentration overpotential corresponded with the expected: it started being a small contribution at BoD and became the predominant effect at the EoD.
- The limitations of our approximation in the separation of the different effects contributing to overpotential were detailed.

4.5.2.1.Overpotential produced at NMC/Li and graphite/Li half-cells

- The overpotential produced at a C/25 discharge rate at the NMC PE and at the graphite NE were estimated.
- The full-cell SoC was not estimated and the matching of the electrodes was not considered.
- The overpotential generated at the lithium metal electrode in the half-cells was not subtracted from the results.
- The overpotentials belonging to some particular SoCs could be associated to the overpotentials at PE or NE.
- The major contributor at BoL was the NE but although both of them increased towards the EoL, the increase in PE overpotential was much higher what lead to same contributions from PE and NE at the EoL unless at PE-SoCs below 20 % where the PE predominated.
- These results suggested that diffusion at the NE and side reactions were limiting the discharge process at BoL. Moreover, diffusion at the PE was also becoming a limiting factor as the cell aged.
- The limiting electrode at the EoD at both BoL and EoL was the PE. It suggested that the depletion of reactants was the cause of the high increase in overvoltage at the EoD.

4.5.3. Entropy

4.5.3.1.Reversible entropy

- The entropic coefficients of the evaluated NMC and LCO cells were negative in all the SoC range.
- The entropic coefficient of VIC cells (LFP) was positive at SoCs above 30 % and negative otherwise.
- The general tendency of the three evaluated chemistries was to decrease as the SoC was decreased.
- Great differences between BoL and EoL were not appreciated.
- LCO was the cell reaching higher negative values at the EoD.

4.5.3.2.Irreversible entropy

- The generation rate of irreversible entropy was calculated from the measured overpotential at different rates and aging levels.
- The generation rate of irreversible entropy refers to the entropy that was produced inside the cells.
- Irreversible entropy was found to be a promising magnitude to characterize battery aging.

4.5.3.2.1. Close-to-equilibrium measurements

- NMC cells produced irreversible entropy faster at the EoL than what they did at BoL.
    - The major contributor was the term related to concentration polarization and side reactions.
    - Ohmic, activation and concentration polarizations tended to increase from BoL to EoL. However, the relative values of ohmic, activation and concentration terms with respect to total generation rate were unchanged from BoL to EoL at SoCs above 75 %.
    - At BoL, diffusional processes and side reactions at the NE dominated the entropy production.
    - At the EoL, diffusional processes and side reactions taking place at the PE produced irreversible entropy at the same rate as the NE.
    - At BoL and EoL the entropy production at the EoD was mainly produced at the PE.
- VIC cells showed a decrease in the generation rate of irreversible entropy from BoL to EoL. Actually, the entropy production decreased during the first 400 cycles and then it started increasing again until the end of the cycling test.
    - The major contributor was the term related to concentration polarization and side reactions.
    - The various contributions at the EoL were not separated because impedance data were not available at this aging level.
- In EVbat cells (LFP) discharged at a C/8 rate, the entropy production remained almost constant during the aging process except at SoCs above 70 % where it increased after 200 cycles.
    - The major contributor was the term related to concentration polarization and side reactions.
- LCO cells increased their generation rate from BoL to EoL in all the SoC range.
    - The predominant effect at 1C at BoL was the term associated to activation polarization and at EoL it was the term related to concentration polarization.
    - At the EoD, the major contributor was the concentration term at both BoL and EoL.
    - Ohmic, activation and concentration contributions increased during the aging process.
    - The relative contribution of the activation term was the same at BoL and EoL.
    - The relative ohmic contribution decreased from BoL to EoL while concentration increased.

4.5.3.2.2. Far-from equilibrium measurements

- Measurements at discharge rates higher than 1C were carried out to NMC and VIC cells.
- Ohmic, activation and concentration related terms related to irreversible entropy production in NMC cells at 3C/2 discharge rate increased from BoL to EoL.
    - The major contributor was the ohmic term at both BoL and EoL.
    - The relative contribution to entropy production of the activation term was independent of aging.
- The generation rate of irreversible entropy at VIC cells (LFP) discharged at a 2C rate, increased from BoL to EoL except at SoCs below 20 %.
    - The major contributor at BoL was the term related to concentration polarization and side effects.
    - The entropy production due to ohmic conduction was slightly higher than the one associated to the charge-transfer process.

4.5.4. Heat generation

- We found that the heat generation during discharge at high and low rates was exothermic in all cases except for VIC cells (LFP).
    - VIC cells (LFP) showed an endothermic behavior at SoCs above 30 – 40 % when discharged at low rates (C/25).
- The irreversible generation of heat at low rates decreased at the EoL compared to BoL.
- At high rates, at which the ohmic contribution is enhanced, the irreversible generation of heat was larger at the EoL.
- The irreversible generation of heat in NMC and LCO increased at both low and high rates from BoL to EoL.
- We found that the reversible term slightly changed with aging compared to the irreversible one.

Chapter 5

Post-mortem analysis

In this chapter, post-mortem analysis of LGC2 cells (NMC/graphite) is carried out. The employed techniques are visual inspection of the electrodes, capacity and impedance measurements of half-cells, ICP-OES, porosimetry and X-Ray diffraction.

5.1. Introduction

Post-mortem analysis consists of a series of invasive techniques carried out to the cells in order to evaluate their internal state. They provide information about the degradation mechanisms that take place [32,49,175,176]. Therefore, they can be used to validate the results from non-invasive electrochemical techniques. Although non-invasive techniques can give accurate results, post-mortem analyses are the only ones that allow direct evaluation of chemical changes. In our case, post-mortem analysis was of high interest to validate some of the previous hypothesis we had made and to understand battery operation. In particular, we aimed to verify our assumptions regarding the different degradation mechanisms that were taking place and their contribution to capacity fade. Moreover, we would be able to determine which electrode mainly contributes to capacity fade or impedance rise. Furthermore, a more comprehensive understanding of how batteries actually work and how they are manufactured would be also obtained.

During a research stay at ISEA in Aachen (Germany), we performed visual inspection of the electrodes, capacity and impedance measurements of half-cells, Inductively Coupled Plasma Optical Emission Spectrometry (ICP-OES), porosimetry and X-Ray Diffraction (XRD) analysis. Visual inspection allowed the determination of the state of the electrodes and the separator. Half-cells

characterization allowed, on the one hand, to validate the homogeneity inside the cell in relationship to their performance at different degradation levels, and on the other hand, to quantify the loss of active material with capacity measurements. In addition, impedance measurements were carried out in order to determine the electrode that was contributing more to the impedance rise due to cycle aging. Thanks to the ICP-OES, metals composition in the cells at different SoH levels were obtained. From the results, loss of lithium and metals migration were estimated. Furthermore, porosimetry analysis gave the mean distribution of particle sizes and pores. Finally, from XRD analysis, changes in the structure of the materials could be obtained.

5.2. Materials and methods

5.2.1. Cell opening

Three LGC2 cells (NMC) and two VIC cells (LFP) previously set to different SoH levels, were opened. (Refer to Chapter 2 for further information about the degradation level of the cells). Moreover, new cells were also open for the sake of comparison between the beginning of life and the end of life of the considered cells.

Before starting the cell-opening procedure, cells were fully discharged, and thus, lithium was expected to be completely at the positive electrode. NMC/graphite cells were discharged at a rate of C/25 followed by remnant capacity at C/25 and VIC cells (LFP) were also discharged at a rate of C/25 but the remnant capacity was discharged at a C/100 rate because of their slower kinetics.

Cell opening was carried out inside a glove box in argon atmosphere. The first step was to remove the plastic that covers the metallic can (refer to Fig. 5.1a). The plastic cover was precisely cut with a ceramic scalpel and removed with plastic tweezers. It is important to work with plastic or ceramic elements instead of metallic ones during the cell-opening procedure to avoid possible internal shortcuts. However, in the first step, it is not relevant because the can is still completely sealed. Once the plastic cover was completely removed, the can was opened with a can-opener (refer to Fig. 5.1b). In this case, only metallic can-opener was available, what made the process more challenging. The can opening had to be done carefully in order to only cut the can without short-circuiting the electrodes. Once the can was opened at one end, the current collector of the positive electrode could be seen at the center of the jellyroll (refer to Fig. 5.1c). The current collector was cut in order to remove the top of the metallic can. After that, the can was completely removed. In our case, it was done with metallic pliers (refer to Fig. 5.1d). This part of the process had to be done carefully trying to not apply a pressure to the cell that could degrade it. Moreover, it was important to be careful with sharp ends of the can to prevent breaking the gloves. When the can was removed, the only remaining part was the jellyroll (refer to Fig. 5.1e). It could be wet or dry depending on whether some electrolyte was still remaining or not. The jellyroll was unrolled in order to separate the electrodes and separators (refer to Fig. 5.1f). At this point, the cell opening was complete and the samples could be harvested from the electrodes, electrolyte or from the separators.

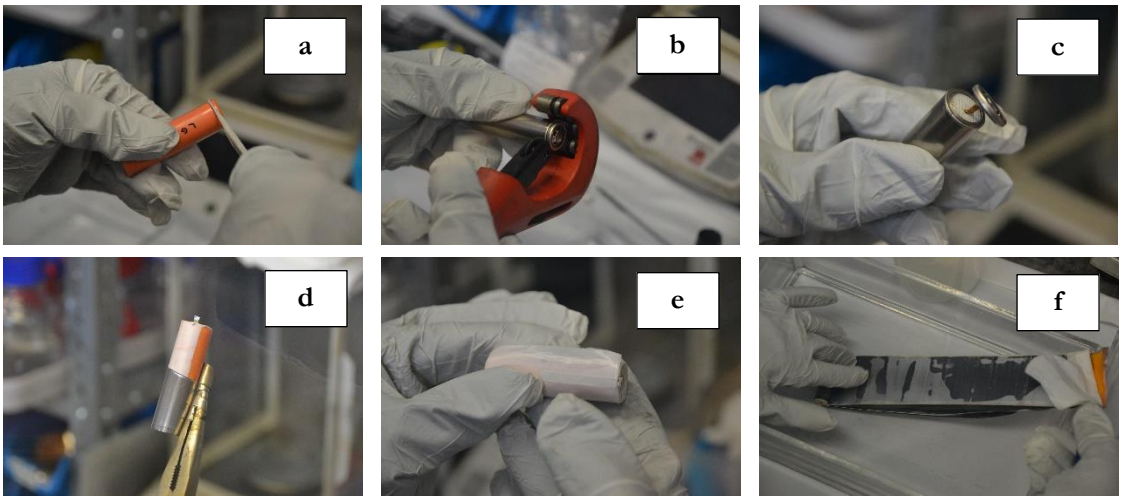

Fig. 5.1. Cell-opening procedure. a) Remove the plastic cover. b) Open the can with a can-opener. c) Cut the current collector of the positive electrode and remove the top of the cell. d) Remove the can completely. e) Keep the jellyroll. f) Unroll the jellyroll and separate the electrodes and the separator.

5.2.2. Preparation of samples

Samples were taken inside the glove box after all the components were weighted separately. The full-cells were weighted before the cell-opening and every single component was weighted separately after the cell-opening. Furthermore, the length of the electrodes, their width and thicknesses were measured. Length and width were measured with a ruler and thickness was measured with a thickness gauge (refer to Fig. 5.2a). Thickness measurements were not precise as the measured value depended upon the pressure exerted on the device.

Samples of different diameter were harvested from the electrodes with a round puncher (refer to Fig. 5.2b, Fig. 5.2c, Fig. 5.2e and Fig. 5.2f). Some of the samples were rinsed in Dimethyl Carbonate (DMC) in order to eliminate the phosphates on the top of the electrode and to compare the results from the non-rinsed samples (refer to Fig. 5.2d). The samples were put in a small glass containing the DMC, moving them for some seconds and then leaving them to dry. It is not clear the actual effect of rinsing the electrodes and different considerations about the time they have to be immersed and drying change from study to study [21,89,152,167,177]. In our case, no relevant differences were found between washed and non-washed electrodes. Thus, no differentiation will be made in the results.

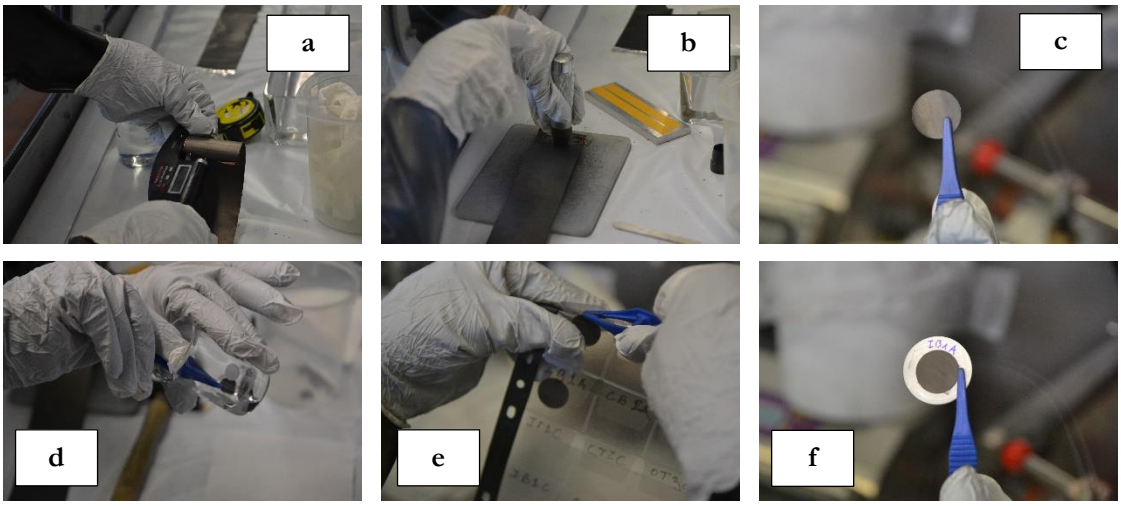

Fig. 5.2. Weighting and samples preparation. a) Thickness measurement of the electrode and current collector. b) Punching the electrode for taking samples. c) Sample taken for building half-cells. d) Rinsing the samples in a solvent. e) Keeping the samples in a labeled box. f) Sample attached to a metallic support ready for XRD analysis.

Samples of the electrodes were taken at different positions. The electrodes were divided into three sections: internal or inner part (which corresponds to the internal part of the jellyroll when rolled), central part and external or outer part of the jellyroll (Fig. 5.3). Depending upon the test to be carried out, samples were taken in different shapes and sizes. Moreover, some of them had to be processed in order to eliminate one of the active-material sides. It was done with N-Methyl-2-pyrrolidone (NMP) solvent, applying it by hand until the active material detached from the current collector. Sizes and shapes of samples were defined accordingly to the test as follows.

- Coin cells (only one side active material) – 16 mm diameter
- ICP (both sides) – 20 mm diameter
- XRD (both sides) – 20 mm diameter
- Porosimetry – 42 x 90 mm

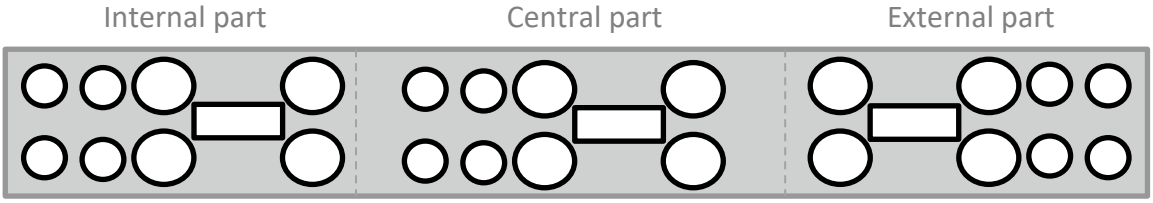

Fig. 5.3. Unrolled electrode divided by sections. Rectangular and circular samples of different sizes were taken along the electrodes.

5.2.3. Visual inspection

There are two types of visual inspection: naked eye and laser microscope. Naked eye observation was directly done during the cell-opening procedure. Positive electrode does not provide much information at first sight but the coloration of the negative electrode can be related to the state-of-charge. In our case, as the cells were disassembled at SoC = 0 %, the color of the negative electrode

was expected to be completely black [178]. Furthermore, possible surface layers and lithium plating formation during charge at the negative electrode could be appreciated if present.

Laser inspection was performed with a Keyence laser inside the glovebox. Samples were placed in holders, which were magnified under the laser microscope in different orders of magnitude depending on the test. Measurements were carried out perpendicular to the top of the sample and perpendicular to the width of the sample. The first one allowed the observation of the shape of the particles and the possible formation of layers on the top of the electrode. Although the transversal measurement of the samples was especially useful for the thickness measurement of the electrodes, current collectors and surface layers, placing the sample in the appropriate way was a difficult task. Quantifiable data were not obtained from this measurement.

5.2.4. Building half-cells

Samples of 16 mm diameter were harvested from both electrodes at different points (inner part, central part and outer part of the jellyroll). They were built into coin cell format introducing the harvested positive or negative electrode, a separator, 90 μL of electrolyte and metallic lithium as the other electrode. For building the half-cells in coin-cell format, metallic lithium was punched circularly. Fresh electrolyte and a new separator were introduced to the coin cells during the manufacturing process. All the steps summarized in Fig. 5.4 are detailed below.

a) Prepare the material.
b) Punch the metallic lithium.
c) Introduce it into the coin cell and add the separator.
d) Prepare the fresh electrolyte.
e) Spread the electrolyte over the separator.
f) Add to the coin cell the harvested sample from the electrode and seal it.

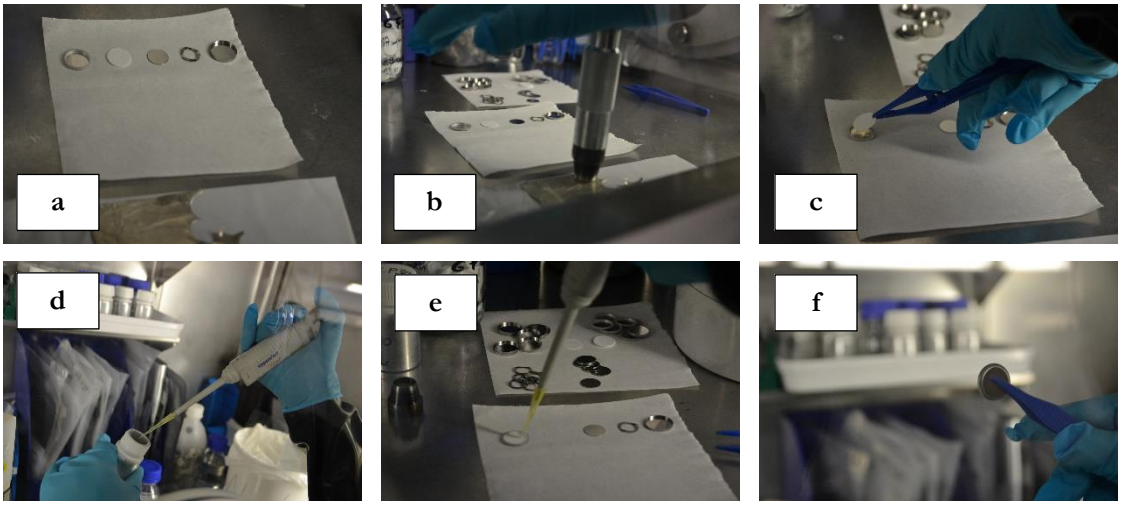

Fig. 5.4. Main steps in the process of building half-cells in a coin cell format where metallic lithium, fresh electrolyte and a new separator were added.

5.2.4.1.Capacity of the half-cells

The capacity of the half-cells was directly related to the amount of active material we introduced in the coin cells. The section of the half-cell electrode (A_{HC}) was the same for NMC and VIC cells and was calculated from the square root of the radius of the samples (r) as in equation (5.1). The harvested samples from the electrodes for building the half-cells were 16 mm diameter.

$$A_{HC} = \pi \cdot r^2 \tag{5.1}$$

Regarding the capacity of half-cells (Q_{HC}), it was calculated from the relation between the area of the full-cell electrode (A_{FC}) and the area of the electrode at the half-cells configuration, and the capacity of the full cell related to active material (Q_{FC}):

$$Q_{HC} = \frac{A_{HC}}{A_{FC}} \cdot Q_{FC} \tag{5.2}$$

The areas and capacities of the electrodes at full-cell and half-cell configurations are detailed in Table 5.1.

Table 5.1. Full-cell and half-cell areas of the electrodes and the related capacities.

Evaluated cell	Parameter	Positive electrode	Negative electrode
LGC2074 (NMC)	Full-cell electrode area A_{FC}	681.15 cm²	698.82 cm²
	Full-cell capacity Q_{FC}	2.8 Ah	
	Half-cell electrode area A_{HC}	2.01062 cm²	
	Half-cell capacity Q_{HC}	8.27 mAh	8.06 mAh
VIC01 (LFP)	Full-cell electrode area A_{FC}	232.4 cm²	257.6 cm²
	Full-cell capacity Q_{FC}	0.4 Ah	
	Half-cell electrode area A_{HC}	2.01062 cm²	
	Half-cell capacity Q_{HC}	3.46 mAh	3.12 mAh

5.2.5. Capacity measurement of half-cells

First, coin cells were left to 12 hours resting period in order to let them stabilize. Then three cycles at C/2 were carried out in order to check if the cells were cycling correctly meaning the manufacturing process was correct. After that, the cell was charged at a lower rate of C/5 and subsequently the capacity was measured at C/25. Measurements were done with a battery tester provided by BasyTec. Capacity measurements were carried out at 23 ºC in a laboratory with controlled temperature.

Voltage limits were defined according to the evaluated cell and chemistry. However, the studied negative electrodes of two different cells were treated equally as they were both made of graphite (Table 5.2).

Table 5.2. Voltage limits for cycling the manufactured half-cells.

	Voltage cut-off	Maximum voltage
LGC2 cell (NMC) – Negative electrode	0.75 mV	2.5 V
LGC2 cell (NMC) – Positive electrode	3 V	4.4 V
VIC cell (LFP) – Negative electrode	0.75 mV	2.5 V
VIC cell (LFP) – Positive electrode	2 V	3.75 V

5.2.6. Impedance measurement of half-cells

Prior to measuring impedance, half-cells were fully charged in galvanostatic mode at a rate of C/10. Thus, partial discharges of approximately 20 % SoC were carried out at C/10. Before each impedance measurement, cells were left to rest for 2 hours.

Impedance measurements were done with a Zennium electrochemical workstation provided by Zahner. Measurements were carried out in potentiostatic mode with an amplitude of 5 mV. It is worth noting that in order to have comparable data; measurements were carried out in the same holder and inside a climatic chamber at 25 ºC.

5.2.7. Inductively Coupled Plasma Optical Emission Spectrometry analysis

Inductively Coupled Plasma Optical Emission Spectrometry (ICP-OES) is a technique that uses the emission spectra of a sample to identify and quantify the composition of metal samples. The ICP-OES equipment is composed of an ionization source (ICP) together with an optical emission spectrometer (OES). When the sample solution is introduced into the device, it is nebulized into the core of an inductively-coupled argon plasma at temperatures around 9000 K. Then, the solution is vaporized and the chemical species are atomized, ionized and thermally excited. A graphical representation of the different steps was plotted in Fig. 5.5. By measuring the intensity of radiation emitted at the element-specific, characteristic wavelength from thermally excited atoms or ions, the

chemical components are detected and quantified. Thus, elemental concentrations are obtained by comparing intensity measurements with calibration standards.

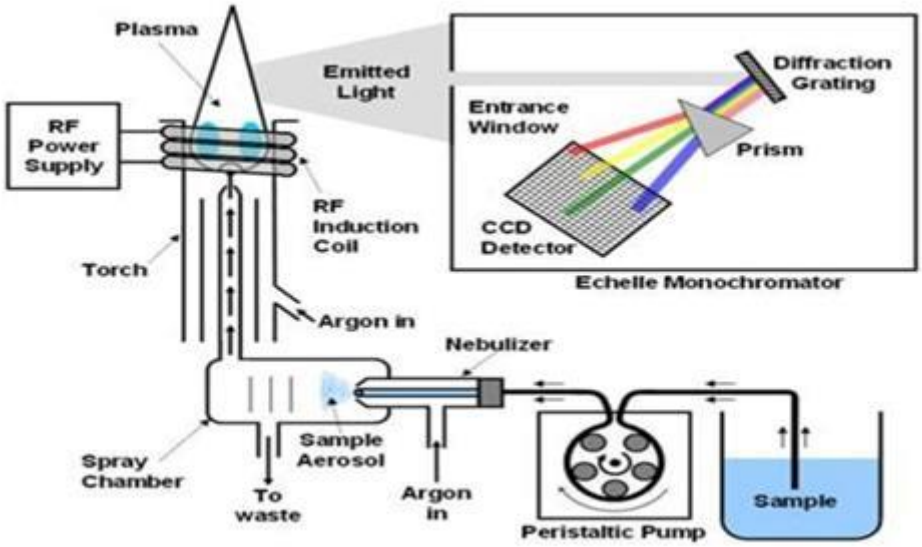

Fig. 5.5. Diagram of the different steps followed during the ICP-OES analysis [179]**.**

Twenty-millimeter diameter samples were harvested from the electrodes during the cell-opening procedure. Therefore, as the samples were solid, they had to be dissolved in proper solvents before the ICP-OES analysis. The ICP-OES measurements were carried out by an expert in the field. The results given by the expert contained the composition of metals expressed in milligrams per liter in a 100 ml solution. Then, during the post-analysis we did, those quantities were converted into moles.

Dissolution and migration of metals and the loss of lithium were estimated from the ICP analysis. During the aging process at positive electrode, metals could dissolve what would cause the loss of active material and a capacity fade as a result. Moreover, these metals can migrate to the negative electrode during the cycling process and would remain at the SEI layer (Fig. 5.6). Consequently, the electrical conductivity of the surface layer would be enhanced allowing the pass of the electrons with the subsequent electrolyte reduction leading to further layer growth [36]. The evaluation of metals migration was done by comparing their concentrations at positive and negative electrodes in a fresh and in an aged cell. Metals that were dissolved and were not added to the surface layer at the negative electrode but remained in the electrolyte could not been quantified because of the variabilities among different cells and the accuracy of the measurement. Moreover, with the ICP analysis, dissolved metals that could be re-deposited at the positive electrode cannot be distinguished from the ones at the electrode itself.

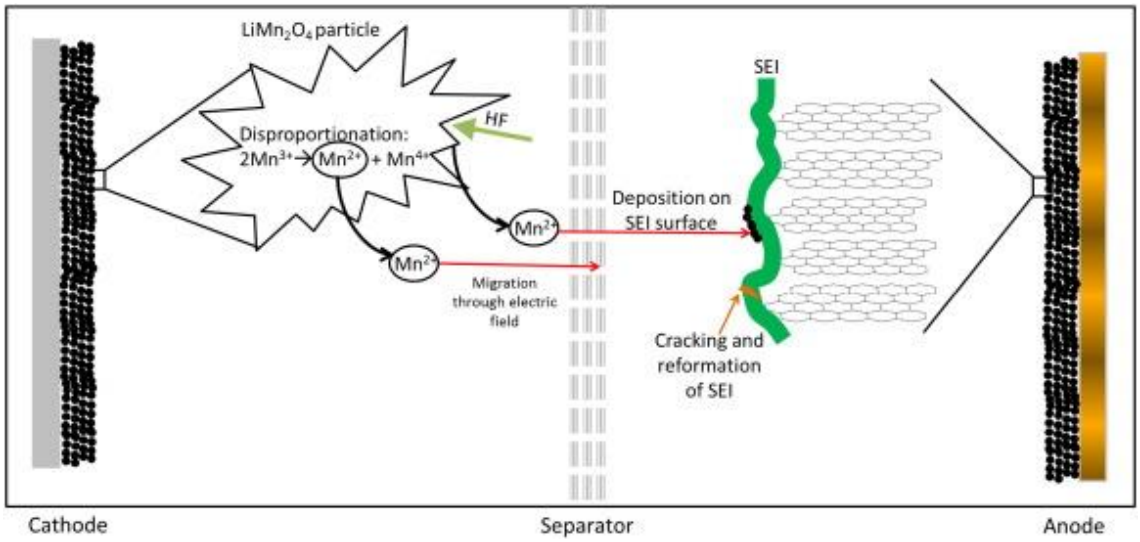

Fig. 5.6. Example of metal dissolution and migration of Manganese and further deposition on SEI surface [180]**.**

5.2.8. Porosimetry

Porosimetry is a technique used to determine the pore volume (porosity) and the pore and particle sizes of a sample. Measurements were carried out on samples extracted from the electrodes with a mercury intrusion porosimeter. The Pascal porosimeter (Thermo Scientific) was used in this study. Only one cell was measured because the equipment was out of service after that. Therefore, no conclusive results were found because fresh and aged cells could not be compared.

5.2.9. X-Ray Diffraction (XRD) analysis

XRD is a technique used to characterize grain sizes and atomic structure. Diffraction occurs when light is scattered by a periodic array with long-range order, producing constructive interference at specific angles. The diffraction pattern is a product of the unique crystal structure of a material and it describes the atomic lattice of the material. Therefore, when the atoms lattice is modified, a different diffraction pattern is produced (i.e. quartz vs cristobalite). Furthermore, the strength with which an atom scatters light is proportional to the number of electrons around the atom and the position of the diffraction peaks are determined by the distance between parallel planes of atoms.

The employed diffractometer was the Empyrean provided by PANalytical.

5.3. Results

5.3.1. Weighting

All single elements contained in the cells were properly weighted and listed during the cell-opening procedure. In particular, the following parameters were reported in Table 5.3 and Table 5.4:

- Full cell before the cell opening
- Negative electrode plus copper current collector (NE + CC)
- Positive electrode plus aluminum current collector (PE + CC)
- Electrolyte

It is worth noting that the electrolyte could not be directly weighted because it was composed of solvents that evaporated when the cell was opened. Therefore, its total weight was estimated from the weight difference of the full cell and the components once they were dry. Therefore, the electrodes and the separators were left to dry inside the glove box for near one hour before being weighted.

Three NMC cells and two VIC cells (LFP) were opened and in both chemistries, no significant weighting differences were appreciated between fresh and aged cells (Table 5.3 and Table 5.4).

Table 5.3. Weighting of the different parts of fresh and aged NMC cells.

	LGC2077 (fresh cell)		**LGC2079 (fresh cell)**		**LGC2074 (aged cell)**	
	g	%	g	%	g	%
Full cell	45,4	**100**	45,21	**100**	46,06	**100**
NE + CC	14,14	**31,15**	13,75	**30,41**	14,88	**32,31**
PE + CC	19,71	**43,41**	18,69	**41,34**	19,53	**42,40**
NE + PE *	33,85	**74,56**	32,44	**71,75**	34,41	**74,71**
Electrolyte	2,12	**4,67**	3,16	**6,99**	2,49	**5,41**

* This weight contained both current collectors

Table 5.4. Weighting of the different parts of fresh and aged VIC cells (LFP).

	VIC05 (fresh cell)		**VIC01 (aged cell)**	
	g	%	g	%
Full cell	15,12	**100**	14,86	**100**
NE + CC	3,21	**21,23**	3,18	**21,42**
PE + CC	5,09	**33,66**	4,89	**32,93**
NE + PE *	8,3	**54,89**	8,08	**54,35**
Electrolyte	0,85	**5,62**	1,31	**8,82**

* This weight contained both current collectors

5.3.2. Visual inspection

5.3.2.1. LGC2 cells (NMC)

At a first sight, the negative electrode of the aged cell (LGC2074) had a completely white/grey colored surface (top-right in Fig. 5.9), whereas the fresh one (LGC2079) showed a black surface (top-left in Fig. 5.7). The white/grey colored surface of the aged cell indicated the formation of a surface layer. In addition to the grey layer, some holes were observed: in some of them, the surface layer was missing and in the others both the surface layer and the active material were missing. It happened because in those regions, the active material and/or the surface layer were completely stuck to the

separator. The holes and the surface layer were clearly observed at the laser microscope (bottom-right in Fig. 5.7). The copper current collector was visible where there was no active material neither surface layer, but the particles of active material could be identified where the surface layer was the only one missing. Moreover, white traces could be appreciated on the top of the surface layer. Regarding to the color of the active material at the laser microscope, the particles of the fresh cell had a blue tone and black for the aged cell (bottom in Fig. 5.7).

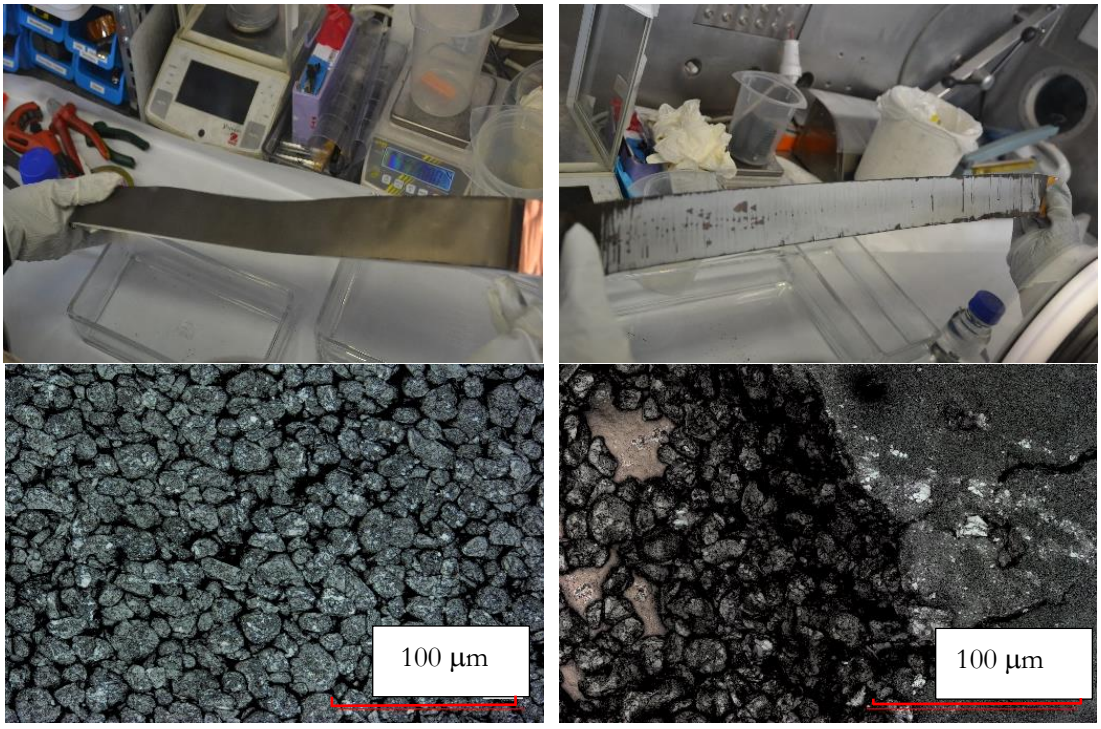

Fig. 5.7. Visual inspection of the negative electrode (top) and image taken with the laser microscope (bottom) of a fresh cell (LGC2079), on the left and an aged cell (LGC2074), on the right.

During the visual inspection, positive electrodes did not show changes due to aging as clear as the negative electrodes did (Fig. 5.8). However, the intensity of laser reflection and the shape of the particles were modified, from what it could be extracted but not quantified that something had changed in the aging process.

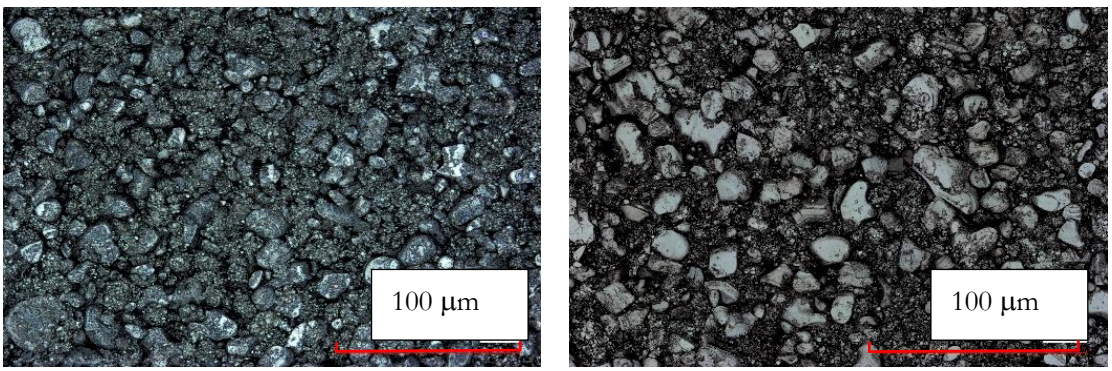

Fig. 5.8. Laser microscope image of the positive electrode of LGC2 cells (NMC) of a fresh cell (left) and an aged one (right).

5.3.2.2. VIC cells (LFP)

During the visual inspection of VIC cells, the negative electrode of the aged cell showed up more pressure lines (top in Fig. 5.9) in comparison to the fresh one. This means that the aged cell suffered more mechanical stress when accommodating lithium at the graphite side. Furthermore, bubbles were found in the aged electrode. Therefore, at some points, the active material was not attached to the current collector anymore. Furthermore, some parts of the active material were completely stuck to the separator. No evidence of surface layer was found at a first sight.

The images taken by the laser microscope to the negative electrodes were not completely comparable because the scales did not match. However, clear differences in laser intensity reflection were found (bottom in Fig. 5.9). The same situation occurred at the positive electrode where not much useful information could be extracted at a first sight (Fig. 5.10).

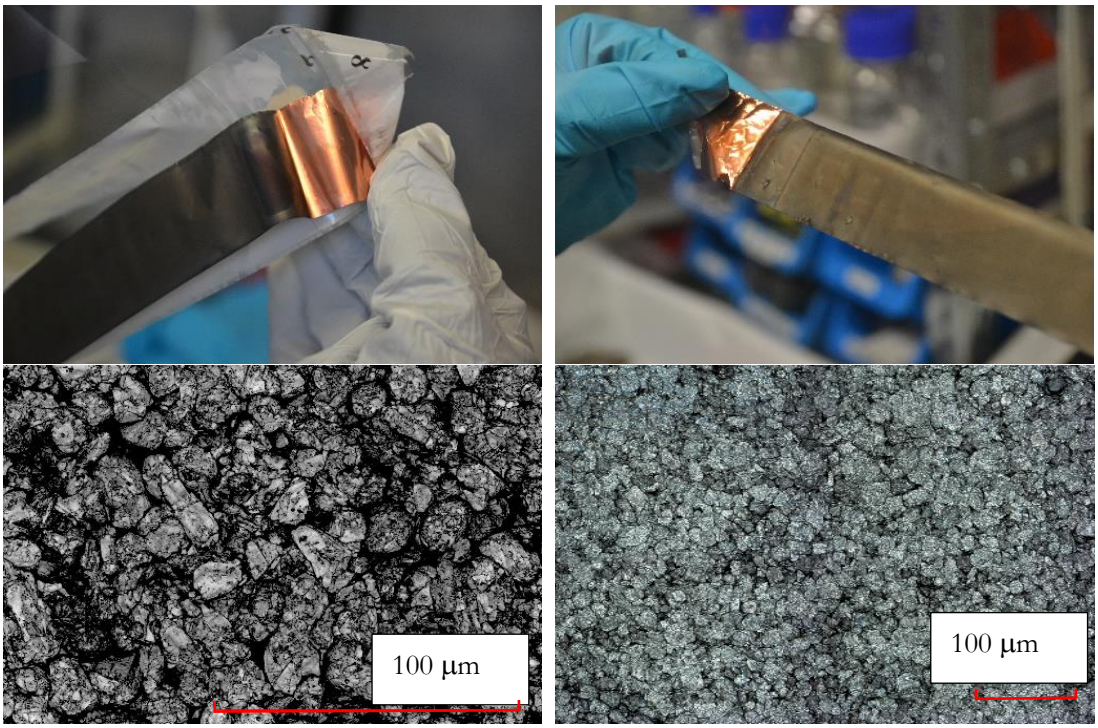

Fig. 5.9. Visual inspection of the negative electrode (top) and image taken with the laser microscope (bottom) of a fresh cell (VIC05), on the left and an aged cell (VIC01), on the right.

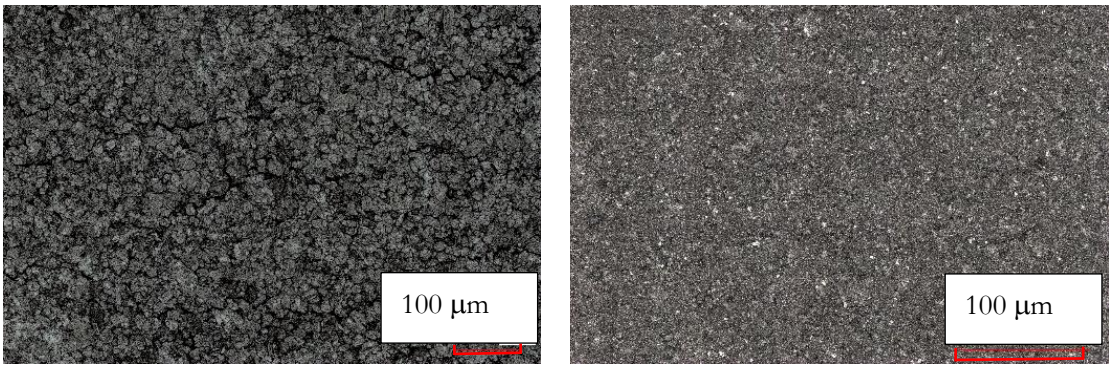

Fig. 5.10. Laser microscope image of the positive electrode of VIC cells (LFP) of a fresh cell (left) and an aged one (right).

5.3.3. Capacity of half-cells

5.3.3.1.LGC2 cells (NMC)

Half-cells were charged and discharged at a rate of C/25. The measured negative electrode capacities of fresh half-cells were around 9 mAh when evaluated between the voltage limits defined in Table 5.2 and the expected capacity was around 8 mAh as defined in Table 5.1. The difference between the calculated and measured capacities was mainly attributed to two factors. On the one hand, it was attributed to the full-cell capacity employed for the calculations was the nominal capacity instead of the measured capacity and, on the other hand, the voltage limits employed for measuring the half-cells were extended with respect to the full-cells in order to account for the possible shiftings between the electrodes during the aging process. Thus, both would allow the insertion of more lithium than that at the full-cell, and thus capacity would increase. Voltage profiles versus delivered capacities were plotted in Fig. 5.11 and Fig. 5.13. These figures represent the delithiation of the negative electrode and the lithiation of the positive one. In fact, this is what occurs to the electrodes when the full cell is subjected to a discharge process. It has to be noted that at the half-cell configuration, the capacity of the half-cells is not affected by loss of lithium because extra metallic lithium was added as a counter electrode to the half-cell during the manufacturing process.

In particular, the cell voltage and corresponding capacities of fresh and aged graphite/Li half-cells were represented in Fig. 5.11. Fresh cells showed similar capacities independently of the location of the harvested samples. Contrarily, in the case of the aged cells the voltage increased faster at the inner and outer parts, thus reducing their capacities. Specifically, the highest loss of capacity at the NE was found at the inner part of the jellyroll, being an 8.80 % (Table 5.5). Central part was apparently not affected by loss of capacity while the outer part suffered a loss of 2.54 %.

Incremental capacity analysis of the NE samples was performed to identify and track the evolution of the various voltage plateaus with aging. Each plateau in the voltage curves correspond to a peak in the incremental capacity analysis. In particular, five plateaus were identified at the graphite-based electrodes corresponding to the different stages of lithiation of graphite (left side of

Fig. 5.12). They were labeled as I, II, III, IV and V. The peak at lower voltages, represented by I, was associated to the phase transition between LiC_6 and LiC_{12} (or $Li_{0.5}C_6$), where both phases coexist [170,181]. During further delithiation of graphite, other stages took place until all the lithium was extracted at the end of discharge. It is generally accepted in literature that the process of lithium extraction from graphite undertakes five different stages, ranging from LiC_6 to pure graphite [18]. The area of the peaks at the ICA representation corresponds to the amount of charge extracted at each of the plateaus, thus the capacity associated to each of them. At a first sight, only the plateau at higher voltages (around 0.23 V) was slightly decreased in intensity from BoL to EoL. Nevertheless, the intensity of peak I was increased from BoL to EoL and intensities of peaks II, III and IV remained constant. However, the width of peaks I and II was reduced during the aging process. Therefore, it was more convenient to quantify the capacity associated to each of them by integrating the peaks (right side of Fig. 5.12). As it was expected, the capacity of peak V was decreased in the aging process. Moreover, the capacities associated to peaks I and II were also reduced. Contrarily, peaks III and IV were unaffected by aging. In addition, the decrease in width measured in peaks I and II was related to a faster increase in voltage after those plateaus during the discharge process.

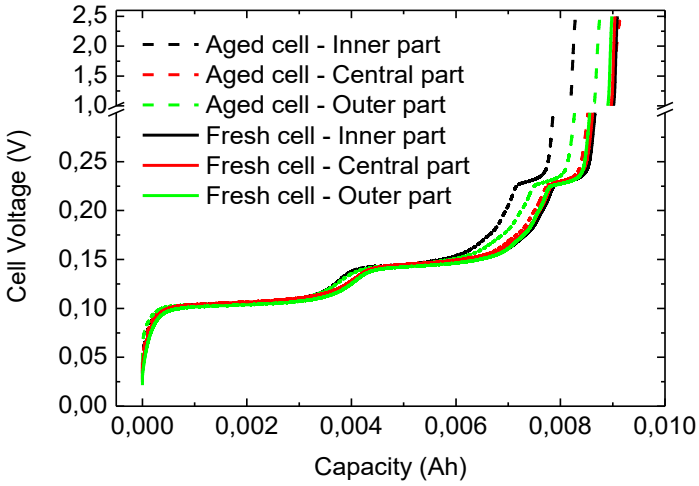

Fig. 5.11. Cell voltage versus delivered capacity of graphite/Li half-cells from samples taken at negative electrodes of fresh and aged NMC cells.

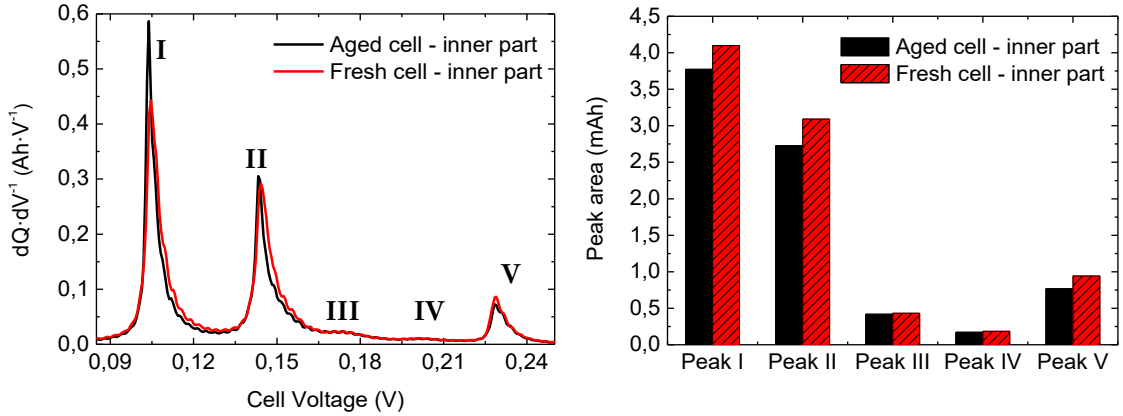

Fig. 5.12. (left) Incremental capacity of fresh and aged graphite/Li half-cells. Peaks (labeled from I to V) are associated to phase transitions of the electrodes. (right) Capacity associated to each one of the peaks obtained from the integration of peaks.

Table 5.5. Capacity of graphite/li half-cells made from negative electrode samples harvested from NMC cells. Absolute and relative decreases are detailed. Capacities of the inner, central and outer parts of the jellyroll are shown separately.

Negative electrode	LGC2079 Fresh Cell	LGC2074 Aged cell	Absolute decrease (mAh)	Relative decrease (%)
Inner part	9.0860	8.2868	0.7992	8.80
Central part	9.0414	9.1438	-	-
Outer part	8.9824	8.7539	0.2285	2.54

In the potential – capacity curves of the NMC/Li half-cells (Fig. 5.13), a decrease in capacity could be appreciated at the inner, central and outer parts of the electrodes during the aging process. The highest decrease in capacity was found at the inner part of the jellyroll (5.88 %), followed by the central part (3.84 %) and the lowest one was found at the outer part (1.24 %). All the results were summarized in Table 5.6.

From ICA, four main peaks corresponding to the voltage plateaus could be identified for the NMC positive electrode of the fresh cell (Fig. 5.14). They were labeled as I, II, III and IV from lowest to highest voltage. The area and the intensity of the main peak (II), which corresponds to the plateau at 3.9 V, drastically decreased during the aging process being the maximum contributor to capacity fade. Moreover, the peak was shifted to lower voltages and a new peak appeared between I and II. In general, the IC curves shifted towards lower voltage values as the cells aged, what could be associated to an increase of the internal resistance.

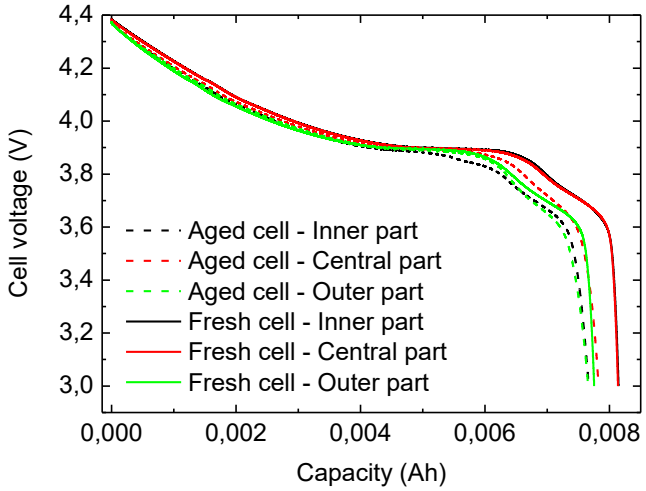

Fig. 5.13. Cell voltage versus delivered capacity of half-cells from samples taken at positive electrodes of fresh and aged NMC cells.

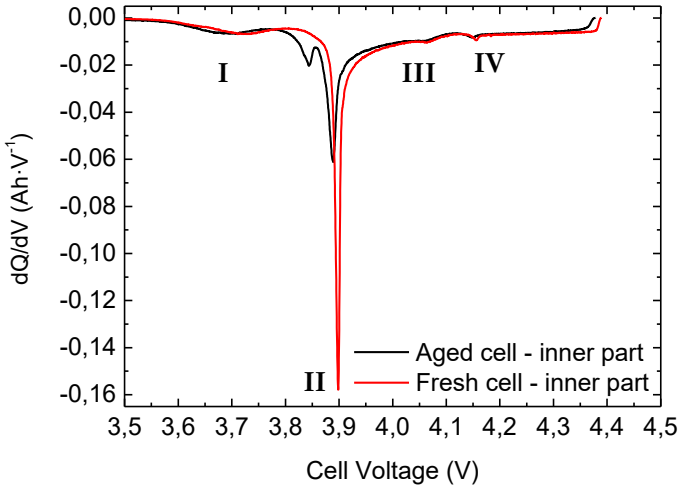

Fig. 5.14. Incremental capacity of NMC/Li half-cells from samples taken from fresh and aged positive electrodes.

Table 5.6. Capacity of half-cells made from positive electrode samples harvested from NMC cells. Absolute and relative decreases are represented. Capacities of the inner, central and outer parts of the jellyroll are shown separately.

Positive electrode	LGC2079 Fresh Cell	LGC2074 Aged cell	Absolute decrease (mAh)	Relative decrease (%)
Inner part	8.1447	7.6661	0.4786	5.88
Central part	8.1355	7.8235	0.312	3.84
Outer part	7.7527	7.6564	0.0963	1.24

5.3.4. Impedance of half-cells

5.3.4.1.LGC2 cells (NMC)

As described in section 5.2.4, the design of half-cells consisted in the combination of the electrode under study with a counter electrode composed of metallic lithium. This counter electrode contributes to the total impedance what must be taken into account when interpreting the results.

In this study, we performed impedance analyses of the negative (NE) and positive electrodes (PE). We found that impedance of the negative electrode was larger than positive electrode. To illustrate those differences, both contributions from the inner parts of a fresh cell were depicted in Fig. 5.15. As it can be seen, positive electrode impedance was found to be approximately two times smaller than that of the negative electrode.

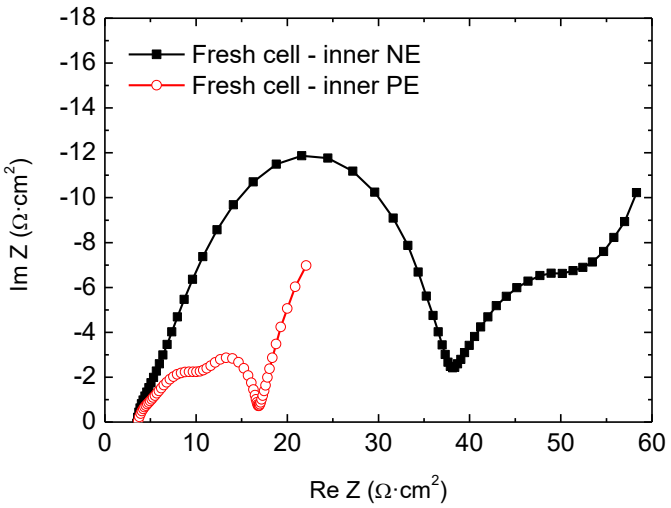

Fig. 5.15. Impedance contribution of Negative (NE) and Positive (PE) electrodes to the total impedance of the full cell at fully charged state. As an example, inner parts of a fresh cell were represented.

Both PE and NE electrodes showed a general increase of impedance with aging (Fig. 5.16 and Fig. 5.20). In order to quantify and compare the data, total impedance was approximated as the intersection of the lowest frequency arc with the real-axis. At the positive electrode, inner and outer parts of the jellyroll showed the highest increase of impedance (Fig. 5.16). Inner and outer parts increased around 20 Ω·cm² while central part increased near 12 Ω·cm² (Table 5.7). The highest relative increase was found at the inner part (127.89 %), followed by the outer part (107.82 %) and the lowest increase was that at the central part of the jellyroll (58.05 %). In particular, the impedance of the PE showed three identifiable effects: three semi-arcs at different frequencies. As mentioned above, the effect at medium frequencies corresponds to the charge transfer at the metallic lithium electrode and the other effects are usually related to charge transfer processes taking place at the electrode of interest. However, further analysis is required in order to assign each of those effects to their corresponding electrochemical process. Furthermore, in order to evaluate if any of the effects

had slowed down due to aging, the characteristic frequencies of the different effects were estimated. The highest frequency effect was found around 20 kHz and the medium frequency around 500 Hz for both the fresh and the aged cells. However, the lowest frequency effect was found around 24 Hz for the fresh cell and at 7.5 Hz for the aged one (Fig. 5.16). Thus, this effect was found to be three times slower for the aged cell. Although the characteristic frequency of the effect at higher frequencies was also estimated, it would require a more detailed analysis because it was overlapped with other effects and frequency could not be identified accurately with such a simple analysis. Unfortunately, a more detailed analysis was not carried out due to the lack of time prior to the end of this study.

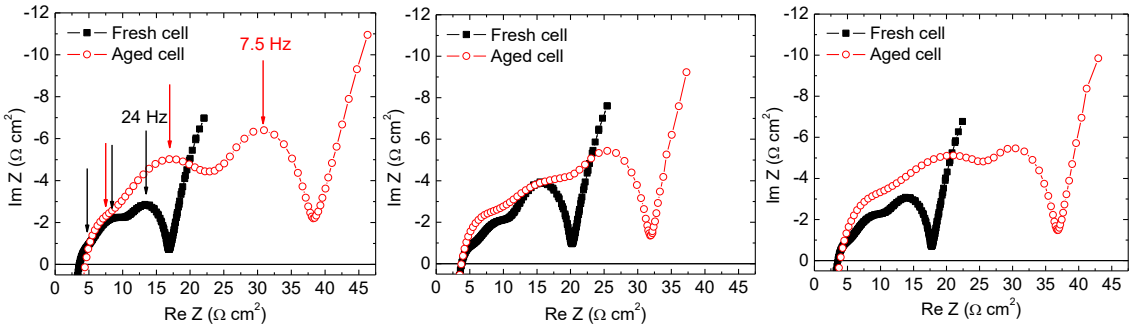

Fig. 5.16. Impedance of half-cells at SoC = 100 % build with samples of the positive electrode of LGC2 (NMC) cells. From left to right, internal part of the jelly roll, central part and external part. Black filled squares represent the fresh cell and red empty circles the aged one.

Table 5.7. Total resistance of fresh and aged NMC/Li half-cells at SoC = 100 % evaluated at 25 ºC.

Positive electrode	Inner part	Central part	Outer part
Fresh cell [Ω·cm²]	16.89	20.24	17.77
Aged cell [Ω·cm²]	38.49	31.99	36.93
Absolute increase [Ω·cm²]	21.60	11.75	19.16
Relative increase [%]	**127.89**	**58.05**	**107.82**

The evolution of impedance with SoC in NMC/Li fresh and aged half-cells was also investigated and results were represented in Fig. 5.17. The effect at higher frequencies remained constant during all lithium insertion but increased when the cell was fully discharged. The semi-arc at medium frequency increased as SoC was decreased and the lowest frequency effect stayed almost constant until 3.91 V from where it also started to increase. Similar behavior was found between fresh and aged positive electrodes.

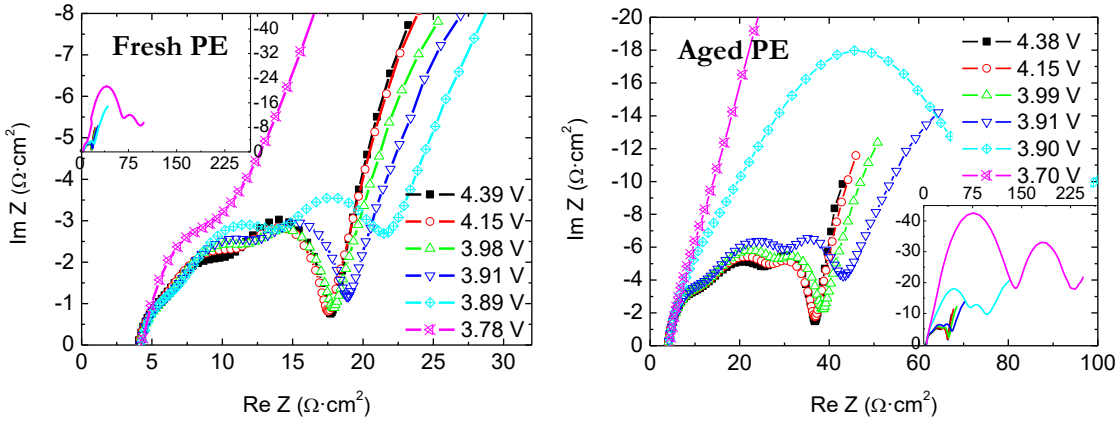

Fig. 5.17. Impedance variation during lithium insertion to the positive electrode. The maximum voltage represents when the full cell is fully charged and every decrease in voltage represents a 20 % of charge extracted until the cell was fully discharged. To the left, data coming from the fresh cell and, to the right, from the aged cell. Notice the different scales.

At the NE, two semicircles were basically distinguishable; one at high frequency with very small radius compared to the other one, and the second one with the highest impedance contribution at medium frequencies (Fig. 5.18). Moreover, there was a third effect at lower frequencies, which was only identifiable at the highest and lowest full-cell SoCs (i.e. the lowest and highest voltages of the NE). At the highest voltage, diffusional branch was evidenced (Fig. 5.19). Even though the impedance values related to the diffusional branch were higher for the fresh cell, the capacitive effect at low frequencies was enhanced as the cell was aged. It can be appreciated when the imaginary part of the impedance increases much faster than what the real does. In addition, regarding to the high frequency effect represented in Fig. 5.18, possible variations could not be identified as it was partially overlapped with the effect at medium frequencies, although drastic differences were not appreciated. Finally, the effect at medium frequencies showed different behaviors at the fresh and the aged cells. For the fresh cell, it started with high polarization but immediately decreased for lower SoCs. Then, it remained almost constant until the end of discharge. Instead, the same effect but taking place at the aged cell did not show the sudden decrease when decreasing the SoC but it was done gradually.

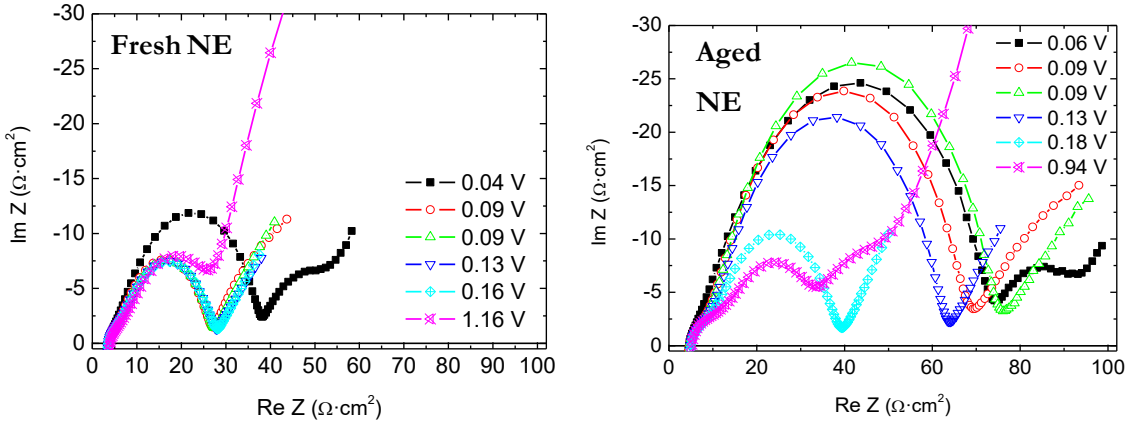

Fig. 5.18. Impedance variation during lithium extraction from the negative electrode. The minimum voltage represents when the full cell is fully charged and every increase of voltage represents a 20 % of charge extracted until the cell was fully discharged. To the left, data coming from the fresh cell and, to the right, from the aged cell. Notice the different scales.

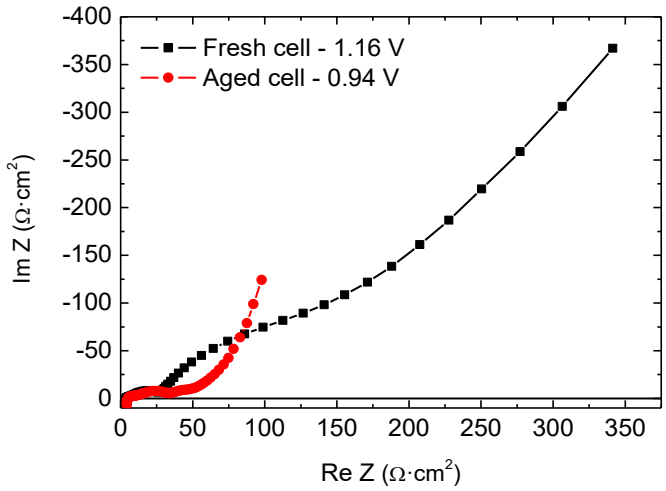

Fig. 5.19. Impedance comparison of a fresh and aged negative electrodes measured in a graphite/Li coin cell configuration in a fully delithiated state.

With regard to the spatial distribution of impedance, the highest impedance contribution of the aged cell was found at the central part of the jellyroll (Fig. 5.20). However, the measured impedance at the central part was also higher for the fresh cell. Thus, relative increases were more appropriate in order to reveal which part was more affected by aging (Table 5.8). The highest increase was found at the inner part with an absolute value of 36.30 Ω·cm², representing an increase of 94.57 %. Nevertheless, impedance at central and outer parts increased similarly, being 27.72 Ω·cm² (41.71 %) and 24.08 Ω·cm² (46.74 %), respectively. The sluggishness due to aging of the different effects could not be quantified in that case due to the overlapping in frequency of the electrochemical processes.

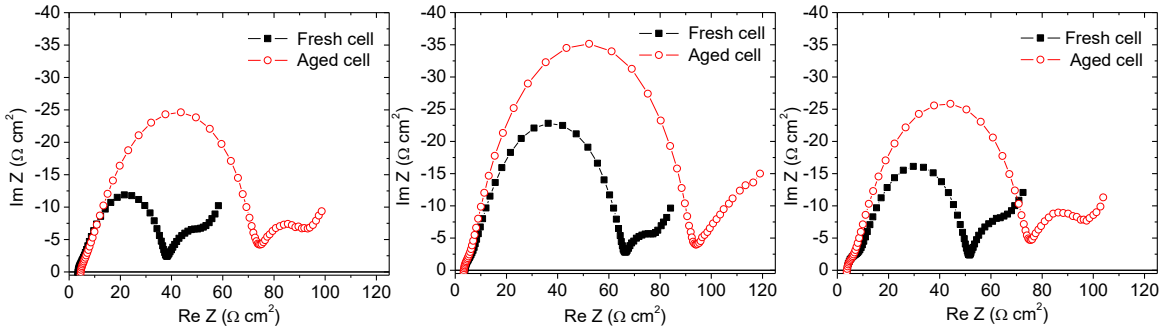

Fig. 5.20. Impedance of half-cells at SoC = 100 % build with samples of the negative electrode of LGC2 (NMC) cells. From left to right, more internal part of the jelly roll, central part and more external part. Black filled squares represent the fresh cell and red empty circles the aged one.

Table 5.8. Total resistance of fresh and aged graphite/Li half-cells at SoC = 100 % evaluated at 25 ºC.

Negative electrode	Inner part	Central part	Outer part
Fresh cell [Ω·cm²]	38.38	66.45	51.52
Aged cell [Ω·cm²]	74.68	94.17	75.60
Absolute increase [Ω·cm²]	36.30	27.72	24.08
Relative increase [%]	**94.57**	**41.71**	**46.74**

5.3.5. ICP analysis

5.3.5.1. LGC2 cells (NMC)

5.3.5.1.1. Metals composition

From the ICP analysis, the stoichiometry of the cells can be determined. Three LGC2 cells (NMC) were evaluated and we found that their compostion of cobalt was very high (Table 5.9). This is not common for these type of cells because cobalt is very expensive so one of the advantages of mixing NMC is that cobalt can be reduced. Thus, we assumed that the positive electrode was configured as LCO-NMC instead of simple NMC, what would justify the extra Cobalt. Furthermore, metal dissolution and migration between the electrodes can also be quantified. As the cells were fully discharged prior to the ICP analysis, all the lithium was expected to be found at the positive electrode. Therefore, if lithium were found at the negative electrode, it would mean it was trapped there; even inside the electrode itself or at the surface forming the SEI layer. Finally, the metals expected to be present at the positive electrode were lithium, nickel, manganese, cobalt, and aluminum (from the current collector). Oxygen also forms the electrode but it cannot be measured with the ICP-OES technique. Therefore, it was estimated from the results, assuming the number of O_2 moles was the same as the NMC moles. In Table 5.10, the number of moles of the measured metals and estimated elements were detailed. A decrease in moles of Li can be noticed, whereas the other elements showed slighter differences. The corresponding masses of the elements and their percentile contribution to the total mass were summarized in Table 5.11.

Table 5.9. Stoichiometry of the evaluated LGC2 cells (NMC) by the ICP-OES technique. LGC2077 and LGC2079 were fresh cells and LGC2074 was an aged cell.

Cell	Li	Ni	Mn	Co
LGC2077	1	0.14	0.0697	0.795
LGC2079	1	0.135	0.0667	0.785
LGC2074	1	0.132	0.0653	0.806

Table 5.10. Relation of moles of different elements comprising the positive electrodes of the evaluated LGC2 cells (NMC) by the ICP-OES technique. LGC2077 and LGC2079 were fresh cells and LGC2074 was an aged cell. The desired elements were highlighted in green and the undesired ones in red.

Positive electrode	Li	Ni	Mn	Co	O_2*	Al	Cu	P
LGC2077 (µmol)	1403	205	102	1163	1470	444	0	3
LGC2079 (µmol)	1465	215	106	1247	1568	460	0	6
LGC2074 (µmol)	1300	200	99	1220	1521	438	0	4

* not measured but estimated (mols of O_2 = mols of NMC)

Table 5.11. Mass of the different elements comprising the positive electrodes of the evaluated LGC2 cells (NMC) by the ICP-OES technique. Mass is represented in units of mg and as a percentage of the total mass of the sample. LGC2077 and LGC2079 were fresh cells and LGC2074 was an aged cell. The desired elements were highlighted in green and the undesired ones in red.

Positive electrode	Li	Ni	Mn	Co	O_2*	Al	Cu	P	Total mass
LGC2077 (mg)	9.744	12.043	5.626	68.553	47.066	11.993	0.016	0.111	155.15
LGC2077 (%)	**6.28**	**7.762**	**3.626**	**44.185**	**30.336**	**7.73**	**0.01**	**0.072**	**100**
LGC2079 (mg)	10.17	12.628	5.858	73.498	50.205	12.438	0.012	0.209	165.016
LGC2079 (%)	**6.163**	**7.652**	**3.55**	**44.54**	**30.424**	**7.537**	**0.007**	**0.126**	**100**
LGC2074 (mg)	9.028	11.773	5.491	71.945	48.682	11.830	0.013	0.133	158.894
LGC2074 (%)	**5.682**	**7.409**	**3.455**	**45.279**	**30.638**	**7.445**	**0.008**	**0.084**	**100**

* not measured but estimated (mols of O_2 = mols of NMC)

At the NE, the expected elements were carbon and copper at the current collector. Carbon had to be estimated because it is not a metal and consequently it could not be measured by the ICP technique. From the difference in the mass of the measured metals and the total mass of the sample before the measurement, the present amount of C_6 was estimated. The relation between the elements was shown in Table 5.12 (in moles) and Table 5.13 (in grams and as a percentage of the total mass). In Table 5.12, we observed an increase of C_6 and Cu in number of moles for the aged cell (LGC2074). However, when we compare it in Table 5.13, LGC2079 (fresh cell) and LGC2074 (aged cell) cells had the similar contributions to the total mass. In contrast, Li at the negative electrode increased for the aged cell (LGC2074). It is important to remember that the cells were fully discharged prior of taking the samples what means all the available lithium was ideally stored at the positive electrode. Furthermore, as it can be appreciated in Table 5.12 some moles of cobalt and aluminum were

dissolved and migrated to the negative electrode during cycling. Regarding to Ni and Mn, amounts below 1 µmol were also migrated to the negative electrode in the case of the aged cell (Table 5.13).

Table 5.12. Relation of moles of different elements comprising the negative electrodes of the evaluated LGC2 cells (NMC) by the ICP-OES technique. LGC2077 and LGC2079 were fresh cells and LGC2074 was an aged cell. The desired elements are highlighted in green and the undesired ones in red.

Negative electrode	C_6*	Cu	Li	Ni	Mn	Co	Al	P
LGC2077 (µmol)	1094	353	60	0	0	0	0	18
LGC2079 (µmol)	1060	383	124	0	0	0	1	19
LGC2074 (µmol)	1230	448	215	0	0	1	2	17

* not measured but estimated from the difference in masses

Table 5.13. Mass of the different elements comprising the negative electrodes of the evaluated LGC2 cells (NMC) by the ICP-OES technique. Mass is represented in units of mg and as a percentage of the total mass of the sample. LGC2077 and LGC2079 were fresh cells and LGC2074 was an aged cell. The desired elements are highlighted in green and the undesired ones in red.

Negative electrode	C_6*	Cu	Li	Ni	Mn	Co	Al	P	Total mass
LGC2077 (mg)	78.89	22.493	0.42	0	0	0.006	0.006	0.583	102.4
LGC2077 (%)	**77.041**	**21.966**	**0.41**	**0**	**0**	**0.006**	**0.006**	**0.569**	**100**
LGC2079 (mg)	75.817	24.375	0.866	0.003	0.001	0.009	0.015	0.596	101.684
LGC2079 (%)	**74.564**	**23.971**	**0.852**	**0.003**	**0.001**	**0.009**	**0.015**	**0.586**	**100**
LGC2074 (mg)	88.644	28.443	1.499	0.015	0.006	0.043	0.042	0.514	119.209
LGC2074 (%)	**74.363**	**23.859**	**1.257**	**0.012**	**0.005**	**0.036**	**0.035**	**0.431**	**100**

* not measured but estimated from the difference in masses

5.3.5.1.2. Metals dissolution and migration

Metals dissolution at the positive electrode and migration to the negative one were quantified through the measurement of their concentrations at both electrodes (Table 5.14). Concentrations are given in milligrams per liter. Total amount of Ni, Mn and Co were obtained by adding the concentrations at positive and negative electrodes. Therefore, the percentage of those metals at the undesired electrode with respect to the other one, were calculated. Fresh cells showed values of Ni up to 0.002 %, while the aged one contained a 0.13 %. Although Mn and Co were found in smaller

percentage at the negative electrode, the increase in concentration between the fresh cells and the aged cell was of the same magnitude.

Table 5.14. Metals dissolution and migration from positive electrode to negative electrode of three LGC2 cells (NMC) at different aging states represented in mg/L and as a percentage.

		LGC2077 Fresh cell	LGC2079 Fresh cell	LGC2074 Aged cell
		Concentrations in mg		
Ni	PE	12,043	12,628	11,773
	NE	0	0,003	0,015
	PE + NE	**12,043**	**12,631**	**11,788**
	% at NE	**0,00%**	**0,02%**	**0,13%**
Mn	PE	5,626	5,853	5,491
	NE	0	0,001	0,005
	PE + NE	**5,626**	**5,854**	**5,496**
	% at NE	**0,00%**	**0,02%**	**0,09%**
Co	PE	68,553	73,498	71,945
	NE	0,006	0,009	0,043
	PE + NE	**68,559**	**73,507**	**71,988**
	% at NE	**0,01%**	**0,01%**	**0,06%**

Concentrations of aluminum and copper at both positive and negative electrodes were summarized in Table 5.15. Cu and Al are the materials that conform the negative and positive current collectors, respectively. Thus, copper was expected to be found at negative electrode but it was also found in the positive electrode in a percentage between the 0.05 % - 0.07 %. However, no changes in Cu concentration at PE were found during the cell aging. It has to be noted that the fresh cells were already subjected to 5-10 formation cycles. Concerning aluminum, it went from 0.05 % - 0.12 % in a fresh cell and to 0.29 % in the aged cell, thus revealing some Al migration during cycling.

Table 5.15. Metals dissolution of current collectors and migration to the opposite electrode of three LGC2 cells (NMC) at different aging states.

		LGC2077 Fresh cell	LGC2079 Fresh cell	LGC2074 Aged cell
		Concentrations in mg		
Al	PE	11,993	12,438	11,83
	NE	0,006	0,015	0,035
	PE + NE	**11,999**	**12,453**	**11,865**
	% at NE	**0,05%**	**0,12%**	**0,29%**
Cu	NE	22,493	24,375	28,443
	PE	0,016	0,012	0,013
	PE + NE	**22,509**	**24,387**	**28,456**
	% at PE	**0,07%**	**0,05%**	**0,05%**

5.3.5.1.3. Loss of lithium Inventory (LLI)

The ICP-OES technique is very useful to evaluate the loss of lithium that the cells have suffered because metals present at each of the electrodes can be quantified. As the cells were fully discharged before the cell opening, loss of lithium was calculated as the number of moles of lithium present at the negative electrode. Samples were taken at different positions of the electrodes in order to evaluate the homogeneity of the process related to loss of lithium. For this purpose, two samples were taken at the inner part (top and bottom) and two at the outer part (top and bottom) of the jellyroll (Table 5.16, Table 5.17 and Table 5.18). Regarding to total lithium calculations, measured lithium (Li) and phosphorous (P) concentrations were added to obtain the total amounts of Li present in the cell. Phosphorous has to be considered as it comes from remaining traces of $LiPF_6$ from the electrolyte. Thus, associated Li to P has to be taken into account. In those tables, the number moles of NMC and lithium were confirmed to be in the expected proportion of 1:1.

Although LGC2077 and LGC2079 were referred as fresh cells, they underwent some formation cycles before the ICP measurements, in order to stabilize the SEI layer. Therefore, the resulting loss of lithium in Table 5.16 and Table 5.17 was associated to initial SEI formation. The employed lithium for that purpose ranged from approximately 5 % to 9 %. In contrast, LLI inventory of the aged cell was between 14.6 % and 15.6 % depending on the position of the sample (Table 5.18).

Table 5.16. Evaluation of the amount of Li at positive and negative electrodes of a fresh LGC2077 cell (NMC) fully discharged.

LGC2077	Inner top	Outer top	Inner bottom	Outer bottom
Li at PE [µmol]	1398	1436	1395	1386
P at PE [µmol]	3	3	4	4
Total Li at PE [µmol]	**1401**	**1439**	**1399**	**1390**
Total Li at PE [%]	**94.3%**	**94.8%**	**94.6%**	**94.9%**
NMC [µmol]	**1469**	**1499**	**1452**	**1463**
Li at NE [µmol]	64	61	61	56
P at NE [µmol]	21	18	18	19
Total Li at NE [µmol]	**84**	**78**	**80**	**75**
Total Li at NE [%]	**5.7%**	**5.2%**	**5.4%**	**5.1%**
Total Li in the sample [µmol]	**1485**	**1518**	**1479**	**1465**
Loss of lithium [%]	**5.7%**	**5.2%**	**5.4%**	**5.1%**

Table 5.17. Evaluation of the amount of Li at positive and negative electrodes of a fresh LGC2079 cell (NMC) fully discharged.

LGC2079	Inner top	Outer top	Inner bottom	Outer bottom
Li at PE [µmol]	1462	1472	1455	1471
P at PE [µmol]	7	7	6	7
Total Li at PE [µmol]	**1469**	**1479**	**1461**	**1478**
Total Li at PE [%]	**91.1 %**	**91.0 %**	**90.9 %**	**91.4 %**
NMC [µmol]	**1568**	**1573**	**1568**	**1567**
Li at NE [µmol]	125	128	126	120
P at NE [µmol]	19	19	20	19
Total Li at NE [µmol]	**144**	**147**	**146**	**139**
Total Li at NE [%]	**8.9 %**	**9.0 %**	**9.1 %**	**8.6 %**
Total Li in the sample [µmol]	**1613**	**1626**	**1608**	**1617**
Loss of lithium [%]	**8.9%**	**9.0%**	**9.1%**	**8.6%**

Table 5.18. Evaluation of the amount of Li at positive and negative electrodes of an aged LGC2074 cell (NMC) fully discharged.

LGC2074	Inner top	Outer top	Inner bottom	Outer bottom
Li at PE [µmol]	1317	1303	1288	1295
P at PE [µmol]	4	5	4	5
Total Li at PE [µmol]	**1321**	**1308**	**1292**	**1299**
Total Li at PE [%]	**85.2%**	**84.6%**	**84.4%**	**85.4%**
NMC [µmol]	**1551**	**1496**	**1537**	**1501**
Li at NE [µmol]	213	221	222	208
P at NE [µmol]	17	17	17	15
Total Li at NE [µmol]	**230**	**238**	**239**	**223**
Total Li at NE [%]	**14.8%**	**15.4%**	**15.6%**	**14.6%**
Total Li in the sample [µmol]	**1551**	**1546**	**1531**	**1522**
Loss of lithium [%]	**14.8%**	**15.4%**	**15.6%**	**14.6%**

5.3.6. Porosimetry

5.3.6.1.LGC2 cells (NMC)

Porosimetry analysis was only carried out to LGC2077 fresh cell. Particle size and pore size distributions at the negative electrode were plotted in Fig. 5.21 and Fig. 5.22. The size of particles and pores showed to be homogeneous along the electrodes. The mean size of the particles and pores was 6.0812 µm and 1.5744 µm, respectively. The accessible porosity was found to be 32.27 %.

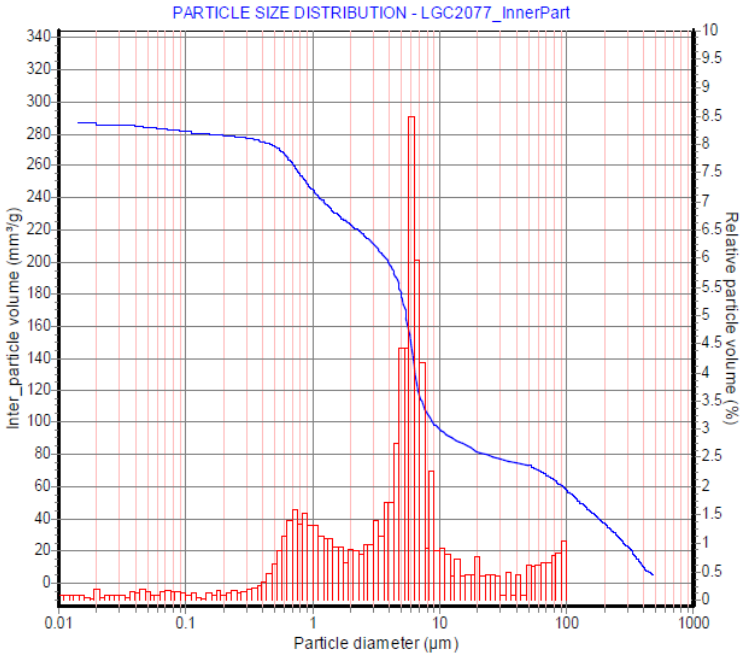

Fig. 5.21. Particle size distribution of the negative electrode of LGC2077 fresh cell (NMC). Mean size of the particles was 6.0812 µm.

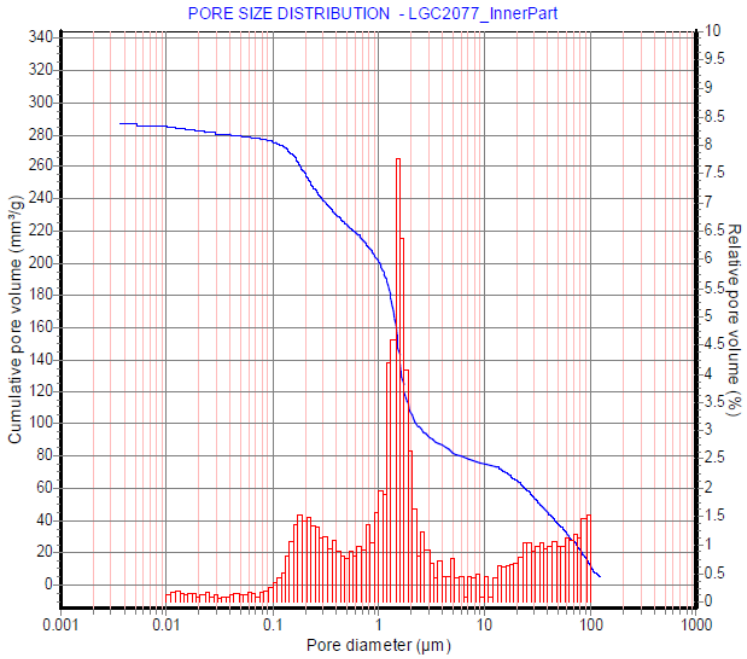

Fig. 5.22. Pore size distribution of the negative electrode of LGC2077 fresh cell (NMC). Accessible porosity was 32.27 %.

The same analysis was carried out to the positive electrode composed of NMC. The results of particle size and pore size distributions were plotted in Fig. 5.23 and Fig. 5.24. The size of particles tended to be around a mean value of 5.7213 µm showing a homogeneous distribution. The accessible porosity at the positive electrode of a fresh cell was of 27.20 %.

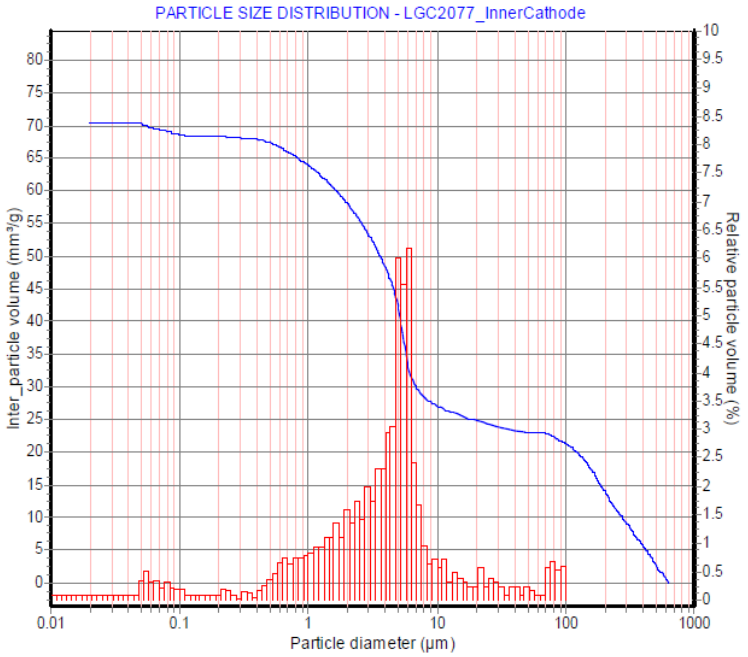

Fig. 5.23. Particle size distribution of the positive electrode of LGC2077 fresh cell (NMC). Mean size of the particles was 5.7213 µm.

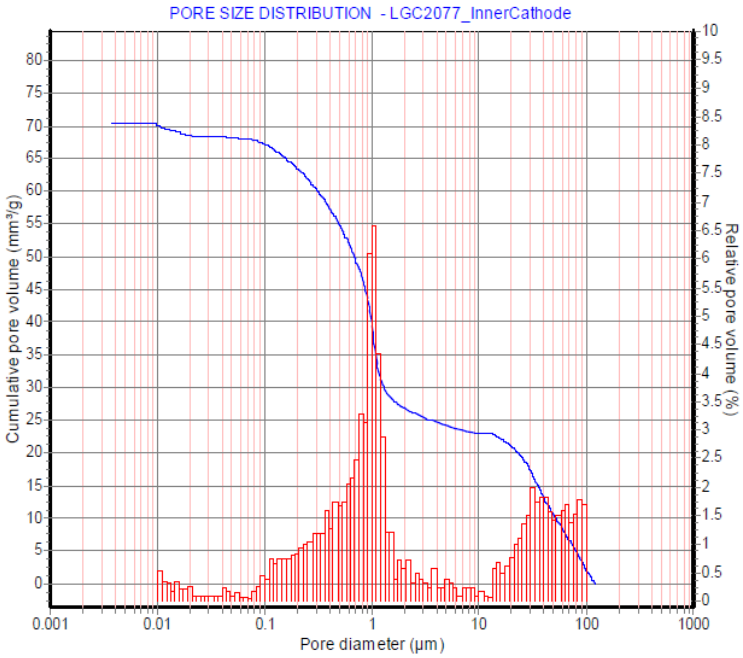

Fig. 5.24. Pore size distribution of the positive electrode of LGC2077 fresh cell (NMC). Accessible porosity was 27.20 %.

5.3.7. XRD analysis

5.3.7.1.LGC2 cells (NMC)

X-ray diffraction is commonly used to determine structural and phase changes. Positive and negative electrodes of fresh and aged NMC cells were evaluated (see Fig. 5.25 and Fig. 5.26). At the graphite-based negative electrode represented in Fig. 5.25, changes in intensity, position of the peaks and appearance/disappearance of peaks due to aging were detected. Peaks at positions 23.80º and 85.42º were suppressed during the aging process. However, new peaks appeared at 35.12º, 52.53º, 57.45º, 66.54º, and 68.13º. Furthermore, some of the peaks changed in intensity and shifted to other positions. Nevertheless, at the positive electrode of NMC represented in Fig. 5.26, new peaks did not appear during the aging process but peaks at positions 15.65º, 37.39º, 39.03º, 66.25º, 69.59º, and 83.83º disappeared. In the same way it happened at the negative electrode, some peaks shifted in position and some others changed in terms of intensity.

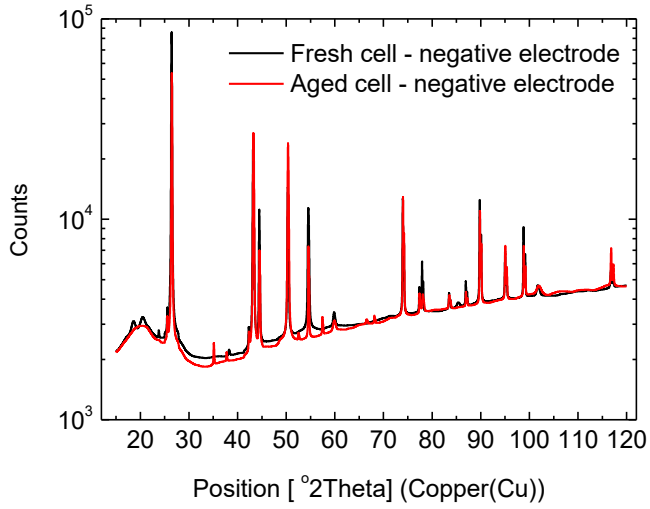

Fig. 5.25. XRD patterns of fresh and aged negative electrodes of LGC2 cells (NMC).

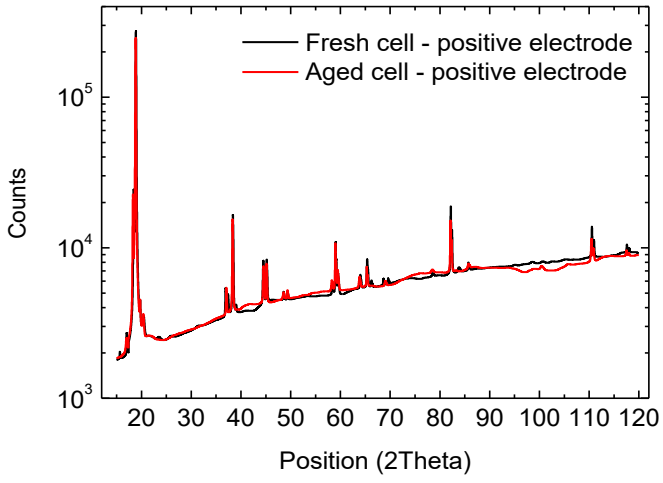

Fig. 5.26. XRD patterns of fresh and aged positive electrodes of LGC2 cells (NMC).

5.3.7.2. VIC cells (LFP)

XRD patterns of positive and negative electrodes of VIC cells were plotted in Fig. 5.27 and Fig. 5.28. At the negative electrode, which was based on graphite, peaks at positions 23.81º, 25.54º, and 116.34º disappeared during the aging process. However, new peaks appeared at positions 39.99º, 41.75º, 48.56º, 64.97º, and 77.42º. Regarding to positive electrode, more complex pattern was found. After the aging process, initial peaks found at positions 34.48º, 68.27º, and 69.42º were not detected anymore. However, new peaks were found at positions 23.69º, 26.48º, 33.11º, 38.70º, 39.32º, 60.98º, and 71.31º. Moreover, in both positive and negative electrodes, some peaks had changed in intensity and position during the process.

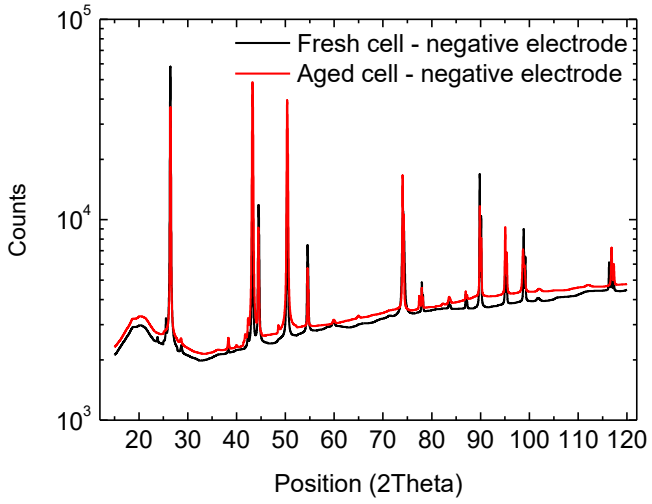

Fig. 5.27. XRD patterns of fresh and aged negative electrodes of VIC cells (LFP).

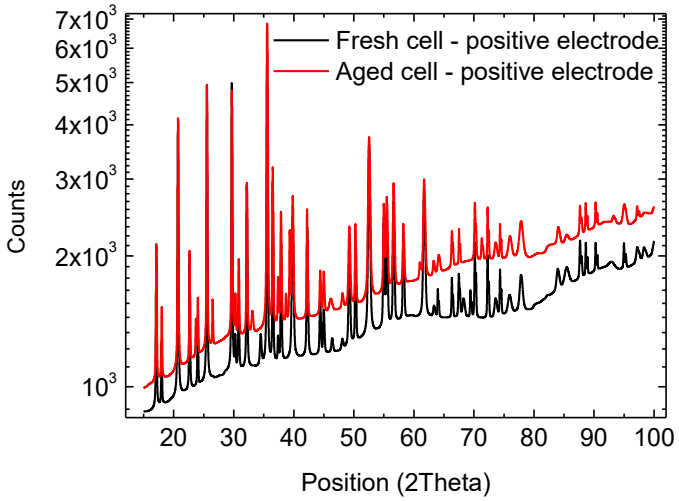

Fig. 5.28. XRD patterns of fresh and aged positive electrodes of VIC cells (LFP).

5.4. Discussions

We discuss here the most relevant results of post-mortem analysis. Discussions are only presented for LGC2 cells (NMC) because post-mortem of VIC cells was carried out but the results are still not evaluated.

5.4.1. Visual inspection

At a first sight during the post-mortem analysis, the most affected electrode by the aging test seemed to be the negative one. It showed a completely different color in comparison to the one of the fresh cell. A white/grey surface layer was clearly observed at the surface of the NE of the aged cell without the need of the microscope (Fig. 5.7). In addition, the electrodes of the fresh cells observed under the laser microscope, showed a blue tonality. The color of the active material particles indicates the lithiation phase of the graphite. Ranging from fully delithiated graphite to fully lithiated, the colors go from black to blue to red and to gold/yellow [18,182,183]. Thus, black color was expected for an electrode empty of lithium but the blue tone indicated that some lithium was trapped there. It could be attributed to LAM which was lithiated at the NE or a mismatching between the electrodes, which would not had allowed the fully delithiation of the graphite. Therefore, during a regular discharge of the full-cell, the NE was not able to be fully delithiated as it was confirmed by the presence of lithium at the NE.

When visualizing the negative electrode of the aged cell at the laser microscope, it was observed that the surface layer was completely covering the active material (Fig. 5.7). The intense white/grey color of the surface layer, suggested metallic plating [95]. Thus, the surface layer was probably a combination of SEI and the plated metals. Moreover, in addition to the observed grey layer, some white traces were found at the surface of it. White traces were also found in other studies: in some of them they were referred as lithium plating [36,184] while, in some others, different metallic residues apart from lithium were found [185]. In addition, in reference [173], also white color substances were found at the surface of the negative electrode but they were associated to lithium salts instead of metallic plating. Furthermore, spots found at the negative-electrode side of the separator corresponded to holes (where surface layer was not present anymore) at the same positions on the electrode. In Fig. 5.29, it can be seen how lithium was adhered to the separator in those spots. Thus, in these parts, the results suggested that lithium plating had created a thick layer, which was completely stuck to the separator.

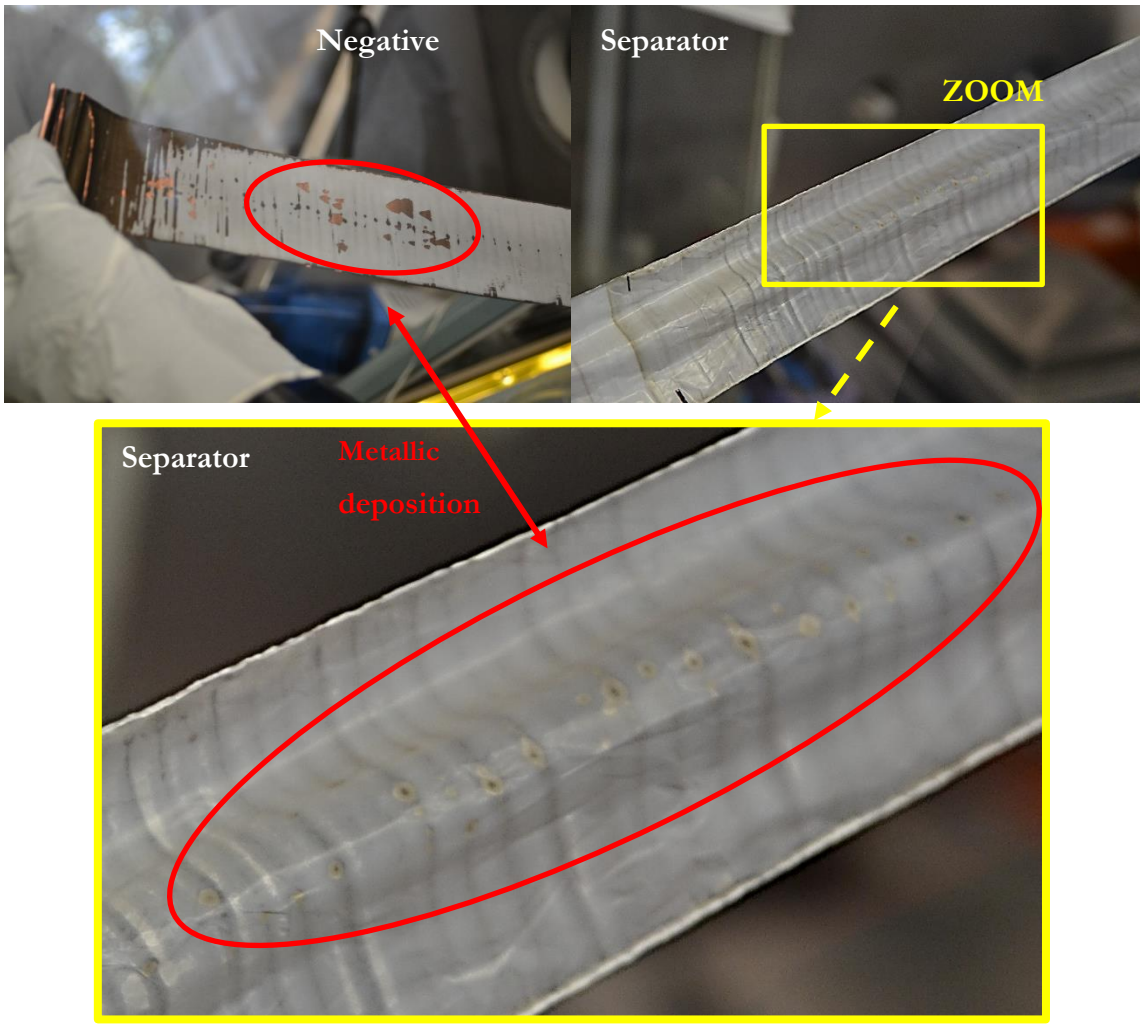

Fig. 5.29. Metallic depositions at the negative electrode, which were stuck to the separator.

At the inner and outer parts of the jellyroll, positive and negative current collector tabs generated a regular pattern at the negative electrode, where the surface layer was unevenly distributed (Fig. 5.30). This pattern generated by the CC tabs was associated to the change in pressure to which the jellyroll was subjected due to the change in volume during lithium insertion/extraction to or from the NE. Similar patterns were found in literature [185] where lithium plating was evident, especially near the edges of the imperfections generated by the tabs. Moreover, lithium plating was also found to be favorable at the edges of the electrode [186]. It is because the current density at the edges tends to be higher because of the concentrated electric field lines, which favors lithium plating [186]. However, in our study, in Fig. 5.30 we appreciated that the grey/white surface layer was not present at the edges of the tabs instead of having plated lithium. We interpreted from the results that, at both the edges of the tabs and those of the electrode itself, the plated lithium was that thick that was attached to the separator, as it happened in Fig. 5.29.

This heterogeneous pressure has been proven to affect lithium ion diffusion through the separator [185]. Lithium plating would also affect the conductivity of the separator especially in the spots where the loose lithium was attached to it as it was shown in Fig. 5.29. Therefore, the impedance

of the cell should have been affected. Unfortunately, information about the ohmic resistance could not be extracted from our impedance measurements of half-cells because the electrolyte and the separator were modified during the manufacturing process. Fresh separator and a different electrolyte were used instead of harvesting samples from the cells.

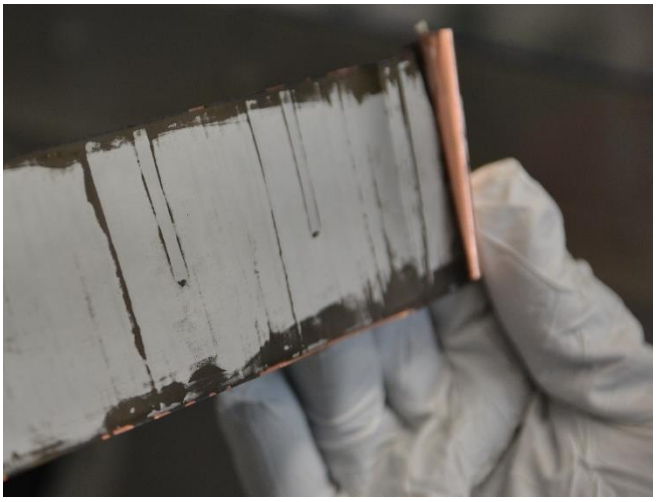

Fig. 5.30. Pressure patterns exerted to the negative electrode by the positive current collector tab during cycling.

5.4.2. Metals dissolution

Traces of Mn, Ni and Co from the positive electrode were found at the negative electrode during the ICP analysis. Metals dissolution and migration to the negative electrode have been reported in other studies [87]. The obtained values are shown in Table 5.19 in comparison to [87]. They also detected Mn, Ni and Co after initial cycles (fresh cells) but a much higher amount of Mn compared to the other metals and to our results. Moreover, they also found that the metals presence increased during cycling but more notably the Mn. Unlike them, in our study all the transition metals increased their concentration at the NE in a comparable way. The highest increase was that of manganese (increasing factor of 5.12) followed by nickel (4.27) and then cobalt (4.08). The increasing factor of Mn in our case was two times higher than the one obtained in [87], more than three times for Ni and almost four times for Co. Li et al. concluded that the cell capacity loss arising from metals dissolution was negligibly small because Mn, Ni and Co contents at the NE were several orders of magnitude smaller than at PE [87]. In contrast, in reference [87] the increasing factors were found to be closer to the ones obtained in this study (Table 5.20). Although the absolute values did not coincide, they found the higher increase in Mn content (increasing factor of 5.4 compared to our 6), followed by Ni (5 as in our study) and Co (3.74 in front of our 4). Despite the higher increases found in Ni and Co, they also concluded metals dissolution affected in a minor extent the capacity fade at the positive electrode. However, both [87] and [87] agree that metals deposited at the negative

electrode enhance the SEI layer growth which consumes more lithium and consequently reduces the capacity.

Table 5.19. Comparison of metals concentrations at the negative electrode of fresh and aged cells between the results reported in reference [87] **and the results obtained in our study.**

	Mn (µg/g)	Ni (µg/g)	Co (µg/g)
Fresh cell in [87]	617	125	63
Aged cell in [87]	1446	167	71
Increasing factor [87]	**2.34**	**1.3**	**1.1**
Our fresh cell	9.83	29.50	88.51
Our aged cell	50.33	125.83	360.71
Increasing factor	**5.12**	**4.27**	**4.08**

Table 5.20. Comparison of metals concentrations at the negative electrode of fresh and aged cells between the results reported in reference [87] **and the results obtained in our study.**

	Mn (mg/Kg)	Ni (mg/Kg)	Co (mg/Kg)
Fresh cell in [87]	136	53	35
Aged cell in [87]	735	265	131
Increasing factor [87]	**5.4**	**5**	**3.74**
Our fresh cell	9.83	29.5	88.51
Our aged cell	59	147.52	354
Increasing factor	**6**	**5**	**4**

5.4.3. Loss of electrolyte

The remaining electrolyte after the cell opening at the three evaluated cells was summarized in Table 5.3. The fresh cells contained different amounts of electrolyte ranging from 2.12 mg to 3.16 mg, representing a 4.67 % and a 6.99 % of their total weights. The LGC2074 aged cell, contained 2.49 mg that corresponds to a 5.41 % of its total weight. Therefore, no significant amount of electrolyte seemed to be lost after the formation cycles. Obviously, some electrolyte was consumed after the formation cycles and during the SEI growth process but it could not be quantified due to the dispersion in values obtained from the fresh cells. However, phosphorous concentration at the negative electrode is usually related to SEI growth due to electrolyte decomposition [32]. In our study, much higher amounts of P were found at the NE than at the positive one as it was summarized in Table 5.16, Table 5.17 and Table 5.18. It supports the fact that a surface layer was formed thanks to electrolyte decomposition. Nevertheless, after the formation cycles, variations in P concentrations at

the NE were not detected during cycling as it was reported in [32]. Therefore, it would coincide with the fact that the highest amount of electrolyte was lost during the initial SEI formation.

5.4.4. Impedance

As mentioned in the results chapter, the effect on impedance associated to charge-transfer process at the metallic lithium electrode was superimposed to the one of the electrode of interest. This undesired effect is usually found between 100 Hz and 800 Hz, depending on temperature (between 0 ºC and 40 ºC) [83]. It could be easily identified at positive electrode measurements where it corresponded to the intermediate frequency semicircle (Fig. 5.16) but it was overlapped with other effects at the negative electrode (Fig. 5.16 and Fig. 5.20). In order to subtract the undesired effect, Li/Li symmetrical cells would have been measured. In this study, subtraction of the effect produced by lithium electrode was not carried out.

5.4.4.1. Positive electrode

5.4.4.1.1. SoC dependency

We discuss here the evolution of impedance of the positive electrode (NMC) with the SoC. Measurements were carried out in a NMC/Li half-cell configuration in a coin cell format. From this analysis, we aim to be able to assign the different effects to their corresponding physical effects.

In particular, three effects were differentiated. The one at lower frequencies was found at 24 Hz for a fresh cell at 100 % SoC. It was associated to charge transfer between the NMC electrode and the electrolyte because the polarization resistance of this effect was smaller at higher SoCs (Fig. 5.17). This has been explained as a charge transfer enhancement when few lithium ions are present in the host electrode [187]. Moreover, activation energies were used to assign each measured effect in impedance to the correspondent physical effect [187]. In our study, activation energies were not obtained as no data was collected at different temperatures, which is necessary for the calculations.

The effect at medium frequencies (around 400 Hz) was the one associated to charge transfer and diffusion at the metallic Li electrode [84]. The polarization resistance associated to this effect increased as the SoC was decreased. According to [187], a possible explanation could be that dendritic lithium deposition during cycling at the surface of the metallic lithium electrode would allow to deposit lithium on the top of these dendrites at high SoCs. Thus, Li ions would not need to pass through the whole surface layer at high SoCs, causing a smaller polarization resistance than at lower SoCs.

The last effect found in impedance was the one at higher frequencies. It was partially overlapped with the other effects but still it was easily identified. Its characteristic frequency was located around 20 kHz. It was found to be invariant in almost all the SoC range except at very low SoCs where it increased. In reference [187], the highest frequency effect was found around 1 kHz and it was also almost independent of the state of charge. Their cell was composed of $LiFePO_4$ instead of

$Li(NiMnCo)O_2$ and it was encased in a different geometry. Thus, different values could be expected but the invariability of this effect had to be maintained. They associated the effect to the interface between the active material and the current collector due to the low activation energy they obtained. Therefore, as we did not measure the diffusion coefficients at different temperatures, which is necessary for the calculation of the activation energies, we assumed the same origin for this effect as our results followed the same tendency.

5.4.4.1.2. SoH tendency

In this section, we aim to discuss the evolution of impedance of the positive electrode (NMC) with the SoH or aging level. Measurements were carried out in a NMC/Li half-cell configuration in a coin cell format. From this analysis, we aim to elucidate the effects causing the impedance variations during the cycle aging process.

Data coming from the inner, central and outer parts of the jellyroll were compared. The highest impedance increases were found at the inner and outer parts, where the total impedance increased in more than 100 %. In particular, the highest increase in polarization was derived from the charge transfer effect (Fig. 5.16). This would imply that the kinetics of the positive electrode was affected during the aging process. The effect at high frequency, which was associated to the electrode/current collector interface, also increased due to aging. The absolute increase was not quantified because no model was adjusted to the data. However, we associated such increase to the loss of contact between the active material particles and the current collector due to cycling. Moreover, if the positive electrode is observed after the cell-opening, pressure lines produced due to the changes in volume during lithium insertion and extraction can be clearly identified (Fig. 5.31). At those pressure lines, the active material was detached from the aluminum current collector. Therefore, it would stand the previous assumption of the loss of contact between the active material and the current collector, which increased the resistance associated to the highest frequencies.

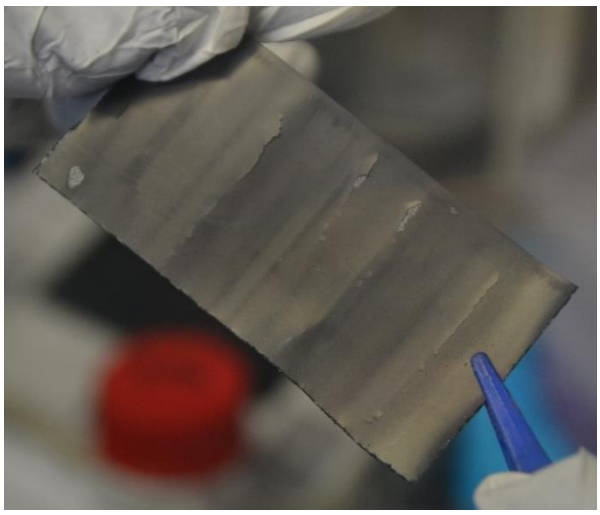

Fig. 5.31. Sample harvested from the positive electrode of an aged NMC cell. Pressure lines were clearly observed and there was an evident detachment of the active material from the current collector, especially at those pressure lines.

5.4.4.2. Negative electrode

5.4.4.2.1. SoC dependency

In the considered frequency range, three arcs were observed at the impedance measurement of the negative electrode and a diffusional branch at the lowest frequencies (Fig. 5.18 and Fig. 5.19). The semi-arc at lower frequencies was only visible at the lowest measured voltage (or highest SoC of the full-cell). Unfortunately, the effect of metallic lithium was completely overlapped with the low frequency effect of graphite, and thus, it was indistinguishable. The higher frequency effect is usually associated to li-ion diffusion across SEI and the lower frequency process to charge-transfer at the surface of the graphitic electrode. Either in this case, no useful information could be extracted from these data because of the pronounced overlapping in frequency of the different processes. The effect caused by the Li counter electrode had to be subtracted from the impedance spectra in order to be able to extract useful information about the harvested samples or, another possibility would be to measure symmetrical cells instead of half-cells. However, fresh and aged cells clearly exhibited different behaviors with respect to SoC variation.

5.4.4.2.2. SoH tendency

Although charge-transfer effect at the negative electrode and the effect at the metallic lithium side could not be separated, the resistance associated to charge-transfer was clearly higher than the surface layer resistance (Fig. 5.20). At every evaluated part of the jellyroll, the impedance raised during the aging process. However, the highest increase of impedance was found at the inner part of the jellyroll (increase of 36.30 $\Omega \cdot cm^2$ or 94.57 %). It will be related to capacity fade in the next section. One possible explanation could be that the inner part of the electrode is the one that suffered more pressure during volume changes, which could cause, among others, loss of contact between active material particles and with the current collector [188]. Moreover, the temperature at the core of the cell rises more than at the outer part what could contribute to thicker and faster SEI formation and impedance rise. Furthermore, metals dissolution, also could contribute to further SEI growth. However, its contribution would not affect the inner part in particular, as the metals concentrations were similar at the inner, central and outer parts of the electrode.

5.4.5. Capacity fade

The capacity fade of the evaluated NMC cells will be related to LLI, LAM and increase in overpotentials.

5.4.5.1. Contributions to capacity fade

5.4.5.1.1. Loss of Lithium Inventory (LLI)

LLI was estimated from the lithium measured at the PE and NE of half-cells by the ICP technique during the post-mortem analysis of NMC cells (Table 5.21). Capacity fade at the full-cell

related to LLI was calculated as a direct relation between the percentage of loss of lithium and the initial capacity of the cells. High variability of the results was found when comparing data of the aged cell with LGC2077 or LGC2079 fresh cells. These differences may arise from some contamination of the samples during the cell opening.

Table 5.21. Amount of lithium measured by the ICP technique in the cell and, in particular, at the NE. Total capacity fade at the full-cell associated to LLI was calculated considering the formation cycles before the BoL we defined. In addition, an estimation of the capacity fade from BoL to EoL (i.e. not considering formation cycles) was also carried out.

Cell	Lithium in average (µmols)	Lithium in average at the NE (µmols)	Associated capacity fade (Ah)	Associated capacity fade after formation (Ah)
LGC2077 (fresh)	1478	80	0.16	0
LGC2079 (fresh)	1616	144	0.27	0
LGC2074 (aged) from 077	1538	233	0.46	0.3
LGC2074 (aged) from 079	1538	233	0.44	0.17

5.4.5.1.2. Ability of the electrode to intercalate lithium ions

As we were measuring half-cells containing extra metallic lithium coming from the added counter electrode when building the half-cells, the possible LLI produced during the aging tests would not be affecting the measured capacity. Thus, a decrease of capacity measured at the half-cells would suggest loss of active material LAM and/or impedance rise. Therefore, the capacity fade would be directly related to the loss of electrode material's ability to intercalate or deintercalate lithium ions [173]. Moreover, as the capacity fade was evaluated at low rates (C/25), the effects related to ohmic conduction were minimized.

In this study, an average of the total capacity fade at the half-cells was calculated by considering that the individual capacity fades at inner, central and outer parts were homogeneous in their corresponding positions and it was also considered that the three parts occupied the same area in the electrode. Therefore, the average capacity fade was calculated by the arithmetic mean of the capacity fade at the inner, central and outer parts (Table 5.22). Therefore, we found that the capacity fade was around 0.34 Ah at the NE and 0.3 Ah at the PE. Unfortunately, the calculous of the capacity fade of the full-cell associated to LAM is not as straightforward as LLI. LAM not always contributes to

capacity fade because it can happen that even though the amount of active material that can be lithiated decreases, there is still enough storage capacity in the active material for the remaining lithium [27].

Table 5.22. Capacity fade at a C/25 discharge rate obtained at inner, central and outer parts of the jellyroll measured in half-cells and the estimated capacity fade in average obtained from the partial contributions.

	Capacity fade at half-cell (mAh)	Capacity fade at half-cell (%)
Inner NE	0.7992	8.80
Central NE	-	-
Outer NE	0.2285	2.54
Average at NE	**0.34**	**3.78**
Inner PE	0.4786	5.88
Central PE	0.312	3.84
Outer PE	0.0963	1.24
Average at PE	**0.3**	**3.65**

5.4.5.1.3. Total capacity fade at the full-cells

Total capacity cell separated by means of LLI, LAM and increase in overpotentials at low discharge rates had to be estimated from the difference in capacity of the full-cell at this rate and the contribution of LLI. As it was previously mentioned and illustrated, a high variability in the LLI was found when comparing the data from the aged cell to two different fresh cells (Table 5.21). Unfortunately, it was not possible to determine which cell was giving the most accurate values. In particular, we found that LLI reduced the capacity of the cells at C/25 in an amount between 6 % and 10.7 %. Thus, as the total capacity fade was 14.8 %, the associated capacity fade to LAM and increase in overpotentials was between 4 % and 8.8 %. The most probable situation would be that in which LLI contributed in a 10.7 % and LAM in a 4 % to the total capacity fade. In fact, around 5 % of LLI would be reasonably attributed to initial SEI formation.

Table 5.23. Capacity fade at a C/25 discharge rate obtained at inner, central and outer parts of the jellyroll measured in half-cells and the estimated average obtained from the partial contributions.

Aging mechanism	Test	Capacity fade (mAh)
LLI	ICP	**Between 170 (6 %) and 300 (10.7 %)**
LAM_{NE} + NE impedance rise	Capacity of half-cells	0.34 (at the half-cell)
LAM_{PE} + PE impedance rise	Capacity of half-cells	0.3 (at the half-cell)
Measured capacity fade at C/25	Current integration in full-cells	**414.7 (14.8 %)**
LAM + overpotentials	Difference between measured capacity and LLI	**Between 114.7 (4 %) and 244.7 (8.8 %)**

5.4.5.2.Negative electrode

The highest decrease in capacity was found at the inner part of the negative electrode. Thus, as it was explained in subsection 5.4.5.1, the main contributor to the capacity fade of half-cells at low rates was attributed to LAM. Loss of active material could be associated to the isolation of active material particles, dissolution of transition metals, changes in the electrode composition or changes in the crystal structure of the active material [155]. In this study, the most relevant possible causes were the isolation of the active material and the changes in the crystal structure. Isolation of the active material particles could be caused because of the evident surface layer that was formed on the top of the negative electrode. It could completely isolate some of the grains that conform the active material. Concerning the other possible source of loss of active material, XRD patterns showed many changes in peaks intensity and positions, which determine the crystal structure. However, those changes in the XRD peaks could be also associated to different states of charge or phase changes [18,169]. Therefore, different amounts of lithium in the graphite would produce different states that would modify some of the peaks of the XRD pattern. A more detailed analysis would be required to confirm if the crystal structure was affected due to aging.

5.4.5.3. Positive electrode

At the positive electrode side, the highest decrease of capacity was also found at the inner part of the jellyroll (5.88 %) followed by the central part (3.84 %). In this case, the most probable degradation causes could be particle isolation, metals dissolution and changes in the crystal structure. It is widely known that an undesired surface layer at the positive electrode is usually formed as SEI at negative electrode [36,152,189]. As it was shown in Table 5.10 and Table 5.12, phosphorous was

also present at the PE even though it was found in higher amounts at the NE, due to the SEI formation. These amounts of P found at the PE supported that the electrolyte was decomposed forming a surface layer on the top of it [189]. Therefore, particle isolation could be caused by this surface layer in which some particles could be completely isolated during the layer growth, and become at the end totally disconnected from the matrix [190]. With regard to the metals dissolution, it was evaluated through the ICP technique. It was concluded that there was migration to the negative electrode of some of those metals, what confirmed that some active material was lost at the positive electrode due to this fact. However, the low amounts of Mn, Ni and Co at the NE suggested that the loss of active material due to metals dissolution had a low impact in the overall capacity fade. Nevertheless, they could have been contributed to the SEI layer growth, which consumes lithium and, thus, contributes to capacity fade. With respect to changes in crystal structure, at the XRD patterns, some peaks were shifted and some others decreased in intensity. However, no drastic changes in crystal structure or phases were identified.

5.5. Conclusions

5.5.1. LGC2 cells (NMC)

- A white/grey surface layer was formed at the surface of the negative electrode of aged cell, which completely covered the active material.

- The active material particles of the fresh NE in a fully delithiated state showed a blue tone what indicated some lithium was trapped there. It could be attributed to LAM which was lithiated at the NE or a mismatching between the electrodes, which would not had allowed the fully delithiation of the graphite.

- Heterogeneous pressure was detected along the electrodes during cycling. Pressure lines were clearly observed at both the PE and the NE. It was associated to the change in pressure to which the jellyroll was subjected due to the change in volume during lithium insertion/extraction to or from the NE.

- Spots found at the negative-electrode side of the separator corresponded to lithium particles that were adhered and corresponded to holes at the same positions on the electrode. It was associated to the thick layer created by lithium plating, which was completely stuck to the separator.

- Traces of Mn, Ni and Co from the positive electrode were found at the negative electrode during the ICP analysis.

  - Metals dissolution affected in a minor extent the capacity fade at the positive electrode.

- Much higher amounts of P were found at the NE than at the positive one, which supported SEI growth at the NE due to electrolyte decomposition. Nevertheless, after the formation cycles, variations in P concentrations at the NE were not altered during cycling what coincide with the fact that no significant amount of electrolyte was lost after the initial SEI formation.

- The highest contributor to impedance of the full-cell was the negative electrode. Furthermore, it was also the major contributor to impedance rise. However, although the total impedance of the positive electrode was much lower than that of the negative electrode, its relative increase was much higher.

- Impedance contribution of the metallic lithium electrode was not subtracted from the impedance of half-cells.

- Impedance of the PE showed three effects; the one at higher frequencies was related to active material/current collector interface and the one at lower frequencies to charge transfer at the NMC/electrolyte interface.

- The highest increase in polarization at the PE was derived from the charge transfer effect, which implied that the kinetics of the positive electrode were affected during the aging process.

- The effect at higher frequencies at PE also increased during the aging process, which was associated to the loss of contact between the active material and the current collector. It was validated at the visual inspection where the active material was deatached from the current collector at several points.

- Impedance at the NE side mainly showed two effects. The one at higher frequencies was associated to SEI transfer while the one at medium frequencies was associated to the overlapping of charge transfer at the graphite/electrolyte and at the Li/electrolyte interfaces.

- Although charge-transfer effect at the negative electrode and the effect at the metallic lithium side could not be separated, the resistance associated to charge-transfer was clearly higher than the resistance of the surface layer.

- In all three regions of the NE of the cell, the contribution to impedance rise came mostly from the increase in charge-transfer resistance.

- The highest decrease in capacity was found at the inner part of the NE. Particularly the plateau at the lower voltages that was related to the transition between LiC_6 and $Li_{0.5}C_6$ was the more affected.

- The most relevant possible causes of capacity fade at the NE were isolation of the active material and changes in the crystal structure.

- The most probably causes of capacity fade at PE were particle isolation, metals dissolution and changes in the crystal structure.

- The highest capacity fades were found at the inner parts of both electrodes.

- LAM and LLI were determined from ICP measurements.

Chapter 6

General discussions

In this section, we aim to elucidate the main aging mechanisms that took place during the cycling tests. For doing so, a relation between these mechanisms and capacity fade, impedance rise and the change in entropy production is sought. In Table 6.1, we summarize the causes and the effects affecting the impedance response of the cells and the main aging mechanisms attributed to them from our experience. As it can be appreciated, they are related to ohmic and charge-transfer resistances. However, mass-transfer resistance was not included. Mass-transfer resistance mainly depends on the thickness and porosity of the electrode and the ease of diffusion through it [191]. Therefore, we associated its increase to morphological or structural changes, which include changes in the structure and porosity of the electrodes. These effects are mainly caused by the change in volume to which the cell is subjected during Li+ insertion/extraction. Once the main degradation mechanisms are related to the loss in performance of the cells, the relation between irreversible entropy production and this loss of performance is presented. All these previously mentioned effects, including morphological or structural changes, affect the generation of irreversible entropy in some way. However, irreversible entropy production applied to battery degradation is introduced for the first time and, thus, is still not clear how the different aging effects affect it.

Table 6.1. Aging mechanisms behind the various effects measured at the impedance.

Aging mechanism	Cause	Effect in resistance
LLI	• SEI formation (electrolyte consumption) • SEI growth • Surface layer at PE • Lithium plating	• R_Ω increases
LAM_{NE}	• SEI growth (particle isolation)	• R_{CT} increases
	• Contact loss (particle isolation)	• Decrease in active surface area → R_{CT} increases
LAM_{PE}	• Metals dissolution	• Decrease in active surface area → R_{CT} increases
	• Layer formation (particle isolation)	• Decrease in active surface area → R_{CT} increases

6.1. Relative-Entropy-Production (REP)

If we recall Fig. 4.72, the process that was graphically depicted can be defined as in equation (6.1). As we know, the work exerted by the cell is equal to the integral over time of the cell voltage multiplied by the current. In addition, we also know that the input energy minus the reversible heat represents the maximum available electrical energy calculated as the integral over time of the OCV multiplied by the current. Therefore, expression (6.1) can be rewritten as (6.2). Then, if the generation rate is evaluated instead of the energy balance, equation (6.2) can be reduced to equations (6.3) and (6.4) in which irreversible entropy production is directly related to the associated overpotentials (η_{heat} and η_{aging}). In our study, d_iS/dt represented the joint contribution of d_iS_{heat}/dt and d_iS_{aging}/dt. In the future, it would be interesting to separate both contributions.

$$W = E - T \cdot \Delta S - T \cdot d_iS = E - T \cdot \Delta S - T \cdot d_iS_{heat} - T \cdot d_iS_{aging} \quad \textbf{(6.1)}$$

$$\int V_{cell} \cdot I \cdot dt = \int OCV \cdot I \cdot dt - T \cdot d_iS_{heat} - T \cdot d_iS_{aging} \quad \textbf{(6.2)}$$

$$V_{cell} \cdot I = OCV \cdot I - T \cdot \frac{d_iS_{heat}}{dt} - T \cdot \frac{d_iS_{aging}}{dt} = OCV \cdot I - \eta_{heat} \cdot I - \eta_{aging} \cdot I \quad \textbf{(6.3)}$$

$$OCV - V_{cell} = \eta = \eta_{heat} + \eta_{aging} \quad \textbf{(6.4)}$$

From these definitions, we introduced a new parameter for system degradation characterization, the Relative-Entropy-Production or REP, defined as the entropy generation ratio at actual state and a reference state. For the sake of simplicity, in this dissertation, we considered the EoL as the actual state. However, when data were available, it was calculated as the ratio between intermediate states and BoL.

$$REP = \frac{(d_i S/dt)_{actual\_state}}{(d_i S/dt)_{BoL}} \quad \textbf{(6.5)}$$

This expression deserves some considerations. It is defined positive, because entropy generation is always positive in irreversible processes. REP can be larger than 1, in contrast to other degradation parameters such as damage, *D* [126] and apparently, it can be applied to any system undergoing irreversible processes.

6.1.1. NMC cells

6.1.1.1.Contributions to capacity fade

Contributions to capacity fade were obtained from the estimated LLI from ICP (post-mortem, refer to Chapter 5) and ICA (refer to Chapter 4) analyses (Table 6.2). As previously mentioned, high variability was obtained from the post-mortem analysis in the amount of lithium that was lost. These variabilities probably came from some contamination of the data during the preparation of the samples. If the results are compared to ICA analysis, the most trustable data seemed to be 10.7 % of LLI (ICP). From ICA it was estimated that the LLI contributed in a 11.8 % to the total capacity fade, what is in a good agreement with ICP results. Then, from the difference in the measured capacity at C/25 by Coulomb-counting method, the associated capacity fade to LAM was 4 % and 3 % from ICP and ICA, respectively.

Table 6.2. Estimated capacity fade of the full-cell at a C/25 discharge rate obtained from ICP and ICA analyses.

Aging mechanism	Test	Capacity fade (mAh)
LLI	ICP	**Between 170 (6 %) and 300 (10.7 %)**
LLI	ICA	**11.8 %**
Measured capacity fade at C/25	Current integration in full-cells	**414.7 (14.8 %)**
LAM + overpotentials	Difference between capacity and LLI from ICP	**Between 114.7 (4 %) and 244.7 (8.8 %)**
LAM + overpotentials	Difference between capacity and LLI from ICA	**3 %**

6.1.1.2. Discussions

From the half-cell measurements, the NE was stated to be the highest contributor to full-cell impedance at BoL and EoL. In particular, the highest absolute impedance rise (without considering ohmic resistance) was found at the inner part of the NE. However, its relative increase was comparable of that at the inner and outer parts of the PE . Thus, indicating that the most degraded parts of the cell in terms of impedance after the aging test were the inner part of NE and inner and outer parts of PE. Nevertheless, the highest absolute and relative decreases in capacity at thermodynamic rates were found at the inner part of the NE. The capacity fade in that case was attributed to possible isolation of the active material due to the formation of a surface layer (SEI), changes in the crystal structure and porosity modifications. The most relevant changes in crystal structure and porosity associated to the inner part of the jellyroll were attributed to the higher pressure suffered at this part during lithium insertion/extraction. Moreover, the temperature that is reached at the core of the cell is known to be higher than that at the surface [177]. Thus, apart from the higher pressure suffered by the inner part of the cell, this higher temperature could also have enhanced the degradation. We pointed out that the consequences of these effects would be LAM_{NE} and the corresponding increase in charge-transfer resistance (reduction of the active area for the electrochemical reaction to take place due to particle isolation caused by either SEI growth or volume changes) and in mass-transfer resistance (modified diffusion due to changes in crystal structure and porosity modification) (Table 6.1). Mass-transfer resistance was not estimated from half-cell measurements but charge-transfer resistances was. In addition, LAM at PE was also expected and, in fact, it was confirmed by ICA and post-mortem analysis. Metals dissolution and migration from PE to NE was detected in the ICP-OES test. Both metals dissolution and a surface layer that forms at

the surface of PE would have contributed to LAM_{PE}. Thus, increasing charge-transfer resistance at PE. Moreover, changes in crystal structure produced due to prolonged cycling would have also contribute to the increase in charge-transfer resistance (Table 6.1). Unfortunately, XRD data were not deeply analyzed in this study so possible variations in crystal structure were not quantified at that time.

In particular, two semicircles were found at the full-cell impedance spectra of these cells. From half-cell measurements, the semicircle at lower frequencies at the full-cell impedance spectrum, which was located around 7.75 Hz at SoC = 100 % at the EoL, was related to charge-transfer at PE, which was also located around 7.5 Hz at the same SoC and aging level (Fig. 6.1). Furthermore, the semicircle at higher frequencies was associated to the joint contribution of the SEI layer at NE and the interface between PE and current collector (Fig. 6.1). Even though it could not be appreciated in the full-cell impedance, the semicircle at higher frequencies suffered an increase during the aging process, which was confirmed in the post-mortem analysis: the resistance associated to the current collector of the PE increased due to aging. Moreover, pressure lines at PE were clearly observed during the cell opening, in which there was an evident detachment of the active material from the current collector, especially at those pressure lines. Unfortunately, the possible changes in the resistance associated to the SEI layer at the NE could not be tracked because the semicircles were all overlapped at the impedance spectra of the NE.

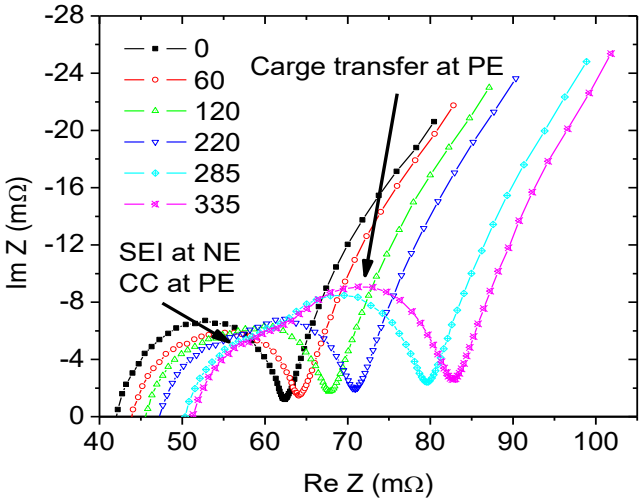

Fig. 6.1. Impedance evolution of a NMC cell at SoC = 100 % during the aging test. Different effects are associated to the positive and negative electrodes thanks to the half-cell measurements carried out during the post-mortem analysis.

During the aging process, the highest increase in resistance was related to charge transfer at PE (Fig. 6.1). Thus, confirming the impedance results previously discussed in which charge-transfer resistance was expected to increase. Specifically, after 175 – 200 cycles there was a higher increasing tendency of the charge-transfer resistance of the PE measured in the full-cell (Fig. 6.2). In particular, we associate this behavior to a change in the aging mechanism that was taking place; during the first

part of the cycling test, we considered that the main degradation mechanism was LLI due to the SEI formation but then shifted to LAM. Especially during the first 75 cycles, the relative increase in ohmic resistance was larger than that of charge-transfer resistance, which we attributed to initial SEI formation (Fig. 6.3). From that cycle on, the increasing rate of the SEI layer was assumed to be moderated because the increasing rates of R_{Ω} and R_{CT} started being equal. These increasing rates were maintained equal until cycles 175 - 200. The results suggested that during these cycles, some active material started to be lost. From ICA, we found that during the first 100 cycles, 5 % of lithium and 2.5 % of NE active material were lost. Nevertheless, from cycle 107 to the end of the test, 6.8 % of lithium, 8 % of NE active material and 1.8 % of PE active material were lost. Thus, confirming that a higher amount of active material at both electrodes started to be lost at some point after cycle 107. In the last part of the aging test (after 175 – 200 cycles were carried out), charge-transfer resistance increased faster than ohmic resistance (Fig. 6.3). Thus, it might indicate LAM was increasing in the last part of the test. It could be attributed to metals dissolution at PE and migration to NE and a formation of a surface layer at the positive electrode surface. Metals dissolution would produce a reformation of the SEI layer on the NE, which is widely known to speed up the degradation of the cells (refer to subsection 1.2.3). Moreover, the previous loss of active material at NE could also have caused lithium plating at the NE. In fact, plated lithium was observed during the cell opening. In particular, lithium plating increases the thickness of the surface layer and therefore increases the charge-transfer resistance. Furthermore, it enhances electronic conduction increasing further the SEI layer. From ICA, we found that the matching of the electrodes decreased and less NE active material compared to PE was available at the EoL. Thus, it would validate the hypothesis of lithium plating. Nevertheless, a change in the rate of capacity fade was not appreciated at low rates (Fig. 6.4). Thus, it might indicate that the contribution to capacity fade of LAM was small compared to LLI. Nevertheless, a change in the tendency of capacity fade was encountered at a discharge rate of 3C/2 (Fig. 6.5). Capacity fade increased faster during the first 50 – 75 cycles. Thus, it would coincide with the previous assumption of higher lithium consumption during these first cycles due to the initial SEI formation. However, if there was a variation in the trend of capacity fade approaching the EoL, it could not be accurately determined from Fig. 6.5. Apparently, the increase in capacity was linear from cycle 75 to the end of the test. Even though charge-transfer resistance was found to start increasing faster from cycle 175 – 200, it was not appreciated in the capacity fade at 3C/2. It might be because the limiting factor at this rate was the ohmic resistance followed by the concentration polarization term (Fig. 4.17) instead of the activation polarization term.

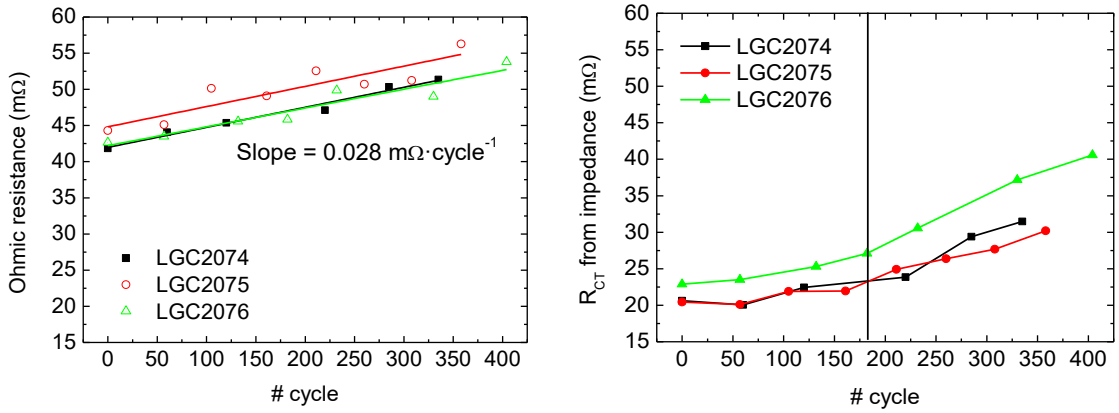

Fig. 6.2. Evolution of ohmic resistance (left) and charge-transfer resistance estimated from the real part of impedance that was covered by the measured semicircles (right) during the aging test. The line at the charge-transfer resistance graph indicates the cycle from which the charge-transfer resistance started increasing faster.

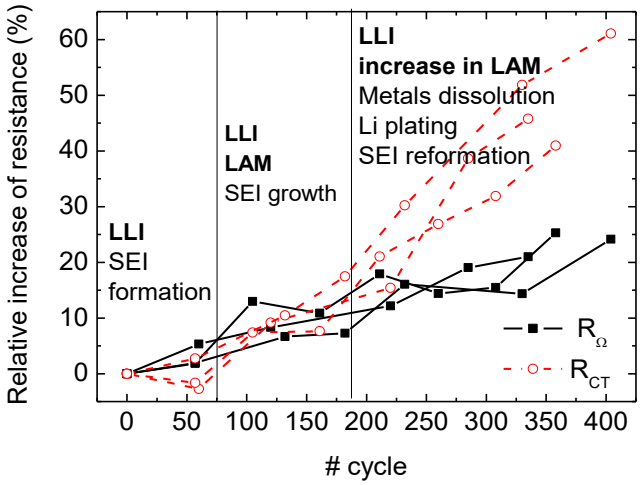

Fig. 6.3. Relative increases of R_Ω and R_{CT} of three NMC cells during the aging process and the associated degradation mechanisms.

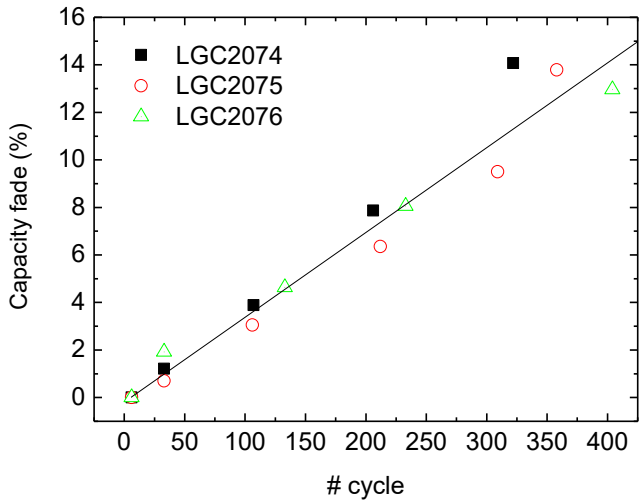

Fig. 6.4. Capacity fade of three NMC cells cycled under the same conditions evaluated at C/25 discharge rate.

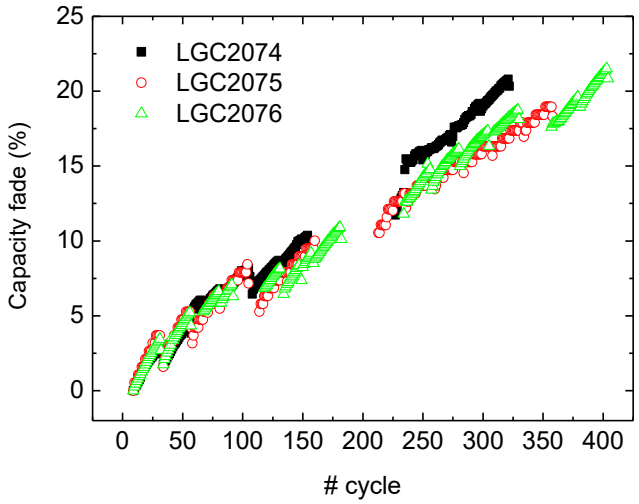

Fig. 6.5. Capacity fade of three NMC cells cycled under the same conditions evaluated at 3C/2 discharge rate.

Ohmic and charge-transfer resistances and their increases with aging were SoC-dependent. In particular, ohmic resistance contributed more to the total impedance rise than charge-transfer resistance. Moreover, during the aging test, the absolute increase in ohmic resistance was above the one of charge-transfer resistance in almost all SoC range (except at SoCs below 17 %) (Fig. 6.6), but the relative increase of charge-transfer resistance was higher in all SoCs. In particular, charge-transfer resistance suffered the highest increase around 17 % SoC. It coincided with a solid-solution phase (transition between two plateaus or phase changes) observed at the full-cell OCV voltage. Therefore, it might indicate that the charge-transfer process was slowed down at the last part of this phase change (around 17 % SoC), whereas the increase in ohmic resistance was roughly constant in all SoC range.

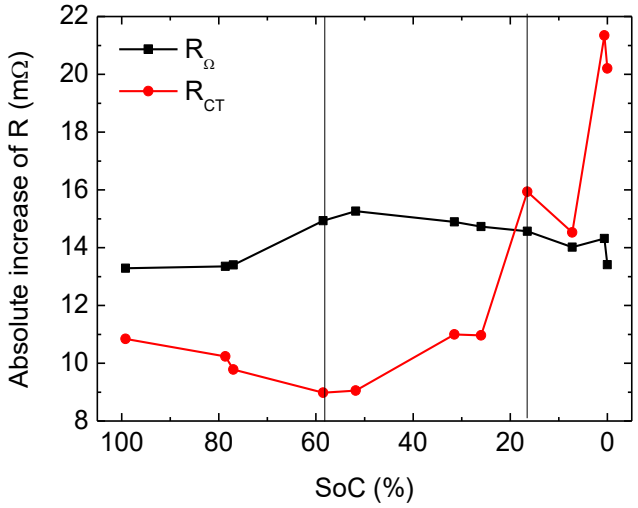

Fig. 6.6. Absolute increase in ohmic and charge-transfer resistances of a NMC cell from BoL to EoL with respect to the SoC.

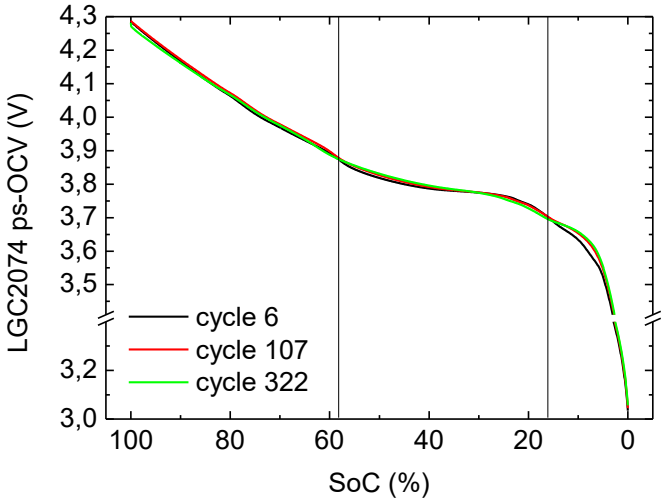

Fig. 6.7. Ps-OCV evolution of a NMC cell during the aging test at room temperature. The vertical lines represent the two easiest identifiable solid-solution phases to the eye.

From the overpotential generated during a discharge process carried out at different SoHs, the irreversible entropy production at these SoHs was estimated. In particular, it was done at C/25 and 3C/2 discharge rates (Fig. 6.8 and Fig. 6.9). In the case of low rates, the overpotential was calculated from ps-OCV and discharge GITT OCV (accounting for hysteresis) curves (Fig. 6.8). In both cases, we found that the generation rate of irreversible entropy was larger when the cells aged. This was true except at some specific SoCs in which the variation was smaller or null (SoCs around 17 % and 60 %). This SoCs corresponded to the solid-solution phases identified in Fig. 6.7. This behavior might indicate that the irreversible entropy production was dominant during the phase transformations. Moreover, the irreversible entropy production at each of those phase transformations, which can be identified as the SoCs between the vertical lines represented in the graphs, followed a particular tendency that was not altered by aging. The same behavior was found at a discharge rate of 3C/2 (Fig. 6.9). At both rates, the highest entropy production was found at SoCs below 17 %. Therefore, it indicated that during this part of the discharge more energy was lost in form of heat or in causing degradation to the cell. Unfortunately, in this study, we could not separate these two contributions although it would be interesting to do it in the future (refer to subsection 6.1).

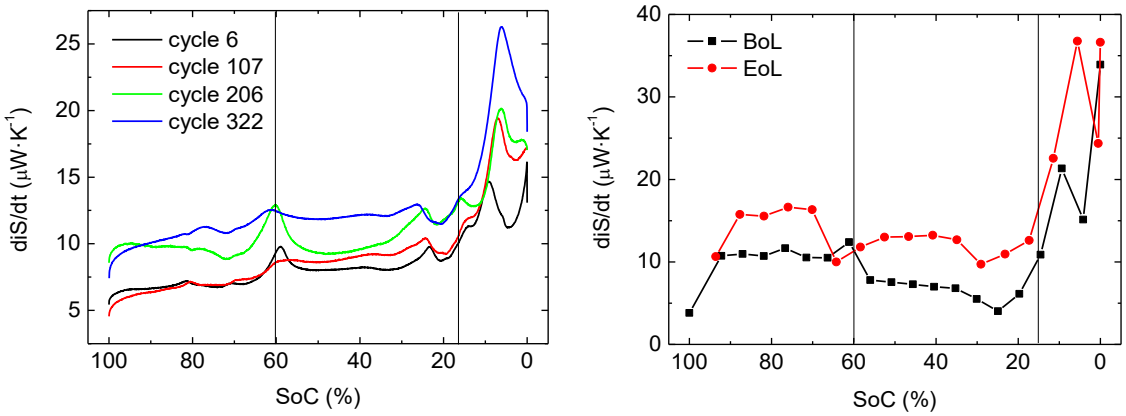

Fig. 6.8. Evolution of the irreversible entropy production in a NMC cell at a C/25 discharge rate during the aging test carried out at room temperature. It was obtained from ps-OCV (left) curves and discharge GITT OCV (right). The vertical lines represent the two easiest identifiable solid-solution phases from the OCV curves.

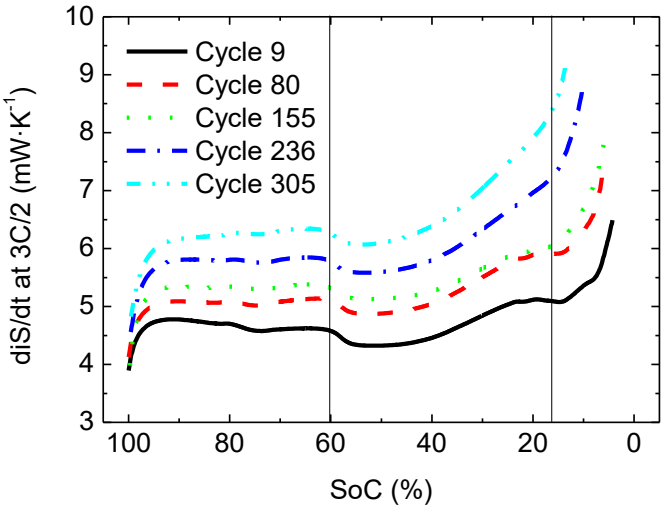

Fig. 6.9. Evolution of the irreversible entropy production in a NMC cell at a 3C/2 discharge rate during the aging test carried out at room temperature. It was obtained from ps-OCV (left) curves. The vertical lines represent the two easiest identifiable solid-solution phases from the OCV curves.

The REP corresponding to the different overpotential sources (ohmic, activation and concentration) were also calculated using equation (6.5) in the particular case of their entropy productions. It has to be noted that when we separated the different contributions, the entropy production due to degradation (d_iS_{aging}/dt) was included in the entropy production related to concentration overpotential (refer to equation (4.34)). In particular, The REP was calculated at low and moderate discharge rates (C/25 and 3C/2) (Fig. 6.10 and Fig. 6.11). At low rates, it was found that the solid-solution phases (previously identified and marked in the graphs), corresponded to a local minima in irreversible entropy production (left part of Fig. 6.10 and Fig. 6.11). This would corroborate the fact that degradation was mainly caused during the phase transformations. The SoE above 1 found in d_iS/dt can be interpreted in two ways. In the one hand, if the increase comes from the term related to heat, it would represent that the cell is more inefficient in the electrochemical

conversions and the transport process due to previous degradation. On the other hand, if the increase comes from the term related to aging, it would mean that the cell would be suffering a higher degradation at the EoL compared to BoL. However, we will not be able to distinguish both contributions. Therefore, we will discuss the results in the joint combination. In the right side of Fig. 6.10, the REP related to ohmic, activation and concentration (including the d_iS_{aging}/dt contribution) terms at C/25 were detailed. As it can be appreciated, the highest increase was found in the term related to concentration polarization between 60 % and 17 % SoCs, which corresponds to one of the identified phase tranformations. In particular, the REP related to concentration polarization and degradation was found at SoC = 25 %. At other SoCs not corresponding to this phase transition, all the contributions showed similar REPs. In addition, at SoC = 17 %, there was the maximum increase in the term related to activation overpotential, which coincided with Fig. 6.6. Moreover, the concentration term had local minima at the identified solid-solution phases.

The same analysis was carried out at a discharge rate of 3C/2 Fig. 6.11. In that case, the solid-solution phase at 60 % SoC also coincide with local minima at the increase of entropy production, especially when calculated from discharge GITT OCV. Nevertheless, at 17 % no local minima was identifiable. Contrarily to what we found at low rates, the local maxims found at REP related to concentration polarization and the aging term at 3C/2 (right part of Fig. 6.11), corresponded to the previously identified solid-solution phases. Nonetheless, the maximum increase in irreversible entropy production due to activation polarization was found at SoC = 17 % at both discharge rates.

At both discharge rates, the concentration term, which includes the irreversible entropy production due to aging (d_iS_{aging}/dt), was the one increasing more during the aging test. Therefore, or the diffusion process was the more affected by degradation (if the term d_iS_{heat}/dt related to diffusion was the one increasing more) or more energy had being used in general to degrade the cell (increase related to the term d_iS_{aging}/dt).

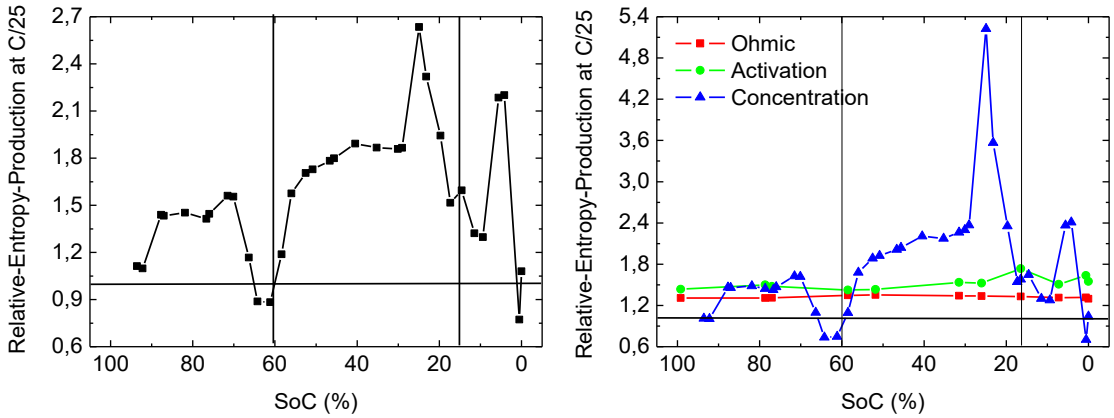

Fig. 6.10. Relative-Entropy-Production of a NMC cell at a C/25 discharge rate during the aging test carried out at room temperature (left) and REP of the various contributions to entropy production (right). It was obtained from discharge GITT OCV curves. The vertical lines represent the two easiest identifiable solid-solution phases from the OCV curves.

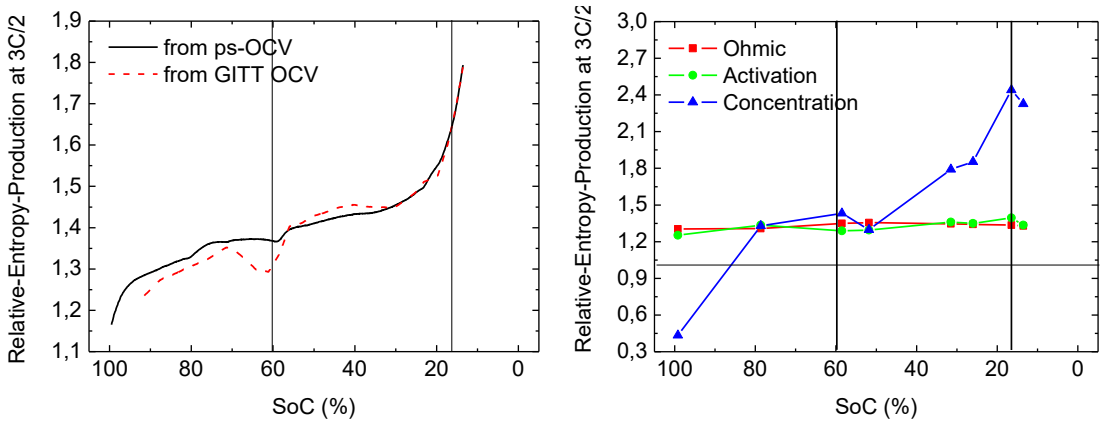

Fig. 6.11. Comparison of the Relative-Entropy-Production in a NMC cell at a 3C/2 discharge rate during the aging test carried out at room temperature calculated from ps-OCV and GITT OCV (left) and REP of the various contributions to entropy production calculated from ps-OCV (right). Vertical lines represent the two easiest identifiable solid-solution phases from the OCV curves.

If REP is evaluated at specific SoCs (15 %, 40 % and 70 % in that case) belonging to the plateaus at the OCV curves (or phase-transformation regions), an initial moderate increase is found between cycles 80 and 155 which increases sharply during subsequent cycles. It coincide with the faster increase in charge-transfer resistance and the corresponding enhanced degradation mechanism represented in Fig. 6.2 and Fig. 6.3. Thus, if REP is tracked during the cycle life of these cells, enhanced degradation could be detected.

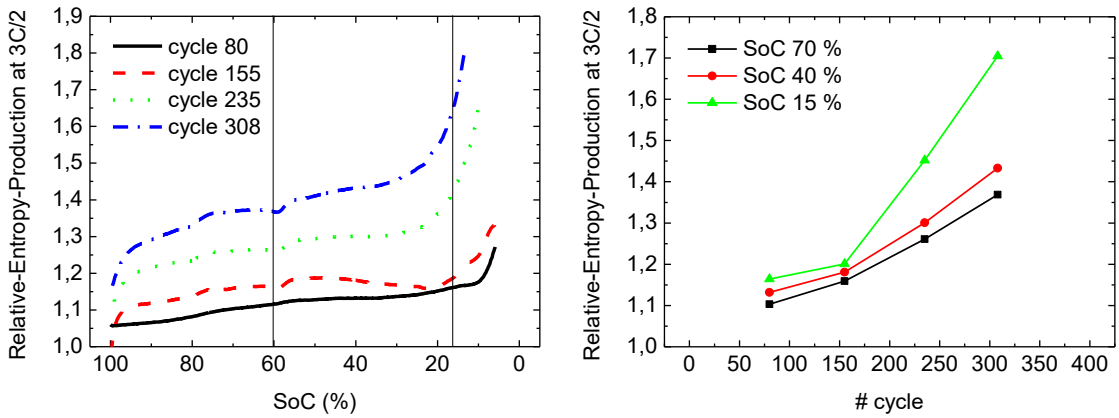

Fig. 6.12. Relative-Entropy-Production in a NMC cell at a 3C/2 discharge rate during the aging test carried out at room temperature (left) and REP during the aging test at various SoCs (right). Vertical lines represent the two easiest identifiable solid-solution phases from the OCV curves.

Finally, REP at low and high rates was compared in Fig. 6.13. As it can be appreciated, similar REP values were obtained independently of the discharge rate. If these results were validated with other chemistries and rates, it would be even more interesting to consider REP as an aging tracker.

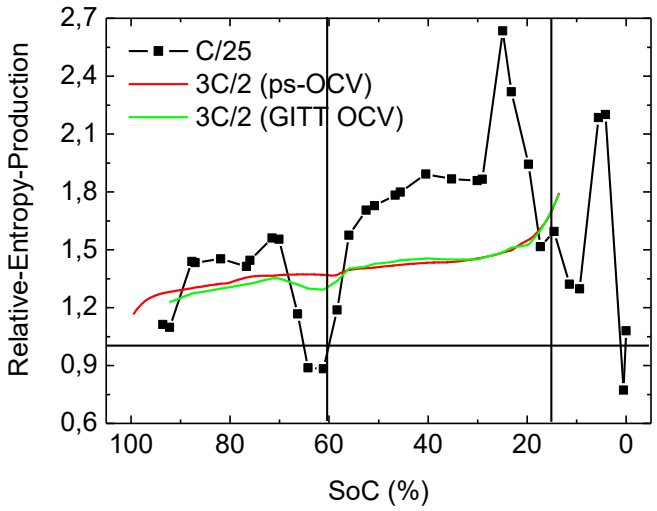

Fig. 6.13. Comparison of the Relative-Entropy-Production in a NMC cell at C/25 and 3C/2 (obtained from ps-OCV and GITT OCV curves) discharge rate during the aging test carried out at room temperature.

6.1.2. LFP cells

In this section, the irreversible entropy generation and the Relative-Entropy-Production will be evaluated for two different LFP cells (VIC and EVbat). Despite post-mortem was carried out to VIC cells, the results were not processed at this time. Thus, only capacity fade and impedance rise will be related to entropy.

6.1.2.1.VIC cells

In VIC cells, relationships between capacity fade at low (C/25) and high rates (2C) and resistance (R_{CT} + R_{MT}) rise were found (Fig. 6.14). During the first 50 cycles at 2C, the joint contribution of these resistances suffered a large decrease (bottom-right) and, at the same time, capacity fade evaluated at 2C decreased (top-right). Lithium sharing between active and passive parts of the NE was accepted as a possible cause to the capacity rise in subchapter 3.4. Nevertheless, the capacity fade at C/25 increased in that region (top-left). The evolution of ohmic resistance depicted in bottom-left part of Fig. 6.14 suggests that capacity fade at C/25 during the first 275 cycles was dominated by the increase in ohmic resistance. However, after cycle 275, in which R_{CT} + R_{MT} suffered a high increase, the capacity fade at both rates was dominated by R_{CT} + R_{MT} instead of the ohmic resistance (linear tendency with different slope than previously). Thus, around cycle 275 we assume there was a change in the main aging mechanism. Unfortunately, we have no data from the post-mortem analysis so we cannot be more specific.

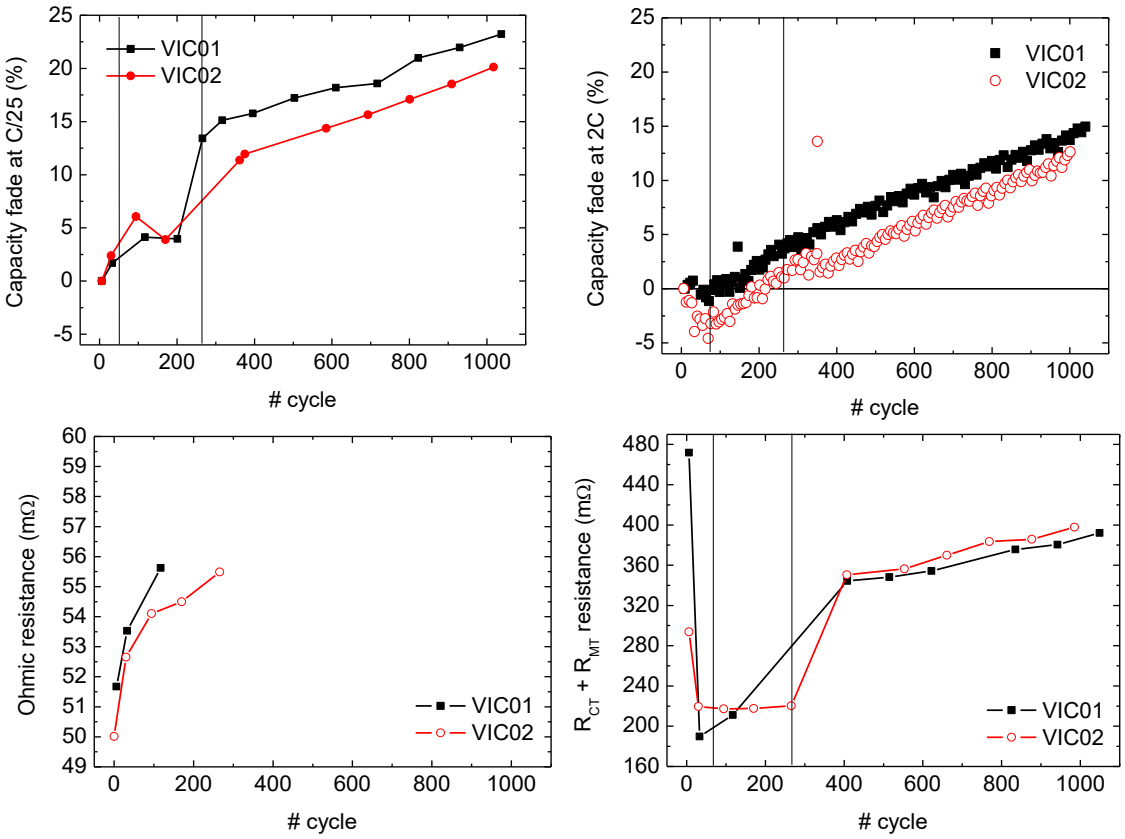

Fig. 6.14. Capacity fade of two VIC cells (LFP) evaluated at C/25 (top-left) and 2C (top-right) discharge rates and ohmic resistance (bottom-left) and joint contribution of charge-transfer and mass-transfer resistances evolution with aging (bottom-right). Vertical lines represent the cycles from which impedance and capacity changed their tendencies.

At the comparison of the OCV with aging, we appreciate that the solid-solution phases were reached sooner during the discharge process as the cells were aged (Fig. 6.15). The irreversible entropy production evolution at low rates at different SoH levels was evaluated from ps-OCV curves (which did not account for hysteresis) (Fig. 6.16) and from the discharge GITT OCV curves (Fig. 6.17). Despite the introduced error due to hysteresis, the advantage of using ps-OCV for the calculations is that intermediate cycles can be also evaluated. We observed that the generation rate of irreversible entropy decreased from BoL to around the 300th cycle from which it started to increase. In fact, this would coincide with the sharp increase in resistance represented in Fig. 6.14. At the irreversible entropy production calculated from GITT OCV (Fig. 6.17), we found a correlation with phase changes and solid solutions. At the phase changes (corresponding to plateaus at the OCV curves), irreversible entropy production increased while we found that it decreased as soon as the solid solution was formed. In addition, we also evaluated the entropy production at high rates (Fig. 6.18). It can be observed that the shape of the curve was maintained but shifted together with the formation of the solid solutions.

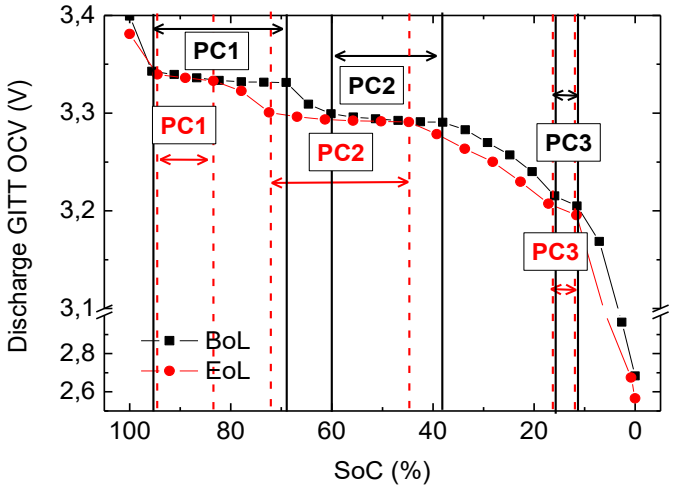

Fig. 6.15. Discharge GITT OCV evolution with aging. Vertical lines represent the two-phase domains (PCx) and the single-phase domains.

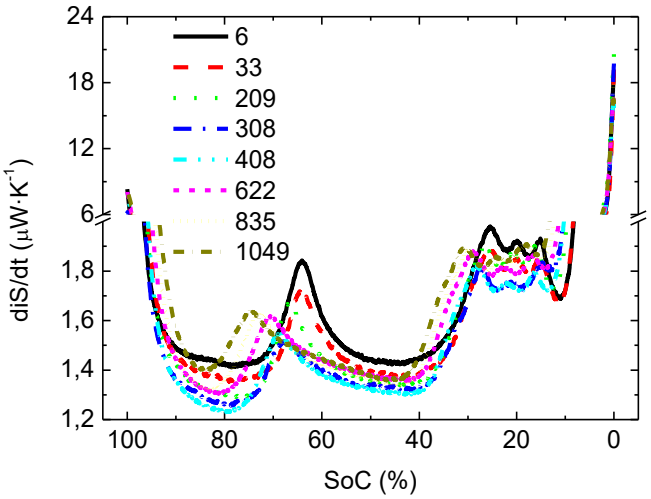

Fig. 6.16. Evolution of the irreversible entropy production in a VIC cell (LFP) evaluated at a C/25 discharge rate from ps-OCV.

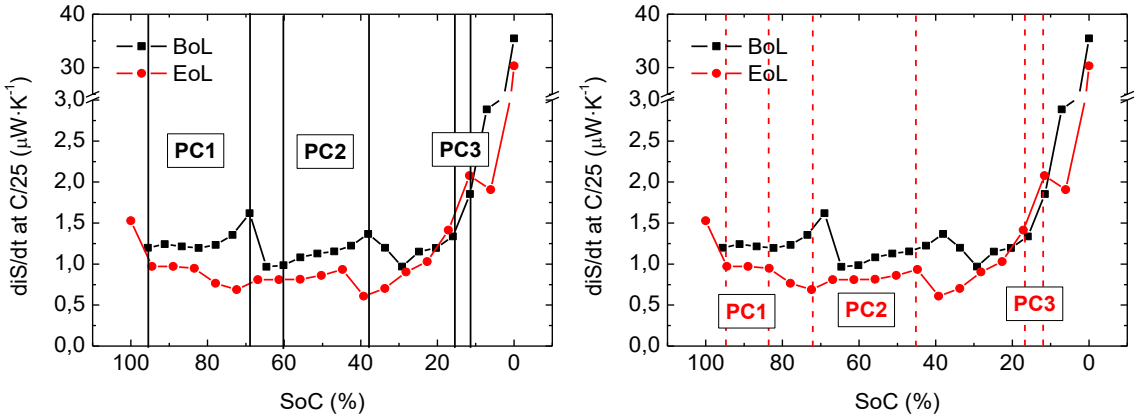

Fig. 6.17. Evolution of the irreversible entropy production in a VIC cell (LFP) evaluated at a C/25 discharge rate from discharge GITT OCV. Vertical lines represent phase changes (PCx) at BoL (left) and at EoL (right).

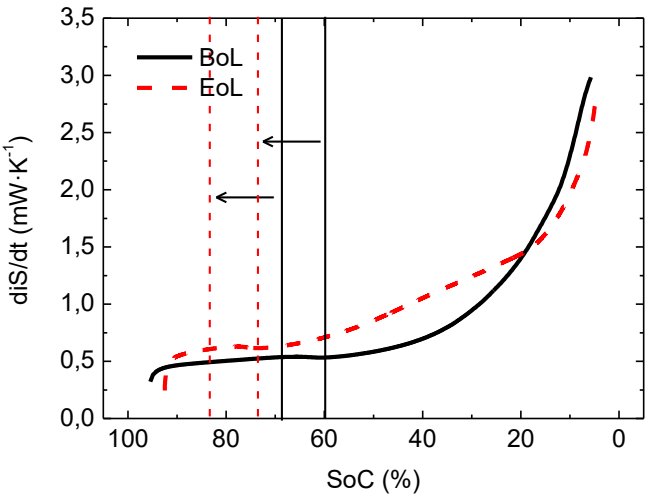

Fig. 6.18. Evolution of the irreversible entropy production in a VIC cell (LFP) evaluated at a 2C discharge rate. Black vertical lines represent intervals corresponding to solid solutions at BoL and red ones at the EoL. The arrows represent the shifting they suffered from BoL to EoL

The Relative-Entropy-Production was calculated from equation (6.5) at low (Fig. 6.19 and Fig. 6.20) and high (Fig. 6.21) discharge rates. At low rates, it was obtained from ps-OCV (Fig. 6.19) and GITT OCV (Fig. 6.20) curves. As it can be appreciated, we found that at some SoCs it stayed above 1 in the case of ps-OCV but it did not coincide with the results obtained from discharge GITT OCV in which it stayed mostly below 1. At the right side of Fig. 6.19, the increase in hysteresis from BoL to EoL was represented. The SoCs at which the hysteresis increased coincide with the SoCs at which the Relative-Entropy-Production was above 1. Thus, these values cannot be taken as valid. However, at SoCs where the increase in hysteresis was null, only an offset was introduced with respect to the results coming from GITT OCV. In Fig. 6.20, Relative-Entropy-Production was below 1 except at some particular SoCs (mostly between 20 % and 10 %) indicating that the irreversible entropy production at the EoL was below that at BoL. As we are estimating the joint contribution of the irreversible entropy production due to heat and degradation, we cannot discriminate which effect is contributing less at the EoL. However, if the entropy production evaluated at intermediate cycles (top-left part of Fig. 6.19) is checked at the SoCs in which hysteresis has not increased during the aging test (around 50 % for instance), its increasing tendency can be tracked (bottom part of Fig. 6.19). The increase in Relative-Entropy-Production after 400 cycles coincides with the increase in resistance we found around the 300th cycle. Nevertheless, charge-transfer resistance only decreased during the first 50 cycles and Relative-Entropy-Production decreased until the 400th cycle. Thus, the entropy production due to dissipation of heat should not have been decreased in those cycles. Therefore, we associated it to a decrease in the irreversible entropy production due to aging. One possible explanation could be that severe aging at a high rate is produced at the very BoL and then, this rate is reduced. In that case, a decrease in REP would be found. In addition, Relative-Entropy-

Production was also calculated at high discharge rates (Fig. 6.21). In that case, it was found to be greater than 1 in all SoCs except at the very BoD and below 20 % SoC. However, REP was found to be especially pronounced around 40 % SoC, which coincide with the change in the solid-solution phase that occurred between BoL and EoL represented in Fig. 6.15.

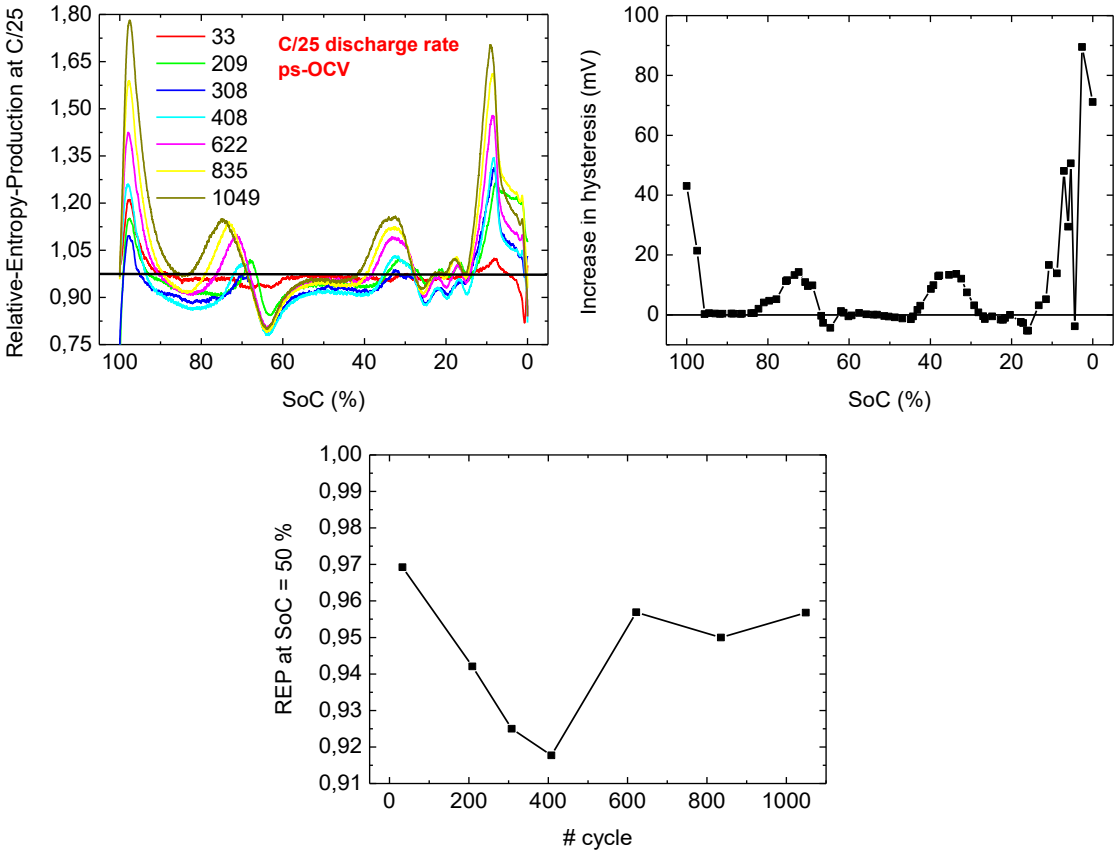

Fig. 6.19. Relative-Entropy-Production calculated from ps-OCV curves (not accounting for hysteresis) at a C/25 discharge rate (top-left) and particular values at SoC = 50 % (bottom). Increase in hysteresis during the aging test (right). Notice that in this case, REP has been calculated for the irreversible entropy production at each cycle at this particular SoC.

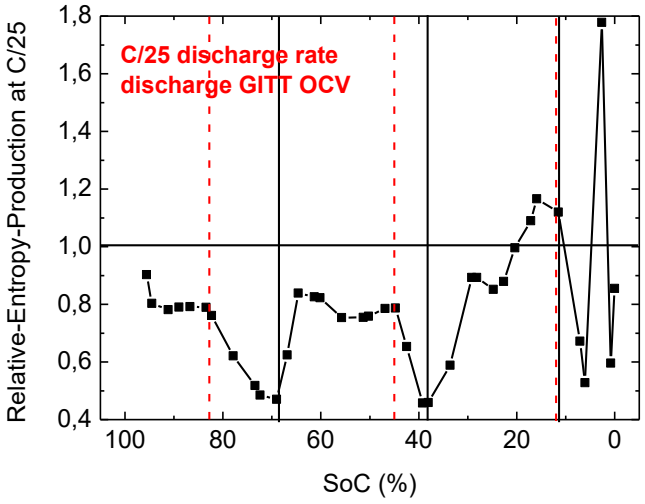

Fig. 6.20. Relative-Entropy-Production calculated from discharge GITT OCV curves at a C/25 discharge rate. Vertical lines represent the end of the plateaus and the starting point of the solid solutions at BoL (black solid line) and EoL (red dashed line).

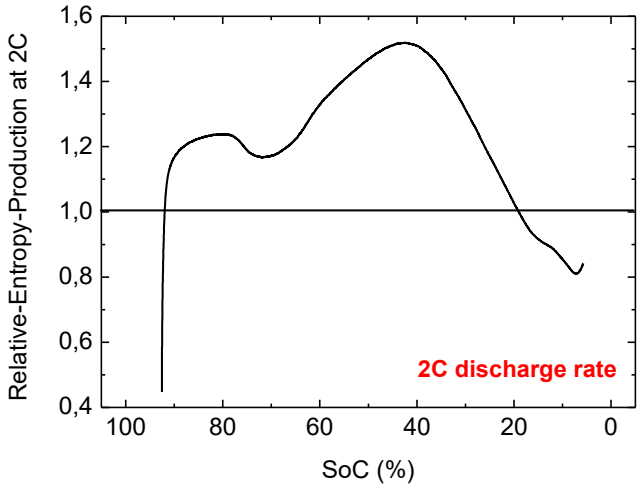

Fig. 6.21. Relative-Entropy-Production at a 2C discharge rate.

If the REP at low and high discharges rates is compared, we find that at low rates it is lower than 1 while it stayed above 1 at high rates. This was true except at SoCs below 20 %, from which REP at high rates went below 1. Similar values at both rates were found in this region.

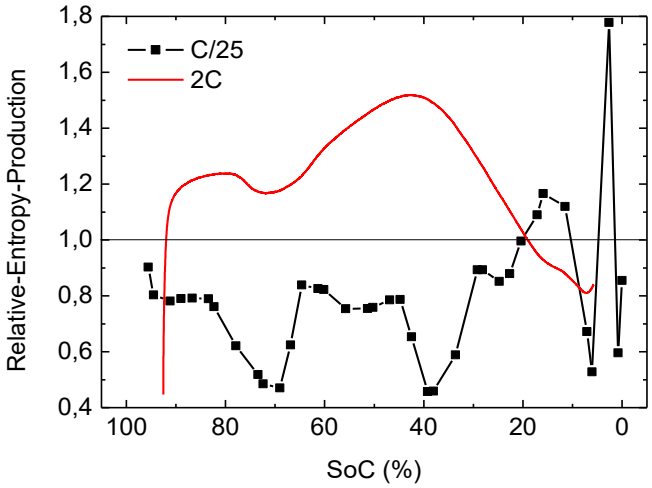

Fig. 6.22. Comparison of the Relative-Entropy-Production in a VIC cell at C/25 and 2C discharge rate during the aging test carried out at room temperature.

6.1.2.2.EVbat cells

The capacity of EVbat cells during the aging test decreased in different amounts depending on the evaluated cell during the first 6 cycles (Fig. 6.23). Unfortunetly, we did not track the impedance evolution before the 50th cycle (Fig. 6.24). Furthermore, we only measured the impedance of every cell at a particular SoH (EVbat_1 after 50 cycles, EVbat_2 after 100 cycles and EVbat_3 after 200

cycles). Thus, we could not know if their initial resistances were comparable. However, if we take the results valid and extrapolable to other cells, ohmic resistance increased linearly from cycles 50 to 200. Nonetheless, charge-transfer resistance decreased in this cycling range but it did it faster from cycles 50 to 100 than from 100 to 200. Capacity fade at 2.5C was more abrupt between cycles 50 and 100 than between 100 and 200. Nevertheless, we observed that total resistance increased faster between cycles 100 and 200. Unfortunately, we had not enough information in order to determine the causes behind these effects.

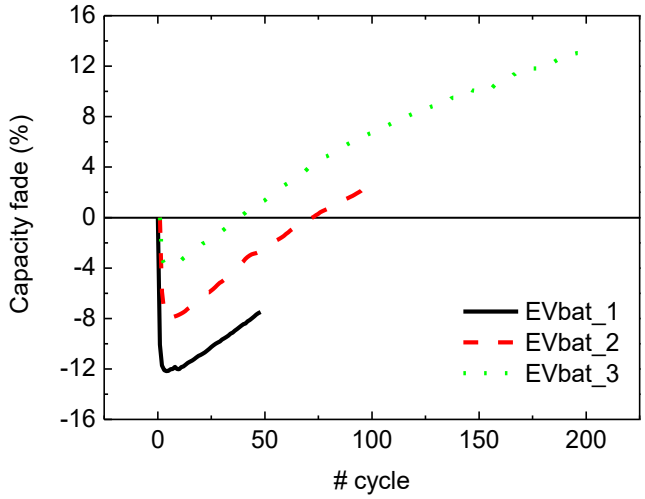

Fig. 6.23. Capacity fade of three EVbat cells (LFP) evaluated at a 2.5 C discharge rate.

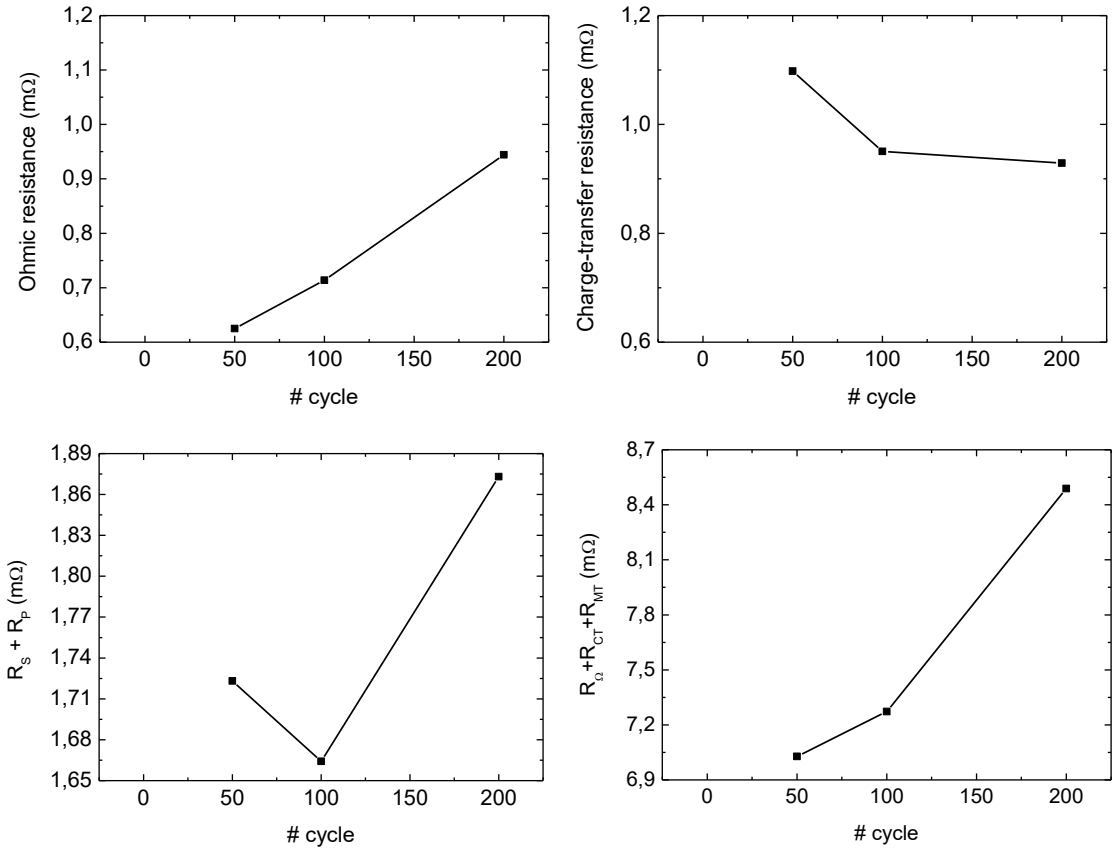

Fig. 6.24. Ohmic (top-left), charge-transfer (top-right), ohmic + charge-transfer (bottom-left) and ohmic + charge-transfer + mass-transfer (bottom-right) resistances of an EVbat cell. Mass-transfer resistance was only measured until the lowest measured frequency at the EIS, independently of the frequency at which the cell was working. Therefore, the absolute value of R_{MT} does not correspond with the actual one.

At the OCV curves measured during the aging test, the easiest plateaus or phase transformations to identify were represented (Fig. 6.25). The main difference was observed in the reduction of the highest voltage plateau from cycles 100 to 200. In addition, we found local maxima in irreversible entropy generation at the end of the plateaus (Fig. 6.26) at both BoL and EoL. Moreover, a decrease in entropy generation followed this increase. Thus, reducing the irreversible entropy production during the solid-solution phase. The same behavior was found in VIC cells, which are also LFP cells (Fig. 6.17), and LGC2 cells (Fig. 6.8), which are NMC cells. Thus, it indicated that irreversible entropy production increases towards the end of phase transformations (a possible explanation will be given in 6.1.5).

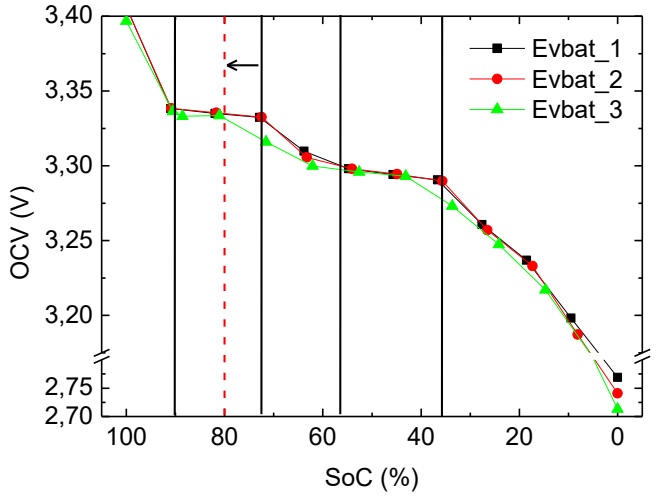

Fig. 6.25. OCV evolution with aging of three EVbat cells at room temperature. Vertical lines represent the two easiest identifiable plateaus (phase transformations). The arrow indicates the shifting of the end of the plateau at the EoL.

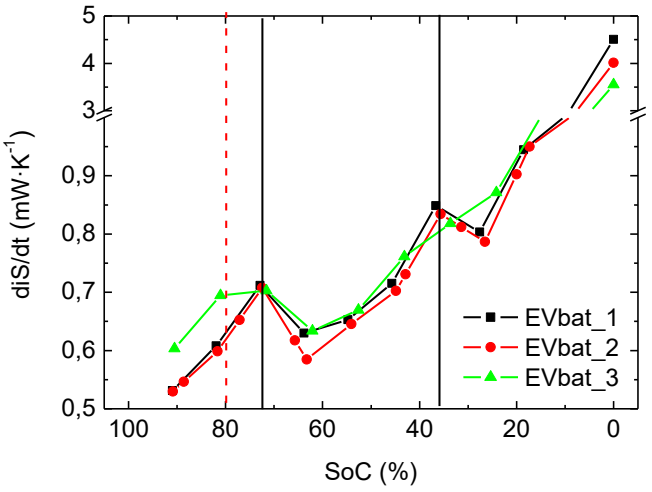

Fig. 6.26. Irreversible entropy production of three EVbat cells evaluated at a discharge rate of C/8. Vertical lines represent the end of phase transformations (in black at BoL and in red at the EoL).

Relative-Entropy-Production was calculated from equation (6.5) at a discharge rate of C/8 rate from cycles 50 to 100 and 100 to 200 (left part of Fig. 6.27). We found that it remained below 1 from cycles 50 to 100 in almost all the evaluated SoC range (except one point at SoC = 9.5 %). However, Relative-Entropy-Production was higher when evaluated at the 200th cycle. It indicated that the irreversible entropy production at BoL decreased from cycles 50 to 100. Nevertheless, it increased from cycles 100 to 200 even though the entropy generation rate at the EoL was only slightly changed from that at BoL, especially at intermediate SoCs. In addition, it can be appreciated that the SoCs corresponding to the end of the plateaus and the beginning of solid-solution phases at BoL (represented with solid vertical lines in Fig. 6.27) showed the minimum variation during the cycling test. Similar results were found in NMC cells (Fig. 6.8) and although it was not previously mentioned, the same trend was also found in VIC cells (LFP). In the SoC ranges belonging to solid-solution phases represented in Fig. 6.17, also minimum differences between entropy generation at BoL and EoL can be appreciated.

Relative-Entropy-Production related to ohmic, activation and concentration polarizations was also estimated (right part of Fig. 6.27). The highest values were found at the ohmic contribution indicating that the ohmic resistance suffered the highest degradation and therefore, it was dissipating more heat at the EoL. REP related to activation polarization was below 1 in all SoCs. Thus, less entropy production was found at the EoL indicating a faster charge-transfer process during the electrochemical reaction. Finally, REP related to concentration, specifically the joint contribution of irreversible entropy production due to heat and aging (refer to equations (6.4) and (4.34)), stayed around 1. However, the two peaks below 1 corresponded to the end of the plateaus at BoL. Values above 1 were found at SoCs above 80 %, around 30 % and at 9.5 %. From these results, we conclude that the most affected part due to aging during the cycling tes was the one associated to ohmic resistance. Some of the main effects producing this increase could be electrolyte decomposition or degradation of the separator. As these cells were charged at a very high rate (2.5 C), it probably accelerated degradation reactions due to the high temperature and possible overcharges, which mainly degrade the cathode and the SEI layer. Thus, the enhanced formation of the SEI layer at these high rates would consume more electrolyte and thus, it would validate the higher degradation in the ohmic part that we inferred from REP.

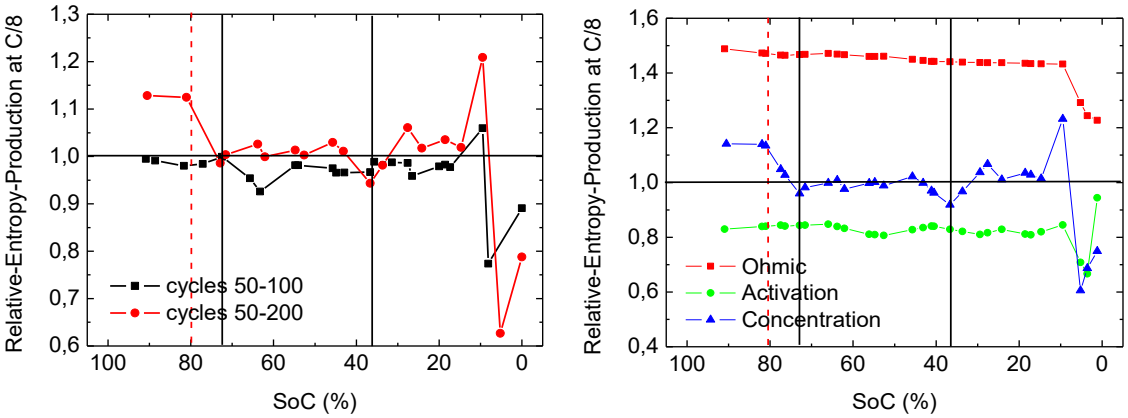

Fig. 6.27. Relative-Entropy-Production of three EVbat cells evaluated at a discharge rate of C/8. Vertical lines represent the end of phase transformations (in black at BoL and in red at the EoL).

6.1.3. LCO cells

At the OCV curves of the LCO cells, with the resolution we obtained, only one plateau could be identified from this curve (Fig. 6.28), although other plateaus were present in the curves. The irreversible entropy production at a discharge rate of 1C increased from BoL to EoL in all SoCs (Fig. 6.29). During the phase transformation, it increased at both BoL and EoL. However, outside this SoC range, no conclusions could be extracted without additional processing. In addition, the Relative-Entropy-Production of the LCO cells was obtained for a discharge rate of 1 C (Fig. 6.30). LCO cells were the first cells evaluated in this study. Thus, many uncertainties arise from the results because of the lack of knowledge about batteries at that time. Thus, non-conclusive conclusions are extracted in this case.

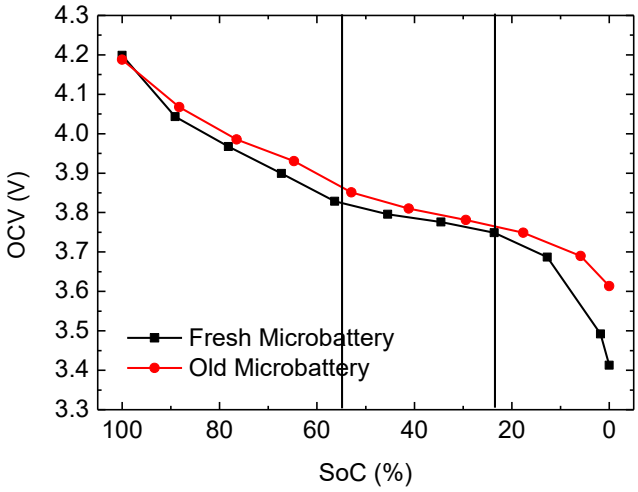

Fig. 6.28. OCV evolution with aging of a LCO cell at BoL and EoL at room temperature. Vertical lines represent the only identifiable plateau to the eye (phase transformation).

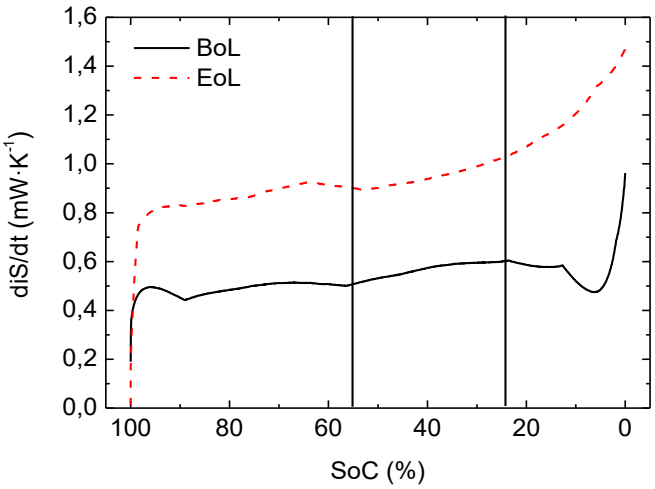

Fig. 6.29. Irreversible entropy production of the LCO cells evaluated at a discharge rate of 1C. Vertical lines represent the minimum and maximum SoC of one phase transformation.

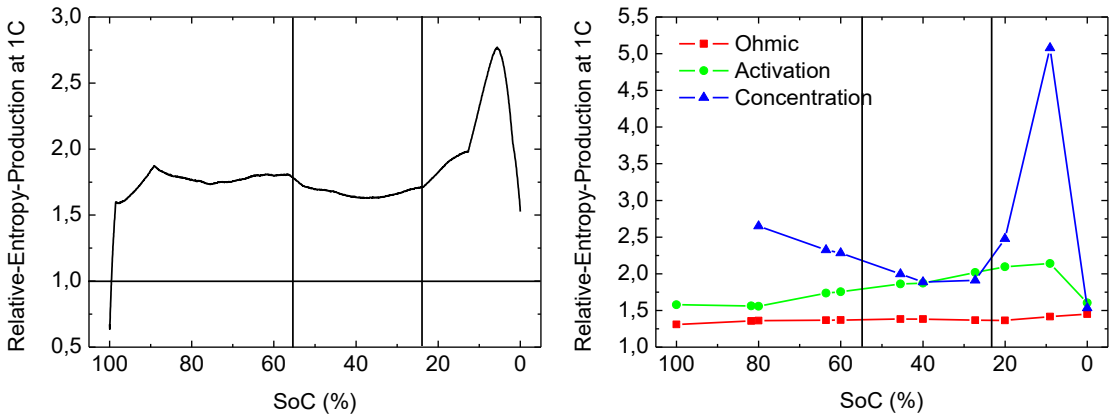

Fig. 6.30. Relative-Entropy-Production of a LCO cell evaluated at a discharge rate of 1C. Vertical lines represent the minimum and maximum SoC of one phase transformation.

6.1.4. Summary of REP evaluated in different chemistries and rates

The REP evolution with aging of the various evaluated chemistries (NMC, LFP and LCO) evaluated at different discharge rates were compared (Fig. 6.31). The results coming from EVbat and LCO cells evaluated at low rates are the most questionable results. However, all the evaluated chemistries showed comparable REP values independently of the discharge rate. This was true for all cells except LFP evaluated at low C-rates, whose REP was mostly below 1.

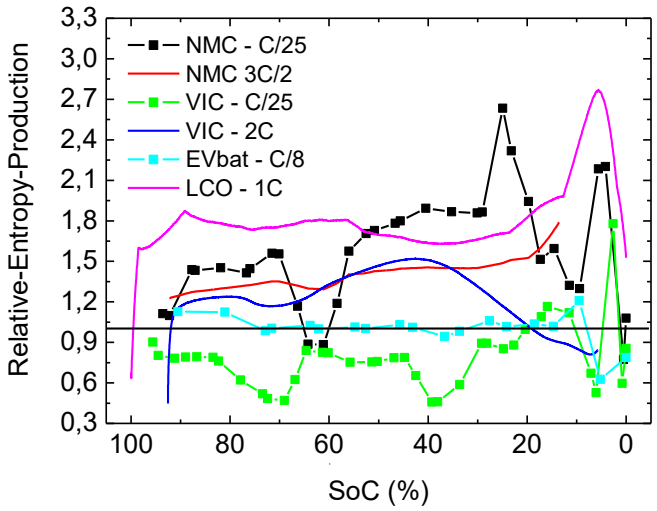

Fig. 6.31. REP of the different chemistries evaluated at different rates.

6.1.5. Increase in $di\mathcal{S}/dt$ at the end of phase transformations

In all the evaluated cells, we found a correspondence between the phase tranformations and the increase in rreversible entropy production. Concretely, the term $d_i\mathcal{S}/dt$ increased as the end of the phase transition approximated. It was controversial because reversible entropy production is known to increase during the pahase changes but we had no indea about what had to happen to the irreversible term. Nevertheless, we found in literature that reversible and irreversible heat generations follow the same tendency during the phase transformations [192]. Therefore, it would confirm the same behavior we found for the reversible and irreversible terms. A possible explanation to the increase in the irreversible term at the end of the phase transformations could be given by the fact that a material going through a phase transition expands and contracts [193]. In the particular case of Li-ion cells, this expansion or contraction is due to the Li^+ insertion/extraction from the lattice structure. This expansion and contraction of the electrodes in a repetitive cycling might produce damage to the cells if form of cracks or other structural deterioration [193].

Chapter 7

General conclusions

At this point, we can say that the hypothesis of the thesis has been validated. In our opinion, the main result of the thesis is that we have layed the foundations for a new research field. We have defined for the first time a parameter that is directly related to the exerted degradation in batteries, which is diSaging/dt. Although irreversible entropy has been used as a damage estimator in other fields, our contribution is the first experimental study about irreversible entropy production in batteries.

Finally, we list the most releavant conclusions of the thesis

Chapter 2 – On capacity fade analysis

1. The capacity of NMC cells was found to decrease during all cycling test.
2. The capacity of LFP cells increased during the initial cycles and then decreased.

Chapter 3 – On impedance and resistance analysis

3. The resistance rise with aging was SoC dependent.
4. The impedance of NMC and LCO increased with aging.
5. The impedance of LFP increased but, in particular, charge-transfer resistance decreased (at least during the first part of cycling).

6. A good approximation of EIS impedance was obtained from the FFT transforms of constant/pulsed charge/discharge profiles of a supercapacitor and the impulse response of a LCO cell.

Chapter 4 – On energetic and entropic characterization

7. OCV depended on the aging level in all the evaluated chemistries.
8. Hysteresis was dependent on the aging level.
9. Ohmic, activation and polarization contributions were separated from the total overpotential at low and high discharge rates.
10. Concentration polarization was the dominant effect at low discharge rates.
11. Ohmic contribution was the dominant effect at high rates, except for LFP cells in which concentration polarization was the major contributor.
12. In reversible entropy, great differences in the entropic coefficient between BoL and EoL were not appreciated.
13. The irreversible entropy production was calculated from the measured overpotential at different rates and aging levels.
14. At low rates, NMC cells produced irreversible entropy faster at the EoL than at BoL.
15. At low rates, VIC cells (LFP) showed first a decrease in the generation rate of irreversible entropy and then an increase during the aging process.
16. At low rates, in EVbat cells (LFP) discharged at a C/8 rate, the entropy production remained almost constant during the aging process.
17. At low rates, LCO cells increased their generation rate of irreversible entropy from BoL to EoL in all the SoC range.
18. At high rates, the irreversible entropy production was larger at the EoL than at BoL in the two evaluated cells (NMC and VIC) except at SoCs below 20 % in the case of VIC cells.
19. At high rates, the major contributors were ohmic (NMC) and concentration polarization (VIC) terms.
20. We found that the heat generation during discharge at high and low rates was exothermic in all cases except in LFP.

Chapter 5 – On post-mortem characterization of NMC cells

21. Heterogeneous pressure was detected along the electrodes during cycling.
22. The highest capacity fade was found at the inner parts of NE and PE.
23. The most relevant possible causes of capacity fade at the NE were isolation of the active material and changes in the crystal structure.

24. The most probably causes of capacity fade at PE were particle isolation, metals dissolution and changes in the crystal structure.
25. Contributions to capacity fade at the full-cell such as LLI, LAM and increase in overpotentials were quantified.

Chapter 6 – Overall discussions

26. We introduced a new parameter for system degradation characterization, the Relative-Entropy-Production or REP, defined as the irreversible entropy generation ratio at actual state and the initial state.
27. A relation was found between capacity fade and impedance rise.
28. The ongoing aging mechanisms in the NMC cells during the aging process were determined.
29. A relation between irreversible entropy production and transitions between two-phase and single-phase domains was found.
30. Local maxims in irreversible entropy production were found at the last stages of phase transformations.
31. In NMC cells, REP was below 1 at low and high rates.
32. In NMC cells and at both discharge rates, the concentration term, which includes the irreversible entropy production due to aging (d_iS_{aging}/dt), was the one increasing more during the aging test. Therefore, or the diffusion process was the more affected by degradation (if the term d_iS_{heat}/dt related to diffusion was the one increasing more) or more energy was being used in general to degrade the cell (increase related to the term d_iS_{aging}/dt).
33. Tracking REP at high rates in NMC cells during the cycle life allowed the detection of enhanced degradation.
34. In VIC cells (LFP), REP was mostly below 1 at low rates and above 1 at high rates. We associated the decrease in REP at low rates to a decrease in the irreversible entropy production due to aging.
35. It was deduced from REP that the most affected part due to aging in EVbat cells evaluated at low rates was the one associated to ohmic resistance.
36. In the SoC ranges belonging to solid-solution phases, minimum differences between entropy generation at BoL and EoL were appreciated in all the evaluated chemistries.
37. Comparable values of REP were obtained independently of the rate in the case of NMC, LFP (high rates) and LCO.

7.1. Future work

Future analysis of already available data

- Fit a model to the impedance data
- Processing data of EVbat cells at high rates
- Process data of post-mortem analysis of VIC cells
- Local entropy production from half-cells
- Entropy production during charge
- Analysis of the formation cycles
- Estimate the matching of the electrodes in NMC cells from half-cell measurements

Other approaches to be carried out

- Measure impedance at different temperatures
- Thermal impedance
- GITT OCV measurements at intermediate SoHs
- Impedance during charge
- Measurement of the dissipated heat with a calorimeter
- Measurement or estimation of the internal temperature of the cells

7.2. Research lines derived from this study

Due to the fact that batteries are complex systems that undergo many degradation mechanisms during their life cycle, we decided to evaluate the entropy production in simplier systems such resistors and capacitors. Concretely, resistors and capacitors were chosen because batteries show resistive and capacitive behavior [172,194]. In these studies, we investigated entropy evolution to characterize commercial resistor or capacitor damage, with the aim of generalizing the effects for any dissipative/capacitive system. Our objective was to demonstrate that entropy is a valuable parameter for studying resistor and capacitor deterioration, even more so than resistance and capacitance. In fact, both resistance and capacitance can increase or decrease due to degradation.

References

[1] D. Linden, T.B. Reddy, "Handbook of batteries," *McGraw-Hill*, 2001. doi:10.1016/0378-7753(86)80059-3.

[2] D.F. Warne, "Electrical Power Engineer's Handbook," *Newnes*, 2005.

[3] C. Daniel, "Materials and processing for lithium-ion batteries," *J. Miner. Met. Mater. Soc.* 60 (2008) 43–48. doi:10.1007/s11837-008-0116-x.

[4] R. Huggins, "Energy Storage," *Springer*, 2010. doi:10.1002/9781118671603.ch8.

[5] PMBL Limited, "History of the Lithium Ion Battery," (n.d.). http://www.pmbl.co.uk/blog/lithium-ion-battery-history (accessed July 2, 2017).

[6] I. Buchmann, "Basics about Batteries," (2014). http://www.cadex.com/en/batteries/basics-about-batteries (accessed July 1, 2017).

[7] Sanyo, "Types of Battery Cells; Cylindrical Cell, Button Cell, Pouch Cell," *Batter. Univ.* (2016) 1. http://batteryuniversity.com/learn/article/types_of_battery_cells (accessed July 1, 2017).

[8] I. Buchmann, "Battery packaging - a look at old and new systems," (n.d.). http://batteryuniversity.com/learn/article/battery_packaging_a_look_at_old_and_new_systems (accessed July 1, 2017).

[9] MTI Corp, "Find Crystal by Application," (2013) 2013. http://www.mtixtl.com/ (accessed July 1, 2017).

[10] CNET, "International Battery expands for utility storage," (n.d.). https://www.cnet.com/news/international-battery-expands-for-utility-storage/ (accessed July 1, 2017).

[11] P. Taheri, A. Mansouri, B. Schweitzer, M. Yazdanpour, M. Bahrami, "Electrical Constriction Resistance in Current Collectors of Large-Scale Lithium-Ion Batteries," *J. Electrochem. Soc.* 160 (2013) A1731–A1740. doi:10.1149/2.041310jes.

[12] M.M. Doeff, Battery Cathodes, in: Encycl. Sustain. Sci. Technol., 2013: pp. 5–49. doi:10.1007/978-1-4419-0851-3.

[13] B. Isidor, "Types of Lithium-ion Batteries – Battery University," *Cadex Electron. Inc.* (2016) 1–16. http://batteryuniversity.com/learn/article/types_of_lithium_ion (accessed July 1, 2017).

[14] J.N. Illig, Physically based Impedance Modelling of Lithium-ion Cells, KIT Scientific Publishing, 2014. doi:10.5445/KSP/1000042281.

[15] C.D. Rahn, C.-Y. Wang, "Battery Systems Engineering," 2013. doi:10.1002/9781118517048.

[16] J.S. Newman, K. Thomas-Alyea, "Electrochemical systems," *J. Wiley*, 2004.

[17] J.B. Gerschler, D.U. Sauer, "Investigation of open-circuit-voltage behaviour of lithium-ion batteries with various cathode materials under special consideration of voltage equalisation phenomena," *24th Int. Batter. Hybrid Fuel Cell Electr. Veh. Symp. Exhib. 2009, EVS 24*. 3 (2009) 1550–1563.

[18] M. Heβ, "Kinetics and stage transitions of graphite for lithium-ion batteries," 2013.

doi:10.3929/ethz-a-010000442.

[19] "Does-the-voltage-of-a-Li-Ion-get-lower-as-it-discharges," (n.d.). https://www.quora.com/Does-the-voltage-of-a-Li-Ion-get-lower-as-it-discharges.

[20] "AN023 | Richtek Technology," (n.d.). http://www.richtek.com/en/Design Support/Technical Document/AN023 (accessed July 11, 2017).

[21] I.H. Buchberger, Electrochemical and structural investigations on lithium-ion battery materials and related degradation processes, 2016. https://mediatum.ub.tum.de/doc/1311652/1311652.pdf (accessed May 31, 2017).

[22] B. Saha, P. Quach, K. Goebel, "Exploring the model design space for battery health management," *Annu. Conf. Progn. Heal. Manag. Soc.* (2011) 1–8.

[23] J.-K. Park, "Principles and Applications of Lithium Secondary Batteries," *Wiley-VCH*, 2013.

[24] V.R. Stamenkovic, B. Fowler, B.S. Mun, G. Wang, P.N. Ross, C. a Lucas, N.M. Marković, C. Song, Y. Tang, J. Lu, J. Zhang, H. Wang, J. Shen, S. Mcdermid, J. Li, P. Kozak, P. Pietrasz, B. Orr, T. Simes, A. Staff, S. Daniel, C. Lim, "III . Reaction Kinetics Lecture 1 3 : Butler-Volmer equation," *Science.* 315 (2007) 493–7. doi:10.1016/j.electacta.2006.09.008.

[25] M.V. Tibor Erdey-Grúz, "Zeitschrift für physikalische Chemie, Abteilung A, Chemische Thermodynamik, Kinetik, Elektrochemie, Eigenschaftslehre," 1930. http://wikivisually.com/lang-de/wiki/Butler-Volmer-Gleichung (accessed May 15, 2017).

[26] E.J. Calvo, The Current-Potential Relationship, in: Encycl. Electrochem., *Wiley-VCH Verlag GmbH & Co. KGaA*, Weinheim, Germany, 2007: pp. 3–30. doi:10.1002/9783527610426.bard020101.

[27] P. Liu, J. Wang, J. Hicks-Garner, E. Sherman, S. Soukiazian, M. Verbrugge, H. Tataria, J. Musser, P. Finamore, "Aging Mechanisms of $LiFePO_4$ Batteries Deduced by Electrochemical and Structural Analyses," *J. Electrochem. Soc.* 157 (2010) A499. doi:10.1149/1.3294790.

[28] Y. Gao, J. Jiang, C. Zhang, W. Zhang, Z. Ma, Y. Jiang, "Lithium-ion battery aging mechanisms and life model under different charging stresses," *J. Power Sources.* 356 (2017) 103–114. doi:10.1016/j.jpowsour.2017.04.084.

[29] C. Lin, A. Tang, H. Mu, W. Wang, C. Wang, "Aging mechanisms of electrode materials in lithium-ion batteries for electric vehicles," *J. Chem.* (2015) 1–11. doi:10.1155/2015/104673.

[30] M. Broussely, "Aging Mechanisms and Calendar-Life Predictions in Lithium-Ion Batteries," *Adv. Lithium-Ion Batter.* (2002) 293–432. doi:10.1007/0-306-47508-1_14.

[31] J. Groot, State-of-health estimation of Li-ion batteries: cycle life test methods, Chalmers University of Technology, 2012.

[32] T. Waldmann, M. Wilka, M. Kasper, M. Fleischhammer, M. Wohlfahrt-Mehrens, "Temperature dependent ageing mechanisms in Lithium-ion batteries – A Post-Mortem study," *J. Power Sources.* 262 (2014) 129–135. doi:10.1016/j.jpowsour.2014.03.112.

[33] R. Arunachala, K. Makinejad, S. Athlekar, A. Jossen, J. Garche, Cycle life characterisation of

large format lithium-ion cells, in: 2013 World Electr. Veh. Symp. Exhib. EVS 2014, 2014. doi:10.1109/EVS.2013.6914865.

[34] E. Prada, D. Di Domenico, Y. Creff, J. Bernard, V. Sauvant-moynot, F. Huet, "A Simplified Electrochemical and Thermal Aging Model of $LiFePO_4$-Graphite Li-ion Batteries : Power and Capacity Fade Simulations," *J. Electrochem. Soc.* 160 (2013) A616–A628. doi:10.1149/2.053304jes.

[35] J. Vetter, P. Novák, M.R. Wagner, C. Veit, K.C. Möller, J.O. Besenhard, M. Winter, M. Wohlfahrt-Mehrens, C. Vogler, A. Hammouche, "Ageing mechanisms in lithium-ion batteries," *J. Power Sources*. 147 (2005) 269–281. doi:10.1016/j.jpowsour.2005.01.006.

[36] K. Jalkanen, J. Karppinen, L. Skogström, T. Laurila, M. Nisula, K. Vuorilehto, "Cycle aging of commercial NMC/graphite pouch cells at different temperatures," *Appl. Energy*. 154 (2015) 160–172. doi:10.1016/j.apenergy.2015.04.110.

[37] E. Sarasketa-Zabala, F. Aguesse, I. Villarreal, L.M. Rodriguez-Martinez, C.M. López, P. Kubiak, "Understanding lithium inventory loss and sudden performance fade in cylindrical cells during cycling with deep-discharge steps," *J. Phys. Chem. C.* 119 (2015) 896–906. doi:10.1021/jp510071d.

[38] E. Ignatev, Performance Degradation Modelling and Techno-Economic Analysis of Lithium-Ion Battery Energy, Lappeenranta University of Technology, 2016.

[39] S.J. An, J. Li, C. Daniel, D. Mohanty, S. Nagpure, D.L. Wood, "The state of understanding of the lithium-ion-battery graphite solid electrolyte interphase (SEI) and its relationship to formation cycling," *Carbon N. Y.* 105 (2016) 52–76. doi:10.1016/j.carbon.2016.04.008.

[40] R. Fu, S.Y. Choe, V. Agubra, J. Fergus, "Development of a physics-based degradation model for lithium ion polymer batteries considering side reactions," *J. Power Sources*. 278 (2015) 506–521. doi:10.1016/j.jpowsour.2014.12.059.

[41] Z. Li, J. Huang, B.Y. Liaw, J. Zhang, "On state-of-charge determination for lithium-ion batteries," *J. Power Sources*. 348 (2017) 281–301. doi:10.1016/j.jpowsour.2017.03.001.

[42] W.-Y. Chang, "The State of Charge Estimating Methods for Battery: A Review," *ISRN Appl. Math.* 2013 (2013) 1–7. doi:10.1155/2013/953792.

[43] M. Murnane, A. Ghazel, "A Closer Look at State of Charge (SOC) and State of Health (SOH) Estimation Techniques for Batteries," n.d. http://www.analog.com/media/en/technical-documentation/technical-articles/A-Closer-Look-at-State-Of-Charge-and-State-Health-Estimation-Techniques-....pdf (accessed July 3, 2017).

[44] S. Piller, M. Perrin, A. Jossen, "Methods for state-of-charge determination and their applications," *J. Power Sources*. 96 (2001) 113–120. doi:10.1016/S0378-7753(01)00560-2.

[45] W. Waag, C. Fleischer, D.U. Sauer, "Critical review of the methods for monitoring of lithium-ion batteries in electric and hybrid vehicles," *J. Power Sources*. 258 (2014) 321–339. doi:10.1016/j.jpowsour.2014.02.064.

[46] L. Lu, X. Han, J. Li, J. Hua, M. Ouyang, "A review on the key issues for lithium-ion battery management in electric vehicles," *J. Power Sources.* 226 (2013) 272–288. doi:10.1016/j.jpowsour.2012.10.060.

[47] V. Pop, "Battery management systems : accurate state-of-charge indication for battery powered applications," *Springer*, 2008.

[48] C.R. Birkl, E. McTurk, M.R. Roberts, P.G. Bruce, D.A. Howey, "A Parametric Open Circuit Voltage Model for Lithium Ion Batteries," *J. Electrochem. Soc.* 162 (2015) A2271–A2280. doi:10.1149/2.0331512jes.

[49] T. Waldmann, A. Iturrondobeitia, M. Kasper, N. Ghanbari, F. Aguesse, E. Bekaert, L. Daniel, S. Genies, I.J. Gordon, M.W. Löble, E. De Vito, M. Wohlfahrt-Mehrens, "Review—Post-Mortem Analysis of Aged Lithium-Ion Batteries: Disassembly Methodology and Physico-Chemical Analysis Techniques," *J. Electrochem. Soc.* 163 (2016) A2149–A2164. doi:10.1149/2.1211609jes.

[50] M. Petzl, M. Kasper, M.A. Danzer, "Lithium plating in a commercial lithium-ion battery - A low-temperature aging study," *J. Power Sources.* 275 (2015) 799–807. doi:10.1016/j.jpowsour.2014.11.065.

[51] M. Berecibar, I. Gandiaga, I. Villarreal, N. Omar, J. Van Mierlo, P. Van Den Bossche, "Critical review of state of health estimation methods of Li-ion batteries for real applications," *Renew. Sustain. Energy Rev.* 56 (2016) 572–587. doi:10.1016/j.rser.2015.11.042.

[52] M. Landi, G. Gross, "Measurement techniques for online battery state of health estimation in vehicle-to-grid applications," *IEEE Trans. Instrum. Meas.* 63 (2014) 1224–1234. doi:10.1109/TIM.2013.2292318.

[53] J. Jiang, C. (Chemist) Zhang, "Fundamentals and applications of lithium-ion batteries in electric drive vehicles," n.d.

[54] J. Garche, C.K. Dyer, "Encyclopedia of electrochemical power sources," *Academic Press*, 2009.

[55] G. Lacey, G. Putrus, A. Salim, The use of second life electric vehicle batteries for grid support, in: EUROCON, 2013 IEEE, 2013: pp. 1255–1261. doi:10.1109/EUROCON.2013.6625141.

[56] V. Pop, H.J. Bergveld, P.H.L. Notten, P.P.L. Regtien, "State-of-the-art of battery state-of-charge determination," *Meas. Sci. Technol.* 16 (2005) R93–R110. doi:10.1088/0957-0233/16/12/R01.

[57] M. Dubarry, V. Svoboda, R. Hwu, B.Y. Liaw, "Capacity and power fading mechanism identification from a commercial cell evaluation," *J. Power Sources.* 165 (2007) 566–572. doi:10.1016/j.jpowsour.2006.10.046.

[58] M. Dubarry, V. Svoboda, R. Hwu, B.Y. Liaw, "Capacity loss in rechargeable lithium cells during cycle life testing: The importance of determining state-of-charge," *J. Power Sources.* 174 (2007) 1121–1125. doi:10.1016/j.jpowsour.2007.06.185.

[59] V. García Fernández, C. Blanco Viejo, D. Anseán González, M. González Vega, Y. Fernández

Pulido, J. Alvarez Antón, "Thermal Analysis of a Fast Charging Technique for a High Power Lithium-Ion Cell," *Batteries*. 2 (2016) 32. doi:10.3390/batteries2040032.

[60] A.J. Bard, L.R. Faulkner, "Elecrochemical Methods : Fundamentals and Applications," *Wiley*, 1980.

[61] A. Rahmoun, M. Loske, A. Rosin, Determination of the impedance of Lithium-Ion batteries using methods of digital signal processing, in: Energy Procedia, 2014: pp. 204–213. doi:10.1016/j.egypro.2014.01.174.

[62] E. Barsoukov, S.H. Ryu, H. Lee, "A novel impedance spectrometer based on carrier function Laplace-transform of the response to arbitrary excitation," *J. Electroanal. Chem.* 536 (2002) 109–122. doi:10.1016/S0022-0728(02)01209-3.

[63] M. Nakayama, K. Fukuda, Y. Ohmori, K. Wakahara, T. Araki, K. Onda, "Battery Impedance Measurement by Laplace Transformation of Charge or Discharge Current/Voltage," *IEEJ Trans. Power Energy*. 125 (2005) 1279–1286. doi:10.1541/ieejpes.125.1279.

[64] J.R. Macdonald, W.B. Johnson, Fundamentals of Impedance Spectroscopy, in: Impedance Spectrosc. Theory, Exp. Appl. Second Ed., *John Wiley & Sons, Inc.*, Hoboken, NJ, USA, 2005: pp. 1–26. doi:10.1002/0471716243.ch1.

[65] Gamry Instruments, "Basics of EIS: Electrochemical Research-Impedance," (2016). https://www.gamry.com/application-notes/EIS/basics-of-electrochemical-impedance-spectroscopy/ (accessed May 7, 2017).

[66] D. Hilmiye, "Impedimetric Biosensors for Label-Free and Enzymless Detection," *State Art Biosens. - Gen. Asp.* (2013) 360. doi:10.5772/45832.

[67] K. Sangüesa, "Determinació de la càrrega de bateries i condensadors mitjançant mesures d'impedància," *Master Thesis*. (2015).

[68] M. Schoenleber, A. Weber, E. Ivers-Tiffée, "Obtaining the Low Frequency Impedance of Li-Ion Batteries from Arbitrary Excitation Signals," *Meet. Abstr.* MA2014-04 (2014) 719.

[69] D.A. Howey, P.D. Mitcheson, V. Yufit, G.J. Offer, N.P. Brandon, "Online measurement of battery impedance using motor controller excitation," *IEEE Trans. Veh. Technol.* 63 (2014) 2557–2566. doi:10.1109/TVT.2013.2293597.

[70] M. Neumann-Spallart, M. Etman, "Calculation of impedance spectra by Laplace transformation of voltage transients generated by current-step excitation," *J. Electroanal. Chem.* 372 (1994) 33–37. doi:10.1016/0022-0728(93)03265-Q.

[71] M. Wickert, "10 Signals and Systems Properties You Never Want to Forget," (n.d.). http://www.dummies.com/education/science/science-engineering/10-signals-and-systems-properties-you-never-want-to-forget/ (accessed June 16, 2017).

[72] A. Cuadras, V.J. Ovejas, Supercapacitor impedance in time and frequency domains, in: Int. Multi-Conference Syst. Signals Devices, SSD 2012, *IEEE*, 2012: pp. 1–6. doi:10.1109/SSD.2012.6198096.

[73] B. Sanchez, G. Vandersteen, R. Bragos, J. Schoukens, "Optimal multisine excitation design for broadband electrical impedance spectroscopy," *Meas. Sci. Technol.* 22 (2011) 115601. doi:10.1088/0957-0233/22/11/115601.

[74] Y. Zheng, K. Qian, D. Luo, Y. Li, Q. Lu, B. Li, Y.-B. He, X. Wang, J. Li, F. Kang, "Influence of over-discharge on the lifetime and performance of $LiFePO_4$/graphite batteries," *RSC Adv.* 6 (2016) 30474–30483. doi:10.1039/C6RA01677D.

[75] Gamry Instruments, "Physical Electrochemistry and Equivalent Circuit Elements," (n.d.). http://mmrc.caltech.edu/Gamry/manuals/Gamry-EIS-Part-2.pdf (accessed June 16, 2017).

[76] X. Feng, "Nanocarbons for Advanced Energy Storage," Volume 1, 2015.

[77] H. Helmholtz, "Ueber einige Gesetze der Vertheilung elektrischer Ströme in körperlichen Leitern mit Anwendung auf die thierisch- elektrischen Versuche," *Ann. Phys.* 165 (1853) 211–233. doi:10.1002/andp.18531650603.

[78] K. Smith, C.Y. Wang, "Solid-state diffusion limitations on pulse operation of a lithium ion cell for hybrid electric vehicles," *J. Power Sources.* 161 (2006) 628–639. doi:10.1016/j.jpowsour.2006.03.050.

[79] C. Lim, "Warburg Impedance," (2011). https://ocw.mit.edu/courses/chemical-engineering/10-626-electrochemical-energy-systems-spring-2014/lecture-notes/MIT10_626S14_S11lec20.pdf (accessed June 16, 2017).

[80] Bio-Logic, "EIS measurements : Potentio (PEIS) or Galvano (GEIS) mode , that is the question," (2013).

[81] Gamry Instruments, "EIS - Potentiostatic or Galvanostatic Mode," (n.d.). https://www.gamry.com/application-notes/EIS/eis-potentiostatic-galvanostatic-mode/ (accessed July 12, 2017).

[82] P.J. Osswald, S. V. Erhard, A. Noel, P. Keil, F.M. Kindermann, H. Hoster, A. Jossen, "Current density distribution in cylindrical Li-Ion cells during impedance measurements," *J. Power Sources.* 314 (2016) 93–101. doi:10.1016/j.jpowsour.2016.02.070.

[83] C. Heubner, M. Schneider, A. Michaelis, "Investigation of charge transfer kinetics of Li-Intercalation in $LiFePO_4$," *J. Power Sources.* 288 (2015) 115–120. doi:10.1016/j.jpowsour.2015.04.103.

[84] J.P. Schmidt, T. Chrobak, M. Ender, J. Illig, D. Klotz, E. Ivers-Tiffée, "Studies on $LiFePO_4$ as cathode material using impedance spectroscopy," *J. Power Sources.* 196 (2011) 5342–5348. doi:10.1016/j.jpowsour.2010.09.121.

[85] W. Waag, S. Käbitz, D.U. Sauer, "Experimental investigation of the lithium-ion battery impedance characteristic at various conditions and aging states and its influence on the application," *Appl. Energy.* 102 (2013) 885–897. doi:10.1016/j.apenergy.2012.09.030.

[86] A. Barai, W.D. Widanage, J. Marco, A. McGordon, P. Jennings, "A study of the open circuit voltage characterization technique and hysteresis assessment of lithium-ion cells," *J. Power*

Sources. 295 (2015) 99–107. doi:10.1016/j.jpowsour.2015.06.140.

[87] B. Stiaszny, J.C. Ziegler, E.E. Krauß, J.P. Schmidt, E. Ivers-Tiffée, "Electrochemical characterization and post-mortem analysis of aged $LiMn_2O_4$-$Li(Ni_{0.5}Mn_{0.3}Co_{0.2})O_2$/graphite lithium ion batteries. Part I: Cycle aging," *J. Power Sources*. 251 (2014) 439–450. doi:10.1016/j.jpowsour.2013.11.080.

[88] J. Costard, M. Ender, M. Weiss, E. Ivers-Tiffée, "Three-Electrode Setups for Lithium-Ion Batteries," *J. Electrochem. Soc.* 164 (2017) A80–A87. doi:10.1149/2.0241702jes.

[89] H. Zheng, Q. Qu, G. Zhu, G. Liu, V.S. Battaglia, H. Zheng, "Quantitative Characterization of the Surface Evolution for $LiNi_{0.5}Co_{0.2}Mn_{0.3}O_2$/Graphite Cell during Long-Term Cycling," *ACS Appl. Mater. Interfaces*. 9 (2017) acsami.7b00427. doi:10.1021/acsami.7b00427.

[90] D.A. Howey, V. Yufit, P.D. Mitcheson, G.J. Offer, N.P. Brandon, "Impedance measurement for advanced battery management systems," *2013 World Electr. Veh. Symp. Exhib.* (2013) 1–7. doi:10.1109/EVS.2013.6914960.

[91] L. Lam, A Practical Circuit-based Model for State of Health Estimation of Li-ion Battery Cells in Electric Vehicles, 2011. doi:10.1109/INTLEC.2011.6099803.

[92] E.U. Franck, R.A. Robinson, R.H. Stokes, "Electrolyte Solutions: The Measurement and Interpretation of Conductance, Chemical Potential and Diffusion in Solutions of Simple Electrolytes. 2e Ed.(rev.).," *Butterworths*, 1968. doi:10.1002/ange.19600721222.

[93] S.S. Zhang, K. Xu, T.R. Jow, EIS study on the formation of solid electrolyte interface in Li-ion battery, in: Electrochim. Acta, 2006: pp. 1636–1640. doi:10.1016/j.electacta.2005.02.137.

[94] J. Illig, T. Chrobak, D. Klotz, E. Ivers-Tiffée, "Evaluation of the Rate Determining Processes for LiFePO 4 as Cathode Material in Lithium-Ion-Batteries," *ECS Trans.* 33 (2011) 3–15. doi:10.1149/1.3564865.

[95] C. Uhlmann, J. Illig, M. Ender, R. Schuster, E. Ivers-Tiffée, "In situ detection of lithium metal plating on graphite in experimental cells," *J. Power Sources*. 279 (2015) 428–438. doi:10.1016/j.jpowsour.2015.01.046.

[96] J. Illig, J.P. Schmidt, M. Weiss, A. Weber, E. Ivers-Tiffée, "Understanding the impedance spectrum of 18650 $LiFePO_4$-cells," *J. Power Sources*. 239 (2013) 670–679. doi:10.1016/j.jpowsour.2012.12.020.

[97] J. Illig, M. Ender, T. Chrobak, J.P. Schmidt, D. Klotz, E. Ivers-Tiffee, "Separation of Charge Transfer and Contact Resistance in $LiFePO_4$-Cathodes by Impedance Modeling," *J. Electrochem. Soc.* 159 (2012) A952–A960. doi:10.1149/2.030207jes.

[98] Y. Li, M. Bettge, B. Polzin, Y. Zhu, M. Balasubramanian, D.P. Abraham, "Understanding Long-Term Cycling Performance of $Li_{1.2}Ni_{0.15}Mn_{0.55}Co_{0.1}O_2$–Graphite Lithium-Ion Cells," *J. Electrochem. Soc.* 160 (2013) A3006–A3019. doi:10.1149/2.002305jes.

[99] J. Groot, M. Swierczynski, A.I. Stan, S.K. Kaer, "On the complex ageing characteristics of high-power $LiFePO_4$/graphite battery cells cycled with high charge and discharge currents,"

J. Power Sources. 286 (2015) 475–487. doi:10.1016/j.jpowsour.2015.04.001.

[100] W. Cao, J. Li, Z. Wu, "Cycle-life and degradation mechanism of $LiFePO_4$-based lithium-ion batteries at room and elevated temperatures," *Ionics (Kiel).* (2016). doi:10.1007/s11581-016-1703-4.

[101] D.I. Stroe, M. Swierczynski, A.I. Stan, V. Knap, R. Teodorescu, S.J. Andreasen, Diagnosis of lithium-ion batteries state-of-health based on electrochemical impedance spectroscopy technique, in: Energy Convers. Congr. Expo. (ECCE), 2014 IEEE, *IEEE Press*, 2014: pp. 4576–4582. doi:10.1109/ECCE.2014.6954027.

[102] M. Safari, C. Delacourt, "Aging of a Commercial Graphite/$LiFePO_4$ Cell," *J. Electrochem. Soc.* 158 (2011) A1123–A1135. doi:10.1149/1.3614529.

[103] T.G. Zavalis, M. Klett, M.H. Kjell, M. Behm, R.W. Lindström, G. Lindbergh, "Aging in lithium-ion batteries: Model and experimental investigation of harvested $LiFePO_4$ and mesocarbon microbead graphite electrodes," *Electrochim. Acta.* 110 (2013) 335–348. doi:10.1016/j.electacta.2013.05.081.

[104] Y. Zhang, C.Y. Wang, X. Tang, "Cycling degradation of an automotive $LiFePO_4$ lithium-ion battery," *J. Power Sources*. 196 (2011) 1513–1520. doi:10.1016/j.jpowsour.2010.08.070.

[105] X. Lin, H.E. Perez, S. Mohan, J.B. Siegel, A.G. Stefanopoulou, Y. Ding, M.P. Castanier, "A lumped-parameter electro-thermal model for cylindrical batteries," *J. Power Sources*. 257 (2014) 1–11. doi:10.1016/j.jpowsour.2014.01.097.

[106] Y. Zheng, Y.B. He, K. Qian, B. Li, X. Wang, J. Li, S.W. Chiang, C. Miao, F. Kang, J. Zhang, "Deterioration of lithium iron phosphate/graphite power batteries under high-rate discharge cycling," *Electrochim. Acta.* 176 (2015) 270–279. doi:10.1016/j.electacta.2015.06.096.

[107] M. Held, U. Sennhauser, "Stress-induced Ageing of Lithium-Ion Batteries," *Chim. Int. J. Chem.* 69 (2015) 737–740. doi:10.2533/chimia.2015.737.

[108] E. Prada, D. Di Domenico, Y. Creff, J. Bernard, V. Sauvant-Moynot, F. Huet, Physics-based modelling of $LiFePO_4$-graphite Li-ion batteries for power and capacity fade predictions: Application to calendar aging of PHEV and EV, in: 2012 IEEE Veh. Power Propuls. Conf. VPPC 2012, *IEEE*, 2012: pp. 301–308. doi:10.1109/VPPC.2012.6422717.

[109] M. Lewerenz, J. Münnix, J. Schmalstieg, S. Käbitz, M. Knips, D.U. Sauer, "Systematic aging of commercial $LiFePO_4$|Graphite cylindrical cells including a theory explaining rise of capacity during aging," *J. Power Sources*. 345 (2017) 254–263. doi:10.1016/j.jpowsour.2017.01.133.

[110] K. Amine, J. Liu, I. Belharouak, "High-temperature storage and cycling of C-$LiFePO_4$/graphite Li-ion cells," *Electrochem. Commun.* 7 (2005) 669–673. doi:10.1016/j.elecom.2005.04.018.

[111] R. Mingant, J. Bernard, V. Sauvant Moynot, A. Delaille, S. Mailley, J.-L. Hognon, F. Huet, "EIS Measurements for Determining the SoC and SoH of Li-Ion Batteries," *ECS Trans.* 33

(2011) 41–53. doi:10.1149/1.3589920.

[112] W. Shi, X. Hu, J. Wang, J. Jiang, Y. Zhang, T. Yip, "Analysis of Thermal Aging Paths for Large-Format $LiFePO_4$/Graphite Battery," *Electrochim. Acta.* 196 (2016) 13–23. doi:10.1016/j.electacta.2016.02.161.

[113] Y.M. Choi, S. Il Pyun, J.S. Bae, S.I. Moon, "Effects of lithium content on the electrochemical lithium intercalation reaction into $LiNiO_2$ and $LiCoO_2$ electrodes," *J. Power Sources.* 56 (1995) 25–30. doi:10.1016/0378-7753(95)80004-Z.

[114] S.S. Zhang, K. Xu, T.R. Jow, "Charge and discharge characteristics of a commercial $LiCoO_2$-based 18650 Li-ion battery," *J. Power Sources.* 160 (2006) 1403–1409. doi:10.1016/j.jpowsour.2006.03.037.

[115] Z. Wang, Z. Wang, W. Peng, H. Guo, X. Li, J. Wang, A. Qi, "Structure and electrochemical performance of $LiCoO_2$ cathode material in different voltage ranges," *Ionics (Kiel).* 20 (2014) 1525–1534. doi:10.1007/s11581-014-1098-z.

[116] A. Matasso, D. Wong, D. Wetz, F. Liu, "Correlation of Bulk Internal Pressure Rise and Capacity Degradation of Commercial $LiCoO_2$ Cells," *J. Electrochem. Soc.* 161 (2014) 2031–2035. doi:10.1149/2.0221414jes.

[117] "Paul Scherrer Institut - Annual Report 2007," (2007). http://ecl.web.psi.ch (accessed May 8, 2017).

[118] B. Zohuri, P. McDaniel, "Thermodynamics In Nuclear Power Plant Systems," 2015. doi:10.1007/978-3-319-13419-2.

[119] D.R. Gaskell, "Introduction to the thermodynamics of materials," *Taylor & Francis*, 2003.

[120] MIT, "Definitions and Fundamental Ideas of Thermodynamics," (2015). http://web.mit.edu/16.unified/www/FALL/thermodynamics/notes/node11.html (accessed May 29, 2017).

[121] P. Atkins, "The Laws of Thermodynamics: A Very Short Introduction," 2010. doi:10.1093/actrade/9780199572199.001.0001.

[122] I. Kondepudi, Dilip, and Prigogine, "Modern Thermodynamics. From heat Engines to Dissipative Structures.," *John Wiley & Sons*, 1998.

[123] M.W. Zemansky, R. Dittman, "Calor y termodyna□ mica," *Madrid: McGraw-Hill.* (1984).

[124] Wikipedia, "Carnot heat engine," (n.d.). doi:https://en.wikipedia.org/wiki/Carnot_heat_engine.

[125] G. Lebon, D. Jou, J. Casas-Vázquez, "Understanding non-equilibrium thermodynamics: Foundations, applications, frontiers," *Springer Berlin Heidelberg*, Berlin, Heidelberg, 2008. doi:10.1007/978-3-540-74252-4.

[126] J. Lemaitre, J.-L. Chaboche, "Mechanics of solid materials," *Cambridge University Press*, 1992. doi:10.1139/l92-025.

[127] C. Basaran, C.-Y. Yan, "A Thermodynamic Framework for Damage Mechanics of Solder

Joints," *J. Electron. Packag.* 120 (1998) 379. doi:10.1115/1.2792650.

[128] M. Amiri, M.M. Khonsari, "On the thermodynamics of friction and wear-A review," *Entropy*. 12 (2010) 1021–1049. doi:10.3390/e12051021.

[129] M. Naderi, M. Amiri, M.M. Khonsari, "On the thermodynamic entropy of fatigue fracture," *Proc. R. Soc. A Math. Phys. Eng. Sci.* 466 (2010) 423–438. doi:10.1098/rspa.2009.0348.

[130] M.M. Khonsari, M. Amiri, "Introduction to Thermodynamics of Mechanical Fatigue," *CRC Pr I Llc*, 2012.

[131] M. Naderi, M.M. Khonsari, "Thermodynamic analysis of fatigue failure in a composite laminate," *Mech. Mater.* 46 (2012) 113–122. doi:10.1016/j.mechmat.2011.12.003.

[132] S. Li, C. Basaran, "A computational damage mechanics model for thermomigration," *Mech. Mater.* 41 (2009) 271–278. doi:10.1016/j.mechmat.2008.10.013.

[133] W. Yao, C. Basaran, "Computational damage mechanics of electromigration and thermomigration," *J. Appl. Phys.* 114 (2013) 103708. doi:10.1063/1.4821015.

[134] C.W. Lewis, J.J. Bohrer, Physics of Resistor Failure, in: First Annu. Symp. Phys. Fail. Electron., *IEEE*, 1962: pp. 11–19. doi:10.1109/IRPS.1962.359980.

[135] K.M. Browne, "Thermodynamic steady states in simple electrical circuits," *J. Non-Equilibrium Thermodyn.* 28 (2003) 147–165. doi:10.1515/JNETDY.2003.008.

[136] E. Sa□nchez-Sinencio, A.G. Andreou, "Low-voltage/low-power integrated circuits and systems : low-voltage mixed-signal ciruits," *IEEE Press*, 1999.

[137] Y. Reynier, J. Graetz, T. Swan-Wood, P. Rez, R. Yazami, B. Fultz, "Entropy of Li intercalation in Li_xCoO_2," *Phys. Rev. B.* 70 (2004) 174304. doi:10.1103/PhysRevB.70.174304.

[138] R. Yazami, J. McMenamin, Y. Reynier, T. Fultz, Brent, A Battery State of Health Assessment System, PCT/US2010/026991, 2010.

[139] M. Amiri, M. Modarres, "An entropy-based damage characterization," *Entropy*. 16 (2014) 6434–6463. doi:10.3390/e16126434.

[140] M. Xiao, S.Y. Choe, "Theoretical and experimental analysis of heat generations of a pouch type $LiMn_2O_4$/carbon high power Li-polymer battery," *J. Power Sources*. 241 (2013) 46–55. doi:10.1016/j.jpowsour.2013.04.062.

[141] M. Petzl, M.A. Danzer, "Advancements in OCV Measurement and Analysis for Lithium-Ion Batteries," *IEEE Trans. Energy Convers.* 28 (2013) 675–681. doi:10.1109/TEC.2013.2259490.

[142] M. Dubarry, B.Y. Liaw, "Identify capacity fading mechanism in a commercial $LiFePO_4$ cell," *J. Power Sources*. 194 (2009) 541–549. doi:10.1016/j.jpowsour.2009.05.036.

[143] Y. Zhu, C. Wang, "Strain accommodation and potential hysteresis of $LiFePO_4$ cathodes during lithium ion insertion/extraction," *J. Power Sources*. 196 (2011) 1442–1448. doi:10.1016/j.jpowsour.2010.08.008.

[144] A. Barai, W. Dhammika Widanage, A. McGordon, P. Jennings, The influence of temperature and charge-discharge rate on open circuit voltage hysteresis of an LFP Li-ion battery, in: 2016

IEEE Transp. Electrif. Conf. Expo, ITEC 2016, 2016. doi:10.1109/ITEC.2016.7520299.

[145] G. Dong, J. Wei, C. Zhang, Z. Chen, "Online state of charge estimation and open circuit voltage hysteresis modeling of $LiFePO_4$ battery using invariant imbedding method," *Appl. Energy*. 162 (2016) 163–171. doi:10.1016/j.apenergy.2015.10.092.

[146] A. Farmann, D.U. Sauer, "A study on the dependency of the open-circuit voltage on temperature and actual aging state of lithium-ion batteries," *J. Power Sources*. 347 (2017) 1–13. doi:10.1016/j.jpowsour.2017.01.098.

[147] V. Srinivasan, J. Newman, "Existence of Path-Dependence in the $LiFePO_4$ Electrode," *Electrochem. Solid-State Lett.* 9 (2006) A110. doi:10.1149/1.2159299.

[148] A. Ter Heijne, O. Schaetzle, S. Gimenez, F. Fabregat-Santiago, J. Bisquert, D.P.B.T.B. Strik, F. Barrière, C.J.N. Buisman, H.V.M. Hamelers, "Identifying charge and mass transfer resistances of an oxygen reducing biocathode," *Energy Environ. Sci.* 4 (2011) 5035. doi:10.1039/c1ee02131a.

[149] C. Breitkopf, K. Swider-Lyons, "Springer Handbook of Electrochemical Energy," 2017. doi:10.1007/978-3-662-46657-5.

[150] F. Béguin, E. Frąckowiak, "Carbons for Electrochemical Energy Storage and Conversion Systems," *CRC Press*, 2009.

[151] K.A. Natarajan, "Exchange Current Density – Polarization Relationships Lecture 9," 2 (2015) 1–6. http://nptel.ac.in/courses/113108051/module2/lecture9.pdf (accessed May 28, 2017).

[152] A. Anderson, Surface Phenomena in Li-Ion Batteries, 2001. doi:10.1149/1.1393357.

[153] J.S. Gnanaraj, Y.S. Cohen, M.D. Levi, D. Aurbach, "The effect of pressure on the electroanalytical response of graphite anodes and $LiCoO_2$ cathodes for Li-ion batteries," *J. Electroanal. Chem.* 516 (2001) 89–102. doi:10.1016/S0022-0728(01)00663-5.

[154] C. Liu, Z.G. Neale, G. Cao, "Understanding electrochemical potentials of cathode materials in rechargeable batteries," *Mater. Today*. 19 (2016) 109–123. doi:10.1016/j.mattod.2015.10.009.

[155] M. Dubarry, C. Truchot, B.Y. Liaw, "Synthesize battery degradation modes via a diagnostic and prognostic model," *J. Power Sources*. 219 (2012) 204–216. doi:10.1016/j.jpowsour.2012.07.016.

[156] K. Onda, T. Ohshima, M. Nakayama, K. Fukuda, T. Araki, "Thermal behavior of small lithium-ion battery during rapid charge and discharge cycles," *J. Power Sources*. 158 (2006) 535–542. doi:10.1016/j.jpowsour.2005.08.049.

[157] C. Zhang, F. Yan, C. Du, J. Kang, R. Turkson, "Evaluating the Degradation Mechanism and State of Health of $LiFePO_4$ Lithium-Ion Batteries in Real-World Plug-in Hybrid Electric Vehicles Application for Different Ageing Paths," *Energies*. 10 (2017) 110. doi:10.3390/en10010110.

[158] M. Dubarry, C. Truchot, B.Y. Liaw, "Cell degradation in commercial $LiFePO_4$ cells with high-

power and high-energy designs," *J. Power Sources*. 258 (2014) 408–419. doi:10.1016/j.jpowsour.2014.02.052.

[159] K. Maher, R. Yazami, "Effect of overcharge on entropy and enthalpy of lithium-ion batteries," *Electrochim. Acta*. 101 (2013) 71–78. doi:10.1016/j.electacta.2012.11.057.

[160] K. Maher, R. Yazami, "A study of lithium ion batteries cycle aging by thermodynamics techniques," *J. Power Sources*. 247 (2014) 527–533. doi:10.1016/j.jpowsour.2013.08.053.

[161] A. Marongiu, D.U. Sauer, "On-board aging estimation using half-cell voltage curves for $LiFePO_4$ cathode-based lithium-ion batteries for EV applications," *Int. J. Automot. Technol.* 17 (2016) 465–472. doi:10.1007/s12239-016-0048-3.

[162] M.A. Roscher, D.U. Sauer, "Dynamic electric behavior and open-circuit-voltage modeling of $LiFePO_4$-based lithium ion secondary batteries," *J. Power Sources*. 196 (2011) 331–336. doi:10.1016/j.jpowsour.2010.06.098.

[163] J. Xu, R.D. Deshpande, J. Pan, Y.-T. Cheng, V.S. Battaglia, "Electrode Side Reactions, Capacity Loss and Mechanical Degradation in Lithium-Ion Batteries," *J. Electrochem. Soc.* 162 (2015) A2026–A2035. doi:10.1149/2.0291510jes.

[164] R. Chandrasekaran, "Quantification of contributions to the cell overpotential during galvanostatic discharge of a lithium-ion cell," *J. Power Sources*. 262 (2014) 501–513. doi:10.1016/j.jpowsour.2014.03.124.

[165] Bazant, "Pseudocapacitors and batteries," *MIT Lect.* (2011) 1–12. https://ocw.mit.edu/courses/chemical-engineering/10-626-electrochemical-energy-systems-spring-2014/lecture-notes/MIT10_626S14_S11lec37.pdf (accessed June 2, 2017).

[166] P. Arora, "Capacity Fade Mechanisms and Side Reactions in Lithium-Ion Batteries," *J. Electrochem. Soc.* 145 (1998) 3647. doi:10.1149/1.1838857.

[167] M.H.-M. Tang, Side Reactions in Lithium-Ion Batteries, 2012. http://escholarship.org/uc/item/331948fw#page-3 (accessed May 24, 2017).

[168] Y. Reynier, R. Yazami, B. Fultz, I. Barsukov, "Evolution of lithiation thermodynamics with the graphitization of carbons," *J. Power Sources*. 165 (2007) 552–558. doi:10.1016/j.jpowsour.2006.10.024.

[169] Y.F. Reynier, R. Yazami, B. Fultz, "Thermodynamics of Lithium Intercalation into Graphites and Disordered Carbons," *J. Electrochem. Soc.* 151 (2004) A422. doi:10.1149/1.1646152.

[170] R. Yazami, Y. Reynier, "Thermodynamics and crystal structure anomalies in lithium-intercalated graphite," *J. Power Sources*. 153 (2006) 312–318. doi:10.1016/j.jpowsour.2005.05.087.

[171] B. Saha, K. Goebel, "Modeling Li-ion battery capacity depletion in a particle filtering framework," *Proc. Annu. Conf. Progn. Heal. Manag. Soc.* (2009) 2909--2924.

[172] A. Cuadras, R. Romero, V.J. Ovejas, "Irreversible entropy model for damage diagnosis in resistors," *J. Appl. Phys.* 118 (2015). doi:10.1063/1.4934740.

[173] G. Ning, B. Haran, B.N. Popov, "Capacity fade study of lithium-ion batteries cycled at high discharge rates," *J. Power Sources*. 117 (2003) 160–169. doi:10.1016/S0378-7753(03)00029-6.

[174] V. V. Viswanathan, D. Choi, D. Wang, W. Xu, S. Towne, R.E. Williford, J.-G. Zhang, J. Liu, Z. Yang, "Effect of entropy change of lithium intercalation in cathodes and anodes on Li-ion battery thermal management," *J. Power Sources*. 195 (2010) 3720–3729. doi:10.1016/j.jpowsour.2009.11.103.

[175] M. Lang, M.S.D. Darma, K. Kleiner, L. Riekehr, L. Mereacre, M. Ávila Pérez, V. Liebau, H. Ehrenberg, "Post mortem analysis of fatigue mechanisms in $LiNi_{0.8}Co_{0.15}Al_{0.05}O_2$ – $LiNi_{0.5}Co_{0.2}Mn_{0.3}O_2$ – $LiMn_2O_4$/graphite lithium ion batteries," *J. Power Sources*. 326 (2016) 397–409. doi:10.1016/j.jpowsour.2016.07.010.

[176] Y. Surace, M. Simões, S. Pokrant, A. Weidenkaff, "Capacity fading in Li_3MnO_4: A post-mortem analysis," *J. Electroanal. Chem.* 766 (2016) 44–51. doi:10.1016/j.jelechem.2016.01.029.

[177] M. Klett, R. Eriksson, J. Groot, P. Svens, K. Ciosek Högström, R.W. Lindström, H. Berg, T. Gustafson, G. Lindbergh, K. Edström, "Non-uniform aging of cycled commercial LiFePO4//graphite cylindrical cells revealed by post-mortem analysis," *J. Power Sources*. 257 (2014) 126–137. doi:10.1016/j.jpowsour.2014.01.105.

[178] C. Julien, Z. Stoynov, "Materials for Lithium-Ion Batteries," *Springer Netherlands*, 2000.

[179] "ICP-OES | RoHS Testing Laboratory," *RoSH Test. Lab.* (n.d.). http://www.rohs-cmet.in/content/icp-oes (accessed June 11, 2017).

[180] M. Evertz, C. Lürenbaum, B. Vortmann, M. Winter, S. Nowak, "Development of a method for direct elemental analysis of lithium ion battery degradation products by means of total reflection X-ray fluorescence," *Spectrochim. Acta - Part B At. Spectrosc.* 112 (2015) 34–39. doi:10.1016/j.sab.2015.08.005.

[181] K. Xu, S. Zhang, R. Jow, "Electrochemical impedance study of graphite/electrolyte interface formed in LiBOB/PC electrolyte," *J. Power Sources*. 143 (2005) 197–202. doi:10.1016/j.jpowsour.2004.11.026.

[182] S. Migge, G. Sandmann, D. Rahner, H. Dietz, W. Plieth, "Studying lithium intercalation into graphite particles via in situ Raman spectroscopy and confocal microscopy," *J. Solid State Electrochem.* 9 (2005) 132–137. doi:10.1007/s10008-004-0563-4.

[183] T.R. Ferguson, M.Z. Bazant, "Phase transformation dynamics in porous battery electrodes," *Electrochim. Acta*. 146 (2014) 89–97. doi:10.1016/j.electacta.2014.08.083.

[184] M. Ouyang, Z. Chu, L. Lu, J. Li, X. Han, X. Feng, G. Liu, "Low temperature aging mechanism identification and lithium deposition in a large format lithium iron phosphate battery for different charge profiles," *J. Power Sources*. 286 (2015) 309–320. doi:10.1016/j.jpowsour.2015.03.178.

[185] T.C. Bach, S.F. Schuster, E. Fleder, J. Müller, M.J. Brand, H. Lorrmann, A. Jossen, G. Sextl, J. Müller, M.J. Brand, H. Lorrmann, A. Jossen, G. Sextl, "Nonlinear aging of cylindrical

lithium-ion cells linked to heterogeneous compression," *J. Energy Storage*. 5 (2016) 212–223. doi:10.1016/j.est.2016.01.003.

[186] Qnovo, "Lithium plating is immensely hazardous," (n.d.). https://qnovo.com/lithium-plating-is-immensely-hazardous/ (accessed June 14, 2017).

[187] J. Illig, T. Chrobak, D. Klotz, E. Ivers-Tiffe□ e, "Evaluation of the Rate Determining Processes for $LiFePO_4$ as Cathode Material in Lithium-Ion-Batteries," *ECS Trans.* 33 (2011) 3–15. doi:10.1149/1.3564865.

[188] E.M. Krieger, Effects of variability and rate on battery charge storage and lifespan, 2013. http://citeseerx.ist.psu.edu/viewdoc/download?doi=10.1.1.876.2485&rep=rep1&type=pdf (accessed April 28, 2017).

[189] T. Liu, A. Garsuch, F. Chesneau, B.L. Lucht, "Surface phenomena of high energy $Li(Ni_{1/3}Co_{1/3}Mn_{1/3})O_2$ /graphite cells at high temperature and high cutoff voltages," *J. Power Sources*. 269 (2014) 920–926. doi:10.1016/j.jpowsour.2014.07.051.

[190] M. Kerlau, J.A. Reimer, E.J. Cairns, "Investigation of particle isolation in Li-ion battery electrodes using 7Li NMR spectroscopy," *Electrochem. Commun.* 7 (2005) 1249–1251. doi:10.1016/j.elecom.2005.09.003.

[191] R. Dell, D.A.J. (David A.J. Rand, "Understanding Batteries," *Royal Society of Chemistry*, 2001. doi:10.1039/9781847552228.

[192] J. Prakash, D. Chu, D. Scherson, M. Enayetullah, I. Tae Bae, "Fundamental understanding of electrode processes in memory of Professor Ernest B. Yeager," *Electrochemical Society*, 2005.

[193] S. Santhanagopalan, K. Smith, J. Neubauer, G.H. Kim, A. Pesaran, M. Keyser, "Design and Analysis of Large Lithium-Ion Battery Systems," *Artech House*, 2014.

[194] A. Cuadras, R. Romero, V.J. Ovejas, "Entropy characterisation of overstressed capacitors for lifetime prediction," *J. Power Sources*. 336 (2016) 272–278. doi:10.1016/j.jpowsour.2016.10.077.